Enhanced Analysis of Falling Weight Deflectometer Data for Use With Mechanistic-Empirical Flexible Pavement Design and Analysis and Recommendations for Improvements to Falling Weight Deflectometers

U.S. Department of Transportation
Federal Highway Administration

FOREWORD

This report documents a study conducted to review the status of falling weight deflectometer (FWD) equipment, data collection, analysis, and interpretation, including dynamic backcalculation, and to develop enhanced analysis procedures and recommendations for the effective use of FWD technology as it relates to the flexible pavement models and procedures incorporated within the *Mechanistic-Empirical Pavement Design Guide* developed by the National Cooperative Highway Research Program and subsequently adopted by the American Association of State Highway and Transportation Officials. In this context, dynamic backcalculation refers to the modeling of the dynamic or impact nature of the FWD loading and resulting pavement response of in-service flexible pavements for pavement structural analysis and rehabilitation design. The research effort resulted in development analysis methodologies, software tools implementing those analysis methodologies and a potential list of recommendations for FWD equipment enhancements, all of which are detailed in this report. This report is intended for use by pavement engineers involved in structural evaluation and rehabilitation design of flexible pavements and researchers involved in development of new procedures for the modeling and analysis of in-service flexible pavements.

Cheryl Allen Richter
Director, Office of Infrastructure
Research and Development

TECHNICAL REPORT DOCUMENTATION PAGE

1. Report No. FHWA-HRT-15-063	2. Government Accession No.	3. Recipient's Catalog No.
4. Title and Subtitle Enhanced Analysis of Falling Weight Deflectometer Data for Use With Mechanistic-Empirical Flexible Pavement Design and Analysis and Recommendations for Improvements to Falling Weight Deflectometers		5. Report Date March 2017
		6. Performing Organization Code
7. Author(s) Karim Chatti, M. Emin Kutay, Nizar Lajnef, Imen Zaabar, Sudhir Varma, and Hyung Suk Lee		8. Performing Organization Report No.
9. Performing Organization Name and Address Michigan State University 426 Auditorium Road East Lansing, MI 48824		10. Work Unit No. (TRAIS)
		11. Contract or Grant No. DTFH61-11-C-00026
12. Sponsoring Agency Name and Address Federal Highway Administration Office of Acquisition Management 1200 New Jersey Avenue SE Washington, DC 20590		13. Type of Report and Period Covered Final Report, April 2011–November 2013
		14. Sponsoring Agency Code

15. Supplementary Notes
The Contracting Officer's Technical Representative was Nadarajah Sivaneswaran, HRDI-20.

16. Abstract
This report describes the efforts undertaken to review the status of falling weight deflectometer (FWD) equipment, data collection, analysis, and interpretation, including dynamic backcalculation, as they relate to the models and procedures incorporated in the *Mechanistic-Empirical Pavement Design Guide*. The work conducted in this project resulted in the following:

- Development of a backcalculation scheme (BACKLAVA) in the time domain using a quasi-static model (LAVA) as its forward solution and genetic algorithm (GA) as its search engine. BACKLAVA is a backcalculation algorithm for a constant asphalt concrete (AC) layer temperature.
- Development of a backcalculation scheme (BACKLAVAP) in the time domain using a quasi-static model (LAVAP) as its forward solution and GA as its search engine. BACKLAVAP is a backcalculation algorithm for a temperature profile in an AC layer.
- Development of a backcalculation scheme (BACKLAVAN) in the time domain using a quasi-static model (LAVAN) as its forward solution and GA as its search engine. BACKLAVAN is a backcalculation algorithm for a viscoelastic AC layer and a nonlinear base layer.
- Development of a backcalculation scheme (DYNABACK-VE) in the time domain using a time-domain viscoelastic dynamic model (ViscoWave-II) as its forward solution and a hybrid approach (GA and Levenberg-Marquardt algorithm) as its search engine. DYNABACK-VE is a backcalculation algorithm for a viscoelastic AC layer with temperature profile and linear unbound layers.
- Short list of recommendations for FWD equipment enhancements.

The tools developed in this project are standalone applications that could be used on most computers.

17. Key Words Pavement management, Falling weight deflectometer, Backcalculation, Time domain analysis, Viscoelastic analysis, Forward solution	18. Distribution Statement No restrictions. This document is available through the National Technical Information Service, Springfield, VA 22161. http://www.ntis.gov/about/contact.aspx		
19. Security Classif. (of this report) Unclassified	20. Security Classif. (of this page) Unclassified	21. No. of Pages 319	22. Price N/A

Form DOT F 1700.7 (8-72)   Reproduction of completed page authorized

SI* (MODERN METRIC) CONVERSION FACTORS

APPROXIMATE CONVERSIONS TO SI UNITS

Symbol	When You Know	Multiply By	To Find	Symbol
LENGTH				
in	inches	25.4	millimeters	mm
ft	feet	0.305	meters	m
yd	yards	0.914	meters	m
mi	miles	1.61	kilometers	km
AREA				
in^2	square inches	645.2	square millimeters	mm^2
ft^2	square feet	0.093	square meters	m^2
yd^2	square yard	0.836	square meters	m^2
ac	acres	0.405	hectares	ha
mi^2	square miles	2.59	square kilometers	km^2
VOLUME				
fl oz	fluid ounces	29.57	milliliters	mL
gal	gallons	3.785	liters	L
ft^3	cubic feet	0.028	cubic meters	m^3
yd^3	cubic yards	0.765	cubic meters	m^3
NOTE: volumes greater than 1000 L shall be shown in m^3				
MASS				
oz	ounces	28.35	grams	g
lb	pounds	0.454	kilograms	kg
T	short tons (2000 lb)	0.907	megagrams (or "metric ton")	Mg (or "t")
TEMPERATURE (exact degrees)				
°F	Fahrenheit	5 (F-32)/9 or (F-32)/1.8	Celsius	°C
ILLUMINATION				
fc	foot-candles	10.76	lux	lx
fl	foot-Lamberts	3.426	candela/m^2	cd/m^2
FORCE and PRESSURE or STRESS				
lbf	poundforce	4.45	newtons	N
lbf/in^2	poundforce per square inch	6.89	kilopascals	kPa

APPROXIMATE CONVERSIONS FROM SI UNITS

Symbol	When You Know	Multiply By	To Find	Symbol
LENGTH				
mm	millimeters	0.039	inches	in
m	meters	3.28	feet	ft
m	meters	1.09	yards	yd
km	kilometers	0.621	miles	mi
AREA				
mm^2	square millimeters	0.0016	square inches	in^2
m^2	square meters	10.764	square feet	ft^2
m^2	square meters	1.195	square yards	yd^2
ha	hectares	2.47	acres	ac
km^2	square kilometers	0.386	square miles	mi^2
VOLUME				
mL	milliliters	0.034	fluid ounces	fl oz
L	liters	0.264	gallons	gal
m^3	cubic meters	35.314	cubic feet	ft^3
m^3	cubic meters	1.307	cubic yards	yd^3
MASS				
g	grams	0.035	ounces	oz
kg	kilograms	2.202	pounds	lb
Mg (or "t")	megagrams (or "metric ton")	1.103	short tons (2000 lb)	T
TEMPERATURE (exact degrees)				
°C	Celsius	1.8C+32	Fahrenheit	°F
ILLUMINATION				
lx	lux	0.0929	foot-candles	fc
cd/m^2	candela/m^2	0.2919	foot-Lamberts	fl
FORCE and PRESSURE or STRESS				
N	newtons	0.225	poundforce	lbf
kPa	kilopascals	0.145	poundforce per square inch	lbf/in^2

*SI is the symbol for the International System of Units. Appropriate rounding should be made to comply with Section 4 of ASTM E380.
(Revised March 2003)

TABLE OF CONTENTS

LIST OF FIGURES

LIST OF TABLES

ACRONYMS

2-D	two-dimensional
3-D	three-dimensional
AC	asphalt concrete
ANN	artificial neural network
BMFLC	band-limited multiple Fourier linear combiner
CPU	central processing unit
CRTB	crumb rubber terminal blend
DFT	discrete Fourier transform
DMI	distance measuring instrument
EKF	extended Kalman filter
FEA	finite element analysis
FEM	finite element method
FFT	fast Fourier transform
FHWA	Federal Highway Administration
FWD	falling weight deflectometer
GA	genetic algorithm
GB	gigabyte
GPR	ground penetrating radar
HMA	hot mix asphalt
HPCC	High Performance Computer Center
KF	Kalman filter
LM	Levenberg-Marquardt
LTPP	Long-Term Pavement Performance
LVDT	linear variable displacement transducer
M-E	mechanistic-empirical
MDOT	Michigan Department of Transportation
MEPDG	*Mechanistic-Empirical Pavement Design Guide*
ML	midlane
MPI	message passing interface
NDT	nondestructive testing
OW	outer wheel
PC	personal computer
PMS	pavement management system
RAM	random access memory
SNR	signal-to-noise ratio
UMAT	user-defined material
USACE-WES	United States Army Corps of Engineers Waterway Experiment Station
WFLC	weighted-frequency Fourier linear combiner

CHAPTER 1. INTRODUCTION

This report describes the efforts undertaken to develop methodologies for the determination of the damaged master curve and unbound material properties of in-service pavements from enhanced falling weight deflectometer (FWD) data.

BACKGROUND

Pavement characterization is important for determining cost-effective treatment type and allocation of funds and resources to maintain and rehabilitate the deteriorating highway infrastructure. The key element in the success of any pavement management system responsible for making preventive and corrective decisions is a proper assessment of the present status and an accurate prediction of the future performance of pavement structure. Characterizing pavement properties plays a critical role in both activities.

Nondestructive testing (NDT) is a well-recognized method for evaluating the structural capacity and integrity of highway and airfield pavements. The use of an FWD is one of the most frequently employed NDT methods for evaluating the structural integrity of an existing pavement. As its full name implies, the FWD is equipped with a falling mass mechanism capable of inducing an impact load on the pavement surface. Because of the nature of the impact load generated by a falling mass, the load typically has a short duration (usually 20 to 40 ms) and gives rise to a stress wave that propagates through the pavement structure. The resulting time-dependent response of the pavement structure, or more specifically, the vertical deflection at the pavement surface resulting from the stress wave, is measured at various radial distances from the load and is recorded for the structural analysis of the pavement system. FWD testing enables the use of a mechanistic approach for pavement design and rehabilitation by allowing for backcalculating in situ material properties from the measured field surface deflections through appropriate analysis techniques. In deflection methods, pavement deflections represent an overall system response of the pavement layers and the roadbed soil to an applied load. Pavement surface deflections have traditionally been used as an indicator of its structural capacity.

The need to accurately characterize the structural condition of existing pavements has increased with the recent development, release, and ongoing implementation of the *Mechanistic-Empirical Pavement Design Guide* (MEPDG).[1] A number of different material inputs are required in the procedure, and it is important that these be adequately characterized and defined. The analysis of deflection data collected by the FWD provides a fast and reliable way of characterizing the properties of the paving layers, as well as assessing the load-carrying capacity of existing pavement structures. With the release of the new MEPDG, there is a strong need for identifying and evaluating the way that FWD testing is operated and integrated in the new design procedure.[1]

PROJECT SCOPE

The MEPDG theoretical and empirical models predict response of flexible and rigid pavements.[1] The dynamic modulus ($|E^*|$) master curve of asphalt concrete (AC) layer is a fundamental material property that is required as an input in MEPDG for a flexible pavement analysis. Knowledge of the $|E^*|$ master curve of an in-service pavement using FWD data can lead to more accurate estimation of its remaining life.

The overall objective of the research was to theoretically determine a static and dynamic viscoelastic flexible pavement response model and relevant FWD data inputs to be used in a backcalculation scheme for determining damaged $E(t)$ master curve and unbound material properties of in-service pavements.

PROJECT OBJECTIVES

The objectives of the project are as follows:

- Review the status of FWD equipment, data collection, analysis, and interpretation, including dynamic backcalculation, as they relate to the models and procedures incorporated in the MEPDG.[1]

- Conduct theoretical analyses to identify suitable data requirements from FWD in light of current FWD technology and feasible equipment enhancements.

- Develop methodologies for the determination of the damaged master curve and unbound material properties of in-service pavements from enhanced FWD data.

- Develop recommendations for FWD equipment enhancements.

REPORT STRUCTURE

The remaining chapters of this report are organized as follows:

- Chapter 2 reviews the status of FWD equipment, data collection, analysis, and interpretation, including dynamic backcalculation, as they relate to the models and procedures incorporated in MEPDG.[1]

- Chapter 3 presents the detailed analysis of the Long-Term Pavement Performance (LTPP) Program database conducted to assess when dynamic effects and nonlinearity are prevalent.

- Chapter 4 outlines the development of a quasi-static viscoelastic flexible pavement response model (LAVA) and a backcalculation scheme (BACKLAVA).

- Chapter 5 describes a newly developed dynamic time-domain viscoelastic flexible pavement response model (ViscoWave-II) and a backcalculation algorithm (DYNABACK-VE). It presents the verification results for the developed algorithm. Verification was accomplished by comparing the simulation results from the developed algorithm to some of the other existing solutions. Then the iteration algorithms were tested using theoretically generated deflection time histories and field measured data.

- Chapter 6 provides recommendations for FWD equipment enhancements.

- Chapter 7 summarizes the work performed under this project, outlines the main research products developed, and presents the main findings of the study.

- Appendix A presents the results of the comparison between the LAVAN and the nonlinear finite element method (FEM) software MICHPAVE. The algorithm was compared for the cases when the unbound layer was considered as a single layer for nonlinearity calculations (Algorithm1) and when the layer was divided into two sections (Algorithm2).

- Appendix B describes the detailed analysis on the effect of using multiple pulses on the backcalculation results.

- Appendix C describes in detail the theoretical development of the new algorithm for ViscoWave-II. The theoretical development for the proposed methodology follows similar steps to those used for the development of LAMDA, the spectral element method, which used the discrete transforms for solving the wave equations.[2] However, the proposed solution uses the continuous integral transforms (namely Laplace and Hankel transforms) that are more appropriate for transient, nonperiodic signals.[3]

- Appendix D presents the FWD site/field data collected as part of this project and used for backcalculation.

CHAPTER 2. LITERATURE REVIEW

This chapter presents a comprehensive review of the status of FWD equipment, market-ready and prototype models, data collection, analysis, and interpretation as they relate to the models and procedures incorporated in the MEPDG.[1]

REVIEW OF STATUS OF FWD EQUIPMENT

The FWD is an impulse load deflection device. According to ASTM D-4694-96, the basic components of an FWD (figure 1) are the following:[4]

- Load cell: The FWD releases known variable weights (from 3,000 to more than 50,000 lbf) from a given height onto a load plate resting on the pavement structure, producing a load on the pavement that is similar in magnitude and duration to that of a moving wheel load. The system should display and store load measurement with a 45-lbf resolution.

- Linear variable displacement transducer (LVDT), geophones, and accelerometers: A series of sensors are located at fixed distances from the load plate, so that a deflection can be measured. The system should display and store deflection measurement with ±0.039 mil or less of resolution. The sensor spacing depends on the pavement surface being tested and the number of sensors on the FWD. For example, for basin testing, the LTPP FWD manual requires that the sensors should be placed at -12, 0, 8, 12, 18, 24, 36, 48, and 60 inches for a nine-sensor FWD and 0, 8, 12, 18, 24, 36, and 60 inches for a seven-sensor FWD.[5]

- Infrared temperature gauges: pavement temperature, air temperature, surface temperature.

- Electronic distance measurement.

- Control/data acquisition unit.

Most FWDs are either trailer-towed or vehicle-mounted systems.[6] Developed in the 1970s, the FWD emerged in the 1980s as the worldwide standard for pavement deflection testing. The equipment of four FWD manufacturers—Grontmij Pavement Consultants, Dynatest®, Foundation Mechanics, Inc. (JILS™), and KUAB—are described in the following sections. The Federal Highway Administration (FHWA) has established four regional FWD calibration centers across the United States to provide annual calibrations of the FWD equipment to ensure the equipment is operating within allowable tolerances.
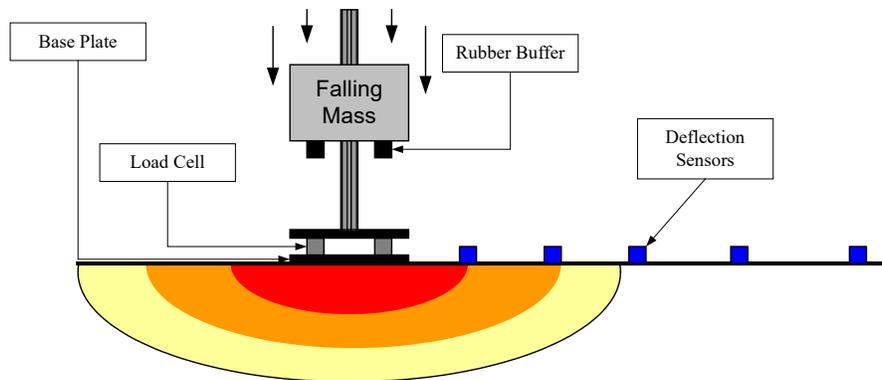
Figure 1. Diagram. FWD testing schematic.

FWD Manufacturers and Equipment

Grontmij Pavement Consultants

The Grontmij Pavement Consultants Group (manufacturers of the Carlo Bro FWD) offers the following three types of FWDs with a modular equipment design ready for upgrade (figure 2):

- The trailer-mounted FWD is mounted to the tow vehicle by a double-axle trailer, and it is supplied with a personal computer (PC), PRIMAX Data Collection FWD software (RoSy DESIGN), time-history module, transport lock, distance-measuring instrument (DMI) integrated in the software, three temperature sensors, 4-split load plate (12 or 18 inches), and 10 to 18 geophones. The system generates forces up to 78,600 lbf.

- The vehicle-mounted FWD is identical to the trailer-mounted FWD except that it is integrated into a van and has up to 18 geophones.

- The portable LWD is delivered with 4- and 12-inch-diameter loading plates, a 22-lb weight, integrated load cell and electronic box, and a center-mounted geophone. Extension with a beam for two extra geophones is possible. A portable PC or a personal digital assistant with a data collection program installed is required.

Source: Grontmij A/S

Figure 2. Photo. Grontmij Pavement Consultants FWDs.

Dynatest®

The Dynatest® FWD is a trailer-mounted system with an operations control computer located in the tow vehicle. The computer controls the complete operation of the FWD, including the lowering and raising of the load plate and deflection sensor bar as well as the sequencing of drop heights. Many FWDs are fitted with external cameras to help operators precisely align on selected testing locations.

Figure 3 shows a comparison of the two Dynatest®FWD trailer-mounted models, the 8000 and the 8082. The 8000 model supports drop masses from 110 to 770 lb, resulting in peak impact loads from 1,500 to 27,000 lbf, whereas the 8082 supports drop masses from 441 to 1,543 lb, resulting in peak impact loads from 6,500 to 54,000 lbf.[7] Typical testing production rates range from about 200 to 300 points per day, depending on traffic control requirements and specific testing locations.

Two different plate sizes can be used with the Dynatest® FWD—an 11.8-inch-diameter plate or a 17.7-inch-diameter plate. The smaller plate is typically used for street and highway pavements, whereas the larger plate is commonly used on airfield pavements (and generally on the heavy-weight FWD model 8082).

The Dynatest® FWD is used in FHWA's LTPP Program, for which pavement deflection measurements have been routinely collected on more than 900 pavement sections since the late 1980s. Dynatest® also performs calibrations at its facilities in Florida and California, and some State transportation departments also have their own calibration facilities.
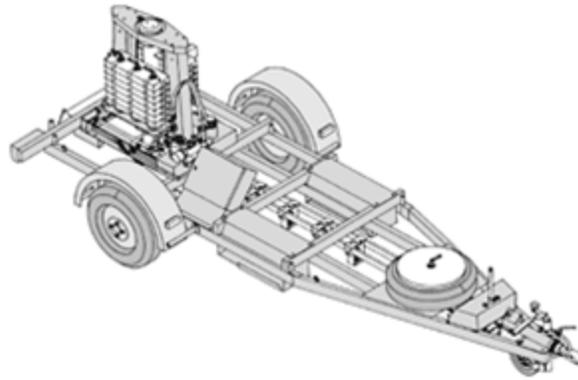
Dynatest® Model 8000 Falling Weight Deflectometer
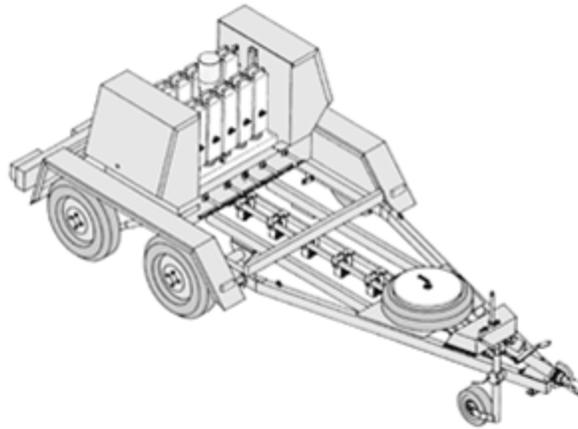
Dynatest® Model 8082 Heavy Weight Deflectometer

Source: Dynatest® Consulting, Inc.

Figure 3. Drawings. Comparison of two Dynatest® FWDs.

JILS™ (Foundation Mechanics, Inc.)

JILS™ produces three FWD systems: JILS-20, JILS-20HF, and JILS-20T with ground-penetrating radar (GPR). The JILS-20 is a trailer-mounted FWD. It is mounted on a double axle trailer. Like the Dynatest® FWDs, the system includes a 12-inch loading plate, DMI, temperature measurement hardware, and a video monitoring system. It has a separate gasoline engine with a 12-V alternator. Also, up to 10 sensors could be mounted in the vehicle. The company also provides its FWD data collection software.[8] The JILS-20HF is a heavy-load FWD. It is designed for testing pavement such as airfields or thick highway pavements. The specifications are similar to the JILS-20. The JILS-20T is identical to the JILS-20 except that it incorporates a GPR system with the FWD.

Applied Research Associates, Inc. (ARA) conducted an independent study to compare the JILS-20T and Dynatest® model 8002 FWDs.[9] Table 1 summarizes the key design and performance features of both FWDs. According to study findings, the two FWDs show similar trends. For AC pavement, the JILS™ FWD gave an average deflection

8

0.38 mil greater than the Dynatest® FWD, corresponding to a 2.4-percent average difference. In the case of chip seal, the average difference was 1.47 mil (3.4-percent difference). The study also compared backcalculated subgrade moduli, average deflection basins, and loading time history data. ARA concluded that both FWDs provided satisfactory data.[9]

Table 1. Comparison of JILS™ and Dynatest® FWD features.

Feature	JILS™ Model 20T	Dynatest® Model 8002
Number and type of deflection sensors	9 geophones available	9 geophones available
Load column tilting mechanism	Air bags	Load plate swivel
Load plate type and diameter	12-inch solid plate	11.8-inch solid split plate and 17.7-inch solid plates are available as options
Measured cycle duration	24 ms	35 ms

KUAB (Engineering and Research International, Inc.)

The KUAB FWD is a trailer-mounted dynamic impulse loading device that can be towed by any suitable towing vehicle.[10] Similar to other FWDs, the KUAB device has a loading system and series of deflection sensors. However, it also has its own defining characteristics, including a metal housing completely enclosing the loading system (see figure 4). A few other features include the following:

- **Two-mass configuration:** The initial load mass is dropped onto an intermediate buffering system. It transmits the force to another buffering system, which in turn transmits the load to the load plate. The use of the two-mass system creates a smoother load pulse that simulates the actual effects of a moving vehicle.[11]

- **Segmented load plate:** This type of plate ensures a uniform pressure distribution over the full area of the plate.

- **Seismometers:** Seven seismometers contact the surface during testing and measure the deflection from the plate. One sensor is placed over the load, while the other six are situated behind and in front of the load to measure displacement at different distances from the plate. Each seismometer includes an LVDT. Compared with other FWD sensors, seismometers may provide more direct deflection readings and have a larger measurement range. The deflection measuring sensors have a range of 0 to 200 mil.

Four KUAB models are available (KUAB 50, KUAB 120, KUAB 150, and KUAB 240), with the primary difference being the magnitude of the load that can be applied. The KUAB 50 is the lightest, with a standard load range of 3,000 to 14,000 lbf. It could be used on highway, street, and parking lot pavements. The KUAB 120 adds an 18-inch segmented load plate and has a standard load range of 1,500 to 27,000 lbf. The KUAB 150 model offers a standard load range of 3,000 to 33,000 lbf, making it a

suitable testing device for airport pavements, as well. The heaviest KUAB 240 device can impart a load of 66,000 lbf, making it suitable for use in airfield applications. All four models support up to seven deflection sensors.

As with the Dynatest® FWD, the KUAB has two loading plates available: 11.8 or 17.7 inches in diameter.

Source: Engineering and Research International, Inc.

Figure 4. Photo. KUAB FWD.[10]

Evaluation of Impulse Load Equipment

The FWDs described in the previous section have the ability to closely simulate the loading characteristics of a moving wheel load and to measure the deflection basin.[10] However, these FWDs are relatively complex electromechanical systems, require traffic control when performing testing, and have a high initial cost.[10]

One characteristic that should be considered when interpreting FWD deflection data is the loading time. The loading time is important to consider when evaluating differences in backcalculated moduli of viscoelastic materials because shorter loading times generally result in higher backcalculated modulus values for hot mix asphalt (HMA)[11]. The Dynatest® FWD produces a loading time of about 28 to 35 ms, whereas the JILS™ and KUAB devices produce a loading time of about 24 and 80 ms, respectively.[11] The Carlo Bro FWD produces a loading time of about 20 to 30 ms.

REVIEW OF STATUS OF FWD DATA COLLECTION, ANALYSIS, AND INTERPRETATION

Data Collection and Related Issues

Typical testing patterns for FWD testing vary depending on the purpose of the testing. For network-level testing, deflection testing is conducted at 500 to 1,500 ft in a single traffic lane.[11] This level of testing is normally sufficient to provide a general indicator of structural adequacy of the pavement network. For project-level testing, the test point spacing should be adequate to capture the variability in structural capacity of the

pavement.[12] Typical project-level testing intervals for HMA pavements are between 100 and 500 ft, with the shorter testing interval warranted for pavements in poorer condition and the larger testing interval appropriate for pavements in better condition. The recommended testing locations are on the outer wheel (OW) path of the outer traffic lane.

The primary issues related to FWD data analysis and interpretation are (1) errors in measurement (relevant to static and dynamic backcalculation) and (2) signal noise and truncation (relevant for dynamic analysis only).

FWD Data Errors

According to Irwin, there are three main sources of errors in FWD data: seating errors, random errors, and systematic errors.[13] Irwin, Yang, and Stubstad showed that even very small deflection errors (on the order of 2 microns or less) can lead to very large errors in the backcalculated moduli.[14] Irwin found the following:

- **Seating errors:** Seating errors were caused by the rough texture of pavements and were of more critical importance in the testing of HMA pavements. These errors could typically be eliminated by applying a seating drop at each new test point, allowing the deflection sensors to become seated. Seating drop data should not be used in analyzing the pavement structure.

- **Random errors:** Random errors were associated with the analog-to-digital conversion of the deflections. They were on the order of ±2 microns.[14] Random errors could not be completely eliminated; however, they could be reduced by taking multiple readings and averaging the results. This reduction was proportional to the square root of the number of observations used in computing the mean. For example, if four replicate FWD drops (with the same height) at the same point were averaged, the random error would be reduced by half. Care must be taken to ensure that the multiple readings were random, i.e., that they were not consistently increasing or decreasing owing to liquefaction or compaction caused by the additional drops.[13]

Systematic Errors

Systematic errors are associated with the particular FWD equipment and its specific sensors. Systematic errors are on the order of ±2 percent. FWD specifications therefore call for an accuracy of ±2 percent or ±2 microns, whichever is greater. This specification combines the systematic error and the random error. Systematic errors can be reduced to 0.3 percent or less for each individual sensor, including the load cell, through calibration.[13]

Noise and Truncation of FWD Sensor Signals

The sensitivity of dynamic backcalculation solutions to signal noise is high. Basically, noisy data alter the error function surface enough to cause optimization errors. This can cause the search algorithm to diverge or to converge to a different modulus when regularization techniques are used. The remedy to noise is to preprocess the raw data by filtering out the high-frequency content of the signal (anything above 100 Hz) in deflection and load pulse data. Also, if synchronization problems occur, the dynamic

backcalculation algorithm may not work as well, although one could shift the signals similar to what was done in the quasi-static viscoelastic solution.

Another issue that is relevant to dynamic analysis is signal truncation. This problem can lead to large errors in the backcalculated layer parameters when using a frequency-based solution.[15] Therefore, signal truncation will affect the frequency-domain backcalculation. On the other hand, the time-domain backcalculation is not affected by FWD signals truncation. In fact, this is one of the major reasons the research team pursued development of a new time-domain dynamic viscoelastic solution.

Integration Drift

The use of numerical integration of acceleration or velocity information from inertial sensors to obtain position information inherently causes errors to grow with time, which is commonly known as "integration drift." The main problem is that integrating a signal contaminated with noise and drift leads to an output that has a root mean square (RMS) value that increases with integration time even in the absence of any motion of the sensor. For a single integration, the errors are a function of the duration of the signal. For that reason, to correct for the drift, estimation of deflections using inertial sensors is usually performed with the help of externally referenced aided sensors or sensing systems or prior knowledge about the motion. With aided sensors or sensing systems, Kalman filters (KFs) or extended-Kalman filters (EKFs) are commonly used to fuse different sources of information in an attempt to correct for the drift. A more detailed discussion about the drift is presented in chapter 6, in the subsection entitled Effects of Numerical Errors and Drifts.

Analysis and Interpretation of FWD Data

Deflection measurements can be used for backcalculating the elastic moduli of the pavement structural layers and for estimating the load-carrying capacity for HMA pavements. A number of factors affect the magnitude of measured pavement deflections, which makes the interpretation of deflection results difficult. The major factors that affect pavement deflections can be grouped into the following categories: pavement structure (thickness), pavement loading (load magnitude and type of loading), and climate (temperature and seasonal effects).

There are various approaches for FWD data analysis and interpretation. These can be grouped into two categories: (1) methods of analysis for calculating pavement response (forward analysis) and (2) methods for interpretation of pavement response (backcalculation).

Forward Analysis

Methods of calculating pavement response (forward calculation) include the following: (1) closed-form solutions based on Boussinesq's original half-space solution, (2) layered elastic solutions based on Burmister's original two- and three-layer solutions, and (3) FEM-based solutions.[16–18]

The method of equivalent thicknesses is based on Odemark's assumptions.[19] This closed-form solution is reported to produce results that are as good as or better than those from static layered elastic and FEM solutions.[19,20] The method can also be adapted to

handle nonlinear subgrade materials. However, the method cannot be used to determine the dynamic modulus master curve of an existing HMA layer.

The layered elastic solutions are the most commonly used among all methods. They are generally restricted to linear elastostatic analysis. The basic assumptions of the solution are the following:

- Surface load is uniformly distributed over a circular area.
- All layers are homogeneous, isotropic, and linearly elastic.
- Upper layers extend horizontally to infinity.
- Bottom layer is a semi-infinite half-space.

These solutions have been shown to produce good results if material behavior remains in the linear range; however, they cannot be used to determine the dynamic modulus master curve of an existing HMA layer.

The available computer programs that use the layered elastic solutions include, but are not limited to, CHEVRON, ELSYM5, and BISAR, NELAPAV, PADAL, VESYS, and KENPAVE. (See references 21–27.)

Finite element analysis (FEA) has also been used for pavement analysis, including three-dimensional (3-D) general-purpose programs, such as SAP, ABAQUS, and ANSYS, and pavement-specific programs for two-dimensional (2-D) axisymmetric (e.g., ILLIPAVE and MICHPAVE) and 3-D solutions (CAPA-3D). The main advantage of FEA is the ability to handle material variability and nonlinearity in both vertical and horizontal directions and to include any number of sophisticated constitutive models. Some of these programs do allow dynamic and/or viscoelastic analyses. However, they are either restricted to a particular constitutive model that may not be suitable for the backcalculation of the dynamic modulus master curve, and/or they involve a large number of elements and input parameters and therefore are much more time consuming to set up and to run.

In addition to the methods discussed here, efficient dynamic solutions were also used for pavement analysis. Computer programs for dynamic analysis of pavement systems use either dynamic damped-elastic finite-layer or FEM models for their forward solutions. The finite layer solutions are based on Kausel's formulation, which subdivides the medium into discrete layers that have a linear displacement function in the vertical direction and satisfy the wave equation in the horizontal direction.[28] Examples of programs containing such solutions include UTDYNAF, UTFWD, GREEN, SAPSI, and SCALPOT. (See references 29–33.)

Backcalculation Analysis

The following paragraphs describe static and dynamic backcalculation methods.

Static Backcalculation Methods: Most existing static backcalculation routines can be classified into three major categories, depending on the techniques used to reach the solution. The first category is based on iteration techniques, which repeatedly use a

forward analysis method within an iterative process. The layer moduli are repeatedly adjusted until a suitable match between the calculated and measured deflection basins is obtained. The second category is based on searching a database of deflection basins. A forward calculating scheme is used to generate a database, which is then searched to find a best match for the observed deflection basin. The third and final category is based on the use of regression equations fitted to a database of deflection basins generated by a forward calculation scheme. In principle, these three techniques can be applied to any of the forward analysis methods previously discussed. However, the iterative method is arguably the easiest to implement for dynamic backcalculation solutions.

Most iterative solutions use a search algorithm that is achieved by minimizing an objective function of any set of independent variables (i.e., layer moduli, thicknesses, etc.), which is commonly defined as the weighted sum of squares of the differences between calculated and measured surface deflections, which minimizes to the equation shown in figure 5.

$$f = \sum_{j=1}^{m} a_j (w_{jm} - w_{jc})^2$$

Figure 5. Equation. Objective function for the search algorithm.

Where:

m = Number of sensors.
w_{jm} = Measured deflection at sensor j.
w_{jc} = Calculated deflection at sensor j.
a_j = Weighing factor for sensor j.

The equation shown in figure 5 can be solved using nonlinear optimization methods, which locate the least value of the objective function. Many minimization techniques are available in the literature, including the following:[34]

- Factored secant update method.
- Modified Levenberg-Marquardt (LM) algorithm.
- Modified Powell hybrid algorithm.

One of the problems of this approach is that the multidimensional surface represented by the objective function may have many local minima. As a result, the program may converge to different solutions if a different set of seed moduli is used. Another problem is that the convergence can be very slow, requiring numerous calls to a forward analysis program.

An example of an iterative program for static backcalculation is EVERCALC, which uses a modified LM algorithm.[35] The program seeks to minimize an objective function formed as the sum of squared relative differences between the calculated and measured surface deflections.

The search method can also take the form of solving the linear set of equations, as shown in figure 6.

$$[F]^k \{d\}^k = \{r\}^k$$

Figure 6. Equation. Search method using set of equations.

Where:

$[F]^k$ = kth iteration of the m by n matrix of partial derivatives $\partial f_j / \partial E_i$, where j = 1 to m and m is the number of deflections measured, and i = 1 to n where n is the number of layers in the pavement with unknown moduli.
$\{d\}^k$ = kth iteration difference vector, $E_i^{k+1} - E_i^k$, between the new and old moduli.
$\{r\}^k$ = kth iteration residual vector, $w_{jc} - w_{jm}$, between the most recently calculated and the measured surface deflections.

An example of an iterative program using the above search method is MICHBACK, which uses the modified Newton-Raphson (also called secant) method. The method of least-squares is used to solve the over-determined system of equations (m equations in n unknowns, $m > n$) in figure 6. If desired, weighting factors can be used for each sensor measurement to emphasize some deflection measurements over others.

Dynamic Backcalculation Methods: Most dynamic backcalculation methods use dynamic, damped-elastic finite-layer or FEMs for their forward solutions. Dynamic backcalculation methods are based on either frequency- or time-domain solutions. For the former procedure, the applied load and measured deflection time histories are transformed into the frequency domain by using the fast Fourier transform (FFT). Backcalculation of layer parameters is done by matching the calculated steady-state (complex) deflection basin with the frequency component of the measured sensor deflections at one or more frequencies. In time-domain backcalculation, the measured deflection time histories are directly compared with the predicted results from the forward analysis. One of the advantages of this method is that matching can be achieved for any time interval desired. Uzan compared the two methods and concluded that time-domain backcalculation was preferred over frequency-domain backcalculation.[36]

BACKCALCULATION COMPUTER PROGRAMS

Static Backcalculation Programs

Numerous computer programs for performing automated backcalculation have been developed. Some of the known static backcalculation computer programs and their characteristics are presented in table 2. Different versions of these programs exist, with improved and/or updated editions being periodically released. Most of the automated backcalculation programs rely on static analysis and a linear elastic layer program. Notable exceptions include ELMOD, which can use either Odemark's method or the FEM in addition to the layered elastic solution, and MODCOMP and EVERCAL, which can handle nonlinear material properties.

Accuracy and Reliability

Many of the programs developed for production purposes are intended to get to an "accurate" solution reliably. While most static backcalculation programs usually converge to a solution reasonably quickly and reliably, one cannot assert the uniqueness of the set of layer moduli derived from any search method. For this reason, many programs use various controls to guide the iterative search toward an "acceptable" set of layer moduli. These include making some assumptions about the type of pavement system being analyzed (e.g., assuming that layer moduli decrease with depth, that the subgrade modulus is constant with depth, that a rigid layer exists a certain depth, etc.) and limiting the acceptable range of moduli for each individual layer type.

Required Inputs

Required inputs typically include peak sensor deflections and their location, peak load values, the number of layers in the pavement system and their thicknesses, and assumed values for Poisson's ratios. Most programs also require seed moduli as input, although some have methods that generate these from the measured deflections or from regression equations.

Resulting Outputs

Typical outputs include the measured and calculated deflections, the differences and percent differences, the final set of layer moduli, and the error sums. Most of the existing backcalculation programs allow for 3 to 5 layers; a notable exception is the MODCOMP5 program, which allows up to 15 layers.

Table 2. Commonly available backcalculation computer programs for flexible pavements.

Program Name	Developer	Forward Calculation Method	Forward Calculation Subroutine	Backcalculation Method	Nonlinear Analysis	Layer Interface Analysis	Maximum Number of Layers	Seed Moduli	Range of Acceptable Modulus	Ability to Fix Modulus	Convergence Scheme	Error Weighting Function
BISDEF	U.S. Army Corps of Engineers—Waterway Experiment State (USACE-WES)	Multilayer Elastic Theory	BISAR	Iterative	No	Variable	Number of deflections; best for 3 unknowns	Required	Required	Yes	Sum of squares of absolute error	Yes
BOUSDEF	Zhou et al. (Oregon State University)	Method of Equivalent Thickness	MET	Iterative	Yes	Fixed (rough)	At least 4	Required	Required	—	Sum of percent errors	—
CHEVDEF	USACE-WES	Multilayer Elastic Theory	CHEVRON	Iterative	No	Fixed (rough)	Number of deflections; best for 3 unknowns	Required	Required	Yes	Sum of squares of absolute error	Yes
COMDEF	USACE-WES	Multilayer Elastic Theory	BISAR	Database	No	Fixed (rough)	3	No	No	—	Various	No
DBCONPAS	Tia et al. (University of Florida)	Finite Element	FEACONS III	Database	Yes?	Yes?	—	No	No	—	—	—
ELMOD/ELCON	Ullidtz (Dynatest®)	Method of Equivalent Thickness	MET	Iterative	Yes (subgrade only)	Fixed (rough)	4 (exclusive of rigid layer)	No	No	Yes	Relative error of 5 sensors	No
ELSDEF	Texas A&M, USACE-WES	Multilayer Elastic Theory	ELSYM5	Iterative	No	Fixed (rough)	Number of deflections; best for 3 unknowns	Required	Required	Yes	Sum of squares of absolute error	Yes
EMOD	PCS/Law Engineering	Multilayer Elastic Theory	CHEVRON	Iterative	Yes (subgrade only)	Fixed (rough)	3	Required	Required	Yes	Sum of relative squared error	No
EVERCALC	Mahoney et al.	Multilayer Elastic Theory	WESLEA	Iterative	Yes	Variable	5	Required (4 and more layers)	Required	Yes	Sum of absolute error	Yes
FPEDD1	Uddin	Multilayer Elastic Theory	BASINF?	Iterative	Yes	Fixed (rough)	—	Program Generated	—	—	—	No
ISSEM4	Ullidtz, Stubstad	Multilayer Elastic Theory	ELSYM5	Iterative	Yes (finite cylinder concept)	Fixed (rough)	4	Required	Required	Yes	Relative deflection error	No
MICHBACK	Harichandran et al.	Multilayer Elastic Theory	CHEVRONX	Newton method	No	Fixed (rough)	Number of deflections; best for 3 unknowns	Required	Required	Yes	Sum of relative squared error	—
MODCOMP 5	Irwin, Szebenyl	Multilayer Elastic Theory	CHEVRON	Iterative	Yes	Fixed (rough)	2 to 15 layers; maximum of 5 unknown layers	Required	Required	Yes	Relative deflection error at sensors	No
MODULUS	Texas Transportation Institute	Multilayer Elastic Theory	WESLEA	Database	Yes?	Fixed?	4 unknown plus stiff layer	Required	Required	Yes	Sum of relative squared error	Yes

Program Name	Developer	Forward Calculation Method	Forward Calculation Subroutine	Backcalculation Method	Nonlinear Analysis	Layer Interface Analysis	Maximum Number of Layers	Seed Moduli	Range of Acceptable Modulus	Ability to Fix Modulus	Convergence Scheme	Error Weighting Function
PADAL	Brown et al.	Multilayer Elastic Theory	—	Iterative	Yes (subgrade only)	Fixed?	—	Required	—	—	Sum of relative squared error	—
RPEDD1	Uddin	Multilayer Elastic Theory	BASINR	Iterative	Yes	Fixed?	—	Program Generated	—	—	—	No
WESDEF	USACE-WES	Multilayer Elastic Theory	WESLEA	Iterative	No	Variable	5	Required	Required	Yes	Sum of squares of absolute error	Yes
RoSy DESIGN	Grontmij Pavement	LET	—	LET	Yes	No	4 in LET	User setting	No	Yes	—	—
PRIMAX-design	Grontmij Pavement	Leaf and LET	—	Backfaa and LET	Yes	No	4 in LET and 10 in Backfaa	User setting	Yes user setting	Yes	—	—

— Indicates not applicable.
LET =Linear elastic theory.

User Friendliness

Because many of the backcalculation programs are developed for production purposes, they are user friendly, require minimum involvement from the user, and provide various features intended to be useful for project-level analysis. Conversely, those programs written for use in research tend to lack the features needed for production. They also usually allow and require significant involvement from the user. These include dynamic backcalculation programs that rely on dynamic analysis to calculate the deflection time histories and those that use available general-use FEM programs.

Advantages and Disadvantages

Attempting to do a one-to-one comparison of different backcalculation programs for the purpose of identifying the best one is a difficult task. Each of these programs has pros and cons, and each may be particularly useful in a specific situation. Before making such comparisons, one should first define the purpose in doing backcalculation and the evaluation criteria that one will use. In general, the advantage of using simpler methods is that they are very fast and easy to use. Their disadvantage is that they are limited in their interpretation of the FWD data. For example, most static backcalculation programs are limited to five layers. This may not be sufficient to characterize realistic pavement profiles that comprise five or more layers, and such programs cannot be used to allow for variation in subgrade modulus with depth, for example. On the other hand, more advanced methods of backcalculation, which theoretically allow backcalculation of a larger number of parameters, are computationally expensive and time consuming. Also, they are not guaranteed to converge when using real field-measured data. For most State transportation departments, the ultimate purpose of backcalculation is to aid in rehabilitation design so that purpose should be a strong criterion for selecting a program.

Dynamic Backcalculation Programs

A number of computer programs have been developed for dynamic backcalculation of flexible pavement layer parameters. Each program employs a particular forward model and a specific backcalculation scheme. All of these programs require the time histories of the load and deflection sensors. Theoretically, because these time histories contain more information than just the peak values of load and deflection, dynamic backcalculation programs can backcalculate a larger number of parameters when using synthetically generated deflection time histories. However, there are serious challenges when using measured field data. For example, the frequency-domain solutions can lead to large errors if the measured FWD records are truncated before the motions fully decay in time.

Time-domain backcalculation solutions present another set of challenges. For example, the time synchronization between the load and sensor records and the digitization of the response can be problematic. Noise in the data and the ill-posed nature of the inversion problem can be amplified when matching traces of time histories, requiring special filtering and regularization techniques that are not easy to implement. In addition, unlike frequency-domain analysis, where the properties are backcalculated at each frequency independently, time-domain backcalculation precludes making a choice on the behavior of material properties with frequency; that is, they either assume a constant HMA modulus (similar to static backcalculation) or a prescribed function of the HMA layer modulus with frequency (e.g., linear relation in the log-log space).

While this assumption may be acceptable for unbound materials, it may significantly affect the predicted response of the HMA layer because of its viscoelastic nature. Finally, none of these programs are considered ready for production mode, because they usually require a lot of involvement from the user, are computationally very expensive, and have not been fully evaluated for use with field-measured data. Some of the dynamic backcalculation computer programs and their characteristics are presented in table 3. A brief overview of the programs developed to date is also provided.

Table 3. Dynamic backcalculation programs for flexible pavements.

Program	Domain	Inverse Method	Forward Program	Reference
BKGREEN	Frequency	Nonlinear least-square optimization	GREEN	31
No formal name	Frequency/time	Newton's method	UTFWIBM	37
PAVE-SID	Frequency	System Identification (SID)	SCALPOT	33
FEDPAN	Time	Linear least squares	SAP IV	38
No formal name	Frequency	LM	SAPSI	39
No formal name	Frequency	Secant Update, LM, Powell Hybrid	LAMDA	40
No formal name	Time	Gauss-Newton method	FEM	41
DYNABACK	Frequency/time	Newton's method with least-square or singular value decomposition	SAPSI	15, 42, and 43
EVERCALCII	Time	Nonlinear least square optimization with Tikhonov regularization and continuation method	FEM	44

BKGREEN models the pavement as a layered elastic system in terms of dynamic Green flexibility influence functions using Kausel's formulation of discrete Green functions for dynamic loads in linear viscoelastic layered media.[28,31] Backcalculation is done at multiple frequencies, and the set of layer moduli is determined using a nonlinear least squares technique. The solution can cause some computational difficulties at certain frequencies because of the numerical complications associated with implementing infinite integration in computer codes.

Uzan presented two dynamic linear backcalculation procedures—one in the time domain and the other in the frequency domain.[37] Both approaches use the program UTFWIBM as the forward model and Newton's method as the backcalculation solution. UTFWIBM uses the finite layer solutions (based on Kausel's formulation), which subdivides the medium into discrete layers that

have a linear displacement function in the vertical direction and satisfy the wave equation in the horizontal direction.

PAVE-SID is a computer program that uses the SCALPOT program to generate frequency response curves; a system identification technique is applied for matching computed frequency data to extract pavement properties.[33] SCALPOT computes the dynamic response of a horizontally layered viscoelastic half-space to a time-dependent surface pressure distribution.

FEDPAN is a FEM program that can perform both static and dynamic backcalculation for three-layer pavement systems using the CHEVDEF backcalculation algorithm.[38,45] This program can simulate the effects of pavement inertia and damping in the dynamic analysis and material nonlinearity in the static analysis.

Losa used SAPSI as the forward program and a nonlinear least squares optimization technique (LM method) for multifrequency backcalculation.[32,39] The HMA and subgrade materials were assumed to be frequency dependent while the base/subbase material was assumed to be frequency independent.

Al-Khoury et al. developed an axisymmetric layered solution as a forward model using the spectral element technique and used the modified LM and Powell hybrid methods for solving the resulting system of nonlinear equations.[2,40,46]

Meier and Rix developed an artificial neural network (ANN) solution that has been trained to backcalculate pavement layer moduli for three-layer flexible pavement systems using synthetic dynamic deflection basins.[47,48] The dynamic pavement response was calculated using an elastodynamic Green function solution based on Kausel's formulation.[28]

Work by Chatti developed the DYNABACK computer program that allows for different dynamic backcalculation algorithms for both frequency-based and time-based solutions.[15,42,43] The DYNABACK program uses the SAPSI program as its forward solution and an expanded version of the modified Newton-Raphson algorithm in the MICHBACK program as its backcalculation solution.[32,49] The solution uses the least squares minimization technique to solve the over-determined set of equations, which are real-valued and correspond to the peak transient deflections and their corresponding time lags relative to the peak load. The DYNABACK program includes two basic solutions with several options for backcalculating different layer parameters: (1) frequency-domain backcalculation at one or multiple frequencies and (2) time-domain backcalculation using peak responses or time history traces. Theoretically, single frequency backcalculation can be used to backcalculate up to 8 parameters while multiple frequency backcalculation can be used to backcalculate up to 15 parameters. The same is true for time-domain backcalculation using peak responses and traces, respectively. However, when using measured deflection time histories, the number of backcalculated parameters must be reduced to fewer than eight.

Finally, Turkiyyah has been developing an improved EVERCALCII program that uses the complete FWD sensor time histories to recover pavement layer moduli distribution and thicknesses using thin computational layers that discretize the profile.[44] In this solution, physical layer thicknesses can be obtained, after backcalculation of thin computational layer moduli, by

grouping thin layers of similar moduli values. Two regularization techniques are employed. One involves the absolute values of the moduli to prevent physically unrealistic solutions with large layer moduli, while the second controls the gradient of the moduli in the vertical direction to prevent convergence to profiles with neighboring layers that alternate between high and low moduli. In addition, a "continuation scheme" is used to control the weights on the regularization terms to overcome the ill-posed nature of the optimization problem. Because this solution relies on backcalculating the moduli of the relatively large number of elements that make up these thin computational layers, the computational effort for solving the inverse problem is very significant. Efforts are underway to speed up the forward (FEM) solution.

MODELING ISSUES

Several specific modeling issues must be considered when selecting backcalculation solutions, as described in the following subsections.

Static Versus Dynamic Response

The FWD test consists of dropping a large weight from a specified height, which creates a 20- to 60-ms impulse load, simulating a moving wheel load. This creates waves in the pavement system and underlying subgrade soil. These elastic waves propagate with distance and are partly reflected at the interface between any given two successive layers, with the remaining wave energy penetrating and propagating to the next layer, and the process is repeated. These waves bounce up and down a few hundred times in a given test. The deflection time histories lag the load pulse, with the time lag increasing as the distance between the load plate and the sensor increases. So, clearly, the FWD test is a dynamic test. Therefore, to maximize the effective interpretation of FWD data, the forward solutions must be able to account for the following physical conditions encountered in FWD testing:

- Transient nature of the FWD load (i.e., time varying pulse load of arbitrary shape).

- Dynamic effects (i.e., ability to model viscous and inertial internal forces).

- Wave propagation effects (i.e., the ability to model the propagation of the stress waves imparted by the FWD impulse in time and space).

- Viscoelastic effects (i.e., the ability to incorporate a frequency-dependent HMA dynamic modulus or its viscoelastic equivalent, the time-dependent relaxation modulus).

The difference between static response and dynamic response can be defined in terms of the internal forces involved. In static analysis, only elastic forces are considered. On the other hand, viscous and inertial forces are considered in addition to the elastic forces in dynamic analysis. The question therefore is whether the effects of viscous and inertial forces are significant enough that one cannot afford to ignore them when characterizing the in situ conditions of a pavement system under an FWD test. Most pavement engineers argue that backcalculation is an exercise that determines pavement parameters—not properties—that are to be used within a given mechanistic framework. Therefore, it is acceptable to use static analysis and to backcalculate parameters that are compatible with the current mechanistic-empirical design framework that is grounded in static and not dynamic

analysis. However, advocates for dynamic analysis maintain that such an approach takes advantage of more information provided by the test, which allows for backcalculating more parameters such as layer thicknesses or, perhaps more important, the modulus versus frequency curve of the HMA layer. Also, in certain cases, such in the presence of a stiff layer or water table at shallow depth, the effect of dynamics on pavement response is more important.

Time-Domain Versus Frequency-Domain Backcalculation

Uzan compared the two methods and concluded that time-domain backcalculation is preferred over frequency-domain backcalculation.[36] Measured field data from FWD tests using current technology contain several types of measurement and calibration errors, and thus the developed algorithms and computer programs for dynamic backcalculation, must address the following serious challenges:

- Large errors can be introduced when the measured deflection signals are truncated before the motions fully decay in time. Such errors are observed when frequency-domain solutions are used.

- The periodicity of the signal assumed in the discrete Fourier transform (DFT) algorithm cannot accurately disclose the frequency content of the transient FWD time histories with short duration.

- The DFT is very sensitive to noise, which is always present in the FWD.[42,50,51]

- The DFT is impractical for representing the fundamental properties of a viscoelastic material, such as creep compliance or dynamic modulus, because of a large number of harmonics necessary for modeling them.[52,53] This is also the reason most of the frequency-domain solutions use the damping ratio concept and hence fail to model and/or backcalculate the fundamental properties of a viscoelastic material.

- The means of an FWD load pulse and corresponding deflection time histories are all nonzero. Dynamic solutions that have been developed in the context of soil dynamics and earthquake engineering take advantage of the FFT, which reduces computation time by orders of magnitude. However, the FFT algorithm assumes a zero mean function. This assumption is valid for earthquake records but not for an FWD pulse. By default, the output of the FFT algorithm is equal to $(A*N)/2$, where A is the amplitude of the input series except for the first element of the Fourier series (when the frequency is equal to zero). The standard magnitude of the DFT of the input series is equal to the FFT amplitude normalized such that the sum of the squares of the inputs is equal to the mean of the squares of the outputs (i.e., the total power determined from the time series equals the mean power determined from the spectrum) as shown in the equation in figure 7.

$$\sum_{n=0}^{N-1}\left|x[n]\right|^2 = \frac{1}{N}\sum_{k=0}^{N-1}\left|X[k]\right|^2 \quad or \quad \sum_{n=0}^{N-1}\left|x[n]\right|^2 = \sum_{k=0}^{N-1}\left|\frac{X[k]}{\sqrt{N}}\right|^2$$

Figure 7. Equation. Parseval theorem.

Where $x[n]$ is the deflection time series; $X[k]$ is the DFT of $x[n]$, both of length N. With the normalization shown in figure 7, the DFT of a nonzero-mean function at zero frequency will be the equation shown in figure 8.

$$X[0] = \frac{1}{\sqrt{N}} \sum_{n=0}^{N-1} x[n]$$

Figure 8. Equation. DFT of a nonzero-mean function at zero frequency.

However, when the input has a nonzero mean, the amplitude of the DFT at zero frequency should be the mean value of the input. Therefore, this normalization is correct only if the input series has a steady state component that is equal to the mean value. However, FWD loading is a transient loading with a mean value but not a steady state component. Also, functions with a nonzero average value may produce a zero frequency component that obscures more interesting components. Adding a large enough quiet zone to a transient nonzero mean signal is a workaround that is often used. However, doing so affects analysis time, and it may not be useful in this case.

All the above issues emphasized the necessity of using a time-domain-based dynamic solution that is also able to model the viscoelastic response of the HMA layer(s).

Linear Versus Nonlinear Material Response

When pavement structures are thin enough or the applied loads and corresponding stresses are high enough, the subgrade material will likely exhibit stress-softening, nonlinear behavior (i.e., its response increases at a higher rate than the load or stress increases). This behavior translates to the subgrade modulus changing with depth and radial distance from the load. If the forward model uses a layered solution that assumes linear material behavior, it can only use one modulus value for an entire layer. Consequently, the backcalculated modulus to match the measured deflections is an averaged value. Typically, the backcalculated subgrade modulus is higher than the value obtained from laboratory measurement by a factor of 2 to 3, although this difference is not entirely caused by nonlinear material response.

On the other hand, granular (cohesionless) materials used in bases and subbases are stress dependent in a different (positive) way (i.e., their modulus increases with increasing confinement). Similar to the subgrade modulus, this leads to a base/subbase modulus that varies with depth and radial distance from the load, and any linear backcalculation exercise can only lead to an averaged modulus value. The combination of these phenomena often leads to a base modulus that is lower than the subgrade modulus despite the base material being superior to the subgrade material. One way of addressing this problem is to introduce an artificial layer. However, a more direct way of addressing the problem is to treat the subgrade as a nonlinear elastic material with a stress-dependent modulus i.e., with a modulus that varies with stress.[54] Ullidtz argued that the effect of the positive nonlinearity in granular base/subbase layers on backcalculation results was less important.[54]

Ideally, only the FEM can model the variation of moduli with depth and radial distance. However, some models based on layered elastic theory can handle nonlinear behavior approximately (e.g., NELAPAVE and KENPAVE). Ullidtz combined the method of equivalent

thickness with a stress-dependent subgrade modulus to handle material nonlinearity and reported that this approach was superior to FEM.[54]

Bedrock or Stiff Layer Effect

A stiff layer condition can exist if there is shallow bedrock, a stiff clay layer, or a groundwater table. The effect of a stiff layer at a shallow depth can be very significant. Assuming the subgrade layer to be a semi-infinite half-space, while in reality the subgrade layer is only a few yards thick, causes the backcalculated moduli for the upper pavement layers to be incorrect. Generally, when the stiff layer is deeper than about 39 ft, its presence has little or no influence on the backcalculated moduli. The depth to the stiff layer can be evaluated by using a relationship between the deflection, δ_Z, and $1/r$, where r is the radius at which it occurs (see figure 9). Several regression equations for different HMA layer thicknesses can be used as a function of r_o and deflection basin parameters.[55]
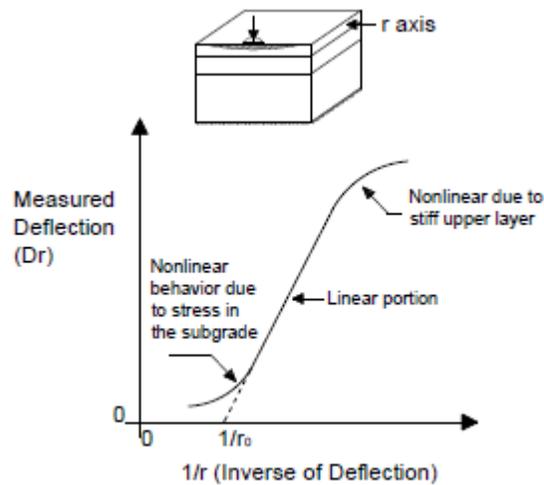
Credit: Washington State Department of Transportation

Figure 9. Drawing and Graph. Plot of inverse of deflection offset versus measured deflection.[55]

An alternative and arguably better way to determine the depth to the stiff layer is to use the free vibration response from FWD deflection sensor measurements and one-dimensional wave propagation theory.[56] Chatti et al. modified Roesset's equations to account for different conditions, as shown in the equations in figure 10 (for saturated subgrade with bedrock, use the first equation; for nonsaturated subgrade with bedrock or groundwater table, use the second equation).[42]

$$D_b = \frac{V_s * T_d}{1.35}$$

$$D_b = \frac{V_s * T_d}{(\pi - 2.24 * u)}$$

Figure 10. Equation. Calculation of the depth to the stiff layer using the modified Roesset's equations.

Where:

V_s = S-wave velocity of subgrade material.
T_d = Natural period of free vibration (see figure 11).
u = Poisson's ratio of subgrade.
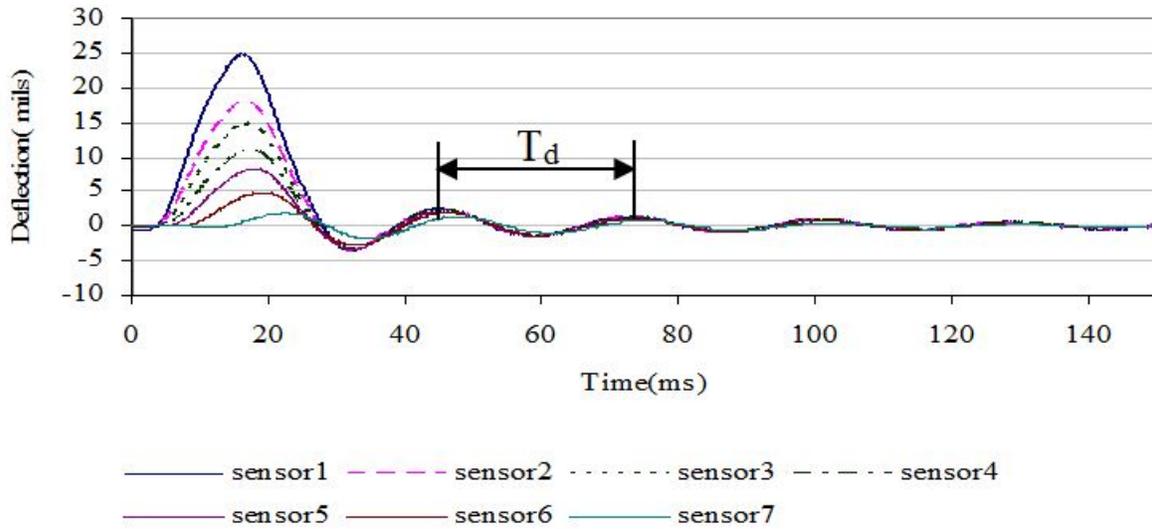
Figure 11. Graph. Natural period T_d from sensor deflection time histories.

The procedure for estimating the depth to the stiff layer described above requires knowledge of the shear wave velocity of the subgrade V_s, which is a function of the modulus value as shown in figure 12.

$$V_s = \sqrt{\frac{G}{\rho}} = \sqrt{\frac{E_{sg}/2(1+\upsilon)}{\rho}}$$

Figure 12. Equation. Shear wave velocity.

However, in the analysis of field data, subgrade properties (shear-wave velocity, unit weight (ρ), and Poisson ratio (u)) are not generally known and therefore need to be either measured or assumed. The method proposed by Lee et al. can be used for estimating the modulus of the subgrade E_{sg}.[35]

Temperature and Moisture Effects

Temperature and moisture conditions in the pavement vary over time. This variation occurs daily as well as seasonally. A pavement is strongest during the freezing season (in a freezing climate) because of the frozen state of the underlying materials. On the other hand, even in a freezing environment, the pavement can be at its weakest state during a thaw period, even if it is temporary (e.g., on a sunny day in late winter or during the warmest hours around midday). In areas where there is little or no freezing, seasonal variations can be very important in terms of moisture changes, which affect the modulus of the subgrade and to a lesser extent that of the base layer. For the HMA layers, hourly temperature variations during a given day need to be taken into account because temperature gradients exist in the pavement that can lead to modulus variation with depth. Also, seasonal variations can have a major effect on the modulus of an HMA layer. These effects must be considered when performing backcalculation. It is crucial to test the pavement at different times of the year to gain information about the seasonal variation. Testing should also be conducted at different times during the day to account for daily temperature variations.

Other Effects

Several other issues may need to be addressed in backcalculation analysis, including the following:

- Major cracks in the pavement or testing near a pavement edge or joint can cause the deflection data to depart drastically from the assumed conditions.

- Layer thicknesses are often not known, and subsurface layers can be overlooked.

- Layer thicknesses are not uniform, and materials in the layers are not homogeneous.

- Some pavement layers are too thin to be backcalculated in the pavement model.

RELEVANCE TO MEPDG USE

The required input material properties for HMA pavements in the new MEPDG that are relevant to the use of FWD data and backcalculation results are the following: (1) the time-temperature dependent dynamic modulus, E^*, for the HMA layer(s), (2) the resilient moduli for the unbound base/subbase and subgrade materials, and (3) the elastic modulus of the bedrock, if present.[1] The MEPDG also provides an option for considering nonlinear material parameters for the unbound layers for level 1 analysis.[1] However, the performance models used in the software have not been calibrated for nonlinear conditions.

HMA Materials

For HMA materials, level 1 analysis requires conducting E^* (complex modulus) laboratory testing at loading frequencies and temperatures of interest for the given mixture. Level 2 analysis does not require E^* laboratory testing; instead, the user can enter asphalt mix properties (gradation parameters) and laboratory binder test data (from G^* testing or other conventional binder tests).[4] The MEPDG software calculates the corresponding asphalt viscosity values; it then uses the modified Witczak equation to predict E^* and develops the master curve for the

HMA mixture.[1] The same procedure is used for level 3 analysis to estimate the HMA dynamic modulus, except no laboratory test data are required for the binder.

For rehabilitation design, the determination of the HMA layer dynamic modulus follows the same general concepts described above, except that the software allows for a modified procedure to account for damage incurred in the HMA layer during the life of the existing pavement. The procedure therefore determines a "field damaged" dynamic modulus master curve as follows:

- For level 1 analysis, the MEPDG calls for the following procedure:[1]

1. Conduct FWD tests in the OW path over the project to be rehabilitated; calculate the mean backcalculated HMA modulus, E_i, for the project, including cracked as well as uncracked areas; record the HMA layer temperature at the time of testing; and determine the layer thickness along the project from coring or GPR testing.

2. Determine mix volumetric parameters and asphalt viscosity parameters from cores and follow the same procedure for determining binder viscosity-temperature properties as for new or reconstruction design.

3. Develop an undamaged dynamic modulus master curve using the data from step 2 and the modified Witczak equation.

4. Estimate damage, $d_j = E_i/E^*$, with E_i obtained from step 1 and E^* obtained from step 3 at the same temperature recorded in the field.

5. Calculate $\alpha' = (1 - d_i)\,\alpha$, where α is a function of mix gradation parameters.

6. Determine the field damaged dynamic modulus master curve using α' instead of α in the modified Witczak equation.

- For level 2 and level 3 analyses, no FWD testing is required. The level 2 procedure is similar to the level 1 procedure, except that the indirect resilient modulus, M_{ri}, obtained from laboratory tests (NCHRP 1-28A) on specimens from field cores, is used in the damage parameter calculation, $dj = M_{ri}/E^*$.[57] For the level 3 procedure, no coring or testing is required; instead, typical estimates of HMA mix parameters are entered, and the software calculates the undamaged master curve. The damage factor d_j is estimated from visual condition data.

Unbound Materials

For unbound materials (and bedrock), only level 1 analysis calls for FWD testing in rehabilitation and reconstruction designs. The resilient modulus, M_r, for each unbound layer (including the subgrade) can be either determined in the laboratory using cyclic triaxial tests or backcalculated using standard backcalculation procedures. As discussed in the previous section, while the MEPDG does allow for the generalized nonlinear, stress-dependent model in the design procedure, this approach is not recommended at this time because the performance models in the software have not been calibrated for nonlinear conditions; therefore, the MEPDG does not discuss the option of backcalculating the k_1, k_2, and k_3 parameters in the nonlinear model. The discussion in MEPDG only includes the backcalculation and use of "effective" moduli that would account for any stress sensitivity, cracks, or any other anomalies in any layer

within the existing pavement. For level 2 analysis, correlations with strength test data are used. For level 3, the guide lists typical modulus values based on soil classification but warns that they are very approximate and strongly recommends some form of testing, especially using FWD testing and backcalculation (level 1).[1]

The MEPDG notes that the reason for caution is related to using the wrong assumptions. Either a fairly strong subgrade material may be erroneously assumed to be semi-infinite while it may actually be less than 3 ft thick (e.g., as part of an embankment) or, conversely, a weak subgrade soil may be assumed to be semi-infinite while it may, in reality, be overlying a stronger soil or bedrock. The MEPDG also notes that for granular materials, moduli values that matched FWD backcalculated results were 50- to 70-percent higher than the typical laboratory-tested values, while for subgrade soils, they were two to three times the typical laboratory-determined values.[1]

Cementitiously Stabilized Materials

Similar to unbound materials, only level 1 analysis calls for FWD testing in rehabilitation and reconstruction designs. The modulus, E or M_r, for any cementitiously stabilized layer (including lean concrete and cement stabilized base, as well as lime/cement/flyash stabilized soils) can be either determined in the laboratory or backcalculated using standard backcalculation procedures. Layer thicknesses can be obtained by coring or using NDT techniques such as the GPR. The MEPDG recommends performing limited testing on cored lime-stabilized soil specimens to verify/confirm the backcalculated values and notes that backcalculation of modulus values for layers less than 6 inches thick located below other paving layers may be problematic, thus requiring laboratory testing. For level 2 analysis, correlations with strength test data are used. For level 3, the MEPDG calls for estimating the moduli based on experience or historical records and lists typical modulus values. The MEPDG also notes that semi-rigid cementitiously stabilized materials are more prone to deterioration due to repeated traffic loads when used in HMA pavements and suggests some typical (minimum) values for such deteriorated materials.[1]

Using Static Backcalculation in the Current MEPDG Procedure

It should be clear from the previous discussion that the analysis in the MEPDG software always uses an E^* master curve and therefore does not accept a constant modulus value for the HMA layer(s). This is necessary because the analysis calculates different HMA moduli for the different sublayers comprising the HMA layer(s) as a function of depth, speed, and temperature, as explained in appendix CC of the MEPDG.[1] For rehabilitation of existing pavements, the current MEPDG procedure (level 1) calls for (static) backcalculation of layer moduli, which leads to constant backcalculated moduli for all layers, including the HMA layer. To maintain compatibility of backcalculated layer moduli with the forward analysis in the software, the MEPDG procedure calls for adjusting the HMA dynamic modulus using the damage factor d_j (ratio of backcalculated HMA modulus to predicted E^* value using Witczak equation). This effectively shifts the undamaged master curve down while essentially maintaining the variation with frequency as predicted by the Witczak equation. The procedure also calls for adjusting the master curve using the aged viscosity value in the predictive E^* equation, which would shift the master curve upward; however, this upward shift would be negligible compared with the downward shift using the backcalculated modulus for the damaged HMA layer, E_i (as explained previously in the HMA Materials section).

Feasibility of Using Dynamic Backcalculation for Future Versions of MEPDG

Ideally, one should be able to determine a curve of HMA layer moduli as a function of frequency using a (dynamic) frequency-based backcalculation algorithm. This would give a more direct estimation of the HMA layer modulus with frequency from actual field conditions as opposed to relying on a laboratory-derived curve such as the Witczak equation. However, care should be taken in interpreting and using such data with the existing MEPDG performance predictions because they have been calibrated using laboratory-derived moduli. Also, recent analyses showed that while dynamic backcalculation methods can backcalculate layer moduli and thicknesses accurately from synthetically generated FWD data for pavement systems with three or more layers, they must address some serious challenges when using field data.[43] The frequency-domain method can lead to large errors if the measured FWD records are truncated before the motions fully decay in time. Dynamic, time-domain backcalculation algorithms present another challenge in that they cannot directly determine the HMA modulus as a function of frequency. They either assume a constant HMA modulus (similar to static backcalculation) or a prescribed function of the HMA layer modulus with frequency.

CHAPTER 3. LTPP DATA ANALYSIS

This chapter describes the results of the statistical analysis performed on a relatively large sample of FWD data from the LTPP database to assess the following: (1) prevalence of dynamic effects, (2) prevalence of nonlinear behavior; and (3) measurement issues based on evidently erroneous deflection sensor time histories. The data cover all climatic zones, seasons, and temperature ranges.

PRELIMINARY STATISTICAL ANALYSIS OF LTPP FWD LOADING HISTORIES

For this analysis, the research team randomly selected 1,224 tests (17 States, 6 sections per State, 3 stations per section, and 4 load levels). Table 4 summarizes the data extracted from the LTPP database. The time-history plots for each test were visually reviewed, and then the sections were classified using the following criteria:

- **Dynamic behavior**: Vibrations in the deflection histories.
- **Nonlinear behavior**: The load-to-deflection ratio shows a consistent trend with load level.

Table 4. LTPP sections used in the statistical analysis.

State	Section	Date	Time	LTPP Code	Climate Zone
Alabama	10101	20050428	16:00	SPS-1	WNF
	10102	20050429	9:00	SPS-1	WNF
	10103	20050429	13:30	SPS-1	WNF
	10505	20050421	9:00	SPS-5	WNF
	10504	20050420	15:00	SPS-5	WNF
	10504	20090324	16:00	SPS-5	WNF
Arizona	40502	20080915	13:37	SPS-5	DNF
	40506	20080915	11:00	SPS-5	DNF
	40509	20080915	10:00	SPS-5	DNF
	41003	20110326	11:45	GPS-6S	DNF
	41006	20110223	10:00	GPS-6S	DNF
	41024	20070116	11:00	GPS-6S	DF
Arkansas	50113	20050512	11:00	SPS-1	WNF
	50115	20050511	11:15	SPS-1	WNF
	50117	20050511	13:30	SPS-1	WNF
	50118	20050510	14:00	SPS-1	WNF
	50122	20050510	9:30	SPS-1	WNF
	50123	20050510	10:30	SPS-1	WNF

State	Section	Date	Time	LTPP Code	Climate Zone
California	62038	20110415	10:00	GPS-6B	WNF
	62038	20100507	8:37	GPS-2	WNF
	67491	20101207	12:30	GPS-6S	DNF
	68150	20100316	12:15	GPS-6B	DNF
	68153	20090730	13:36	GPS-6B	DNF
	68156	20110322	13:30	GPS-1	DNF
Colorado	81029	20101026	13:18	GPS-6	DF
	81053	20101027	12:30	GPS-6	DF
	87035	20101013	11:40	GPS-7	DF
	87780	20101015	12:35	GPS-6	DF
	87781	20110928	12:00	GPS-6	DF
	87783	20101021	12:14	GPS-6	DF
Florida	120101	20090506	12:00	SPS-1	WNF
	120105	20050117	13:45	SPS-1	WNF
	120161	20050117	10:15	SPS-1	WNF
	120502	20090504	10:30	SPS-5	WNF
	120508	20090504	15:00	SPS-5	WNF
	120509	20090504	17:00	SPS-5	WNF
Georgia	130502	20050503	13:00	SPS-5	WNF
	130508	20050503	10:00	SPS-5	WNF
	130566	20050505	10:00	SPS-5	WNF
	130563	20050505	9:00	SPS-5	WNF
	134096	20090331	9:30	GPS-2	WNF
	134420	20090514	11:00	GPS-6	WNF
Idaho	161001	20090410	10:15	GPS-1	DF
	161007	20110622	11:15	GPS-6	DF
	161020	20110428	12:00	GPS-1	DF
	161020	20111003	11:35	GPS-1	DF
	165025	20090422	8:40	GPS-7	DF
	169034	20110525	11:55	GPS-1	DF
Illinois	171002	20090408	13:40	GPS-1	WF
	171003	20050525	13:10	GPS-1	WF
	17A310	20040901	12:37	SPS-3	WF
	17B320	20040526	10:17	SPS-3	WF
	17A340	20040902	11:00	SPS-3	WF
	17B350	20040527	12:15	SPS-3	WF

State	Section	Date	Time	LTPP Code	Climate Zone
Louisiana	220113	20100219	15:40	SPS-1	WNF
	220115	20100219	12:10	SPS-1	WNF
	220117	20100219	13:00	SPS-1	WNF
	220119	20100218	10:20	SPS-1	WNF
	220121	20100218	12:52	SPS-1	WNF
	220123	20100218	15:20	SPS-1	WNF
Maryland	240504	20090408	13:40	SPS-5	WF
	240505	20050525	13:10	SPS-5	WF
	240563	20050629	12:37	SPS-5	WF
	240903	20100622	10:17	SPS-9	WF
	242401	20101202	11:00	GPS-2	WF
	242805	20100623	12:15	GPS-6 S	WF
Michigan	260115	20101110	12:40	GPS-6S	WF
	260116	20101109	10:00	GPS-6S	WF
	260118	20101108	9:30	GPS-6S	WF
	260123	20101109	12:00	GPS-6S	WF
	260124	20101109	11:00	GPS-6S	WF
	260159	20101109	9:00	GPS-6S	WF
Montana	300113	20100712	10:15	SPS-1	DF
	300115	20100712	11:15	SPS-1	DF
	300117	20100713	12:00	SPS-1	DF
	300121	20100714	8:40	SPS-1	DF
	300123	20100713	11:55	SPS-1	DF
	300119	20100713	11:35	SPS-1	DF
Nevada	320101	20090622	10:15	SPS-1	DF
	320102	20040331	11:15	SPS-1	DF
	320106	20090623	12:00	SPS-1	DF
	320108	20090623	11:35	SPS-1	DF
	320110	20050322	8:40	SPS-1	DF
	320112	20090623	11:55	SPS-1	DF
Oklahoma	400114	20100317	9:45	SPS-1	DNF
	400116	20100317	12:20	SPS-1	DNF
	400118	20100317	11:00	SPS-1	DNF
	400120	20100318	10:30	SPS-1	DNF
	400121	20100318	11:45	SPS-1	DNF
	400124	20100318	14:30	SPS-1	DNF

State	Section	Date	Time	LTPP Code	Climate Zone
Texas	480901	20101005	9:50	SPS-9N	DNF
	480903	20101005	12:00	SPS-9N	DNF
	481092	20101006	14:15	GPS-1	DNF
	481096	20101006	10:00	GPS-1	DNF
	482108	20110131	14:00	GPS-2	WNF
	483865	20110715	10:45	GPS-1	DNF
Washington	530801	20110512	10:00	SPS-8	DF
	530801	20090415	9:48	SPS-8	DF
	530802	20110512	11:18	SPS-8	DF
	531005	20090408	9:53	GPS-6B	DF
	536056	20100520	14:00	GPS-6A	DF
	537322	20090413	12:18	GPS-6D	DF

SPS = Specific pavement studies.
GPS = General pavement studies.
WF = Wet freeze.
WNF = Wet no-freeze.
DF = Dry freeze.
DNF = Dry no-freeze.

Figure 13 and figure 14 show examples of FWD time histories exhibiting free vibrations (dynamic behavior) and no dynamic behavior, respectively. Figure 15 and figure 16 show examples of nonlinear behavior with stress stiffening and softening, respectively.

The research team observed that dynamics were present in about 65 percent of the cases while nonlinearity could be prevalent in a range of as low as 24 percent of the cases to as high as 65 percent of the cases, depending on severity level and sensor location. Nonlinearity was more prevalent for the sensors that were far from the center of the load. A more detailed analysis was performed to identify when dynamics and nonlinearity were prevalent.
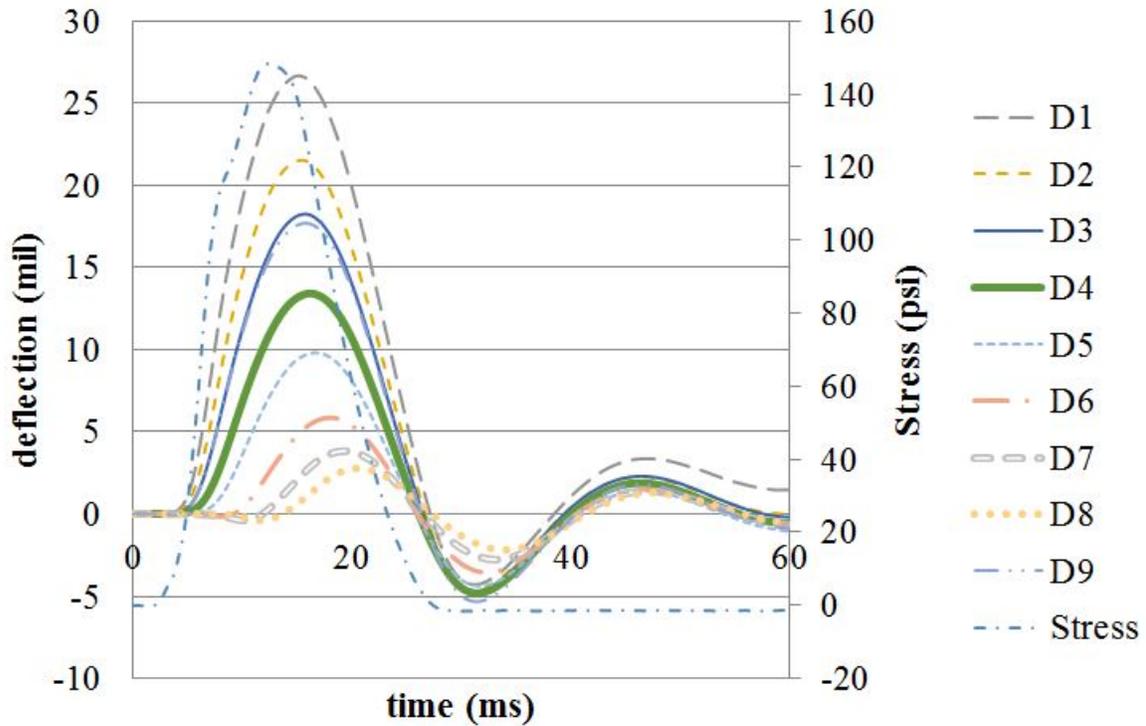
Figure 13. Graph. Example of time histories showing dynamic behavior for LTPP section 161020, station 1.
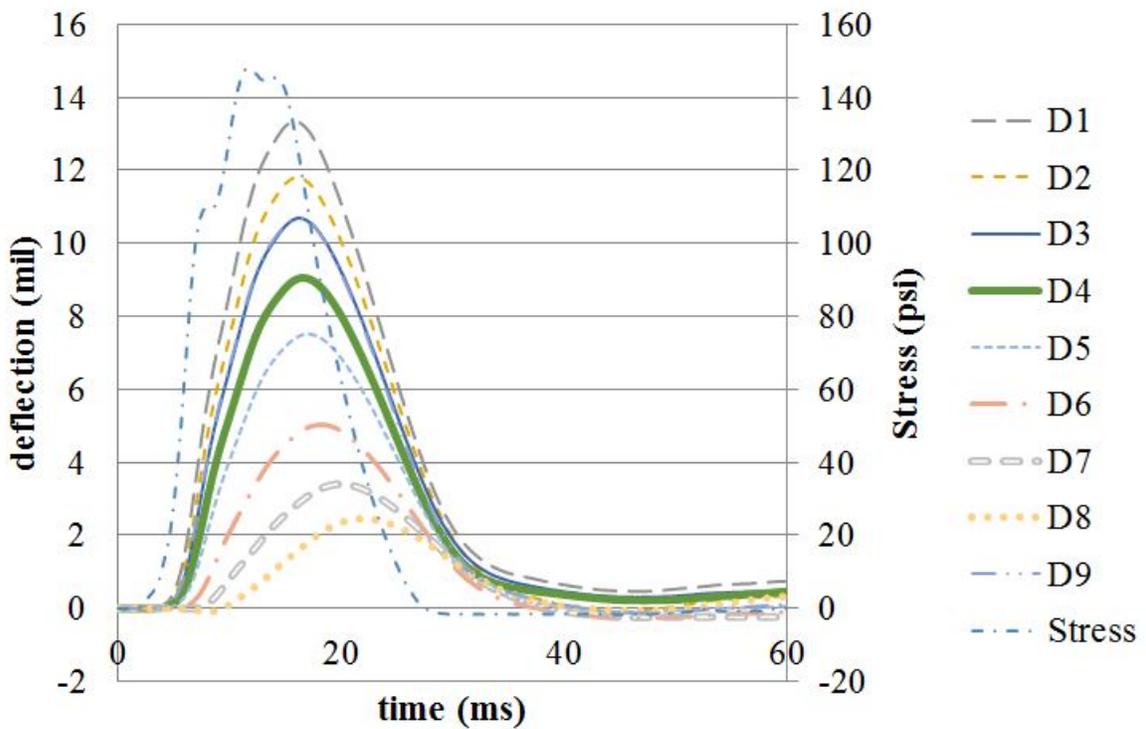
Figure 14. Graph. Example of time histories showing no dynamic behavior for LTPP section 169034, station 3.

35

$Load/Def8 = 0.0156*Load + 50.678$

$Load/Def7 = 0.0062*Load + 37.34$

$Load/Def6 = 0.0051*Load + 27.151$

$Load/Def5 = 0.0072*Load + 19.066$

$Load/Def4 = 0.0079*Load + 15.894$

$Load/Def3 = 0.0074*Load + 13.401$

$Load/Def2 = 0.0068*Load + 12.126$

$Load/Def1 = 0.0055*Load + 10.794$
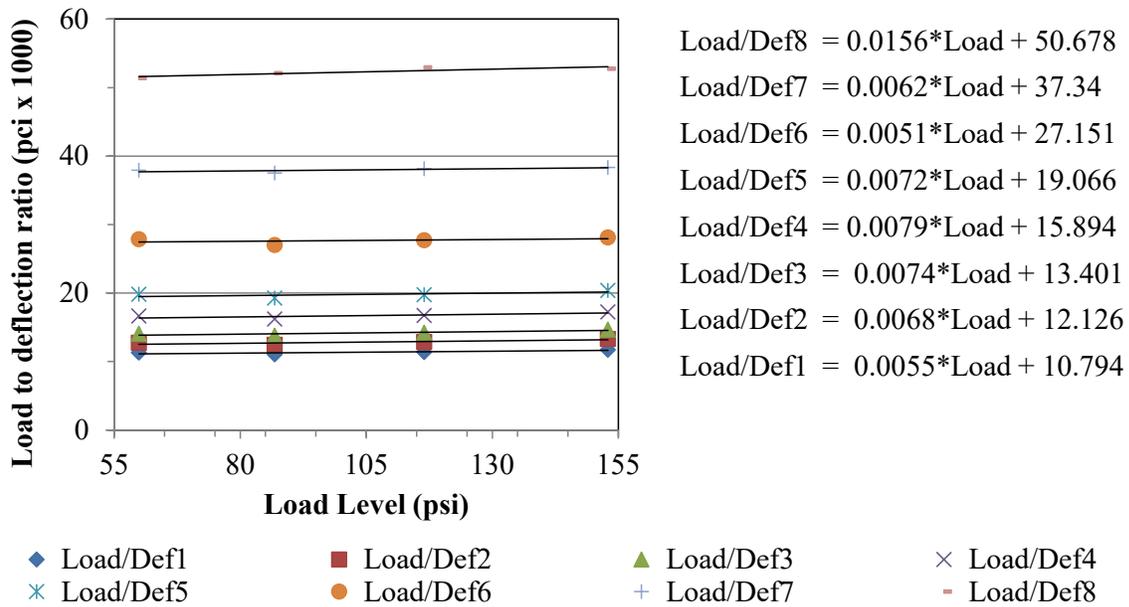
Figure 15. Graph. Example of stiffening behavior for LTPP section 81053, station 3.

$Load/Def8 = -0.0302*Load + 60.633$

$Load/Def7 = -0.0465*Load + 47.095$

$Load/Def6 = -0.0371*Load + 35.564$

$Load/Def5 = -0.0156*Load + 24.43$

$Load/Def4 = -0.0094*Load + 19.882$

$Load/Def3 = -0.0061*Load + 16.352$

$Load/Def2 = -0.0009*Load + 13.8$

$Load/Def1 = -0.0008*Load + 10.79$
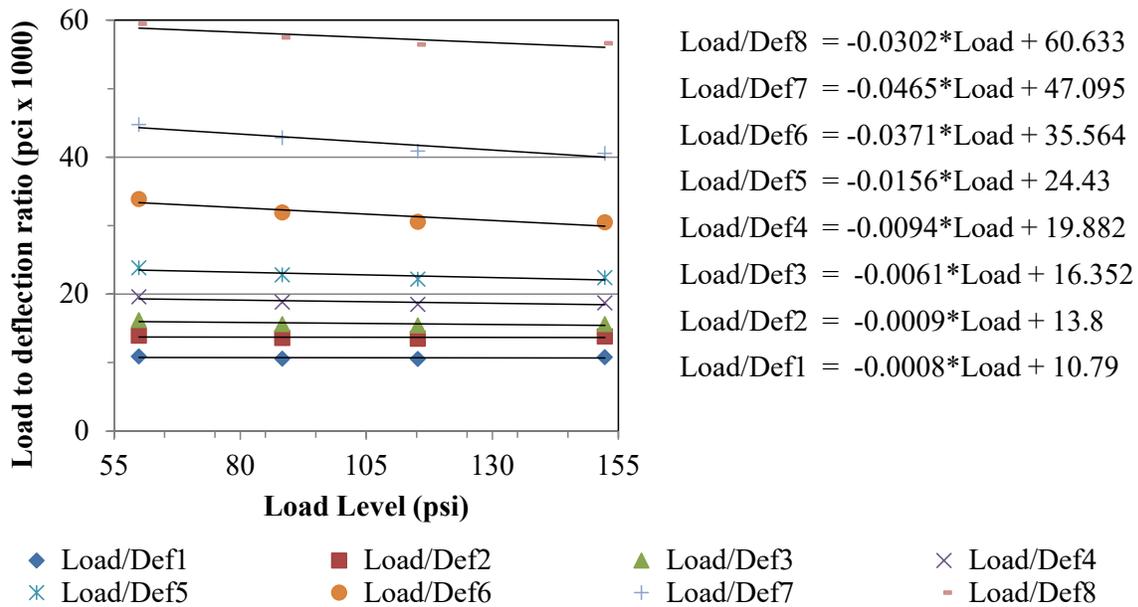
Figure 16. Graph. Example of softening behavior for LTPP section 87781 station 3.

DETAILED STATISTICAL ANALYSIS

Dynamic Behavior

As explained above, the time-histories plots for each test were visually reviewed, and then the sections were classified as follows: (1) season, (2) air temperature, (3) wet/dry, or (4) freeze/no freeze. Figure 17 shows the percentage of sections per category where dynamics were prevalent.

The results showed no particular trend with season and temperature, and the sections in the dry and freeze climate zones appeared to be more prone to dynamic behavior. *t*-tests were performed to assess whether the means of the two groups (wet/dry and freeze/no freeze) were statistically different from each other. Table 5 shows the results of the *t*-tests. The analysis showed that the difference between dry and wet as well as freeze and no-freeze was statistically significant, with dynamics statistically more prevalent in dry freeze sections (figure 18).
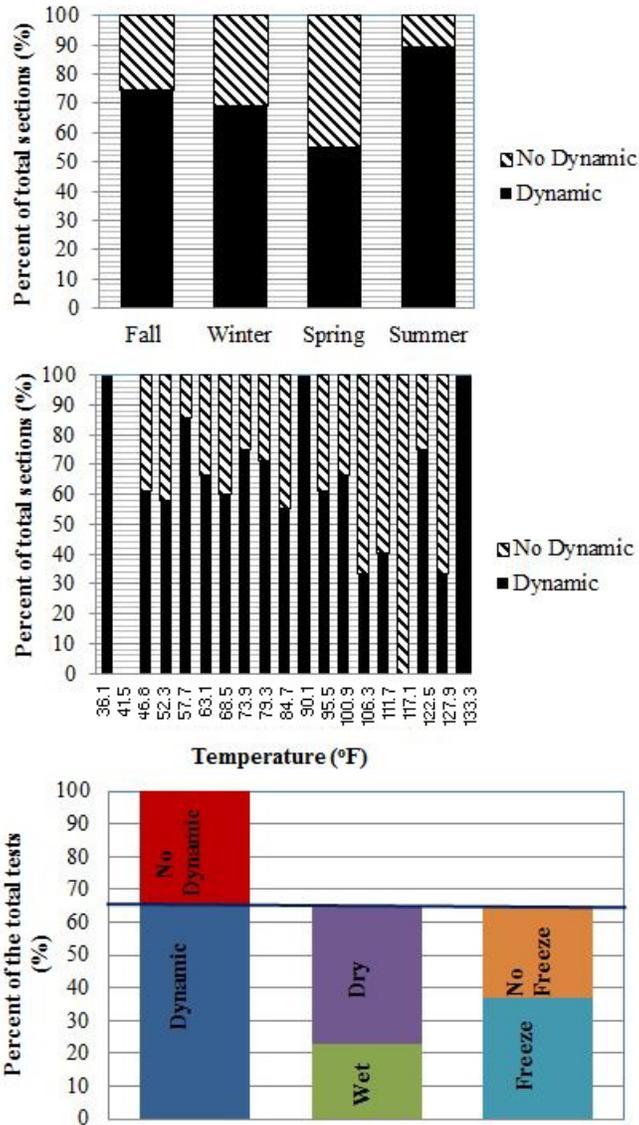
Figure 17. Graphs. Preliminary results—evidence of dynamic behavior by climatic information: classification by season (top), temperature (middle), and climate zone (bottom).

Table 5. LTPP sections used in the statistical analysis.

Statistics	Wet	Dry	Freeze	No-Freeze
Mean percentage of dynamic cases (dynamic = 1; no dynamics = 0)	0.46	0.84	0.79	0.55
Variance	0.10	0.03	0.04	0.11
Number of observations	51	51	49	53
Hypothesized mean difference	0		0	
Degree of freedom	81		84	
t stat	-7.15		4.54	
p-value[1]	0.00		0.00	

[1]Statistically significant if less than 0.05.
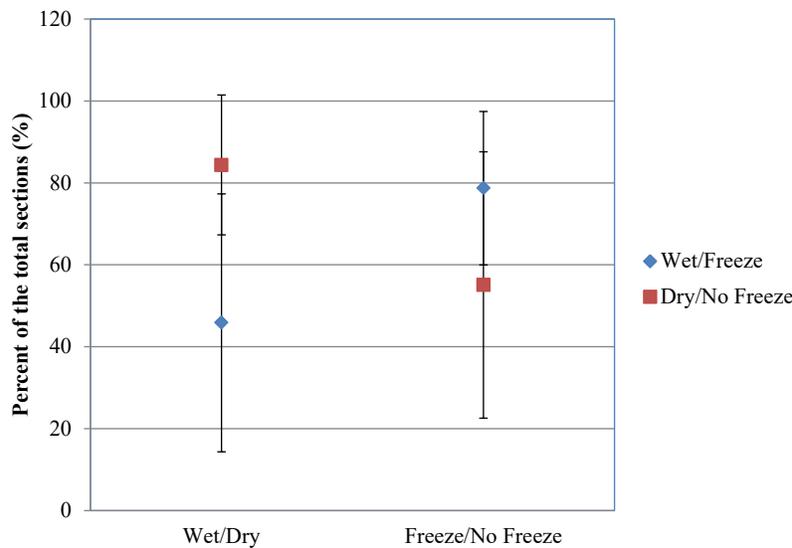
Figure 18. Graph. Mean and standard deviation of percent of sections with dynamics for wet/dry and freeze/no freeze.

Nonlinear Behavior

The following two separate analyses were considered to determine when nonlinearity was prevalent: (1) using all the sections that showed a nonlinear behavior and (2) using only the sites that exhibited no dynamics. The purpose of the second analysis was to investigate the interaction between dynamic and nonlinear effects because both affect the farther sensors. However, the number of sections for the second analysis was small (91 sections) and did not cover all climatic zones, seasons, and temperature ranges, which made the results from the second analysis not reliable. Therefore, only the results from the analysis using all the data are reported. In the analysis, the sections were classified as follows according to the slope of the load-to-deflection ratio trend:

- **Softening**: The slope is negative.
- **Stiffening**: The slope is positive.

Table 6 and figure 19 show the distributions of load-to-deflection slope for all sensors. It can be seen that the slope was mainly within ±20-percent range and that it shifted from more positive (stiffening) to more negative (softening) with increasing sensor number, i.e., increasing sensor distance from the load. This means that, as expected, stress softening was more prevalent in the lower pavement layers.

Table 6. Distribution of load-to-deflection slope by sensor.

Slope (percent)[1]	Frequency (percent)							
	Sensor 1	Sensor 2	Sensor 3	Sensor 4	Sensor 5	Sensor 6	Sensor 7	Sensor 8
-40	0	0	0	0	0	0	1	1
-35	0	0	0	0	0	0	1	1
-30	0	0	0	0	0	1	1	1
-25	0	0	0	1	2	1	3	3
-20	0	1	2	3	4	4	4	4
-15	3	4	5	7	8	6	6	6
-10	8	9	12	13	14	16	15	15
-5	17	16	16	16	20	26	23	23
0	23	26	24	26	23	22	21	21
5	26	22	19	16	16	13	17	17
10	10	11	10	10	9	8	6	6
15	7	7	7	5	3	1	3	3
20	4	3	3	2	1	0	0	0
25	1	1	1	0	0	0	0	0
30	1	1	0	0	0	0	0	0

[1]Stiffening when negative slope and softening when positive slope.
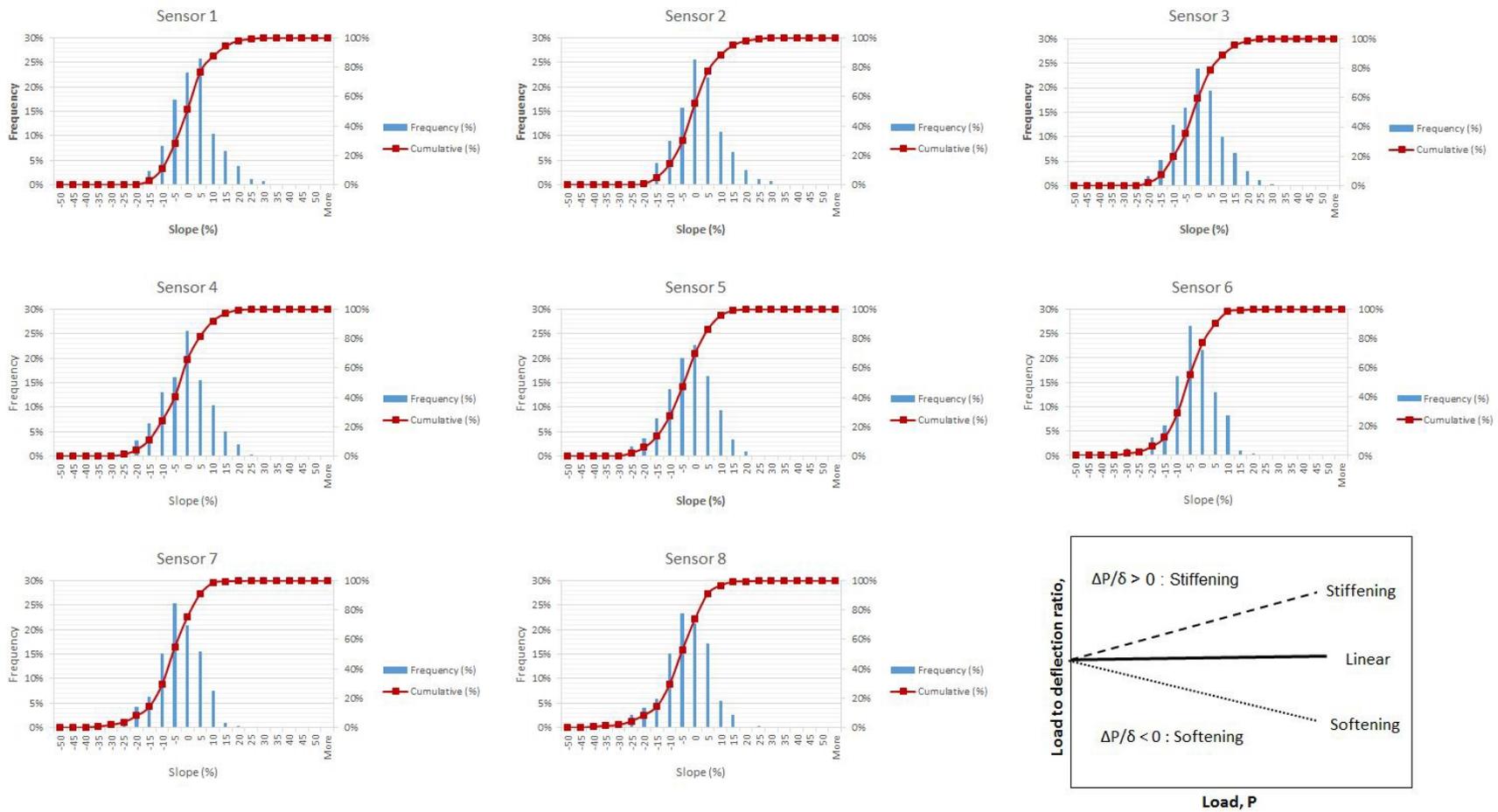
Figure 19. Graphs. Distribution of load-to-deflection slope by sensor.

To further examine the degree of nonlinearity observed, the research team filtered the data by varying the minimum threshold on the slope for defining when nonlinear behavior was observed. For example, if the threshold for nonlinear behavior was ±5 percent, then any section that exhibited a load-to-deflection slope of more than ±5 percent would be considered as exhibiting nonlinear behavior (stiffening if the slope was positive and softening if the slope was negative). The thresholds were set at 5, 6, 7, 8, 9, and 10 percent. Table 7, figure 20, and figure 21 show the percent of sections showing linear versus nonlinear behavior for the various thresholds and for each sensor. The table and figures also show the split between stiffening versus softening behavior (within those exhibiting nonlinear behavior).

Table 7. Distribution of linear versus nonlinear behavior by sensor and percent slope.

Threshold Slope (percent)	Category	Percent of Stations							
		Sensor 1	Sensor 2	Sensor 3	Sensor 4	Sensor 5	Sensor 6	Sensor 7	Sensor 8
5	Linear	48	47	43	41	39	35	36	38
	Nonlinear	52	53	57	59	61	65	64	62
	Stiffening	45	43	37	31	23	15	15	15
	Softening	55	57	63	69	77	85	85	85
6	Linear	55	53	50	49	47	42	44	43
	Nonlinear	45	47	50	51	53	58	56	57
	Stiffening	47	43	37	29	20	15	12	14
	Softening	53	57	63	71	80	85	88	86
7	Linear	63	59	56	55	54	49	50	50
	Nonlinear	37	41	44	45	46	51	50	50
	Stiffening	51	44	37	28	19	13	9	12
	Softening	49	56	63	72	81	87	91	88
8	Linear	69	65	61	58	58	57	58	56
	Nonlinear	31	35	39	42	42	43	42	44
	Stiffening	54	43	36	29	19	11	8	12
	Softening	46	57	64	71	81	89	92	88
9	Linear	72	69	66	63	62	66	64	62
	Nonlinear	28	31	34	37	38	34	36	38
	Stiffening	55	46	37	28	18	7	9	13
	Softening	45	54	63	72	82	93	91	87
10	Linear	76	74	69	68	68	69	69	67
	Nonlinear	24	26	31	32	32	31	31	33
	Stiffening	54	46	36	25	14	6	7	11
	Softening	46	54	64	75	86	94	93	89
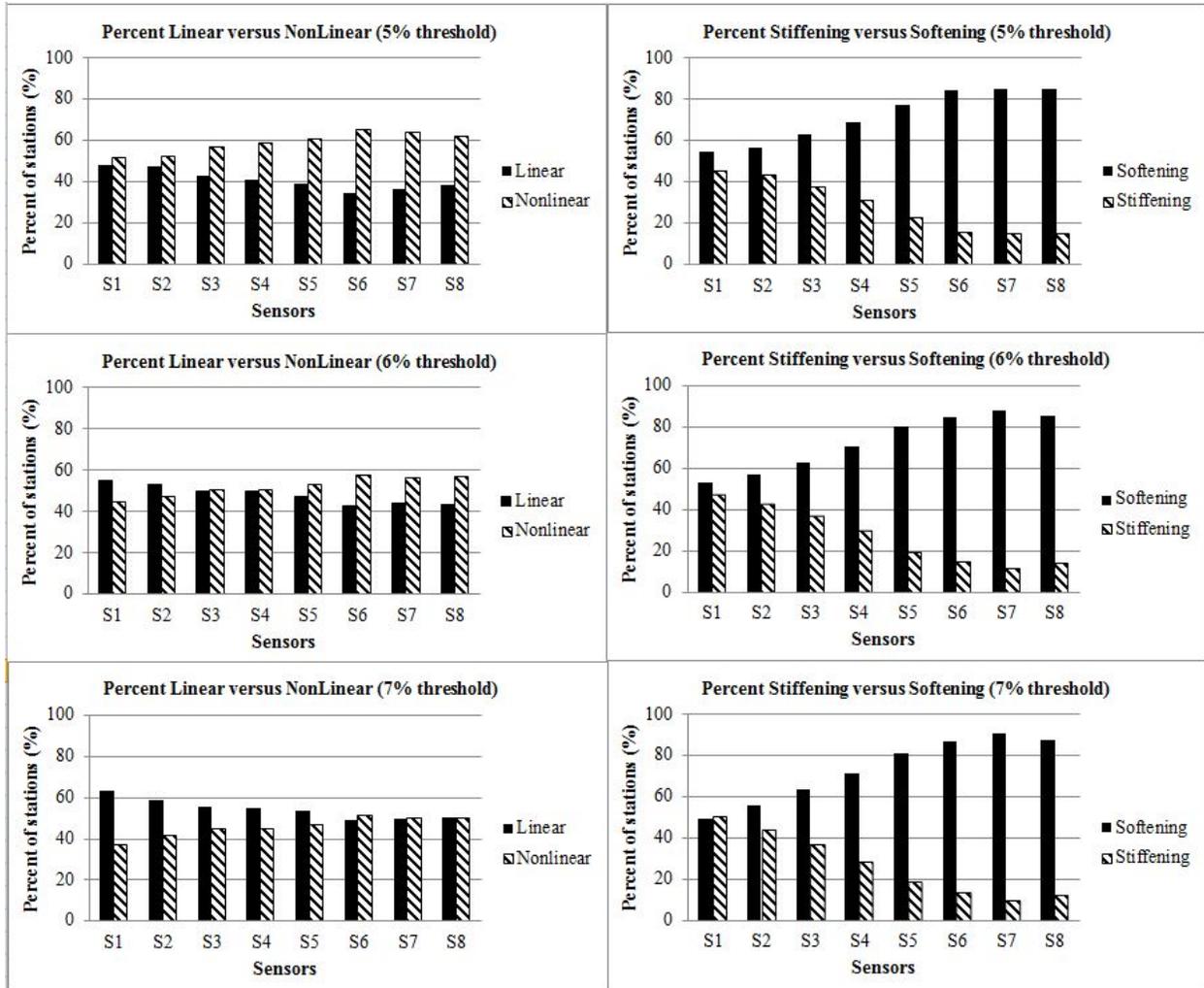
Figure 20. Graphs. Distribution of linear versus nonlinear behavior for 5- to 7-percent threshold load-to-deflection slope.
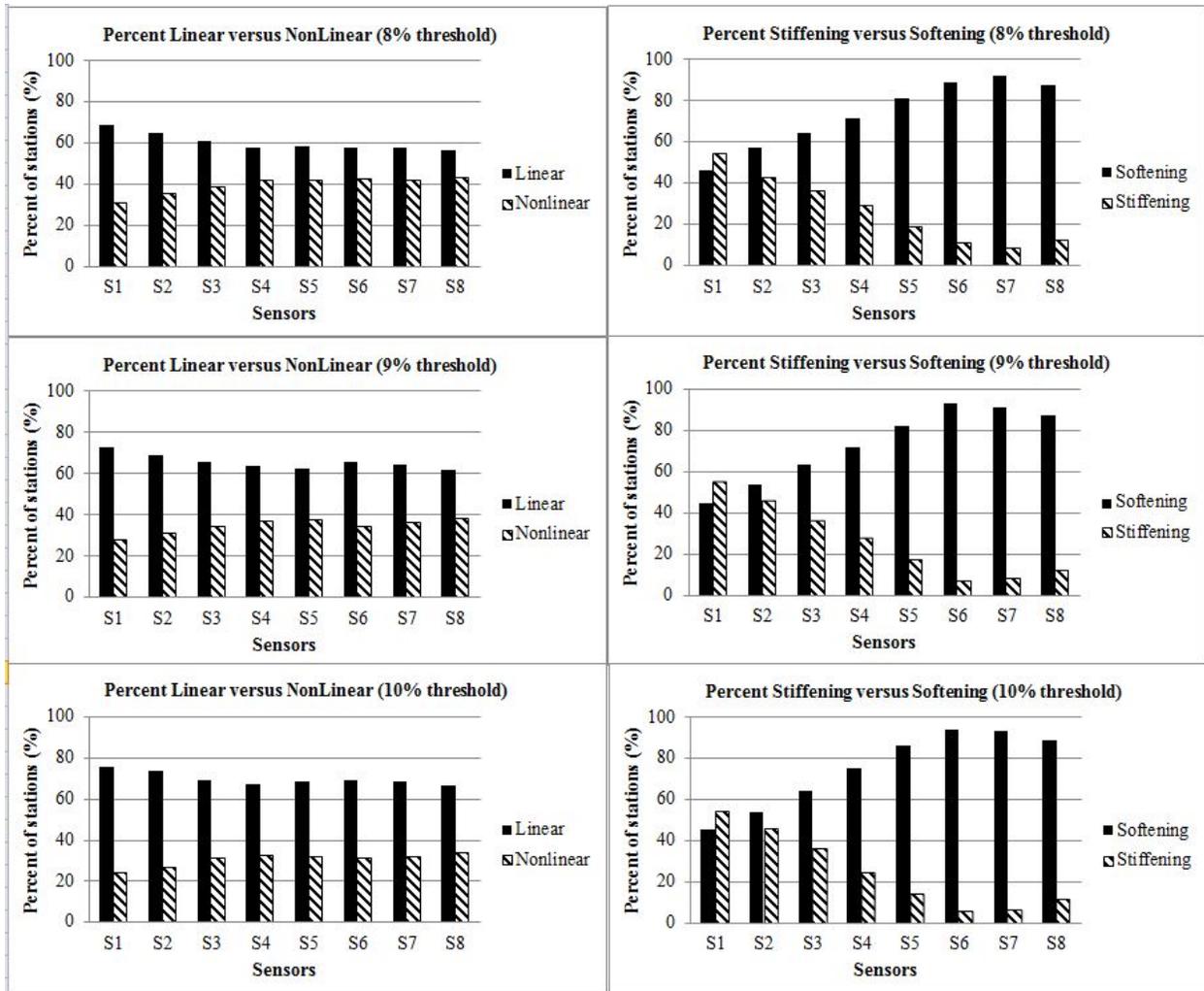
Figure 21. Graphs. Distribution of linear versus nonlinear behavior for 8- to 10-percent threshold load-to-deflection slope.

The results showed a trend of increasing nonlinearity and more softening as sensor number increased and as the sensor distance from the load increased. This means that, as expected, nonlinearity was more prevalent in the farther sensors, which reflected the behavior of the underlying deeper layers, and that these materials showed much more stress softening than stress stiffening behavior.

Assuming a minimum slope of ±5 percent as a threshold for defining nonlinear behavior, the lowest percent of sections with nonlinear behavior was 52 percent (sensor 1) while the highest was 65 percent (sensor 6). Increasing the threshold to ±10 percent reduced these percentages by about half; the lowest percent of sections with nonlinear behavior became 24 percent, and the highest became 33 percent.

Within the sections exhibiting nonlinear behavior, the percent of sections showing stress softening versus stress stiffening was fairly similar irrespective of the threshold on the slope. The split was about 50-percent softening and 50-percent stiffening for the close sensors and gradually

shifted to about 85- to 90-percent softening and 10- to 15-percent stiffening for the intermediate and most distant sensors.

The sections were also classified by: (1) season, (2) temperature, (3) wet/dry, or (4) freeze/no freeze for each sensor, with the nonlinearity threshold slope set at ±5 percent. Figure 22 through figure 24 show the percentage of sections by season, temperature, and climatic zone, respectively, for each sensor where nonlinearity was prevalent.

Figure 22 shows that the percent of sections that exhibited nonlinearity for sensors 1 through 5 was generally highest for summer, followed by fall and spring, and lowest in winter. Sensors 6 through 8 exhibited more nonlinear behavior in the fall. The trend with seasons suggests that nonlinearity is more prevalent when the pavement system is less stiff, as expected. This trend was also generally true with temperature, as shown in figure 23, although there was more variability in the data. Figure 24 shows that there was no particular trend with climatic zone, however. Nonlinear and linear behavior seems to have been evenly split between wet and dry climates and freeze and no-freeze climates. t-tests were performed to assess whether the means of the two groups (wet/dry and freeze/no freeze) were statistically different from each other for all the sensors. Table 8 shows the results of the t-tests. It appears that climate had no effect on the number of sections that exhibited nonlinearity. Table 9 show the distribution of load-deflection slope by sensors in sections that exhibited nonlinearity.
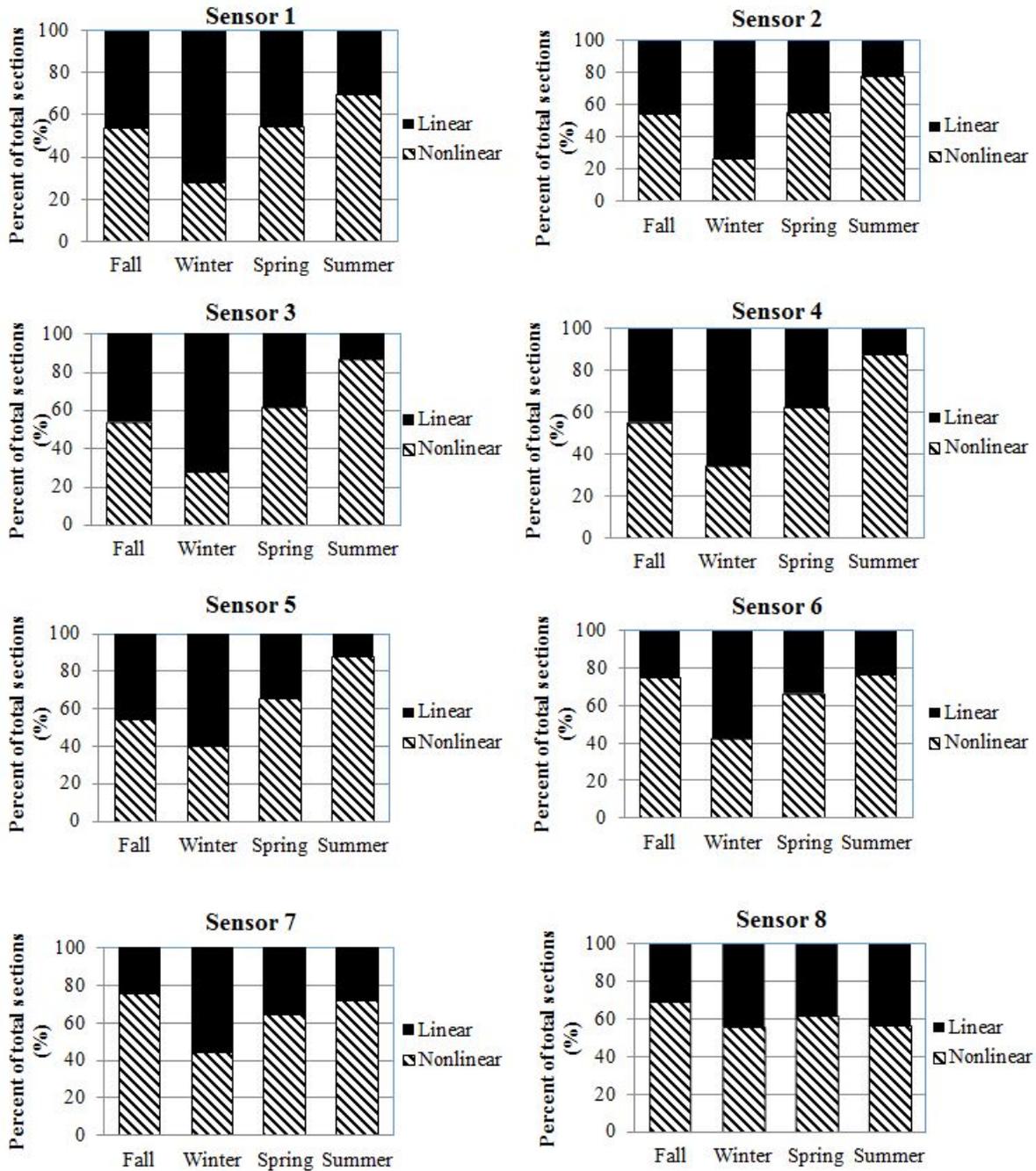
Figure 22. Graphs. Percent of sections by season where nonlinear behavior was prevalent.
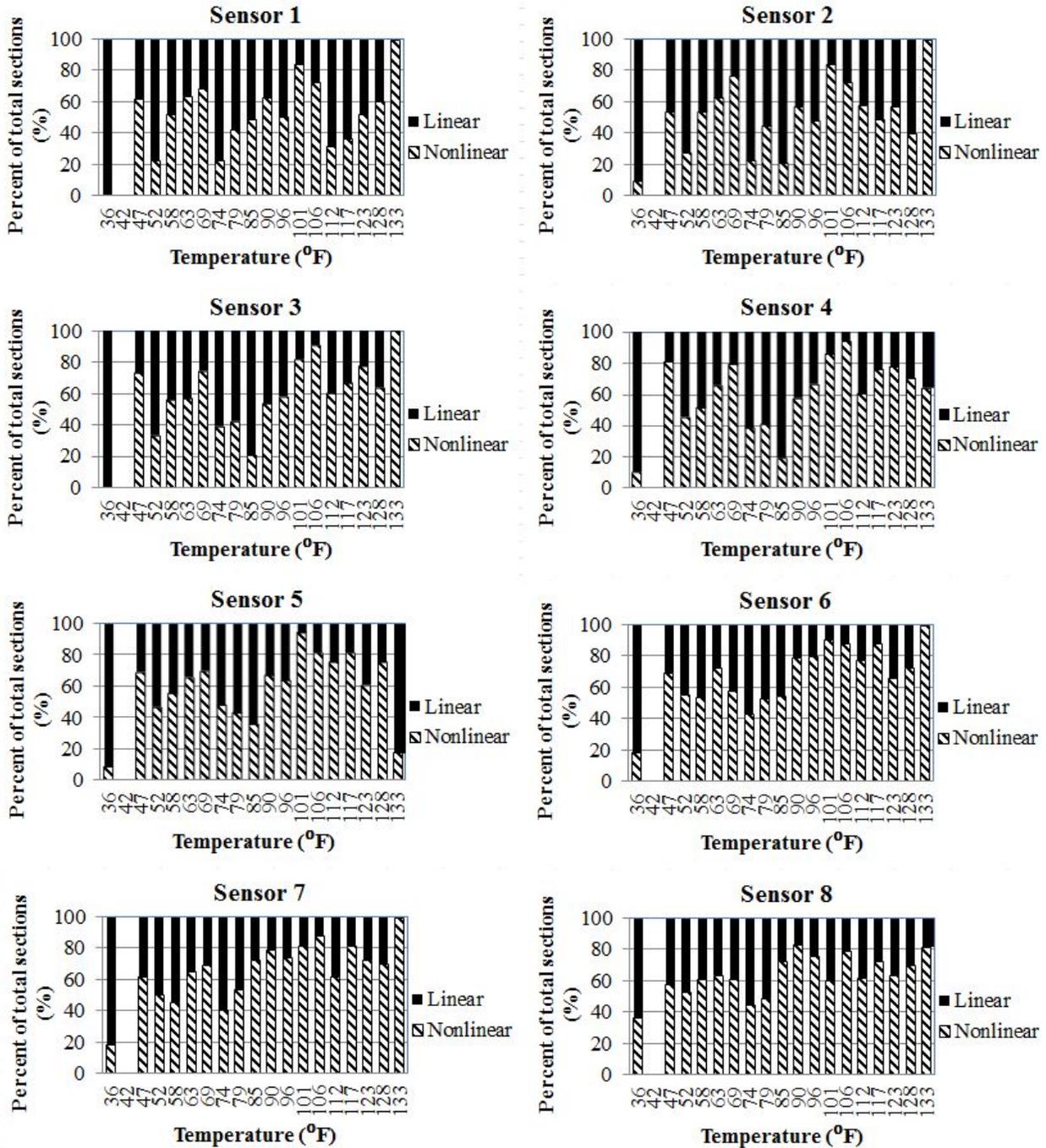
Figure 23. Graphs. Percent of sections by temperature where nonlinear behavior was prevalent.
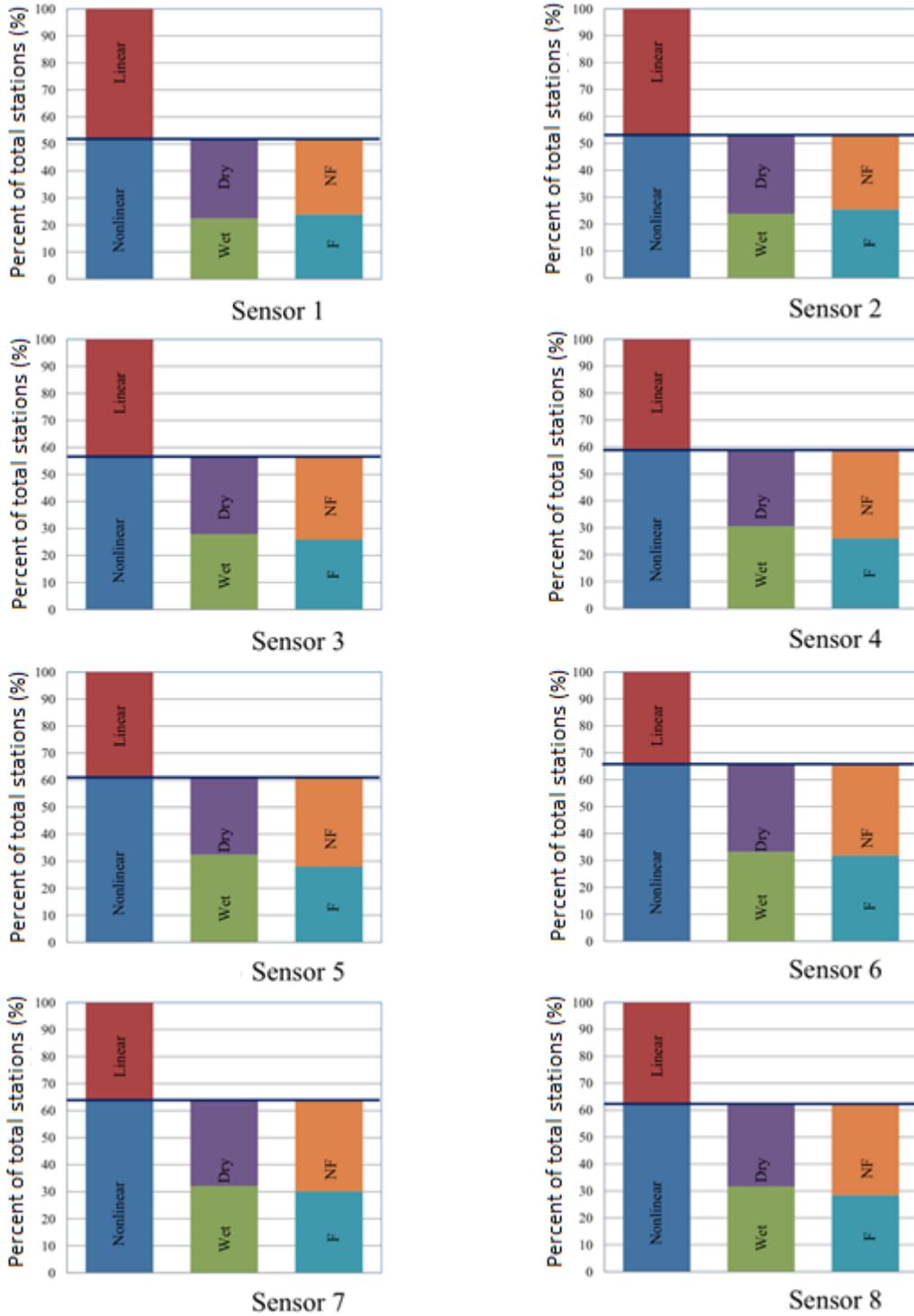
Figure 24. Graphs. Percent of sections by climate zone where nonlinear behavior was prevalent.

Table 8. Results of the *t*-tests on nonlinearity for wet/dry and freeze/no freeze conditions for all sensors.

| Sensor | Mean (percent) | | *p*-Value | Significance | Mean (percent) | | *p*-Value | Significance |
	Wet	Dry			Freeze	No Freeze		
1	43.2	57.2	0.07	No	45.4	54.7	0.24	No
2	51.0	56.9	0.47	No	53.9	54.0	0.99	No
3	59.5	57.6	0.81	No	56.1	60.8	0.56	No
4	64.6	56.9	0.33	No	57.1	64.1	0.38	No
5	69.0	57.8	0.13	No	61.5	65.1	0.64	No
6	71.8	64.3	0.26	No	69.6	66.6	0.65	No
7	68.1	63.6	0.51	No	64.9	66.8	0.78	No
8	67.5	60.6	0.30	No	62.3	65.7	0.61	No

Table 9. Distribution of load-deflection slope by sensor.

| Slope[1] (percent) | Frequency (percent) | | | | | | | |
	Sensor 1	Sensor 2	Sensor 3	Sensor 4	Sensor 5	Sensor 6	Sensor 7	Sensor 8
-40	0	0	0	0	0	0	0	1
-35	0	0	0	0	0	0	0	1
-30	0	0	0	1	0	0	0	0
-25	0	0	0	1	0	0	1	2
-20	0	0	1	3	4	3	4	4
-15	4	3	5	7	11	10	6	5
-10	7	12	19	22	24	23	22	15
-5	21	19	18	19	22	32	31	29
0	32	35	36	36	25	21	21	22
5	26	22	14	10	9	7	9	11
10	8	7	5	1	3	1	4	5
15	1	1	1	1	1	1	1	4
20	1	1	1	0	0	0	1	0
25	0	0	0	0	0	0	0	0
30	0	0	0	0	0	0	0	0

[1]Negative slope means stress-softening; positive slope means stress-stiffening.

MEASUREMENT ISSUES

During the analysis of the LTPP FWD data, signs of measurement issues were also encountered in some tests. Figure 25 presents some samples of these errors. These issues included erroneous deflection sensors (middle row: section 130508 station 1 and section 130566 station 1) or drift (bottom row, left: section 260116 station 1), or data truncation (top row: section 220125 station 3 and section 220125 station 6; and bottom row, left: section 482108 station 1).
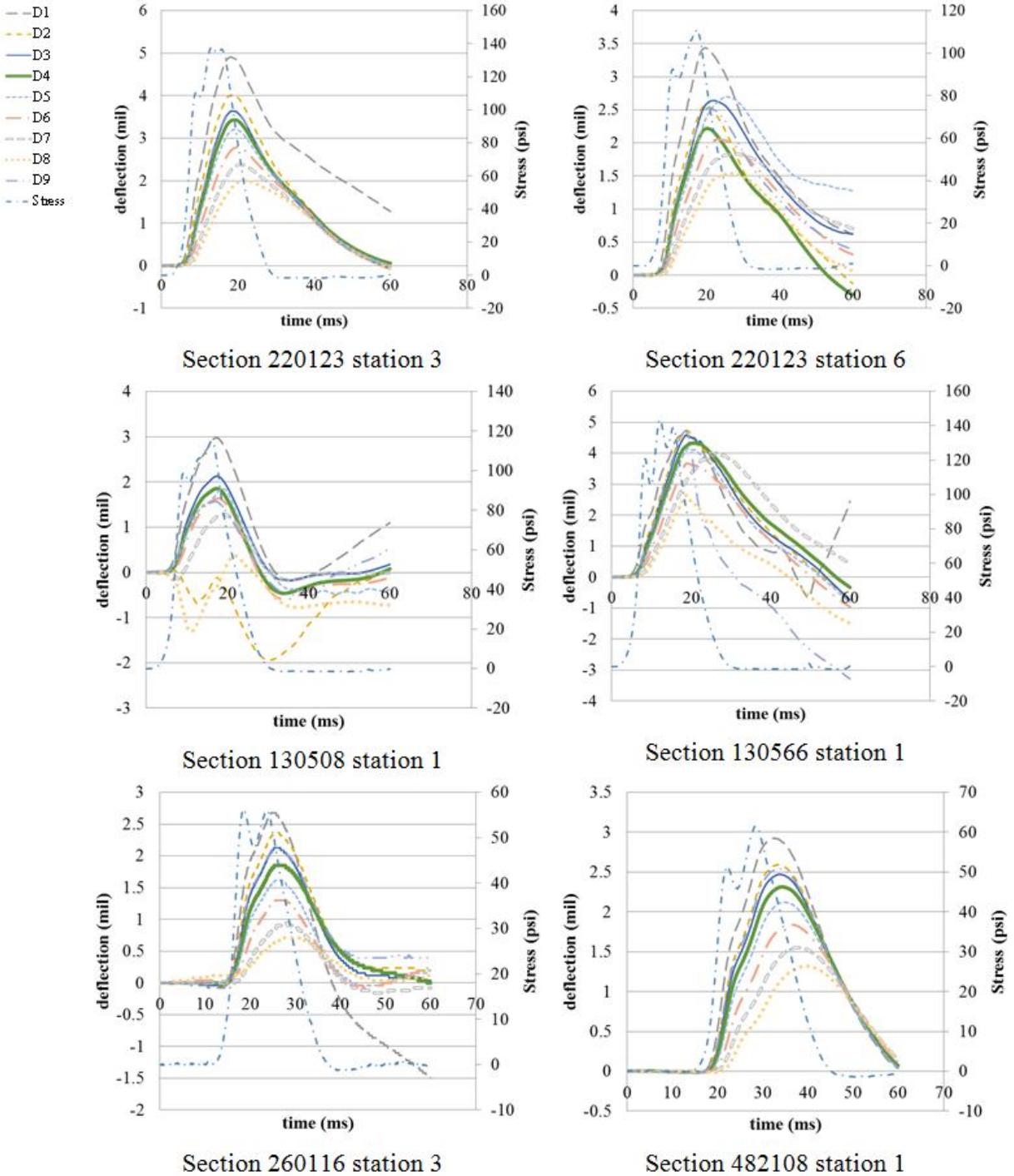
Figure 25. Graphs. Examples of measurement issues.

CONCLUSION

In this chapter, detailed exploratory analyses on a relatively large sample of FWD test results from the LTPP database were conducted to assess (1) prevalence of dynamics, (2) prevalence of nonlinear behavior, and (3) measurement issues based on apparently erroneous deflection sensor time histories. The data covered all climatic zones, seasons, and temperature ranges. It was

observed that dynamics were present in about 65 percent of the cases, while nonlinearity could be prevalent in a range as low as 24 percent of the cases to as high as 65 percent of the cases, depending on severity level and sensor location. Nonlinearity was more prevalent for the sensors that were far from the center of the load. Because of the prevalence of dynamic behavior (in the form of free vibrations of deflection sensor time histories) observed in the large sample of LTPP FWD test data, it was hypothesized that in the great majority of the cases, the stiff layer condition might not correspond to the presence of shallow bedrock. Such bedrock would be highly unlikely given that it typically lies at much greater depths. Instead, the stiff layer condition could be manifested anytime the soils below the subgrade layer are stiffer than the subgrade layer itself. This could be caused by increased confinement with depth, overconsolidation, or existence of a shallow groundwater table, for example; these situations are very common in any soil profile. This would explain the high percentage of sections from the LTPP database that showed dynamic behavior.

CHAPTER 4. VISCOELASTIC APPROACH

Flexible pavements are multilayered structures typically with viscoelastic AC as the top layer and with unbound/bound granular layers below it. The combined response of linear viscoelastic and elastic materials that are in perfect bonding is linear viscoelastic. Assuming there is full bonding between the asphalt layer and the underlying base and subgrade layers, the overall response of the entire pavement system becomes viscoelastic. The characteristic mechanistic properties of an isotropic-thermorheologically simple viscoelastic systems are the relaxation modulus $E(t)$, the creep compliance $D(t)$, the complex (dynamic) modulus $|E^*|$, and the time-temperature shift factors ($a_T(T)$). These characteristic properties are often expressed at a specific reference temperature, in terms of a "master curve." For thermorheologically simple materials, these characteristic properties can be generated at any time (or frequency) and temperature using the time-temperature superposition principle. It can be shown that if any of the three properties $E(t)$, $D(t)$, or $|E^*|$ is known, the other two can be obtained through an interconversion method such as the Prony series.[57] The dynamic modulus ($|E^*|$) master curve of an AC layer is a fundamental material property that is required as an input in the MEPDG for a flexible pavement analysis. Knowledge of the $|E^*|$ master curve of an in-service pavement using FWD data can lead to a more accurate estimation of its remaining life and rehabilitation design.

The specific objectives of this component of the project were to (1) develop a layered viscoelastic flexible pavement response model in the time domain; (2) investigate whether the current FWD testing protocol generated data that were sufficient to backcalculate the $|E^*|$ master curve using such a model; and (3) if needed, recommend enhancements to the FWD testing protocol to be able to accurately backcalculate the $|E^*|$ master curve as well as the unbound material properties of in-service pavements. Readers should note that the methods presented in this report were developed for a single AC layer. However, in-service pavements may be composed of multiple layers of different types of asphalt mixtures. In such cases, the present form of the backcalculation algorithms would provide a single equivalent $|E^*|$ master curve for the asphalt mixture sublayers.

The models presented in this chapter can consider the unbound granular material as both linear elastic as well as nonlinear stress-dependent material. Depending on the assumed unbound granular material property, two generalized viscoelastic flexible pavement models were developed. The developed forward and backcalculation models for linear viscoelastic AC and elastic unbound layers are referred to as LAVA and BACKLAVA, respectively, in this report. The developed forward and backcalculation models for linear viscoelastic AC and nonlinear elastic unbound layers are termed LAVAN and BACKLAVAN, respectively, in the report. The LAVA and BACKLAVA algorithms assumed a constant temperature along the depth of the AC layer. The algorithms were subsequently modified for the temperature profile in the AC layer, and modified versions are referred to as LAVAP and BACKLAVAP in this report. The viscoelastic properties backcalculated from FWD data included two functions—a time function and a temperature function. The time function referred to the relaxation modulus master curve $E(t,T_0)$ in which t was physical time and T_0 was the corresponding (constant) reference temperature. The temperature function referred to the time-temperature shift factor $a_T(T)$, which was a positive definite dimensionless scalar. In the present study, AC was assumed to be thermorheologically simple, which allowed applying $E(t,T_0)$ for any temperature level T

(different than T_0) by simply replacing physical time with a reduced time $t_R = t/a_T(T)$; therefore, $a_T(T)$ is a function of both T and T_0, such that $a_T(T)=1$ if $T = T_0$.

Typically, a load-displacement history of 60 ms is recorded in an FWD test (which constitutes 25 to 35 ms of applied load pulse); it is generally observed that the later portion of deflection history (after the peak) is not reliable. This is due to the numerical error generated by velocity integration. (Most FWD sensors measure velocity or acceleration, which is integrated to obtain the deflections.) This can give only limited information about the time-varying $E(t)$ behavior of the AC layer. However, in theory, it should be possible to obtain the two sought-after functions (i.e., $E(t)$ and $a_T(T)$). In this report, two different approaches are discussed to obtain the comprehensive behavior of asphalt: (1) using series of FWD deflection time histories at different temperature levels and (2) using uneven temperature profile information existing across the thickness of the asphaltic layer during a single or multiple FWD drops deflection histories.[59,60] Both of the models are presented in detail. Finally, the models were validated using frequency and FEM-based solutions.

Further, the effect of FWD test temperatures and number of surface deflection sensors on backcalculation of the $|E^*|$ master curve were studied. These suitable FWD test data requirements are discussed in the key findings from the study.

LAYERED VISCOELASTIC (LAVA) PAVEMENT MODEL

Traditionally, flexible pavements are analyzed using analytic multilayered elastic models (e.g., KENLAYER, BISAR, and CHEVRONX), which are based on Burmister's elastic solution of multilayered structures. (See references 21, 23, 27, and 61–64.) These models assume the material in each pavement layer is linearly elastic. However, the AC (typically the top layer) is viscoelastic at low strain.[60,65,66] As with any viscoelastic material, it shows properties dependent on time (or frequency) as well as temperature.

In the proposed approach, the AC pavement system was modeled as a layered half-space, with the top layer as a linear viscoelastic solid. All other layers (base, subbase, subgrade, and bedrock) in the pavement were assumed linear elastic. Assuming there was full bonding between the AC layer and the underlying base and subgrade layers, the overall response of the entire pavement system became viscoelastic. Therefore, its response under arbitrary loading was obtained using Boltzmann's superposition principle (i.e., the convolution integral) as shown in figure 26.[65,66]

$$R^{ve}(x,y,z,t) = \int_{\tau=0}^{t} R_H^{ve}(x,y,z,t-\tau)\frac{dI(\tau)}{d\tau}d\tau$$

Figure 26. Equation. Boltzmann's superposition principle.

Where:

$R^{ve}(x,y,z,t)$ I = the linear viscoelastic response at coordinates (x,y,z) and time t.
$R_H^{ve}(x,y,z,t)$ = the (unit) viscoelastic response of the pavement system to a Heaviside step function input $(H(t))$.
$dI(\tau)$ is the change in input at time τ.

It is worth noting that for a uniaxial viscoelastic system (e.g., a cylindrical AC mixture), if response $R^{ve}= \varepsilon(t)$ = strain, then R_H^{ve} = $D(t)$ = creep compliance and $I(t) = \sigma(t)$ = stress. Using Schapery's quasi-elastic theory, the viscoelastic response at time t to a unit input function was efficiently and accurately approximated by the elastic response obtained using relaxation modulus at time t as shown in figure 27.[67,68]

$$R_H^{ve}(x,y,z,t) \cong R_H^e(x,y,z,E(t))$$

Figure 27. Equation. Quasi-elastic approximation of a unit response function such as the creep compliance..

Where $R_H^e(x,y,z,E(t))$ is the unit elastic response at elastic modulus equal to relaxed modulus $(E(t))$. Flexible pavements are exposed to different temperatures over time, which in turn influence their response. For thermorheologically simple materials, this variation in response can be predicted by extending the equations shown in figure 26 and figure 27 to the equation shown in figure 28.

$$R^{ve}(x,y,z,t) = \int_{\tau=0}^{t_R} R_H^e(x,y,z,E(t_R-\tau))\frac{dI(\tau)}{d\tau}d\tau$$

Figure 28. Equation. Hereditary integral using quasi-elastic approximation of a unit response function such as the creep compliance..

Where:

$t_R = t/a_T(T)$.
$a_T(T) = a_1(T^2 - T_{ref}^2) + a_2(T - T_{ref})$ is the shift factor at temperature T.
T_{ref} I = the reference temperature
a_1 and a_2 are the shift factor's polynomial coefficients.

Using figure 28, the formulation for predicting vertical deflection of a linear viscoelastic AC pavement system subjected to an axisymmetric loading can be expressed as the equation shown in figure 29.

$$u_{vertical}^{ve}(r,z,t) = \int_{\tau=0}^{t_R} u_H^e - vertical(E(t_R - \tau), r, z)\frac{d\sigma(\tau)}{d\tau}d\tau$$

Figure 29. Equation. Hereditary integral using quasi-elastic approximation of unit vertical deflection at the surface.

Where:

$u_{vertical}^{ve}(r,z,t)$ = the viscoelastic response of the viscoelastic multilayered structure at time t and coordinates (r,z).

$u_{H-vertical}^e(E(t_R - \tau), r, z)$ i= the elastic unit response of the pavement system at reduced time t_R due to the unit (Heaviside step) contact stress (i.e., $\sigma(t) = 1$).

$\sigma(\tau)$ is the applied stress at the pavement surface.

Detailed derivation of the equation in figure 29 can be found in Levenberg's research and are not repeated here for brevity.[69] In this implementation, the vertical surface displacements, i.e., $u_H^{ve}(t) \cong u_H^e(t)$ values at the points of interest, were computed using the CHEVRONX layered elastic analysis program. Then the convolution integral in figure 29 was used to calculate the viscoelastic deflection $u^{ve}(t)$. A description of the algorithm is given in the following section.

Layered Viscoelastic (Forward) Algorithm (LAVA)

The algorithm steps were as follows:

1. Define the geometric (layer thicknesses, contact radius) and material ($E(t)$, E_{base}, $E_{subgrade}$, and Poisson's ratio) properties of a layered system similar to the one in figure 30.

2. Select a stress versus time history ($\sigma(t)$) and divide the data into N_s discrete intervals as shown in figure 31.
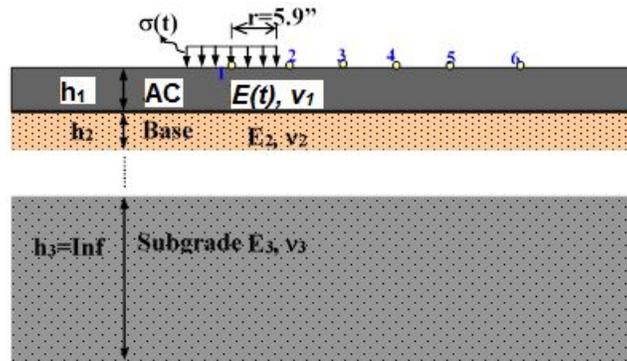
Figure 30. Diagram. Typical flexible pavement geometry for analysis.
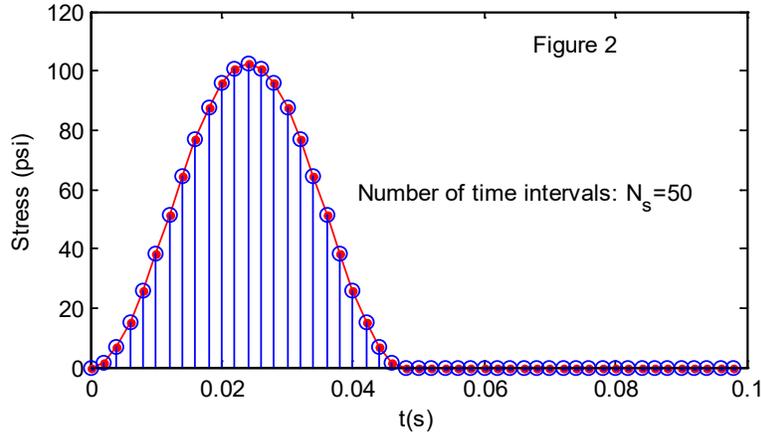
Figure 31. Graph. Discretization of stress history in forward analysis.

3. Divide the relaxation modulus master curve into N_E, the number of time steps in log scale. The relaxation modulus $E(t)$ can be approximated with a sigmoid function as shown in figure 32.

$$\log(E(t)) = c_1 + \frac{c_2}{1 + \exp(-c_3 - c_4 \log(t_R))}$$

Figure 32. Equation. Sigmoid form of relaxation modulus master curve.

Where t_R is the reduced time ($t_R = t/a_T(T)$) and c_i are sigmoid coefficients. The shift factor coefficients were computed using the second order polynomial given in figure 33.

$$\log(a_T(T)) = a_1(T^2 - T_{ref}^2) + a_2(T - T_{ref})$$

Figure 33. Equation. Shift factor coefficient polynomial.

Where a_1 and a_2 are the shift factor coefficients.

4. Calculate the elastic response (i.e., vertical surface deflections) of the structure to a unit stress using $E(t_i)$ evaluated at different reduced times (i.e., t_1, t_2, t_3 ....t_{NE}). In this implementation, the surface deflections at several radial distances to a circular plate load shown in figure 30 were of interest. Therefore, these surface deflections were computed using the CHEVRONX program with the AC modulus value corresponding to different times in figure 34 (i.e., $E(t_1)$, $E(t_2)$, $E(t_3)$, $E(t_4)$... $E(t_{NE})$) as shown in figure 35.[67,68]
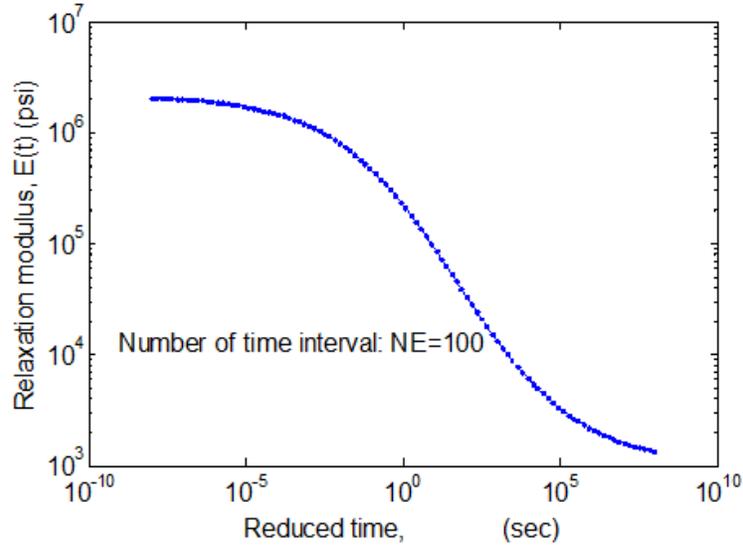
Figure 34. Graph. Discretization of the relaxation modulus master curve.

$$u_H^{ve}(t_i) \cong u_H^e$$

Figure 35. Equation. Quasi-elastic approximation of unit vertical deflection at the surface.

The equation in figure 35 is calculated using $E(t_i)$ where i = 1,2,3…N_E. Figure 36 shows the u_H^e values calculated for points at different distances from the centerline of the circular load at the surface. These curves are called *unit response master curves*.
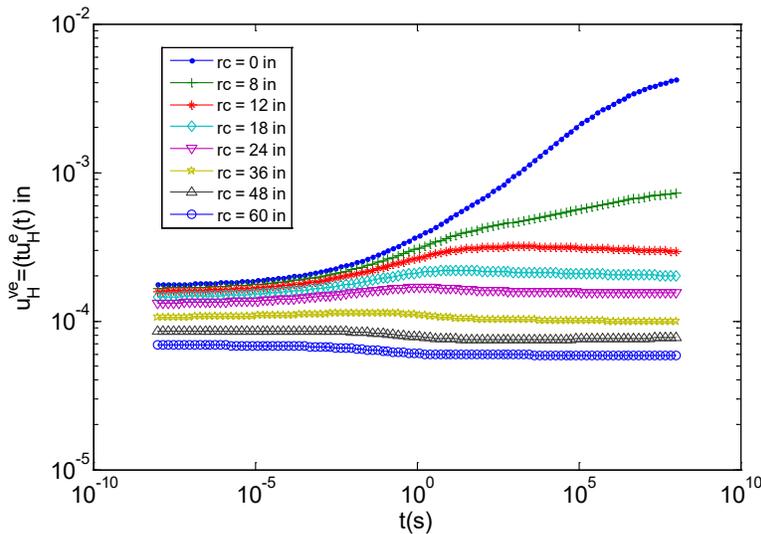
Figure 36. Graph. Deflections calculated under unit stress for points at different distances from the centerline of the circular load at the surface.

5. Calculate the viscoelastic response using the discrete form of figure 29 given in figure 37. The equation was evaluated at each discrete time *t* using the stress history shown in figure 38. Figure 38 illustrates the $d\sigma(\tau_j)$ in figure 37 for each time step τj.

58

$$u^{ve}(t_i) = \sum_{j=0}^{i} u_H^e(t_i - \tau_j) d\sigma(\tau_j)$$

Figure 37. Equation. Discrete formulation.

Where $I = 1,2,\dots N_s$.
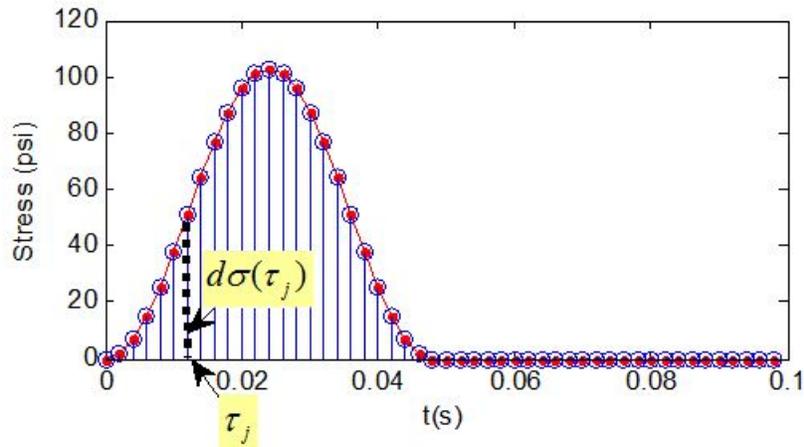
Figure 38. Graph. $d\sigma(\tau_j)$ for each time step τ_j.

To illustrate an example, the viscoelastic surface deflections of the three-layer pavement structure shown in figure 39 were computed. Figure 40 shows the vertical surface deflections at points located at different radial distances from the centerline of the load. Figure 40 clearly shows the relaxation behavior of deflection at each point.
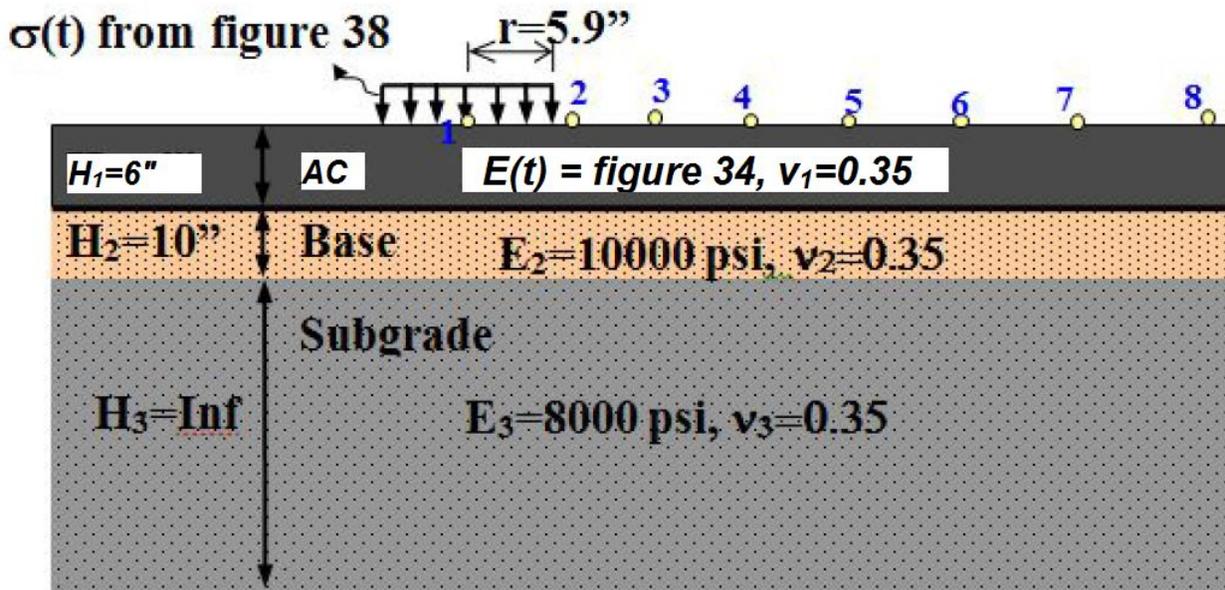
Figure 39. Diagram. Example problem geometry.

59
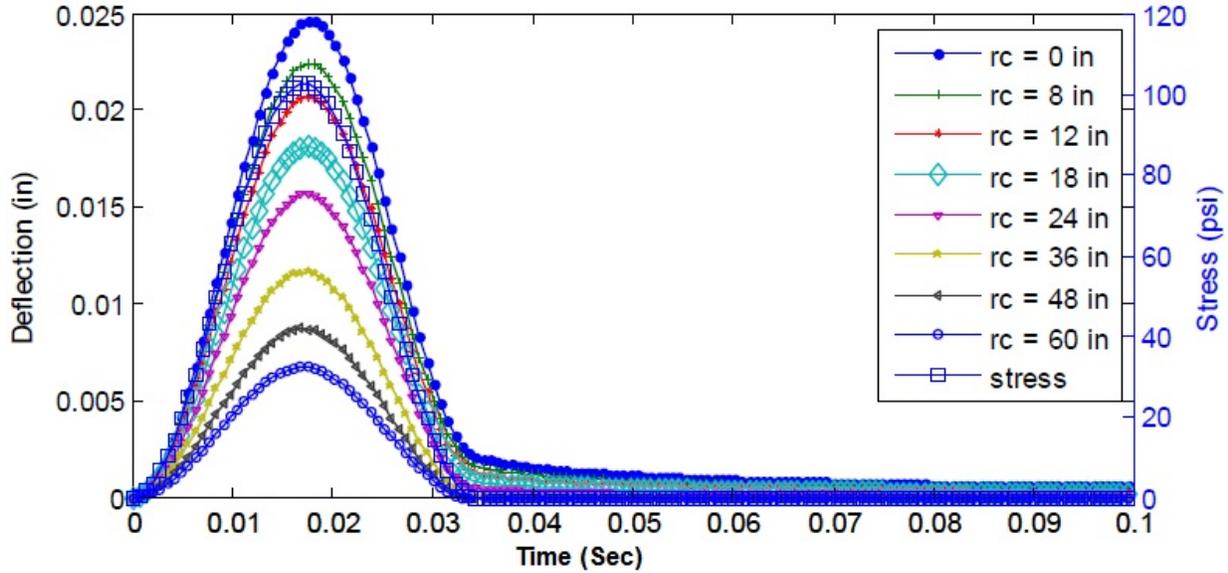
Figure 40. Graph. Examples of computed viscoelastic surface deflections at different radial distances from the centerline of the load.

One of the primary reasons for implementing Schapery's quasi-elastic solution is its extreme computational efficiency. Using a Pentium 2.66 GHz computer with 3.25 gigabytes (GB) of random access memory (RAM), the computation of the results shown in figure 40 took 1.96 s to calculate the solution for the three-layer system shown in figure 39 and $N_S = 50$, $N_E = 50$. Table 10 shows the computation times for different numbers of discrete time steps in the three-layer system.

Table 10. LAVA computation times for different numbers of discrete time steps.

N_S	N_E	Computation Time (s)
50	50	1.96
24	100	2.88
50	100	3.03
100	100	3.05
100	200	5.01
200	200	5.13

Verification of the Proposed Layered Viscoelastic Solution (LAVA)

The layered viscoelastic algorithm was verified by using two pavement structures selected from the SPS-1 experiment of the LTPP database (table 11). Surface deflections at different radial distances due to a circular loading pulse of 0.045 s followed by 0.055-s rest period were calculated using two commonly known software packages, SAPSI and LAMDA, and compared with the layered viscoelastic solution implemented in this research. SAPSI is based on damped-elastic layer theory and FEM, whereas LAMDA is based on the spectral element technique, axisymmetric dynamic solution.[32,2] These software packages were selected because they were known to provide robust dynamic solutions, and their algorithms were based on frequency-

domain calculations. This allows truly independent verification because the layered viscoelastic solution is in the time domain, whereas SAPSI and LAMDA are in the frequency domain.

Table 11. Pavement properties used in LAVA validation with SAPSI and LAMDA.

Case No.	Physical Layer	Elastic Modulus	Thickness (inches)	Poisson's Ratio
116	AC	$\lvert E^*\rvert$-f_{ro}	3.9	0.35
	TB base	29 ksi	12.0	0.40
	Subgrade (SS)	14.5 ksi	Infinity	0.45
120	AC	$\lvert E^*\rvert$-f_{ro}	3.6	0.35
	PATB base	26.1 ksi	4	0.40
	GB base	21.8 ksi	8	0.40
	Subgrade (SS)	14.5 ksi	Infinity	0.45

TB = Treated base.
SS = Sandy subgrade.
PATB = Permeable asphalt treated base.
GB = Granular base.

Figure 41 and figure 42 show the comparison between the layered viscoelastic solution and solutions calculated with SAPSI and LAMDA. The figures clearly show that the layered viscoelastic result matched very well to the SAPSI and LAMDA solutions. Note that the layered viscoelastic algorithm did not consider the dynamics, whereas SAPSI and LAMDA did.

The dynamic solution developed a time delay in response to wave propagation. However, because the scope of this portion of the project included the backcalculation of viscoelastic characteristics of the AC layer, the effect of dynamics was not considered. Therefore, the time delay in dynamic solutions was eliminated by shifting the deflection curves to the left such that the beginning of each sensor response matched.
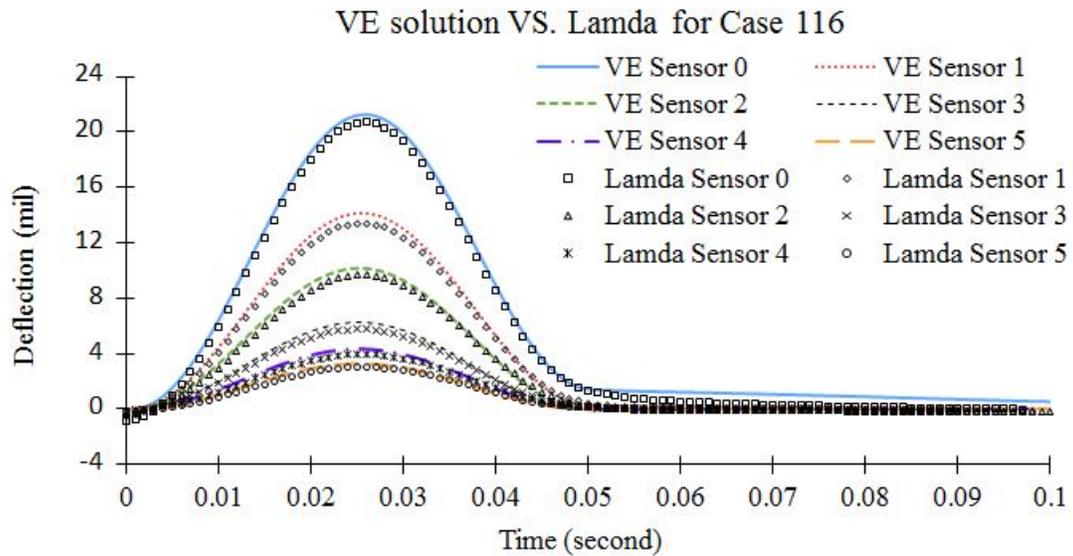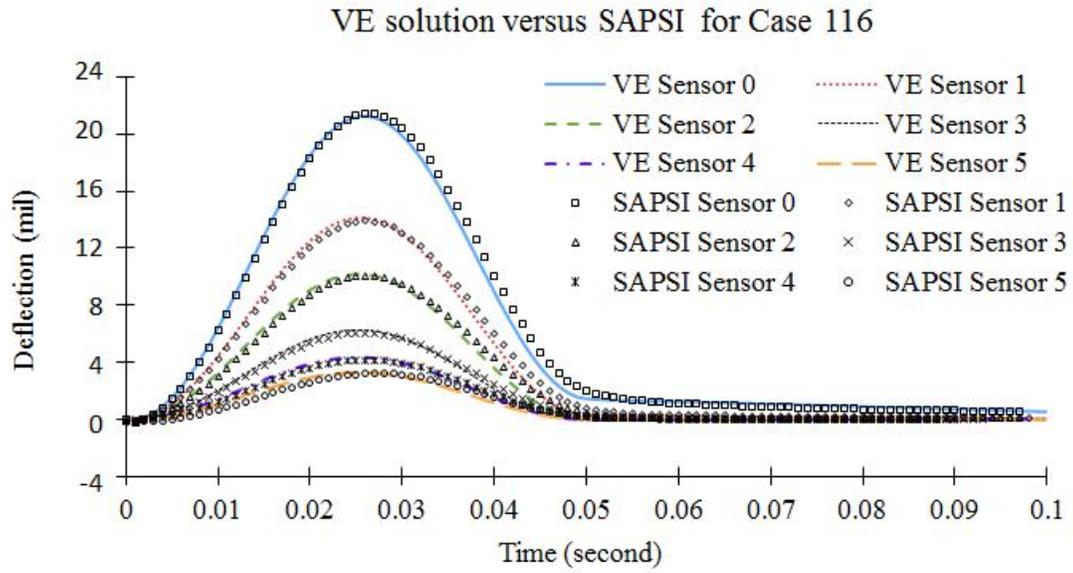
VE = viscoelastic.

Figure 41. Graphs. Comparison of dynamic solutions (time delay removed) and viscoelastic solution for case 116.
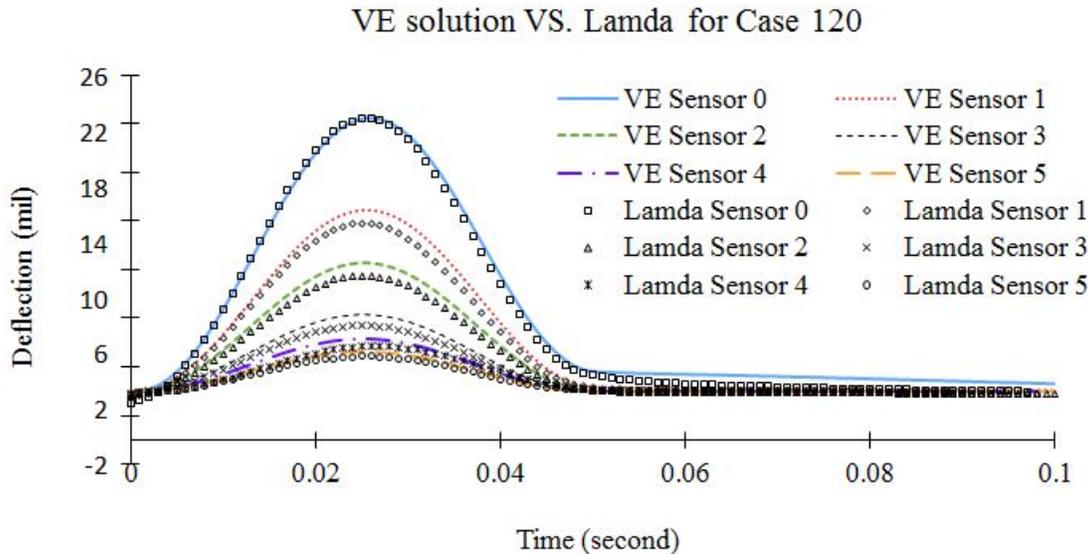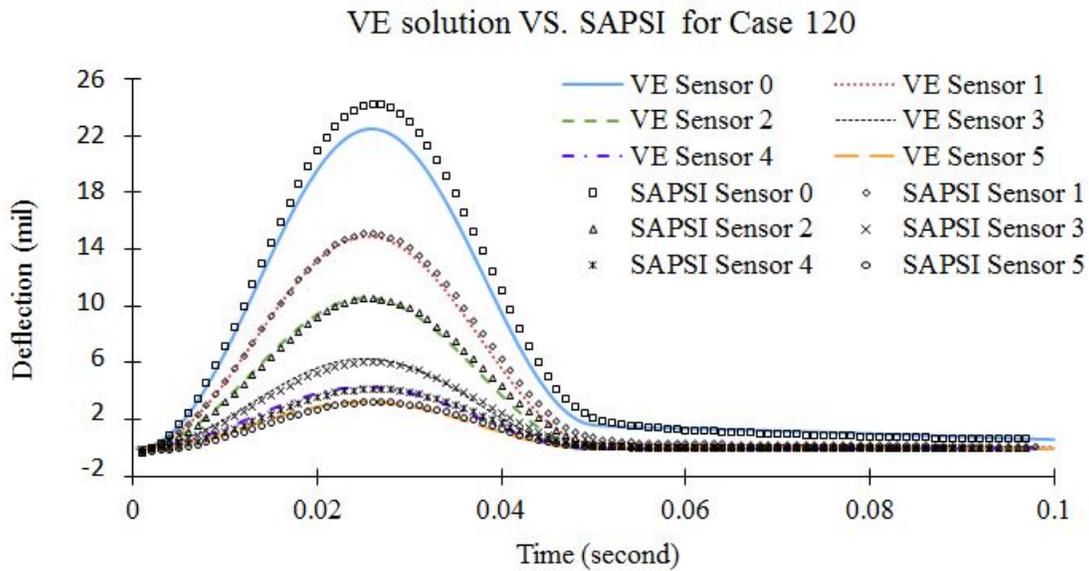
VE = viscoelastic.

Figure 42. Graphs. Comparison of dynamic solutions (time delay removed) and viscoelastic solution for case 120.

IMPLEMENTATION OF TEMPERATURE PROFILE IN LAVA

Temperature in pavements typically varies with depth, which affects the response of the HMA to the applied load. As shown in figure 43, the temperature may increase with depth (profile 1—linear, 2—piecewise, and profile 3—nonlinear) or decreasing with depth (profile 4—linear, profile 5—piecewise, and profile 6—nonlinear) depending on the time of the day. This variation in temperature with depth can be approximated with a piecewise continuous temperature profile function as shown in figure 43 (profiles 2 and 5). The advantage of using a piecewise function is that it can be used to approximate any arbitrary function.

63
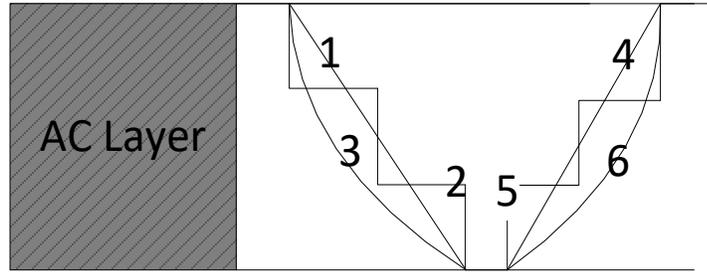
Figure 43. Diagram. Schematic of temperature profile.

An algorithm that considers HMA sublayers with different temperatures within the HMA layer was developed and is referred to as LAVAP (T-profile LAVA). The algorithm was compared with LAVA as well as ABAQUS. Comparison with LAVA was made for deflection response at all the sensors for constant temperature throughout all the sublayers. The pavement section and layer properties used in the forward analysis are shown in table 12. Figure 44 shows the response obtained from the temperature profile algorithm at 32, 86, and 122 °F matched very well with LAVA.

Table 12. Pavement properties used in (T-profile LAVA) LAVAP validation with ABAQUS.

Property		Constant Temperature	Temperature Profile (Three-Step Function)
Thickness (inches)	AC sublayers	6	2, 2, 2
	Granular layers	20, infinite	20, infinite
Poisson ratio {layer 1, 2, 3…}		0.35, 0.3, 0.45	0.35, 0.3, 0.45
$E_{unbound}$ {layer 2, 3…}, psi		11,450, 15,000	11,450, 15,000
Total number of sensors		8	
Sensor spacing from the center of load (inches)		0, 7.99, 12.01, 17.99, 24.02, 35.98, 47.99, 60	
$E(t)$ sigmoid coefficient {AC}		0.841, 3.54, 0.86, -0.515	0.841, 3.54, 0.86, -0.515
$a(T)$ shift factor polynomial coefficients {AC}		4.42E-04, -1.32E-01	4.42E-04, -1.32E-01
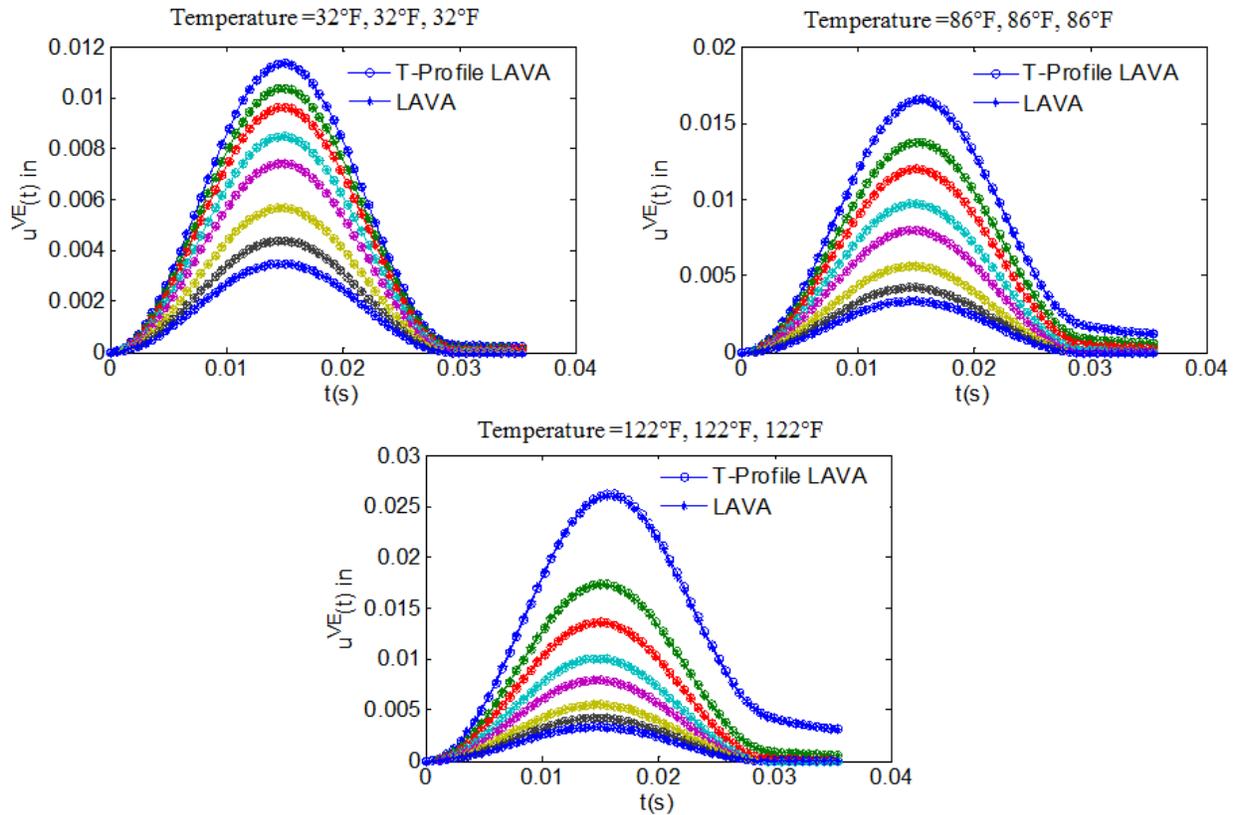
Figure 44. Graphs. Comparison of response calculated using (T-profile LAVA) LAVAP and original LAVA.

To qualitatively examine the response of flexible pavement predicted using the (T-profile LAVA) LAVAP algorithm, the response obtained under temperature profile was compared with the response obtained under constant temperatures. As an example, a comparison of the response under a temperature profile of {104, 86, 68} °F, with that corresponding to a constant temperature of 104, 86, and 68 °F for the entire depth, is shown in figure 45, figure 46, and figure 47, respectively. It can be seen from the figures that the effect of AC temperature was most prominent in sensors closer to the load center (sensors 1 through 4). For sensors away from the loading center (sensors 5, 6, 7, and 8), the deflection histories were not influenced by the AC temperature. Figure 48 shows the region of the $E(t)$ master curve (at 66.2 °F reference temperature) used by the (T-profile LAVA) LAVAP algorithm in calculating time histories.
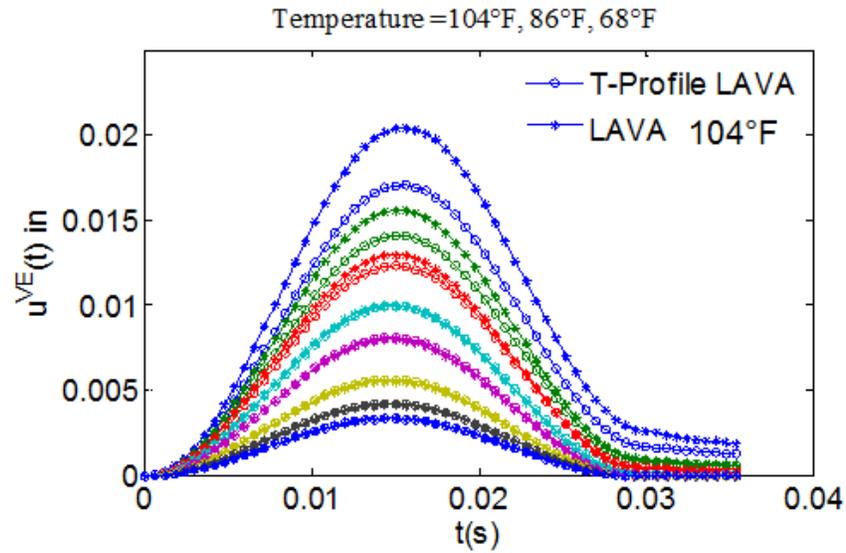
Figure 45. Graph. Comparison of responses calculated using (T-profile LAVA) LAVAP at temperature profile {104, 86, 68} °F and original LAVA at constant 104 °F temperature.
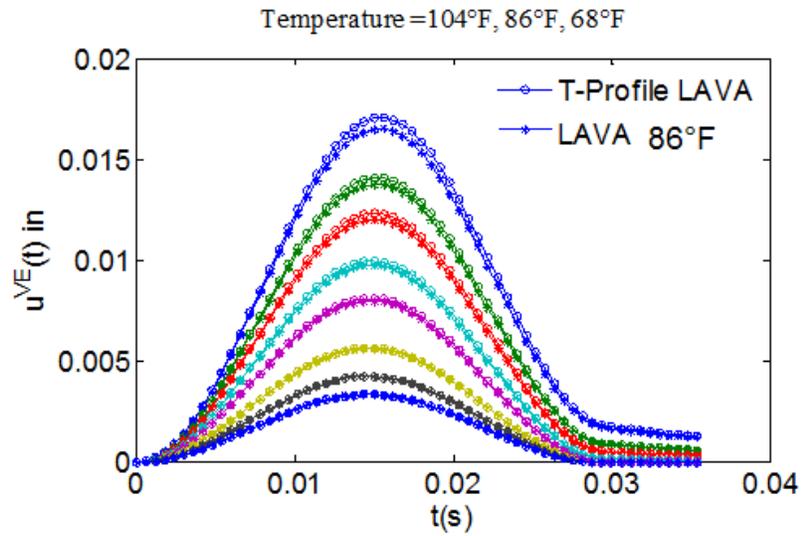
Figure 46. Graph. Comparison of responses calculated using (T-profile LAVA) LAVAP at temperature profile {104, 86, 68} °F and original LAVA at a constant temperature of 86 °F.
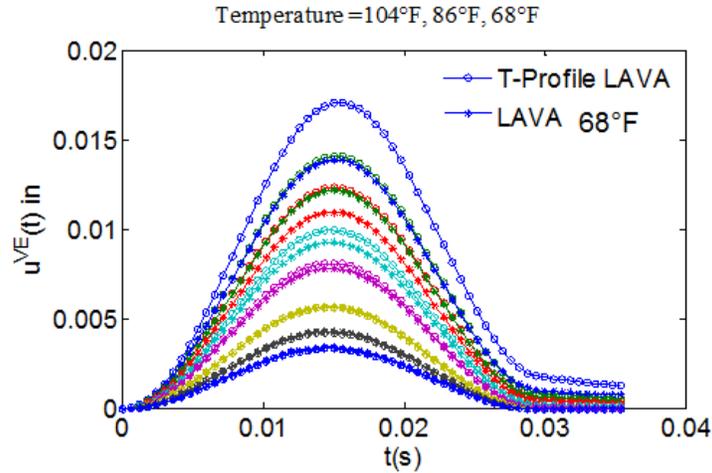
Figure 47. Graph. Comparison of responses calculated using (T-profile LAVA) LAVAP at temperature profile {104, 86, 68} °F and original LAVA at a constant temperature of 68 °F.
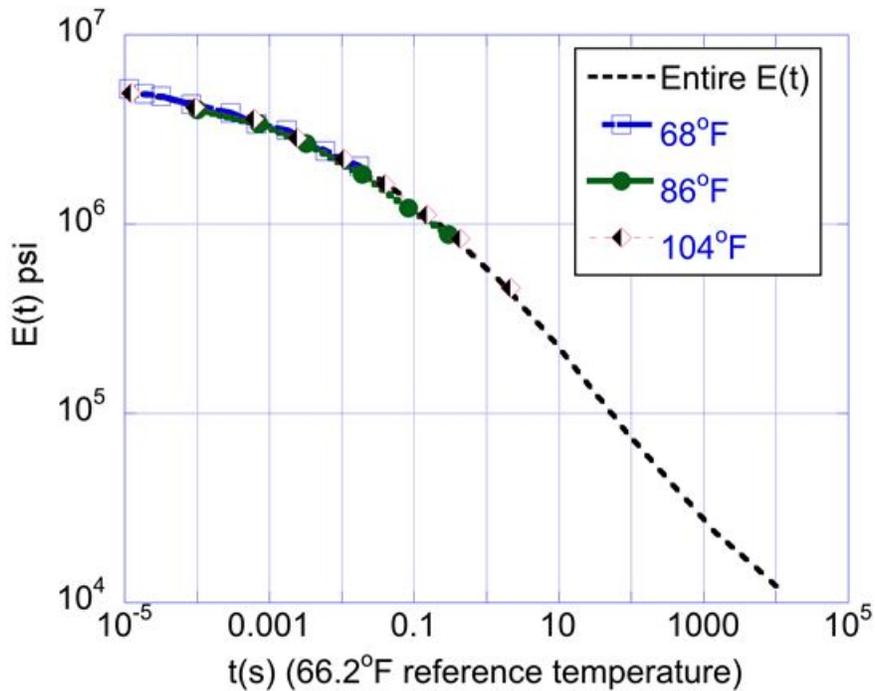
Figure 48. Graph. Region of *E*(*t*) master curve (at 66.2 °F reference temperature) used by (T-profile LAVA) LAVAP for calculating response at temperature profile {104, 86, 68} °F .

As expected, for a condition of higher temperature at the top and lower temperature at the bottom, the response with a higher constant temperature was always greater than the response with a temperature profile. The response with a lower constant temperature was always less than the response with a temperature profile. The response with a medium constant temperature may or may not be less than the profile response, depending on the temperature profile and thickness of the sublayering.

Next, the LAVA algorithm was validated against a well-known FEM software, ABAQUS, where the temperature profile in the AC layer was simulated as two sublayers of AC with different temperatures. For this purpose, two different HMA types were considered, Terpolymer and SBS 64-40. The viscoelastic properties of these two mixes are shown in figure 49. As shown in table 13, for both mixes, the AC layer was divided into two sublayers, with temperature in the top and bottom sublayer assumed to be 66 and 86 °F, respectively.
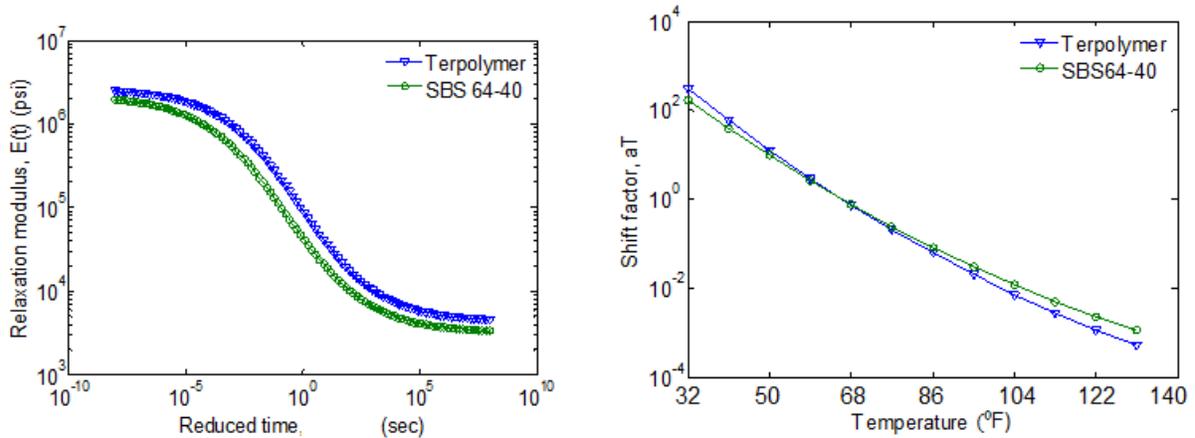
Figure 49. Graphs. Relaxation modulus and shift factor master curves at a reference temperature of 66 °F.

Table 13. Pavement section used in (T-profile LAVA) LAVAP validation.

Layer	Modulus ($E(t)$ or E)	Thickness (inches) (Temperature °F)	Poisson's Ratio
AC	Mix 1: Terpolymer ($E(t)$ see figure 49) Mix 2: SBS 64-40 ($E(t)$ see figure 49)	Sublayer1 = 3.94 inches (66 °F) Sublayer2 = 3.94 inches (86 °F)	0.45
Base	15,000 psi (linear elastic)	7.88 inches	0.35
Subgrade	10,000 psi (linear elastic)	Infinity	0.45

Figure 50 and figure 51 show a comparison of surface deflection time histories measured at radial distances of 0, 7.99, 12.01, 17.99, 24.02, 35.98, 47.99, and 60 inches for mixes 1 and 2. From the figures, it can be observed that the results obtained from LAVAP and ABAQUS matched well.
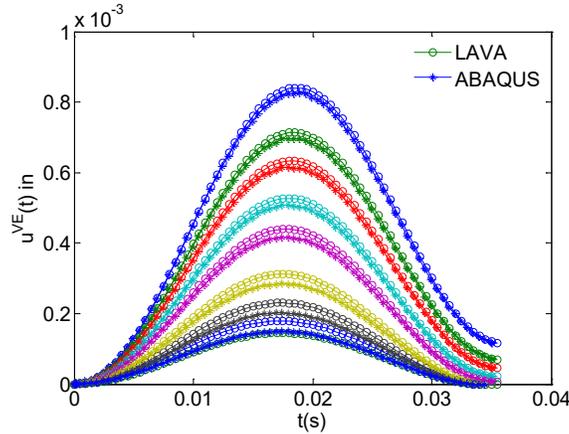
Figure 50. Graph. Comparison between LAVAP and ABAQUS at a temperature profile of {66, 86} °F (terpolymer).
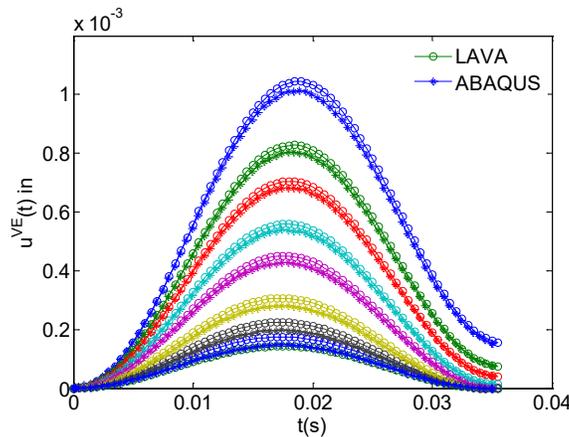
Figure 51. Graph. Comparison between LAVAP and ABAQUS at a temperature profile of {66, 86} °F (SBS 64-40).

As expected, it can be seen from table 14 that for both mixes, surface deflection in the pavement section at the two-step AC temperature profile of {66, 86} °F was between the deflections obtained for constant AC temperatures of 66 and 86 °F.

Table 14. Peak deflections at temperature profile {66, 86}°F and at a constant temperature of 86 °F using LAVA.

Mix	Temperature (°F)	Sensor Deflection (mil)							
		1	2	3	4	5	6	7	8
Terpolymer	Constant: 66	28.1	24.7	22.5	19.5	16.8	12.4	9.3	7.2
	Profile: 66, 86	33.0	28.1	24.9	20.7	17.3	12.2	9.1	7.0
	Constant 86	38.4	30.9	26.8	21.8	17.8	12.2	8.9	6.9
SBS 64-40	Constant 66	35.2	29.1	25.7	21.3	17.6	12.3	9.1	7.0
	Profile: 66, 86	40.9	32.5	27.7	22.0	17.7	12.0	8.8	6.9
	Constant 86	47.6	35.1	29.2	22.7	17.9	12.0	8.7	6.8

LAYERED VISCOELASTIC NONLINEAR (LAVAN) PAVEMENT MODEL

This section presents a computationally efficient layered viscoelastic nonlinear model called LAVAN. LAVAN can consider linear viscoelasticity of AC layers as well as the stress-dependent modulus of granular layers. The formulation was inspired by quasilinear-viscoelastic (QLV) constitutive modeling, which is often used in analyzing nonlinear viscoelastic materials. In the literature, the various forms of the model are also called Fung's model, Schapery's nonlinearity model, and modified Boltzmann's superposition. (See references 70–75.)

LAVAN combines Schapery's quasi-elastic theory with generalized QLV theory to predict the response of multilayered viscoelastic nonlinear flexible pavement structures. Before introducing the generalized QLV model, a brief overview of granular nonlinear pavement models is presented. This is followed by development of a generalized QLV model for a multilayered system and numerical validation in which the response of flexible pavements under the FWD test was analyzed. The model was validated against the general-purpose FEM software, ABAQUS.

Layered Nonlinear Elastic Solutions

Under constant amplitude cyclic loading, granular unbound materials exhibit plastic deformation during the initial cycles. As the number of load cycles increases, plastic deformation ceases to occur, and the response becomes elastic in further load cycles. Often, elastic response in a triaxial cyclic loading is defined by resilient modulus (M_R) at that load level, which is expressed as shown in figure 52.

$$M_R = \frac{\sigma_d}{\varepsilon_r}$$

Figure 52. Equation. Resilient modulus.

Where:

$\sigma_d = (\sigma_1 - \sigma_3)$, is the deviatoric stress in a triaxial test.
ε_r = recoverable strain.

If the granular layer reaches this steady state under repeated vehicular loading, then further response can be considered recoverable, and figure 52 can be used to characterize the material. The M_R value shown in figure 52 is affected by the stress state (or load level). Typically, unbound granular materials exhibit stress hardening, i.e., M_R increases with increasing stress.[76,77] As shown in figure 53, Hicks and Monismith related bulk stress and the resilient modulus obtained in figure 53 to characterize the stress dependency of the material.[78]

$$M_R = k_1 (\theta)^{k_2}$$

Figure 53. Equation. Resilient modulus as a function of stress invariant.

Where:

θ = the sum of principal stresses (i.e., $\theta = \sigma_1 + \sigma_2 + \sigma_3$)
k_1 and k_2 = regression constants.

The model suggested by Uzan and by Witczak and Uzan (figure 54 and figure 55, respectively) incorporated the distortional shear effect into the model using deviatoric and octahedral stresses, respectively.[79,80]

$$M_R = k_1 \left(\frac{\theta}{p_a}\right)^{k_2} \left(\frac{\sigma_d}{p_a}\right)^{k_3}$$

Figure 54. Equation. Uzan's nonlinearity model.

Where:

p_a = atmospheric pressure.
θ = the sum of principal stresses (i.e., $\theta = \sigma_1 + \sigma_2 + \sigma_3$).

σ_d = deviatoric stress.
k_1, k_2, and k_3 = regression constants.

$$M_R = k_1 \left(\frac{\theta}{p_a}\right)^{k_2} \left(\frac{\tau_{oct}}{p_a}\right)^{k_3}$$

Figure 55. Equation. Witczak and Uzan's nonlinearity model.

Where:

τ_{oct} = octahedral shear stress.
p_a = atmospheric pressure.
θ = the sum of principal stresses (i.e., $\theta = \sigma_1 + \sigma_2 + \sigma_3$).

σ_d is deviatoric stress.
k_1, k_2, and k_3 = regression constants.

The model has been further modified by various researchers. Yau and Von Quintus analyzed LTPP M_R test data using the generalized form of the Uzan model expressed as the equation in figure 56.[76,79]

$$M_R = k_1 P_a \left(\frac{\theta - 3k_6}{P_a}\right)^{k_2} \left(\frac{\tau_{oct}}{P_a} + k_7\right)^{k_3}$$

Figure 56. Equation. Generalized Uzan's model.

Where k_1, k_2, k_3, k_6, k_7 are regression constants. They found that parameter k_6 regressed to zero for more than half of the tests, and hence the coefficient was set to zero for the subsequent analysis. The modified equation is shown in figure 57.

$$M_R = k_1 P_a \left(\frac{\theta}{P_a}\right)^{k_2} \left(\frac{\tau_{oct}}{P_a} + 1\right)^{k_3}$$

Figure 57. Equation. MEPDG model for resilient modulus.

Although the resilient modulus, M_R, is not the Young's modulus (E), when formulating granular material constitutive equations, it is often used to replace E in the equation in figure 58.[81]

$$\sigma_{ij} = \frac{\nu E}{(1+\nu)(1-2\nu)} \varepsilon_{kk} \delta_{ij} + \frac{E}{1+\nu} \varepsilon_{ij}$$

Figure 58. Equation. Elasticity constitutive equation.

Where:

E = Young's modulus
ν = Poisson's ratio.
σ_{ij} is the stress tensor.
ε_{ij} is the strain tensor.
$\varepsilon_{kk} = (\varepsilon_{11} + \varepsilon_{22} + \varepsilon_{33})$.
δ_{ij} is the Kroenecker delta.

Nonlinear M_R in flexible pavements has been implemented in many FEM-based models, assuming AC layer to be elastic. These include GTPAVE, ILLIPAVE, and MICHPAVE.[82–84] Typically, FEM-based nonlinear pavement analysis is performed by choosing a user-defined material (UMAT) in FEM-based software packages such as ABAQUS and ADINA.[10,85,86] However, although FEM-based solutions are promising, they are computationally expensive.

An approximate nonlinear analysis of pavement can also be performed using Burmister's multilayered elastic based solution.[62,63] However, because the multilayer elastic theory assumes each individual layer is both vertically and horizontally homogeneous, it can be used to depict nonlinearity only through approximation. For incorporating variation in modulus with depth, Huang suggested dividing the nonlinear layer into multiple sublayers.[27] Furthermore, he suggested choosing a representative location in the nonlinear layers to evaluate modulus based on the stress state of the point. He showed that when the midpoint of the nonlinear layer under the load was selected to calculate modulus values, the predicated response near the load was close to the actual response. However, the difference between actual and predicted response increased at points away from the loading. Zhou studied stress dependency of base layer modulus obtained from base layer mid-depth stress state.[87] He analyzed FWD testing at multiple load levels on two different pavement structures. The study showed that reasonable nonlinearity parameters k_1 and k_2 (figure 53) can be obtained, regressing backcalculated modulus with stress state at mid-depth of the base layer.

In the present study, the elastic nonlinearity was solved iteratively assuming an initial set of elastic moduli. The stresses computed at mid-depth of each nonlinear layer using the initial values of modulus were used to compute the new set of moduli. The iteration was continued until E computed from the stresses predicted by the layered solution and the E used in the layered solution converged. Note that the appropriate stress adjustments were made because unbound granular material cannot take tension. This means that in such a case, either residual stress would be generated such that the stress state obeyed a yield criterion or the tensile stresses would be replaced with zero.

The algorithm developed to obtain response in a nonlinear system was compared with a robust nonlinear FEM software—MICHPAVE. The algorithm was compared for the cases when the unbound layer was considered as a single layer for nonlinearity calculations (Algorithm1) and when the layer was divided into two sections (Algorithm2). The analysis results are presented in appendix A. From the results, it was observed that subdividing the unbound base layer into two layers for computing nonlinearity did not produce much improvement in the results, hence it was decided to use the base layer as a single layer in further analysis.

Proposed Layered Viscoelastic Nonlinear (LAVAN) Pavement Model

Mechanistic solutions for nonlinear viscoelastic materials exhibit variation depending on the type of nonlinearity present. Typical nonlinear viscoelasticity equations involve convolution integrals that are based on unit responses (e.g., relaxation modulus and creep compliance), which are a function of stress or strain. Figure 59 and figure 60 show typical forms of such expressions.

$$\sigma(t) = \int_0^t E(t-\tau, \varepsilon) \frac{d\varepsilon(\tau)}{d\tau} d\tau$$

Figure 59. Equation. Nonlinear viscoelastic formulation for stress when relaxation modulus is a function of strain.

$$\varepsilon(t) = \int_0^t D(t-\tau, \sigma) \frac{d\sigma(\tau)}{d\tau} d\tau$$

Figure 60. Equation. Nonlinear viscoelastic formulation for strain.

Where:

ε = strain.
σ = stress.
$E(t,\varepsilon)$ = strain-dependent relaxation modulus.
$D(t,\sigma)$ = stress-dependent creep compliance.

Typically, in many nonlinear materials, the shape of the relaxation modulus of the material is preserved, even though the material presents stress or strain dependency.[74,87] Such nonlinear viscoelastic (NLV) problems are solved by assuming that time dependence and stress (or strain) dependence can be decomposed into two functions as shown in figure 61 and figure 62.

$$D(t,\sigma) = g(\sigma)D_t(t)$$

Figure 61. Equation. Nonlinear creep compliance formulation.

$$E(t,\varepsilon) = f(\varepsilon)E_t(t)$$

Figure 62. Equation. Nonlinear relaxation modulus formulation.

Where:

$g(\sigma)$ = a function of stress.
$D_t(t)$ = the (only) time-dependent creep compliance.
$f(\varepsilon)$ = a function of strain.
$E_t(t)$ = the (only) time-dependent relaxation modulus.

For such materials, the expression in figure 63 has been typically used in NLV formulations to develop the convolution integral.

$$\sigma(t) = \int_0^{t_R} E_t(t_R - \tau)\frac{df(\varepsilon(\tau))}{d\varepsilon}\frac{d\varepsilon(\tau)}{d\tau}d\tau$$

Figure 63. Equation. Nonlinear viscoelastic formulation for stress when relaxation modulus is separated from strain dependence function.

Where E_t is a relaxation function that remains unchanged at any strain level and $f(\varepsilon(\tau))$ is a function of strain, such that $df(\varepsilon(\tau))/d\varepsilon$ represents the elastic tangent stiffness.

These models are designated as Fung's nonlinear viscoelastic material models, which were first proposed by Leaderman in 1943.[70] A generalized form of this nonlinearity model was presented by Schapery using thermodynamic principles.[71] Yong et al. used the model to describe nonlinear viscoelastic viscoplastic behavior of asphalt sand, whereas Masad et al. used the model to describe nonlinear viscoelastic creep behavior of binders.[72,73] The model suggests that the nonlinear relaxation function can be expressed as a product of the function of time ($E_t(t_R - \tau)$) and the function of strain $df(\varepsilon(\tau))/d\varepsilon$. In figure 63, nonlinearity was introduced by the elastic component, $df(\varepsilon(\tau))/d\varepsilon$, and the viscoelasticity comes from E_t.

Concepts of nonlinear viscoelastic material behavior can be used to develop formulations for a layered system where the unbound layer is nonlinear and the AC layer is linear viscoelastic. If the previous argument is directly adopted, then the corresponding QLV analysis of viscoelastic nonlinear multilayered analysis can be represented as shown in figure 64.

$$\sigma(t) = \int_0^{t_R} E_t(x,y,z,t_R - \tau)\frac{df(x,y,z,\varepsilon(\tau))}{d\varepsilon}\frac{d\varepsilon(\tau)}{d\tau}d\tau$$

Figure 64. Equation. Nonlinear viscoelastic formulation for stress when relaxation modulus is separated from strain dependence function and when formulation is applied to a multilayered pavement structure.

Where $E_t(x,y,z,t_R)$ is the relaxation function, and $f(x,y,z, \varepsilon(\tau))$ is a function of strain $\varepsilon(\tau)$ at location (x,y,z). Alternatively, to obtain vertical surface deflection in pavements, figure 64 can be expressed in terms of vertical deflection response to Heaviside step loading as shown in figure 65.

$$u^{ve}(t) = \int_{\tau=0}^{t_R} g(\sigma)\, u_{H-t}^{e}(t_R - \tau, \sigma = 1) d\sigma(\tau)$$

Figure 65. Equation. Nonlinear viscoelastic formulation for deflection.

Where:

$u^{ve}(t)$ = the surface (nonlinear viscoelastic) displacement.
$u_{H-t}^{e}(t, \sigma = 1)$ = the unit nonlinear elastic response due to a unit stress.
$g(\sigma)$ = a function of stress, which can be expressed as shown in figure 66.

$$g(\sigma) = \frac{u_H^{e}(t_R, \sigma)}{u_{H-t}^{e}(t_R, \sigma = 1)}$$

Figure 66. Equation. Nonlinear viscoelastic formulation.

Where $u_H^{e}(t_R, \sigma)$ is the nonlinear elastic unit displacement due to a given stress (σ). For Fung's theory to hold (i.e., figure 63 through figure 66), $g(\sigma)$ must be purely a function of stress. To investigate this, the $g(\sigma)$ values were computed using figure 66 and plotted against surface stress and relaxation modulus (i.e., time). The LAVA algorithm was modified to implement an iterative nonlinear solution for the granular base, which was assumed to follow the following two nonlinearity expressions: $M_R = k_1(\theta / p_a)^{k_2}$ and $M_R = k_1(\theta / p_a)^{k_2}(\tau_{oct}/p_a + 1)^{k_3}$. Analysis using the k-$\theta$-$\tau$ model is presented here whereas the k-θ model is presented in appendix A. The pavement section properties and material properties are shown in table 15 and figure 67.

Table 15. Pavement geometric and material properties for nonlinear viscoelastic pavement analysis.

Property	Value
Thickness (inches)	5.9 (AC), 9.84 (base), infinity (subgrade)
Poisson ratio (v)	0.35 (AC), 0.4 (base), 0.4 (subgrade)
Density (pci)	0.0752 (AC), 0.0752 (base), 0.0752 (subgrade)
Nonlinear E_{base} (psi)	$k_0 = 0.6$; $k_1 = 3{,}626$; $k_2 = 0.5$; $k_3 = -0.5$
$E_{subgrade}$ (psi)	10,000
AC: $E(t)$ sigmoid coefficient (c_i)	1.598, 2.937, 0.512, -0.562
Haversine stress: 35 ms	Peak stress = 137.79 psi
Sensor spacing from the center of load (inches)	0, 7.99, 12.01, 17.99, 24.02, 35.98, 47.99, 60
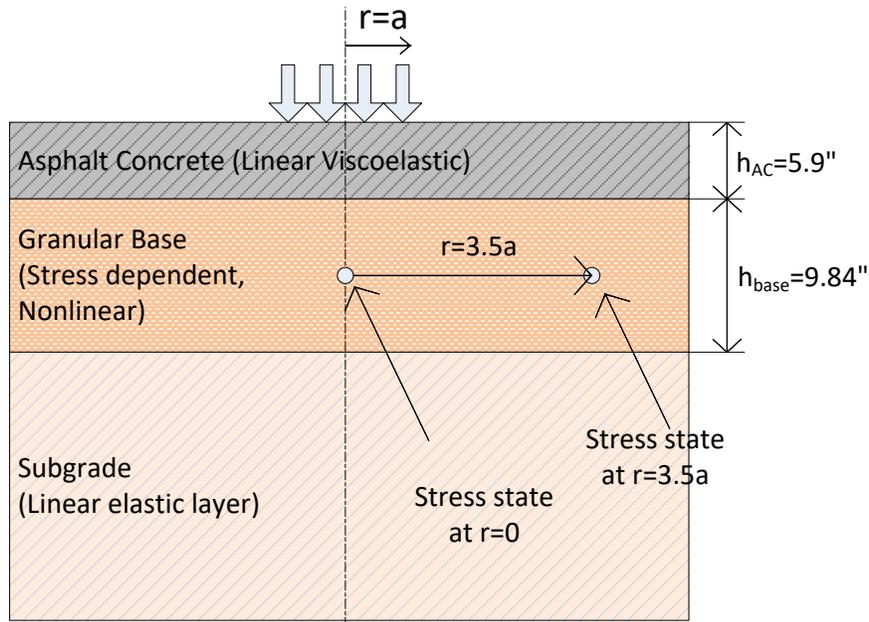
Figure 67. Diagram. Flexible pavement cross section for nonlinear viscoelastic pavement analysis.

The $u_H^e(t,\sigma)$ in figure 66 was calculated at a range of stress values from 0.1 to 140 psi and using $E(t)$ values for AC from 10^{-8} to 10^8 s. Then, $u_{H-t}^e(t,\sigma=1)$ was calculated for unit stress, and $g(\sigma)$ was calculated using figure 66. Figure 68 shows the variation of $g(\sigma)$, where the $g(\sigma)$ values decrease with increasing stress (σ).
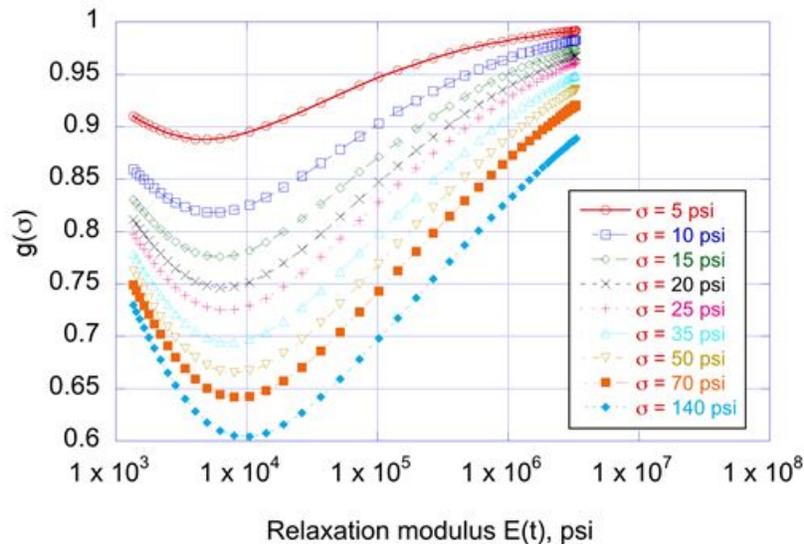
Figure 68. Graph. Variation of $g(\sigma)$ with stress and $E(t)$ of AC layer.

This is expected behavior for a nonlinear material because as the stress increases, the unbound layer moduli also increase. However, figure 68 also illustrates that the $g(\sigma)$ varies with change in

76

$E(t)$. This means that $g(\sigma)$ is not solely based on the stress, and, as a result, Fung's model cannot be used in a layered pavement structure. This is meaningful because the change in the stress distribution within the pavement layers due to viscoelastic effect (as $E(t)$ varies) imposes changes in the behavior of stress-dependent granular layer. Note that as shown in appendix A, similar results were obtained when nonlinearity of k-θ type model was assumed. Hence, even though the viscoelastic layer in a nonlinear multilayered system is linear, it cannot be formulated as a Fung's QLV model. The QLV model can still be formulated as a convolution integral, provided the stress-dependent relaxation function of the multilayered structure under all the load levels is known. Such a generalized QLV model for a multilayered structure can be expressed as nonlinear viscoelasticity equations involving the convolution integrals of unit response function of the structure, which is a function of stress or strain as shown in figure 69.

$$R^{ve}(x,y,z,t) = \int_0^{t_R} R_H^e\left(x,y,z,I(\tau),t_R - \tau\right)\frac{dI(\tau)}{d\tau}d\tau$$

Figure 69. Equation. Generalized nonlinear viscoelastic formulation.

Where:

$R^{ve}(x,y,z,t)$ = the nonlinear viscoelastic response of the layered pavement structure.
$R_H^e\left(x,y,z,I(\tau),t_R - \tau\right)$ = the unit response function that is both a function of time.
input $I(\tau)$ = stress applied at the surface of the pavement.

Note that in this formulation, unlike Fung's QLV model, time dependence and stress (or strain) dependence were not separated.

Forward Algorithm: Numerical Implementation of the Proposed Model (LAVAN)

Figure 69 can be rewritten in terms of vertical surface deflection under axisymmetric surface loading (see figure 67) as shown in figure 70.

$$u_{vertical}^{ve}(z,r,t) = \int_{\tau=0}^{t_R} u_{H-vertical}^e(z,r,\sigma(\tau),t_R - \tau)\frac{d\sigma(\tau)}{d\tau}d\tau$$

Figure 70. Equation. Generalized nonlinear viscoelastic formulation for deflection.

Where:

$u_{vertical}^{ve}(z,r,t)$ is the vertical deflection at time t and location (z,r).
$u_{H-vertical}^e(z,r,\sigma(\tau),t_R - \tau) = u_{vertical}^e(z,r,\sigma(\tau),t_R - \tau)/\sigma$ where $u_{vertical}^e(z,r,\sigma,t_R - \tau)$ is the nonlinear response of the pavement at a loading stress level of σ.

The model in figure 70 can be expressed in discretized formulation as shown in figure 71.

$$u_{vertical}^{ve}(z,r,t_i) = \sum_{j=1}^{N} u_{H-vertical}^{e}(z,r,t_{Ri} - \tau_j, \sigma(\tau_j))\Delta\sigma(\tau_j)$$

Figure 71. Equation. Discretized nonlinear formulation.

Where $\tau_1 = 0$, $\tau_N = t$. The $u_H^e(\sigma, t_{Ri} - \tau_j)$ values are computed via interpolation using the two-dimensional matrix pre-computed for $u_H^e(t, \sigma)$ (which was computed at a range of stress values and $E(t)$ values). The developed model has been referred to as LAVAN (short for LAVA-Nonlinear) in this report. The following step-by-step procedure can be used to numerically compute the response:

1. Define a discrete set of surface stress values: $\sigma_k = 0.1$ to 140 psi.
2. Calculate nonlinear elastic response $u^e(t_{Ri}, \sigma_k)$ at a range of t_{Ri} values, by using $E_{AC} = E(t_{Ri})$ for each t_{Ri} value. Recursively compute E_{base} until the stress in the middle of the base layer, at a radial distance r, results in the same E_{base} as the one used in the layered elastic analysis (within acceptable error). For this step, the nonlinear formulation shown in figure 72 is assumed for the base.

$$E_{base} = M_R = k_1\left(\frac{\theta}{p_a}\right)^{k_2}\left(\frac{\tau_{oct}}{p_a} + 1\right)^{k_3}$$

Figure 72. Equation. Resilient modulus.

Where:

$\theta = \sigma_1 + \sigma_2 + \sigma_3 + yz(1 + 2K_0)$ (where K_0 is the coefficient of earth pressure at rest).
τ_{oct} = octahedral shear stress.
$k_1, k_2,$ and k_3 = regression constants.
p_a = atmospheric pressure.

3. Calculate the nonlinear unit elastic response $u_{H-vertical}^e(r,z,t_i,\sigma_k) = \dfrac{u_{vertical}^e(r,z,t_i,\sigma_k)}{\sigma_k}$.

4. Perform convolution shown in figure 71 to calculate the nonlinear viscoelastic response.

Verification of the LAVAN model

To validate the LAVAN algorithm, ABAQUS was used. A flexible pavement was modeled as a three-layer structure, with a viscoelastic AC top layer over a stress-dependent granular base layer on an elastic half-space (subgrade). Figure 67 shows the geometric properties of the pavement structure used in the validation, where $h_{AC} = 5.9$ inches and $h_{base} = 9.84$ inches. The viscoelastic properties of two HMA mixes, called crumb rubber terminal blend (CRTB) and control (two materials from FHWA's Accelerated Load Facility 2002 experiment) were used for the AC layer in the analysis as case 1 and 2, relaxation modulus master curve for the two mixes are shown in figure 73.[89] These curves were computed from their $|E^*|$ master curves by following the interconversion procedure suggested by.[58] The pavement properties in the analysis for each test case were the same, as shown in figure 15.
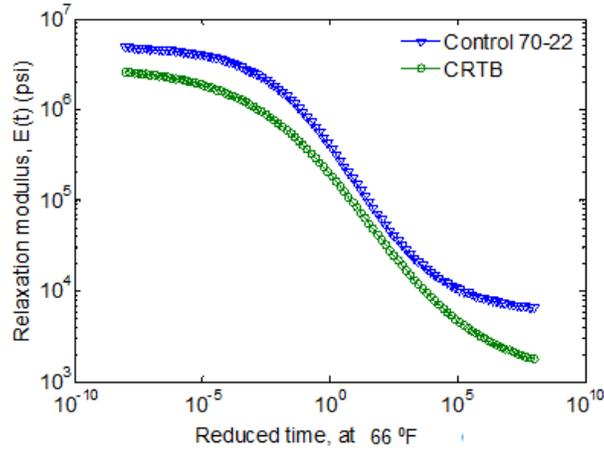
Figure 73. Graph. Relaxation moduli of mixes used in LAVAN validation.

In ABAQUS, the viscoelastic properties of the HMAs were input in the form of normalized bulk modulus (K) and normalized shear modulus (G).[90] For the unbound nonlinear layer, a UMAT was written, incorporating the nonlinear constitutive modeling as explained in the previous section. ABAQUS requires that any UMAT have at least two main components: (1) update of the stiffness Jacobian Matrix and (2) stress increment. Figure 74 and figure 75 show the mathematical expressions for these two operations implemented in the UMAT.

$$J_{ijkl} = \frac{\partial \sigma_{ij}}{\partial \varepsilon_{kl}}$$

Figure 74. Equation. ABAQUS Jacobian formulation.

$$\sigma_{ij}^{n+1} = \sigma_{ij}^{n} + J_{ijkl}\, \partial \varepsilon_{kl}^{n+1}$$

Figure 75. Equation. ABAQUS stress update formulation.

Where J is the Jacobian matrix; σ_{ij}^{n+1} is the updated stress; and i, j, k, and l represent r, z, t, and θ in the cylindrical coordinate system. For nonlinear analysis using LAVAN, the unbound modulus was calculated using the stress state at the midpoint of the unbound base layer (vertically). Because LAVAN cannot incorporate nonlinearity along the horizontal direction, for comparison, modulus values were calculated using stress at $r = 3.5a$ (r shown in figure 67). In ABAQUS, the FE domain size of 133R in the vertical direction and 53R in the horizontal direction was found to produce stable surface deflection (with less than 1-percent error at the center). For the selected domain size, the FEM mesh refinement of 0.4 inch in the AC layer and 1 inch in the base layer were used. ABAQUS took approximately 17 min to analyze a haversine loading of 138 psi and 35 ms, whereas LAVAN could generate the results in 3.6 min.

Comparison of surface deflection between LAVAN and ABAQUS for the control mix (figure 76) and CRTB mix (figure 77) shows good predictability of LAVAN. As expected, the stiffer mix (control) generated a lower response compared with the softer mix (CRTB) under the same geometric and loading conditions. The top graph in figure 76 shows the results when stress

at $r = 0$ is used in LAVAN and was provided for comparison purposes. The bottom graph in figure 76 shows the results when stress at $r = 3.5a$ was used in LAVAN. Note that S1, S2, S3, S4, S5, S6, S7, and S8 in the figures correspond to surface deflection Sensor-1 ($r = 0$ inches), Sensor-2 ($r = 8$ inches) etc. Sensors 1 through 8 were 0, 8, 12, 18, 24, 36, 48, and 60 inches away from the centerline of the load.
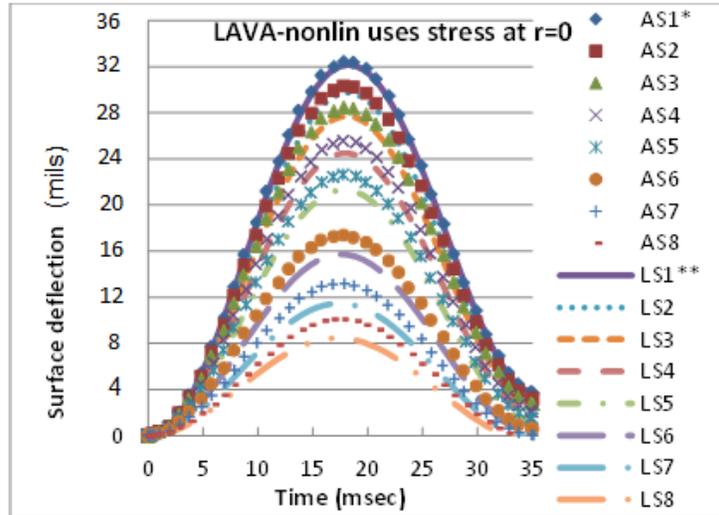
LAVAN uses stress at r = 0
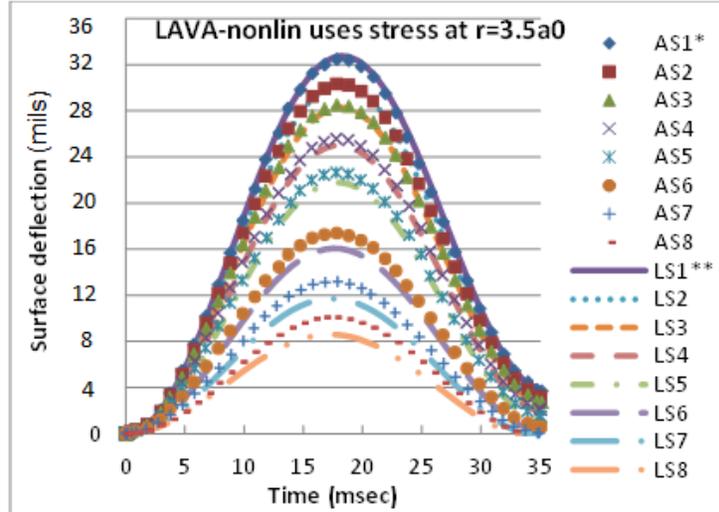
LAVAN uses stress at r = 3.5a
(*LS1=LAVAN sensor 1; **AS1= ABAQUS sensor 1).

Figure 76. Graphs. Surface deflection comparison of ABAQUS and LAVAN for the control mix.
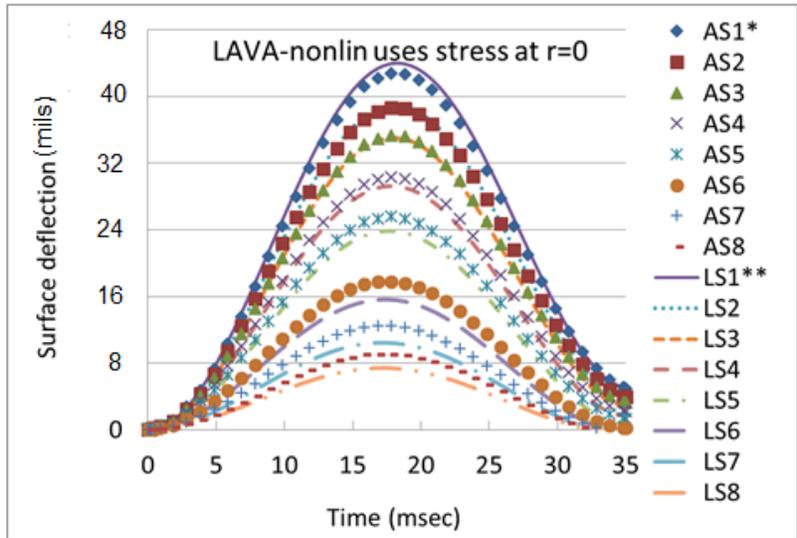
LAVAN uses stress at r = 0
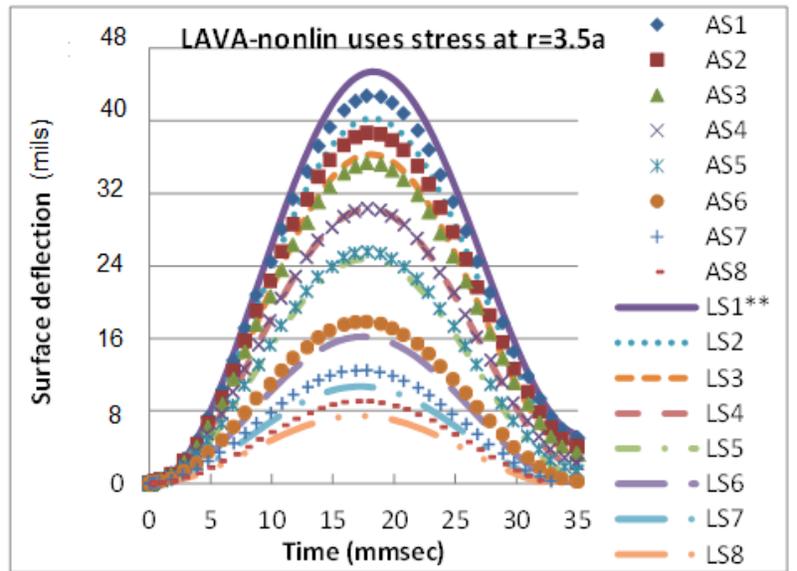
LAVAN uses stress at r = 3.5a
(*AS1=ABAQUS sensor 1; **LS1=LAVAN sensor 1).

Figure 77. Graphs. Surface deflection comparison of ABAQUS and LAVA for the CRTB mix.

The difference between ABAQUS and LAVAN was quantified using the two variables shown in figure 78 and figure 79.

$$PE_{peak} = \frac{\left| \delta_{ABAQUS}^{peak} - \delta_{LAVAN}^{peak} \right|}{\delta_{ABAQUS}^{peak}} x100$$

Figure 78. Equation. Error in peak deflection.

81

$$PE_{avg} = \frac{1}{N}\sum_{i=1}^{N}\frac{\left|\delta_{ABAQUS}(t_i)\big/\delta_{ABAQUS}^{peak} - \delta_{LAVAN}(t_i)\big/\delta_{LAVAN}^{peak}\right|}{\delta_{ABAQUS}(t_i)\big/\delta_{ABAQUS}^{peak}} x100$$

Figure 79. Equation. Average error in normalized deflection history.

Where:

PE_{peak} = Percent error in the peaks.
δ_{ABACUS}^{peak} = Peak deflection predicted by ABAQUS.
δ_{LAVAN}^{peak} = Peak deflection predicted by LAVAN.
PE_{avg} = Average percent error in normalized deflection history.
$\delta_{ABAQUS}(t_i)$ = Deflection predicted by ABAQUS at time t_i.
$\delta_{LAVAN}(t_i)$ = Deflection predicted by LAVAN at time t_i.
N = Number of time intervals in the deflection time history.

Because the model integrates both viscoelastic and nonlinear material properties, both peak deflection and creeping of deflection should be predicted with accuracy. PE_{avg} was used to examine the model performance in creeping.

As shown in figure 80 and figure 81, the PE_{peak} and PE_{avg} values for the control mix showed a slight improvement in the results when $r = 3.5a$ was used. However, from figure 82 and figure 83, it can be seen that PE_{peak} and PE_{avg} values for CRTB mix showed more sensitivity to the location of the stress state.

In general, for the deflection basin at farther sensors, a better match between the ABAQUS and LAVAN results was found when stress state at $r = 3.5a$ was used while incorporating nonlinearity. However, note that $r = 0$ also produced relatively good results, especially in the first four to five sensors. Also, note that, for the structure in table 15, the procedure leads to $r = 2.8a$ when the trapezoidal stress distribution with (0.5 horizontal slope and 1 vertical slope) is assumed.[27]
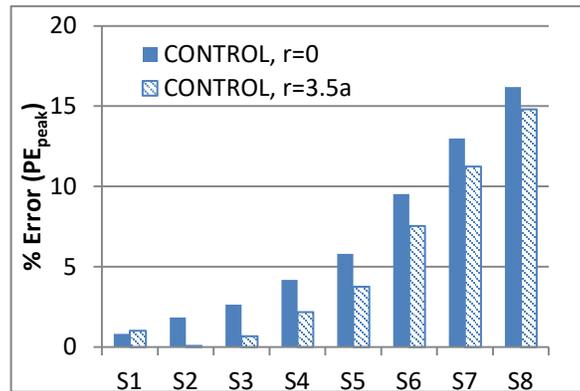
Figure 80. Graph. Percent error (PE_{peak}) calculated using the peaks of the deflections for LAVAN-ABAQUS comparison (control mix).
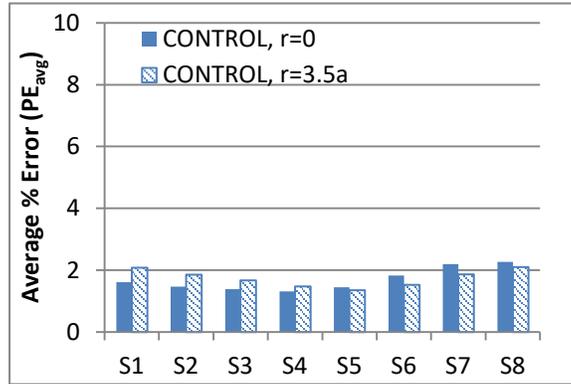
Figure 81. Graph. Average percent error (*PE$_{avg}$*) calculated using the entire time history for the LAVAN-ABAQUS comparison (control mix).
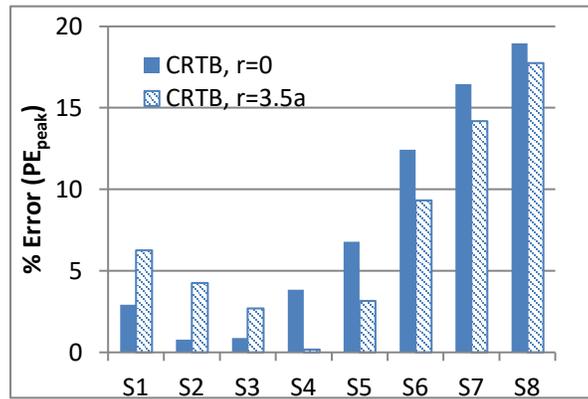
Figure 82. Graph. Percent error (*PE$_{peak}$*) calculated using the peaks of the deflections for the LAVAN-ABAQUS comparison (CRTB mix).
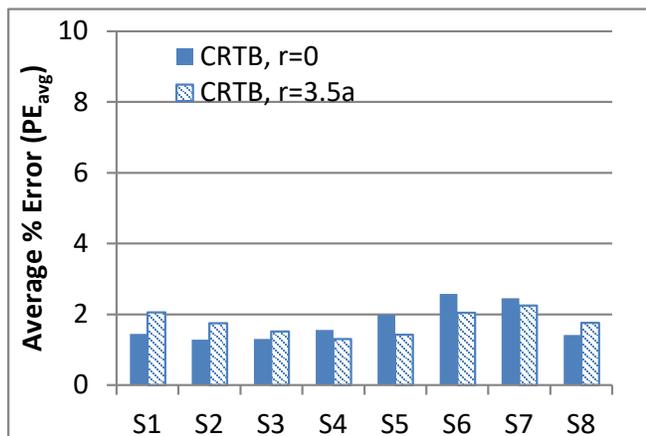
Figure 83. Graph. Average percent error (*PE$_{avg}$*) calculated using the entire time history for the LAVAN-ABAQUS comparison (CRTB mix).

BASICS OF GENETIC BACKCALCULATION ALGORITHM

Backcalculation of pavement properties using FWD data is essentially an optimization problem. The analysis is based on formulating an objective function, which is minimized by varying the pavement properties. Response obtained from the forward analysis is matched with response obtained from the FWD test, and the difference is minimized by adjusting the layer properties of the system until a best match is achieved. Typically, the existing backcalculation methods either use RMS or percentage error of peak deflections as the objective function. However, because the viscoelastic properties are time dependent, the entire deflection history needs to be used. Hence, the primary component of the proposed backcalculation procedure was a layered viscoelastic forward solution. Such a solution should provide accurate and rapid displacement response histories owing to a time-varying (stationary) surface loading. For a linear viscoelastic pavement model, the research team used the computationally efficient layered viscoelastic algorithm LAVA to support the backcalculation algorithm called BACKLAVA, whereas for viscoelastic nonlinear pavement model, the team used the computationally efficient layered viscoelastic algorithm LAVAN to support the backcalculation algorithm called BACKLAVAN.[65]

Whenever mechanical properties are derived with inverse analysis, it is desirable to minimize the number of undetermined parameters by using an economical scheme. Such an approach is both advantageous from a computational speed perspective and addresses the non-uniqueness issue, i.e., test data may not be detailed, accurate, or precise enough to allow calibration of a complicated model. Moreover, it is beneficial to have some inherent "protection" within the formulation, forcing the analysis to a meaningful convergence—fully compliant with the physics of the problem. Therefore, as discussed before, the relaxation modulus ($E(t)$) master curve (figure 32) was initially assumed to follow a sigmoid shape defined by the equation in figure 84:

$$\log(E(t)) = c_1 + \frac{c_2}{1 + \exp(-c_3 - c_4 \log(t_R))}$$

Figure 84. Equation. Sigmoid form of relaxation modulus curve.

Where c_i are the sigmoid coefficients and t_R is the reduced time, which is defined as $t_R = t/a_T(T)$ (or $\log(t_R) = \log(t) - \log(a_T(T))$), where, as discussed before (Figure 33), $a_T(T)$ is the shift factor coefficient, which is a function of temperature (T) and t is time. The shift factor coefficients has been defined as a second-order polynomial of the form $\log(a_T(T)) = a_1(T^2 - T_{ref}^2) + a_2(T - T_{ref})$, where a_1 and a_2 are the shift factor coefficients. As shown by the relaxation modulus and shift factor equations, a total of six coefficients were needed to develop the $E(t)$ master curve, including the temperature dependency (i.e., the shift factor coefficients).

In theory, it should be possible to obtain these six coefficients in two ways: (1) using data containing time-changing response at different temperature levels and (2) using uneven temperature profile information existing across the thickness of the asphaltic layer during a single drop containing time changing response data.

Reliability and accuracy of the backcalculated results depend on the optimization technique used. In the present work, several optimization techniques were tried to formulate a procedure to backcalculate these six viscoelastic properties along with unbound material properties. These

optimization techniques can be broadly classified as classical methods and evolutionary methods. In this study, simplex-based classical optimization method was performed using MATLAB® function fminsearch, whereas, genetic algorithm (GA)-based evolutionary optimization method was performed using the MATLAB® function ga. The objective function, which is based on deflection differences in the current work, is a multidimensional surface that can include many local minima. In elastic backcalculation methods, the modulus of the AC layer is defined using a single value. However, in the present problem, the AC properties were represented by a sigmoid containing four parameters for $E(t)$ and by a polynomial containing two parameters for $a_T(T)$. Hence, it was naturally expected that the probability of number of local minima would increase. In traditional methods, because of the presence of multiple local minima, selection of different initial solutions may lead to different subsequent solutions. Typically, classical optimization methods (such as the fminsearch) have the following issues:

- Solution may depend on initial seed values.
- Convergence can be achieved at a local minimum.

These disadvantages do not mean that classical methods cannot be used in the backcalculation procedure. In fact, the classical methods can be hybridized along with evolutionary optimization techniques in developing more effective backcalculation procedures.

It is important to develop a backcalculation process such that FWD data obtained at a relatively small range of pavement temperatures can be sufficient to derive the viscoelastic properties of AC. Among various optimization techniques, GA was chosen because of its capability to converge to a unique global minimum solution, irrespective of the presence of local solutions.[91–93] GA was implemented using MATLAB® function ga. In general terms, GA performs the following operations: (1) initialization, (2) selection, (3) generation of offspring, and (4) termination. In initialization, GA generates a pool of solutions using a subset of the feasible search space, the so-called "population." Each solution is a vector of feasible variable values. In the selection process, each solution is evaluated using an objective function, and the best fitted solutions are selected. The selected solutions are then used to generate the next generation population (offspring). This process mainly involves two operators: crossover and mutation. In crossover, a new solution is formed by exchanging information between two parent solutions, which is done by swapping a portion of parent vectors. In mutation, a new solution is formed by randomly changing a portion of the parent solution vector. The newly generated population is evaluated using the objective function. This process is repeated until a termination criterion is reached. Through guided random search from one generation to another, GA minimizes the desired objective function.

Formulation of the optimization model using GA is shown in figure 85.

$$E_r = \sum_{k=1}^{m} 100 \sum_{i,o=1}^{n} \frac{\left|\left(d_i^k - d_o^k\right)\right|}{d_i^k}$$

Figure 85. Equation. Optimization model.

Where:

m = Number of sensors.
d_i = Input deflection information obtained from field at sensor k.
d_o^k = Output deflection information obtained from forward analysis at sensor k.
n = Total number of deflection data points recorded by a sensor.
c_i = Sigmoid coefficients.
E_b and E_s = Base and subgrade moduli.
a_i = Shift factor polynomial coefficients.
l = Lower limit.
u = Upper limit.

This model is also subject to the following constraints:

- $c_1^l \leq c_1 \leq c_1^u$.
- $c_2^l \leq c_2 \leq c_2^u$.
- $c_3^l \leq c_3 \leq c_3^u$.
- $c_4^l \leq c_4 \leq c_4^u$.

and

- $a_1^l \leq a_1 \leq a_1^u$.
- $a_2^l \leq a_2 \leq a_2^u$.
- $E_b^l \leq E_b \leq E_b^u$.
- $E_s^l \leq E_s \leq E_s^u$.

To obtain the lower and upper limits of c_i and a_i, values of sigmoid and shift factor coefficients of numerous HMA mixtures were calculated. Table 16 shows these limits, which were used in the GA constraints shown in figure 85. Limits to the elastic modulus were arbitrarily selected (based on typical values presented in the literature). Note that the sigmoid obtained by using the lower or upper limits of the coefficients gave a larger range compared with the actual range of $E(t)$. This could potentially slow down the backcalculation process. Therefore, as described later in the report, additional constraints were defined to narrow the search window.

Table 16. Upper and lower limit values in backcalculation.

Limit	c_1	c_2	c_3	c_4	a_1	a_2	E_1	E_2
Lower	0.045	1.80	-0.523	-0.845	-5.380E-04	-1.598E-01	10,000	22,000
Upper	2.155	4.40	1.025	-0.380	1.136E-03	-0.770E-01	13,000	28,000

BACKCALCULATION OF RELAXATION MODULUS MASTER CURVE USING A SERIES OF FWD TESTS RUN AT DIFFERENT TEMPERATURES

The duration of a single pulse of an FWD test is very short, which limits the portion of the $E(t)$ curve used in the forward calculation using LAVA. As a result, it was not possible to backcalculate the entire $E(t)$ curve accurately using deflection data of such short duration. The longer the duration of the pulse, the larger portion of the $E(t)$ curve used in LAVA in the forward calculation process. Therefore, one may conclude that FWD tests need to produce a long-duration deflection-time history. However, owing to the thermorheologically simple behavior of AC, the time-temperature superposition principle can be used to obtain longer duration data by simply running the FWD tests at different temperatures and using the reduced time concept described at beginning of this chapter.

Before discussing into the details of the required number of FWD test temperatures and magnitudes, an analysis on the effects of different FWD deflection sensor data on the backcalculated $E(t)$ master curve is presented in the following section.

Sensitivity of *E(t)* Backcalculation to the Use of Data From Different FWD Sensors

This section presents an analysis of the contribution of individual and a group of sensors on the backcalculation of the $E(t)$ master curve. Note that the analysis was based on a real coded GA, which uses double vector variables. All the existing applications of GA in pavement inverse analysis were based on a binary coded GA, and hence the GA parameters suggested in these references were not applicable to the approach presented in this section.[91–93] As a result, a new set of optimum parameters was determined. The backcalculation process was run using a population and generation of 70 and 15, respectively (selected after trying various combinations), using FWD time histories obtained at a temperature set of {32, 50, 68, 86, 104, 122, 140, 158, and 176} °F. The pavement properties used (see table 17) were kept the same throughout the study.

Table 17. Pavement properties in viscoelastic backcalculation of optimal number of sensors.

Property	Case 1
Thickness (AC followed by granular layers) (inches)	10, 20, infinity
Poisson ratio {layer 1,2,3…}	0.35, 0.3, 0.45
$E_{unbound}$ {layer 2,3…} (psi)	11,450, 15,000
$E(t)$ sigmoid coefficient {layer 1}	0.841, 3.54, 0.86, -0.515
$a(T)$ shift factor polynomial coefficients {layer 1}	4.42E-04, -1.32E-01
Sensor spacing from the center of load (inches)	0, 8, 12,18,24, 36,48, 60

Convergence was evaluated based on the backcalculated moduli of the base and subgrade layers as well as the $E(t)$ curve of the AC layer. Average error in the moduli of base and subgrade are defined as shown in figure 86.

$$\xi_{unbound} = \left|\left(\frac{E_{act} - E_{bc}}{E_{act}}\right)\right| \times 100$$

Figure 86. Equation. Average error in backcalculated moduli of base and subgrade layers.

87

Where:

$\xi_{unbound}$ =Absolute value of the error in the backcalculated unbound layer modulus.
E_{act} and E_{bc} are the actual and backcalculated moduli (of the unbound layer), respectively.

The variation of error in the backcalculated $E(t)$ at different reduced times is defined as shown in figure 87.

$$\xi_{AC}(t_i) = \frac{E_{act}(t_i) - E_{bc}(t_i)}{E_{act}(t_i)} \times 100$$

Figure 87. Equation. Error in backcalculated relaxation moduli at different reduced times.

Where:

$\xi_{AC}(t_i) = E(t)$ error at reduced time t_i, where i ranges from 1 to n such that $t_1 = 10^{-8}$ and $t_n = 10^8$ s.
n = Total number of discrete points on the $E(t)$ curve.
$E_{act}(t_i)$ = Actual $E(t)$ value at point i.
$E_{bc}(t_i)$ = Backcalculated $E(t)$ value at i.

Finally, average error in $E(t)$ is defined as shown in figure 88.

$$\xi_{AC}^{avg} = \frac{1}{n}\left(\sum_{i=1}^{n} \left| \xi_{AC}(t_i) \right| \right)$$

Figure 88. Equation. Average error in backcalculated relaxation moduli.

Where ξ_{AC}^{avg} is the average error in the $E(t)$ of the AC layer.

Figure 89 shows the variation of $\xi_{unbound}$ when data from different FWD sensors are used. As shown, the error decreased as data from farther sensors were incorporated in the backcalculation. This may be because at farther sensors, the deflections were primarily, if not solely, due to deformation in the lower layers.
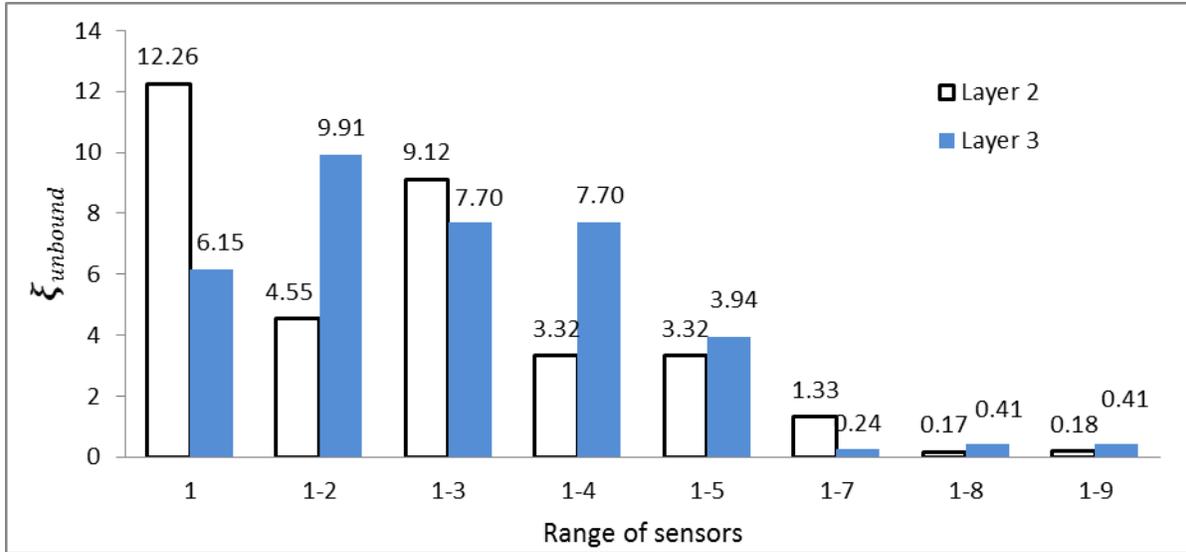
Figure 89. Graph. Error in unbound layer modulus in optimal number of sensor analysis.

Figure 90 shows the actual and backcalculated $E(t)$ curve, which is only based on data from sensor 1 (at the center of load plate). As shown, there was a very good match between the backcalculated and actual curves. Figure 91 shows the variation of percentage error in $E(t)$ (calculated using figure 87) with time. The magnitude of percent error ranged from about -9 to 23 percent and increased with reduced time. This was expected because the $E(t)$ in longer durations ($> 10^{-6}$ s) were not used in the forward computations. Note that the result is shown over a time range of 10^{-8} to 10^{8} s. However, the forward calculations were actually made using temperatures ranging from 32 to 176 °F, which corresponded to a reduced time range of approximately 10^{-6} to 10^{6} s.
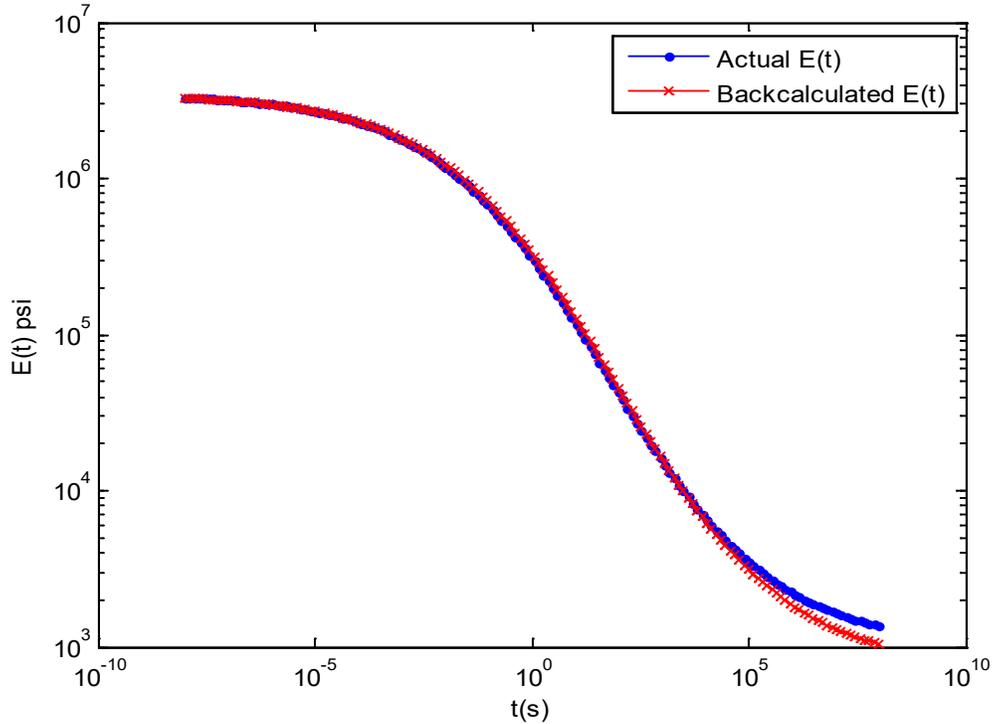
Figure 90. Graph. Backcalculated and actual *E*(*t*) master curve at the reference temperature of 66 °F using FWD data from only sensor 1.
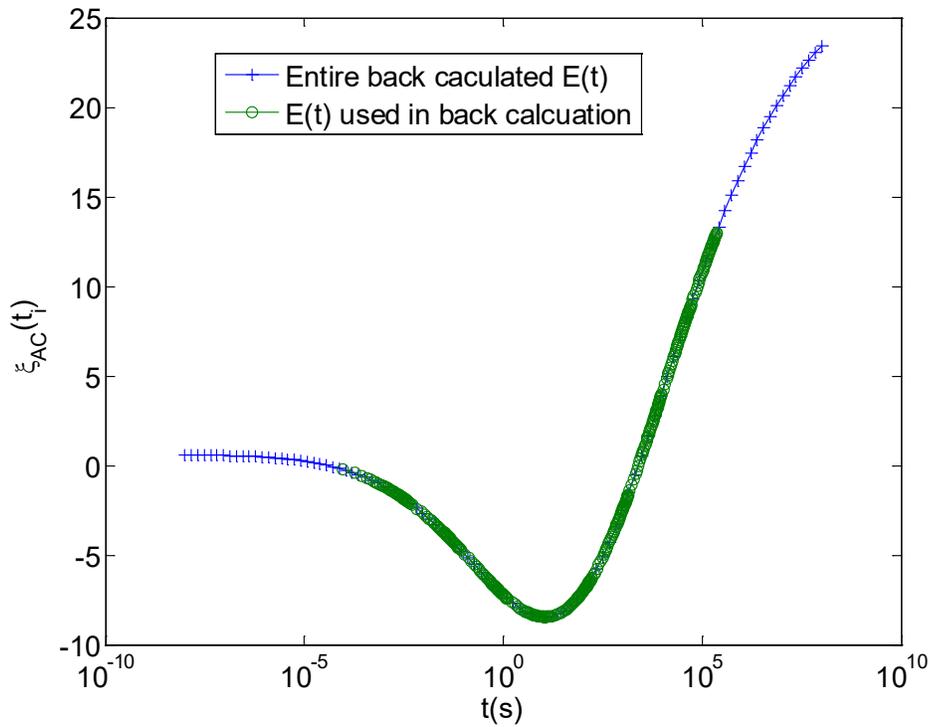
Figure 91. Graph. Variation of error when using FWD data from only sensor 1.

To investigate whether using just the farther sensors improved the backcalculated $E_{unbound}$ values, backcalculations were performed using data from different combinations of farther sensors. Figure 92 shows the error in backcalculation of the modulus of the base (layer 2) and the subgrade (Layer 3), when data from only further sensors were used. As shown, for layer 3, error ranged between 0.27 to 1.43 percent, with no specific trend. The error in the modulus of the base (layer 2) was higher, ranging from 1 to 8.96 percent. However, a clear trend was not observed. By comparing with figure 89, one can conclude that using all the sensors produces the least error in $E_{unbound}$.
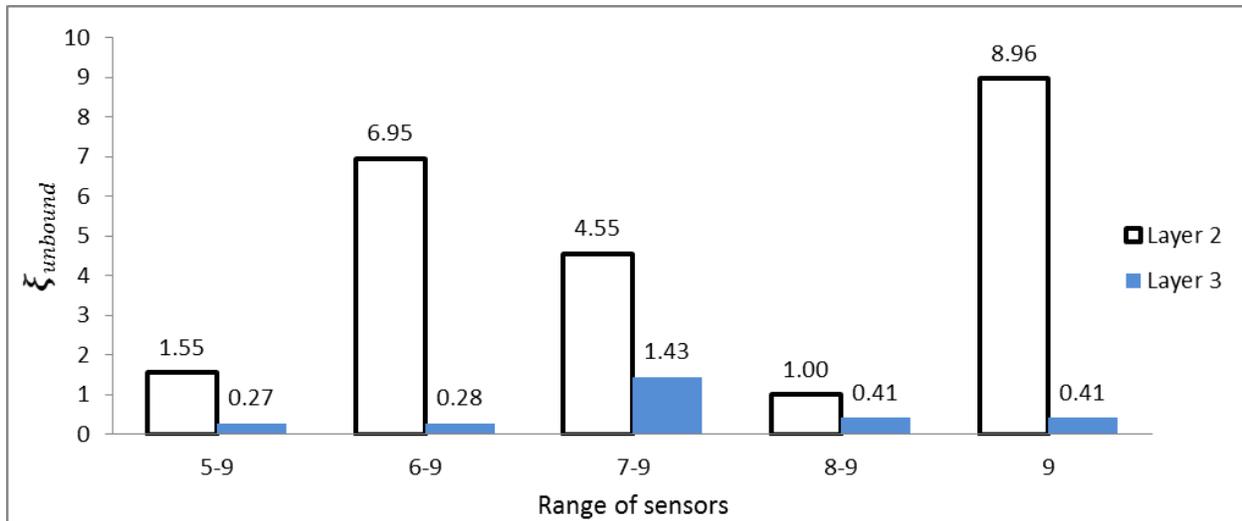
Figure 92. Graph. Error in unbound layer modulus using FWD data from only farther sensors.

Effect of Temperature Range of Different FWD Tests on Backcalculation

It is typically not feasible to run the FWD test over a wide range of temperatures (e.g., from 32 to 176 °F). Depending on the region and the month of the year, the variation of temperature in a day can be anywhere between 50 and 86 °F during the fall, summer, and spring when most data collection is done. This means that the performance of the backcalculation algorithm needs to be checked for various narrow temperature ranges. The purpose of the study explained in this section was to determine the effect of different temperature ranges on the backcalculated $E(t)$ values. Further, it was recognized that the results obtained from GA might not be exact but only an approximation of the overall solution. Hence a local search method was carried out through fminsearch using the results obtained from GA as seed. Figure 93 shows the error in the backcalculated elastic modulus values of base and subgrade when different pairs of temperatures were used. As shown, in most cases, the error was less than 0.1 percent. Note that the errors shown in figure 93 were less than the ones shown in figure 89 (when all sensors were used). This was because in figure 89, only GA was used, whereas in figure 93, fminsearch was used after the GA, which improved the results.
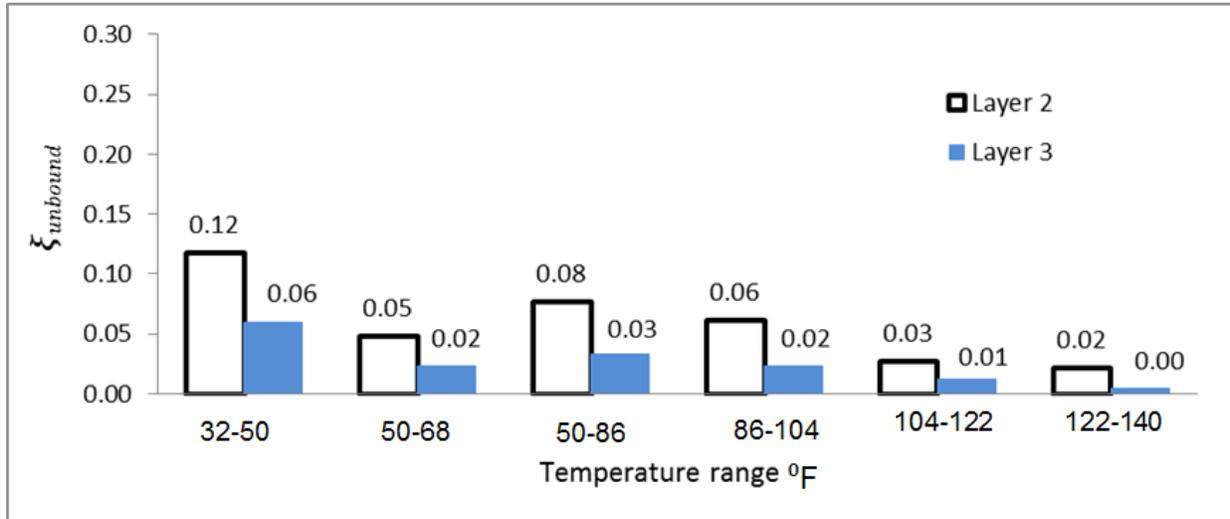
Figure 93. Graph. Variation of error in backcalculated unbound layer moduli when FWD data run at different sets of pavement temperatures are used.

Figure 94 shows the average error in $E(t)$ (i.e., ξ_{AC}^{avg} given in figure 88), where a pattern was observed. The error was the least when intermediate temperatures (i.e., {50-68}, {50-68-86}, {68-86-104}, {86-104}, {86-104-122} °F) were used. At low temperatures, the error seemed to increase. This was meaningful because at low temperatures, a small portion (upper left in figure 90) was used in BACKLAVA. Therefore, the chance of mismatch at the later portions of the curve (lower right in figure 90) was high. At high temperatures, error also seemed to increase. Theoretically, the higher the temperature, the larger the portion of the $E(t)$ curve that was used because of the nature of the convolution integral, which starts from zero (figure 29). However, if only the high temperatures were used, the discrete nature of load and deflection time history led to a big jump from zero to the next time t_i, during evaluation of the convolution integral. This jump occurred because when the physical time at high temperatures was converted to reduced time, actual magnitudes became large and, in a sense, a large portion at the upper left side of the $E(t)$ curve was skipped during the convolution integral. At intermediate temperatures, however, a more balanced use of the $E(t)$ curve in BACKLAVA improved the results.
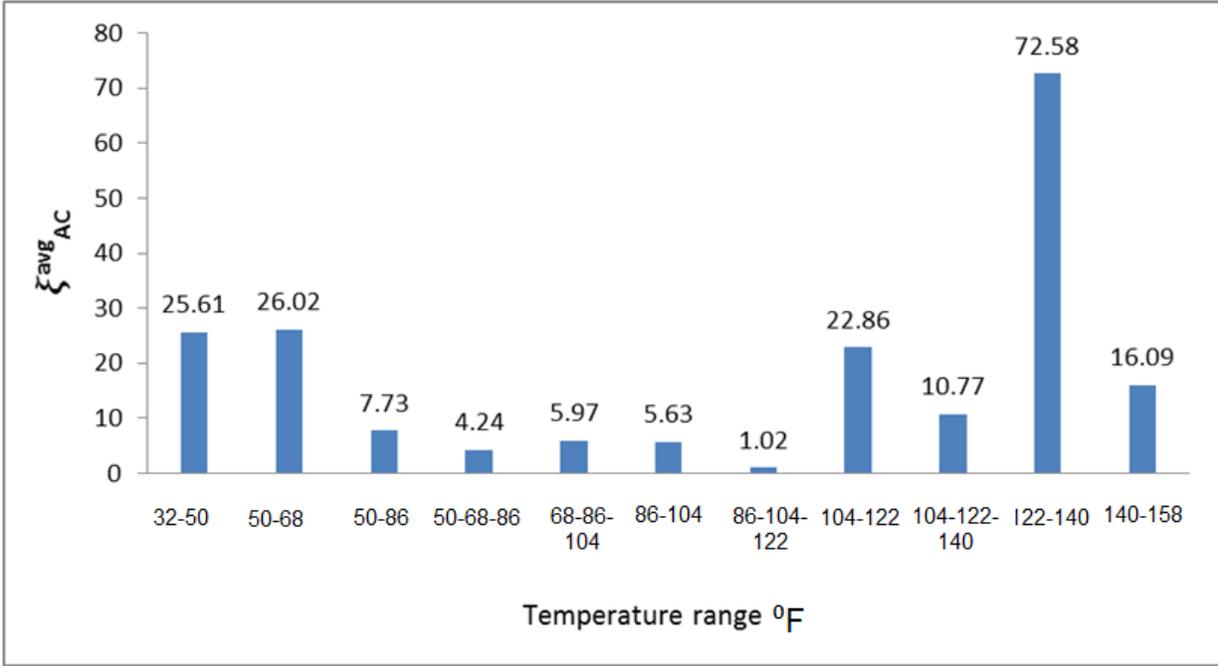
Figure 94. Graph. Error in backcalculated *E*(*t*) curve in optimal backcalculation temperature set analysis minimizing percent error.

When results from GA were used as seed values in fminsearch, it was observed that in general, error in *E*(*t*) was reduced. Figure 95, figure 96, and figure 97 show backcalculated *E*(*t*) master curve using GA and corresponding backcalculated *E*(*t*) master curves obtained using GA and fminsearch. As shown, combined use of GA and fminsearch resulted in improved backcalculation.
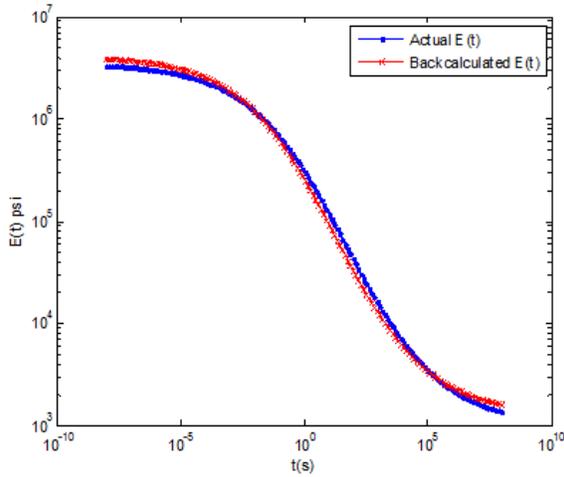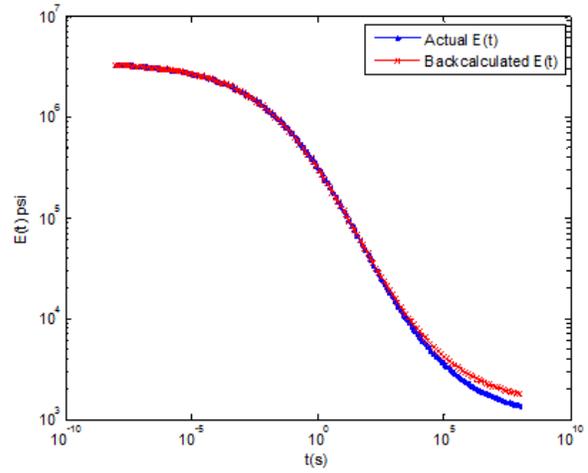
Backcalculated E(t) curve using GA only

Backcalculated E(t) curve using GA + fminsearch
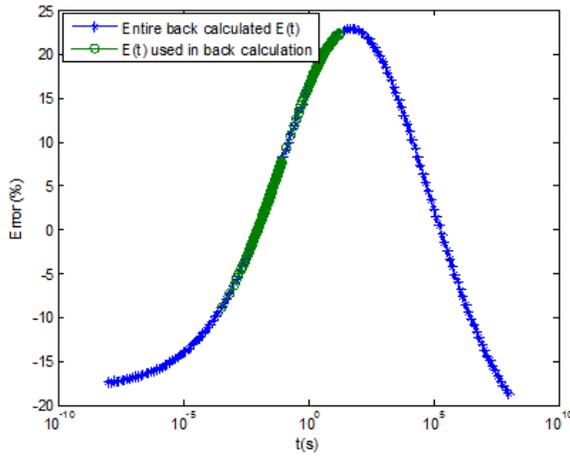
Variation of error, $\xi_{AC}(t_i)$: GA only.
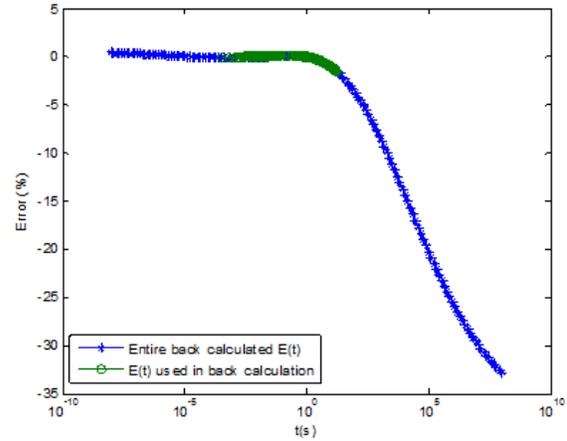
Variation of error, $\xi_{AC}(t_i)$: GA+fminsearch

Figure 95. Graphs. Results for backcalculation at {50, 86} °F temperature set: left side—only GA used, right side—GA+fminsearch used.
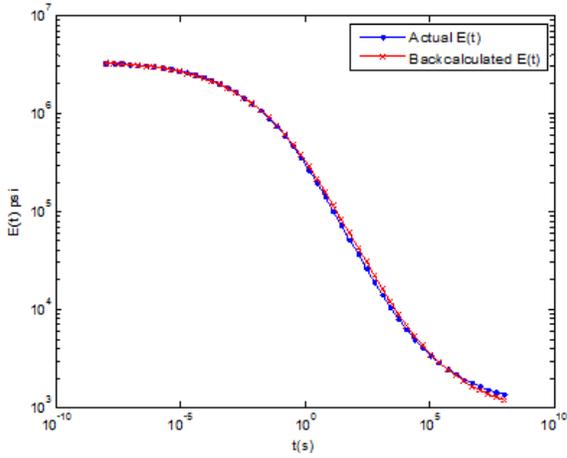
Backcalculated E(t) curve using GA only
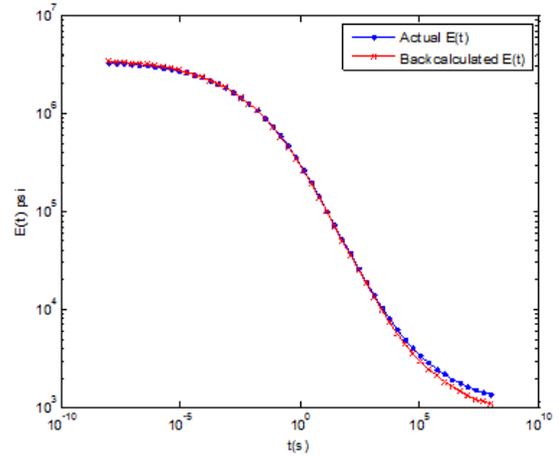
Backcalculated E(t) curve using GA +
fminsearch
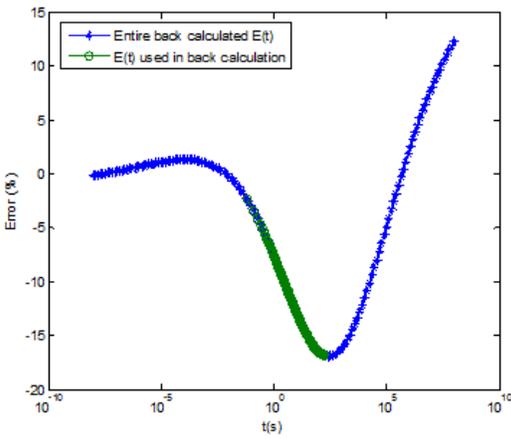
Variation of error, $\xi_{AC}(t_i)$: GA only
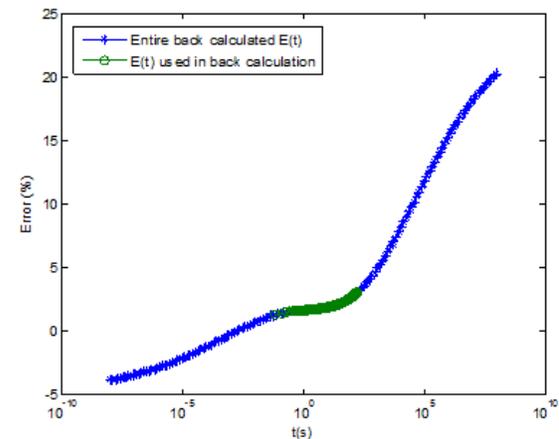
Variation of error, $\xi_{AC}(t_i)$: GA + fminsearch

Figure 96. Graphs. Results for backcalculation at {86, 104} °F temperature set.
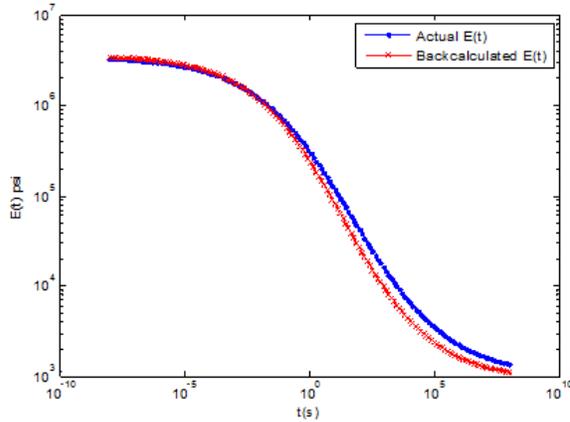
Backcalculated E(t) curve using GA only
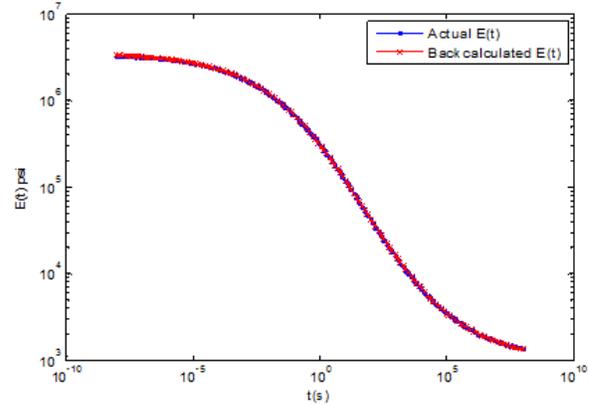
Backcalculated E(t) curve using GA + fminsearch
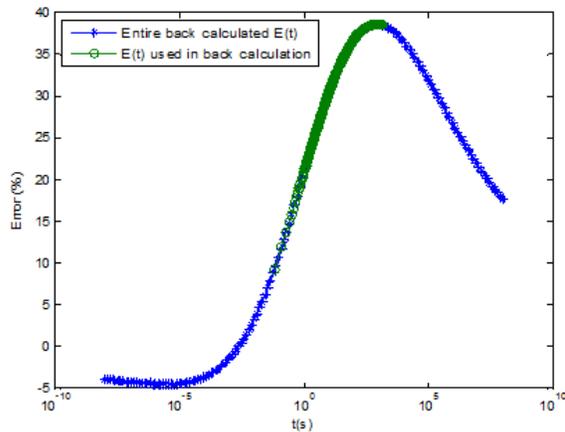
Variation of error, $\xi_{AC}(t_i)$: GA only
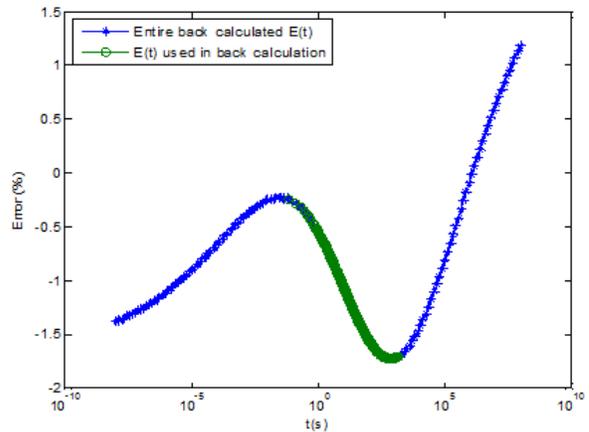
Variation of error, $\xi_{AC}(t_i)$: GA + fminsearch

Figure 97. Graphs. Results for backcalculation at {86, 104, 122} °F temperature set.

Table 18 shows the time it takes to run the GA for population-generation size of 70 to 15, followed by fminsearch. The results are shown for a computer that has Intel Core 2, 2.40 GHz, and 1.98 GB RAM.

Table 18. Backcalculation runtime for GA-fminsearch seed runs.

Number of Temperature Data	Backcalculation time (min)
Two (e.g., {50, 86}°F)	30
Three (e.g., {50, 68, 86} °F)	40
Seed run (fminsearch)	15–20

Normalization of Error Function (Objective Function) to Evaluate Range of Temperatures

In the analysis presented in the previous sections, percent error between the computed and measured displacement was used as the minimizing error. However, the deflection curve obtained from the field often includes noise, especially after the end of load pulse. If percent

96

error is used as the minimizing objective, it may lead to overemphasis of lower magnitudes of deflections at the later portion of the time history, which typically includes noise and integration errors. Hence, another fit function was proposed in which the percent error was calculated with respect to the peak of deflection at each sensor. This approach penalized the tail data by normalizing it with respect to the peak, as shown in figure 98.

$$Er = \sum_{k=1}^{m} 100 \sum_{i,o=1}^{n} \frac{\left|\left(d_i^k - d_o^k\right)\right|}{\{d^k\}_{max}}$$

Figure 98. Equation. Normalized error in deflection history.

Where:

$\{d^k\}_{max}$ = Peak response at sensor k.
m = Number of sensors.
d_i^k = Measured deflection at sensor k.
d_o^k = Output (calculated) deflection from forward analysis at sensor k.
n = Total number of deflection data points recorded by a sensor.

The limits considered for $E(t)$ so far were the limits on the individual parameters of the sigmoid curve (table 16). The $E(t)$ curves obtained by considering the upper and lower limits of the parameters represent curves well beyond the actual data base domain. To curtail this problem, constraints were introduced putting limits shown in figure 99 on the sum of the sigmoid coefficients c_1 and c_2.

$$c_1 + c_2 \leq s_1 \text{ and } c_1 + c_2 \geq s_2$$

Figure 99. Equation. Constraints in optimization model.

Where s_1 and s_2 are arbitrary constants.

The arbitrary constants s_1 and s_2 were obtained by calculating maximum and minimum values of the sum of sigmoid coefficients c_1 and c_2 from numerous HMA mixes. Alternatively, the problem was reframed by incorporating the constraints in limit form by redefining the variables as shown in figure 100.

$$\begin{aligned} var\ 1 &= c_1 \\ var\ 2 &= x = c_1 + c_2 \text{ and } x^1 \leq x \leq x^u \\ var\ 3 &= c_3 \\ var\ 4 &= c_4 \end{aligned}$$

Figure 100. Equation. Sigmoid variables in optimization model.

Where c_1 through c_4 are sigmoidal function coifficents, and x^u and x^1 are the upper and lower limits of $c_1 + c_2$, respectively. The problem was then resolved after replacing the inequality constraint with limits on the variables. The new function gave good results at temperature sets of {50, 86} °F, {86, 104} °F, {50, 68, 86} °F, {68, 86, 104} °F, and {86, 104, 122} °F. The backcalculated $E(t)$

curves were then converted to $|E^*|$ using the interconversion relationship given in Kutay et al.[65] Mathematically, the dynamic modulus can be defined as shown in figure 101:

$$E^*(f) = E'(f) + iE''(f)$$

Figure 101. Equation. Dynamic modulus in complex form.

Where f is frequency, $E'(f)$ is storage modulus, and $E''(f)$ loss modulus, which can be obtained for a generalized Maxwell model using the following equations shown in figure 102 and figure 103:

$$E'(f) = |E^*(f)| * \cos(\phi) = E_0 + \sum_{i=1}^{N} E_i \frac{(2\pi f \rho_i)^2}{1 + (2\pi f \rho_i)^2}$$

Figure 102. Equation. Real component of dynamic modulus.

$$E''(f) = |E^*(f)| * \sin(\phi) = \sum_{i=1}^{N} E_i \frac{2\pi f \rho_i}{1 + (2\pi f \rho_i)^2}$$

Figure 103. Equation. Imaginary component of dynamic modulus.

Where:

ϕ = the phase angle.
$|E^*|$ = the absolute value of the complex E^* function (figure 101).
E_i = modulus of each Maxwell spring.
$\rho_i = \eta_i / E_i$ = relaxation time
η_i = the viscosity of each dashpot element in the generalized Maxwell model as shown in figure 104.

$$| E^* | = \sqrt{E'^2 + E''^2} \qquad\qquad \phi = \tan^{-1}(E''/E')$$

Figure 104. Equation. Dynamic modulus and phase angle.

Backcalculated $E(t)$ and $|E^*|$ master curves were compared with the actual curves for temperature sets {50, 86} °F and {50, 68, 86} °F in figure 105 and figure 106, respectively.
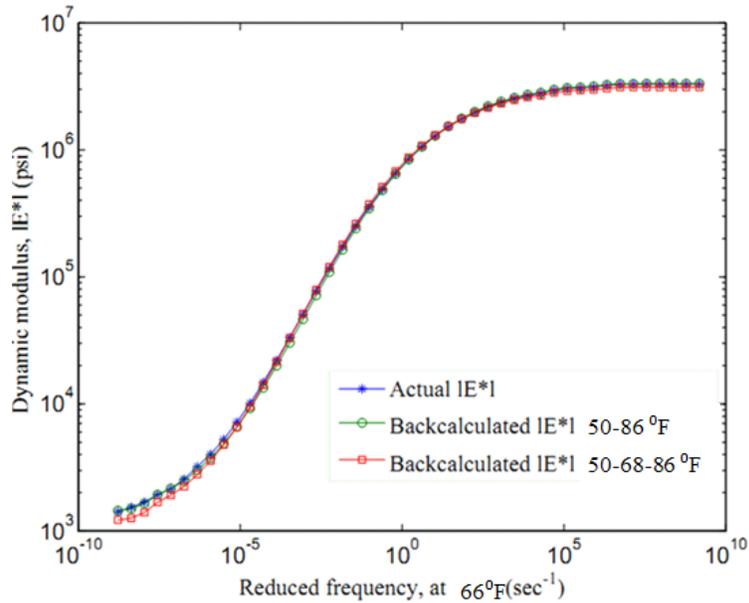
Figure 105. Graph. Backcalculated |*E**| master curve using FWD data at temperature set {50, 86} °F, minimizing normalized error.
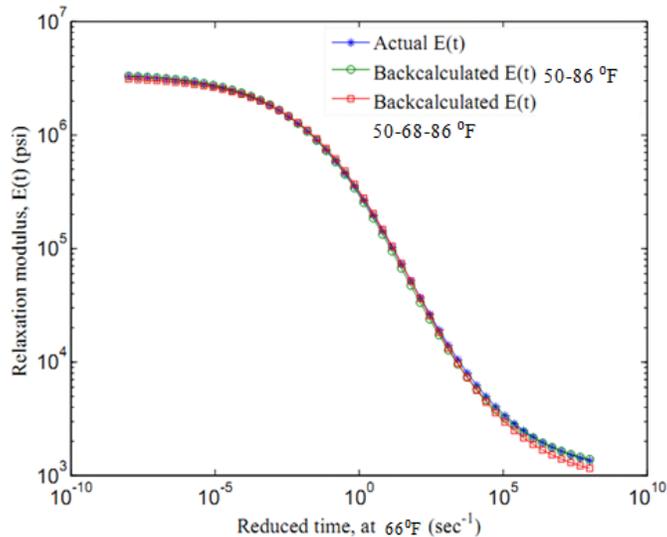
Figure 106. Graph. Backcalculated *E*(*t*) master curve using FWD data at temperature set {50-68-86} °F, minimizing normalized error.

It can be seen from figure 107 that the results obtained for $E(t)$ errors over temperature sets showed a distinct pattern. The $E(t)$ and $E_{unbound}$ errors with respect to temperature sets showed a trend similar to that observed in the case of percentage error (figure 93 and figure 94, respectively). The error was observed to be high at sets of low ({32, 50} °F) and high ({122, 140} °F, {104, 122, 140} °F, {122, 140, 158} °F) temperatures. This is because the backcalculated $E(t)$ at lower temperatures represents the left portion of the sigmoidal $E(t)$ curve and higher temperatures represents the right. As explained earlier, both regions are fairly flat and

99

hence represent constant values of $E(t)$, which may not optimize to the actual $E(t)$ curve. Better results were obtained for the temperature range of {50, 68} °F to {86, 104, 122} °F (figure 108). The backcalculated $E(t)$ master curves and corresponding errors obtained at {50, 86} °F and {68, 86, 104} °F for the proposed backcalculation model are shown in figure 109.
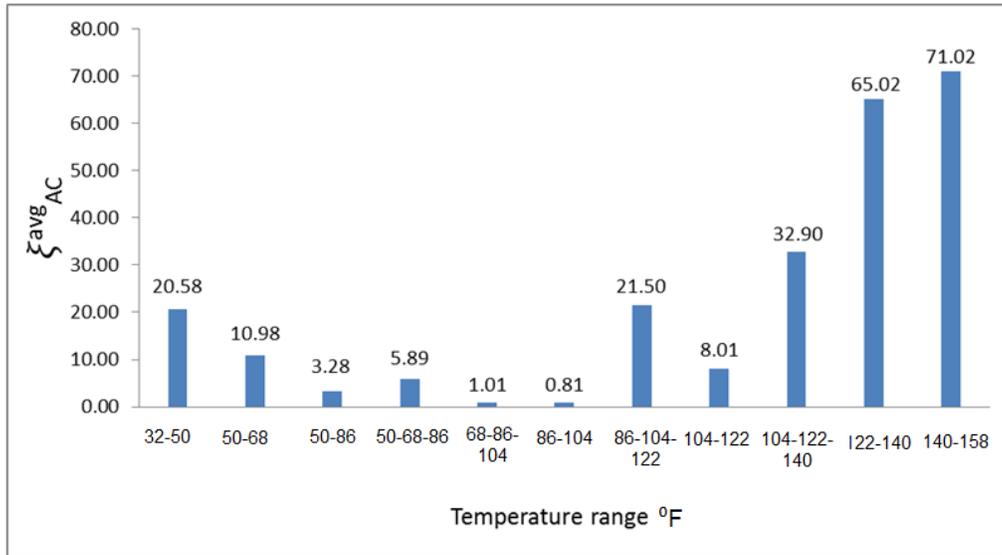
Figure 107. Graph. Variation of ξ_{AC}^{avg} at different FWD temperature sets.
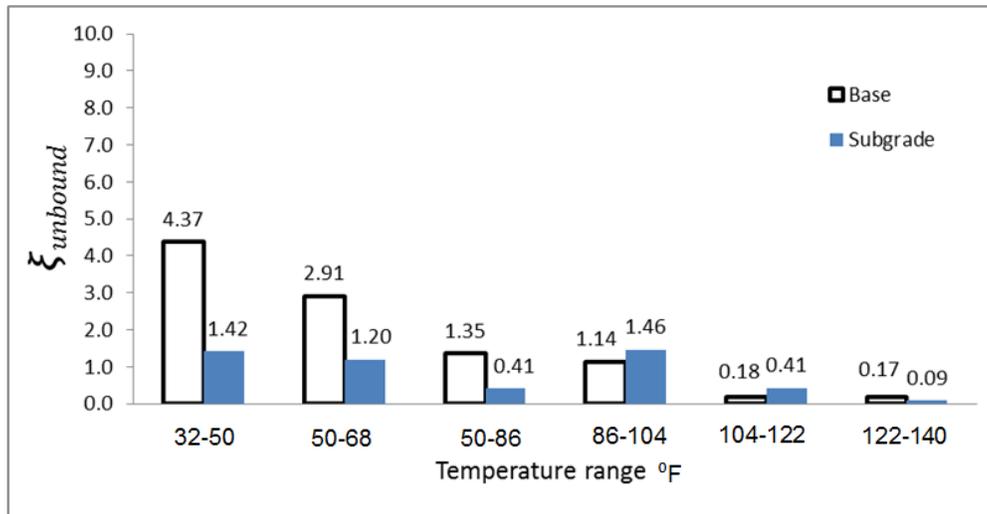
Figure 108. Graph. Variation of $\xi_{unbound}$ at different FWD temperature sets.
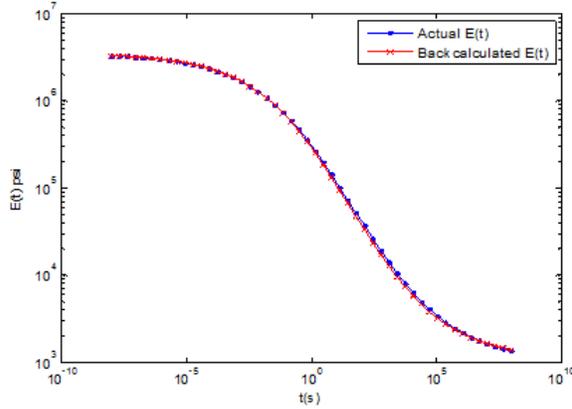
Backcalculated $E(t)$ curve using GA (at {50, 86} °F)
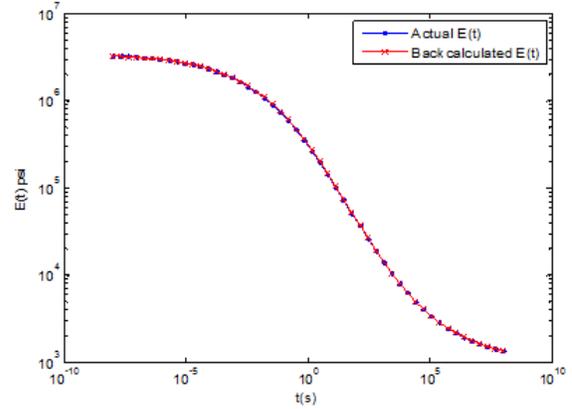
Backcalculated $E(t)$ curve using GA (at {68, 86, 104} °F)
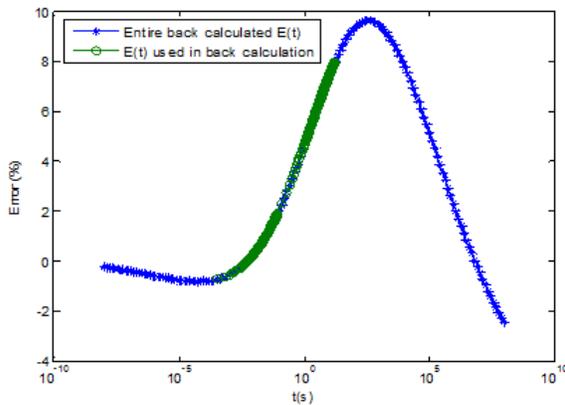
Variation of error, $\xi_{AC}(t_i)$ (result at {50, 86} °F)
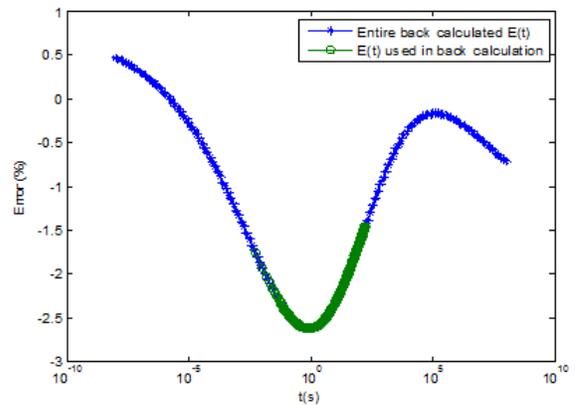
Variation of error, $\xi_{AC}(t_i)$ (result at {68, 86, 104} °F)

Figure 109. Graphs. Backcalculation results obtained using modified sigmoid variables.

Backcalculation of Viscoelastic Properties Using Various Asphalt Mixtures

In the previous sections, analyses were performed using only a single mix. To verify the conclusions made in the previous sections regarding the optimum range of temperatures of FWD testing, backcalculations were performed on nine typical mixtures. Actual viscoelastic properties—relaxation modulus and shift factors of the selected mixtures—are shown in figure 110.
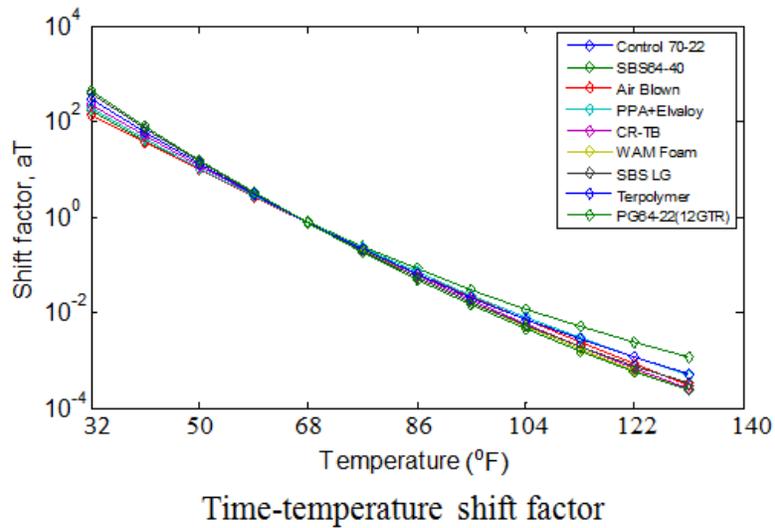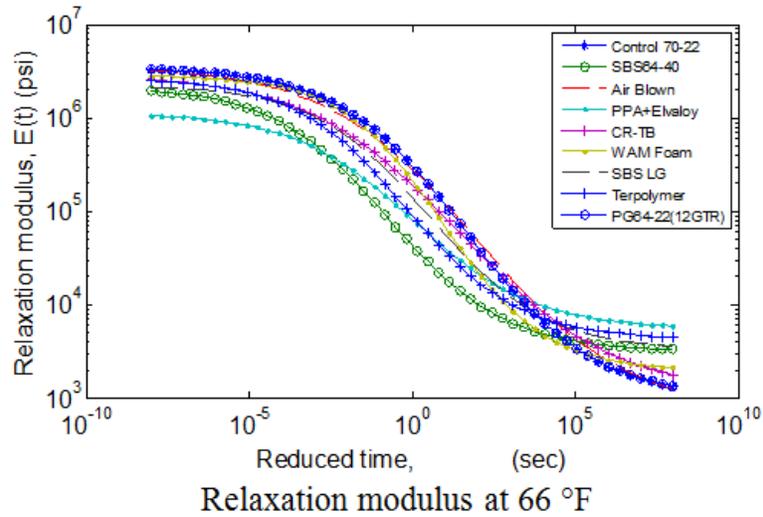
Figure 110. Graphs. Viscoelastic properties of field mix in optimal temperature analysis.

Comparison of the average error in the backcalculated relaxation modulus function calculated over three time ranges—10^{-5} to 1 s, 10^{-5} to 10^2 s, and 10^{-5} to 10^3 s—as shown in figure 111. It can be seen from the figure that, for all the mixes, relaxation modulus curve can be predicted close to less than 15 percent over a range of relaxation time less than 10^{+3} s. Furthermore, it can be seen that, as suggested, the backcalculated relaxation modulus prediction provided a good match over an approximate temperature range of 50 to 86 °F.
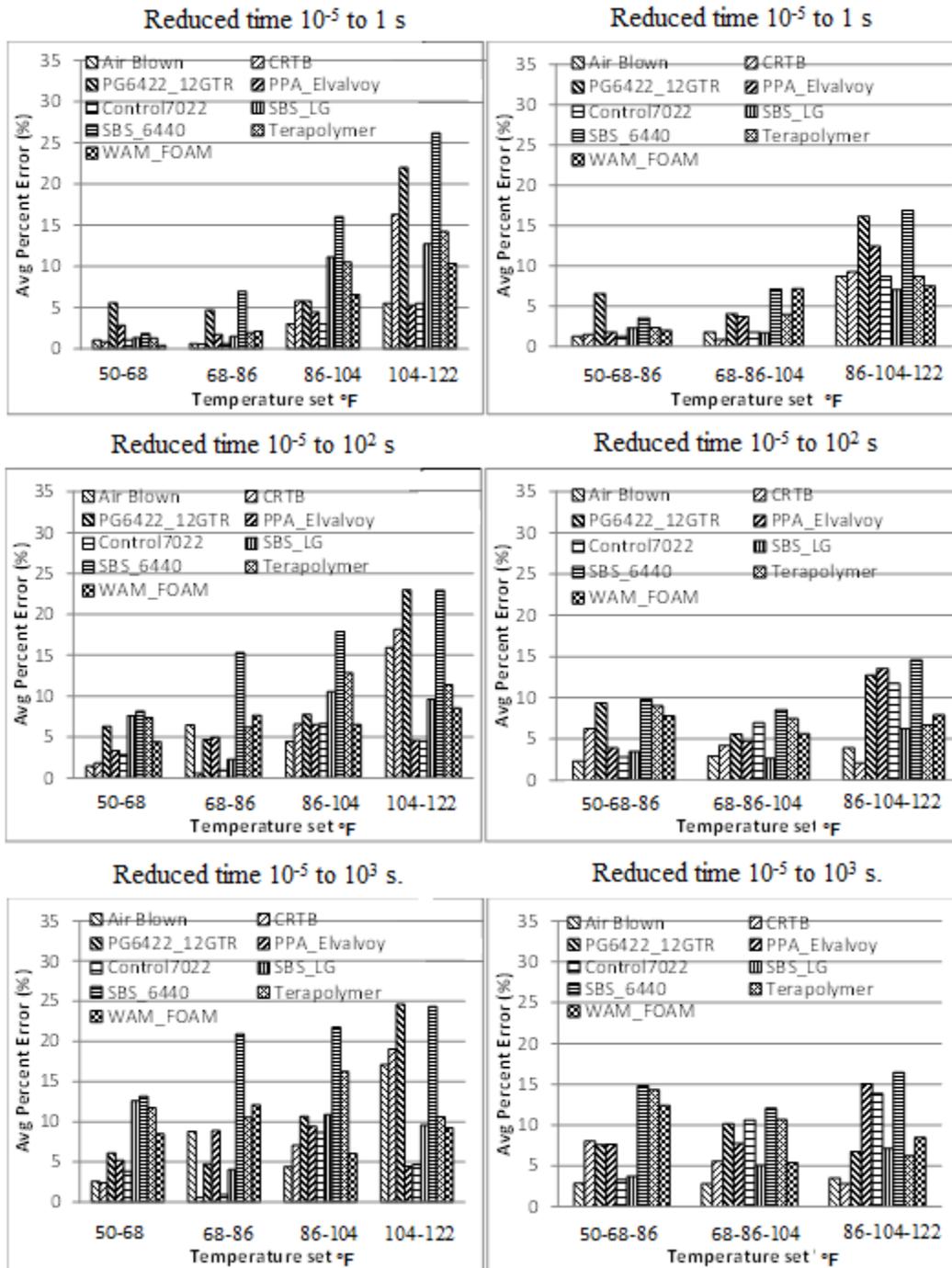
Figure 111. Graphs. Variation of error calculated over three ranges of reduced time—top = 10^{-5} to 1 s, middle = 10^{-5} to 10^2 s, and bottom = 10^{-5} to 10^3 s.

Theoretical Analysis on Multiple-Pulse FWD in Backcalculation

In theory, it should be possible to obtain a relaxation modulus master curve if data containing the time-changing response at different temperature levels were known. The available analysis window in the current FWD devices is short, extending up to 25 to 35 ms of stress pulse, which

103

could be used to infer part of the relaxation function. Although series of FWD tests at different temperatures could be useful in developing the entire master curve, in theory, the prediction could be improved if information at different rates of loading or over a larger time interval were known.

As shown in figure 112, a load of four successive pulses with a duration of 35 ms followed by four pulses with 10s duration each was simulated to generate the deflection basin. This example was used to investigate whether a different loading history could result in better estimation of $E(t)$. Figure 113 shows the backcalculated $E(t)$, where a good fit is visible. Note that the accuracy of the backcalculated $E(t)$ depended on the duration of the stress pulse, where longer duration allowed calculation of $E(t)$ at longer durations. It is also important to apply a high-frequency (short duration) pulse load to increase the accuracy of $E(t)$ at very short times. Note that backcalculation of $E(t)$ for this example took less than 5 min in the MATLAB® optimization tool fminsearch. These possibilities are explored in detail in appendix B.
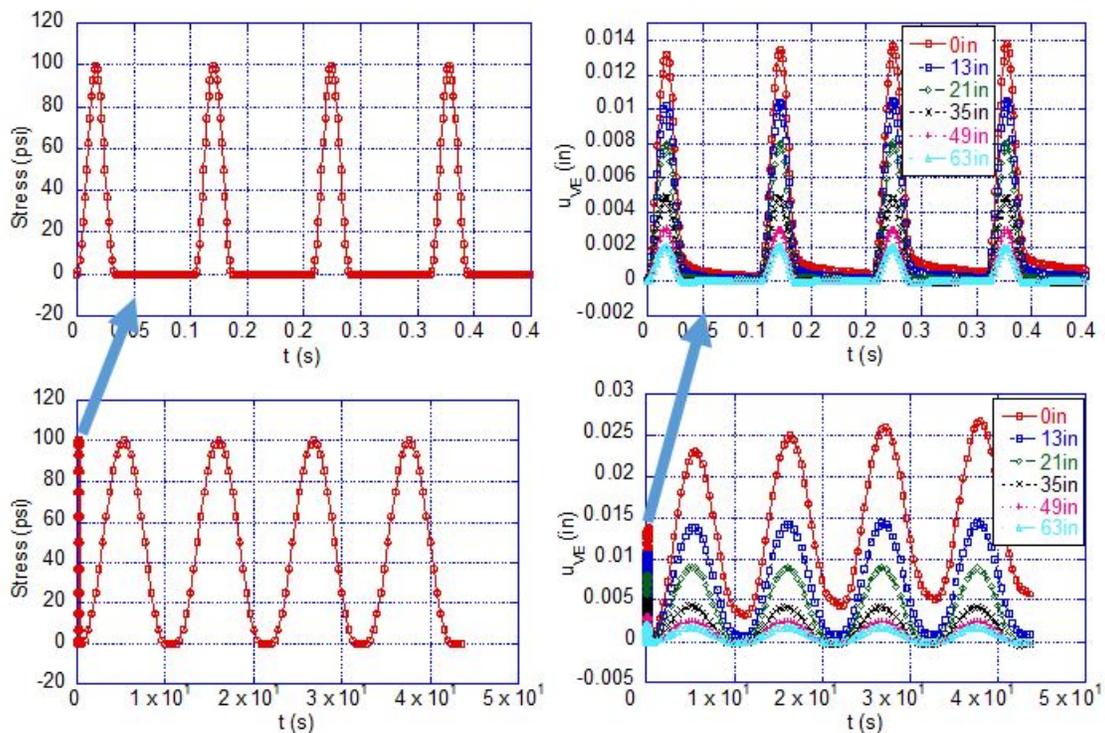
Figure 112. Graphs. Applied stress and resulting deflection basin for multiple pulse loading analysis.
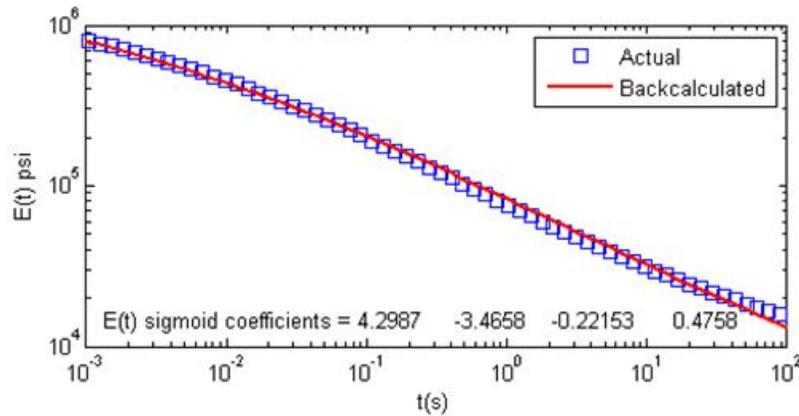
Figure 113. Graph. Backcalculated $E(t)$ and deflection histories using the multiple stress pulses.

BACKCALCULATION OF RELAXATION MODULUS MASTER CURVE USING A SINGLE FWD TEST AND KNOWN PAVEMENT TEMPERATURE PROFILE

The uneven temperature profile existing across the thickness of the AC layer during a single FWD drop can theoretically be used to backcalculate the $E(t)$ master curve and the shift factor coefficients ($a_T(T)$). The AC layer can be divided into several sublayers with same viscoelastic properties but with different temperature levels. Two different approaches of backcalculation are discussed in this section. In the first approach, all the unknown variables (sigmoid coefficients, shift factor coefficients, and unbound modulus) in the forward algorithm were varied during backcalculation. In the second approach, a two-staged backcalculation procedure was adopted. The two-stage method involved static backcalculation in the first stage (unbound modulus assuming elastic AC layer) followed by viscoelastic backcalculation in the second (sigmoid and shift factor coefficients). Both approaches were explored in the present study.

Linear Viscoelastic Backcalculation Using Single Stage Method

As discussed earlier, a total of six coefficients are needed to represent the relaxation properties of the AC layer, including the temperature dependency. The backcalculation procedure used was same as used in the previous section (i.e., BACKLAVA), except the forward analysis was replaced by LAVAP, which can consider varying temperature along the depth of the AC layer. Subsequently, the new backcalculation algorithm was referred as BACKLAVAP. For executing the GA, the same lower and upper limits of c_i and a_i (sigmoid and shift factor coefficients) and other specifications were retained.

As a first step, the backcalculation algorithm was validated with a synthetic FWD deflection history, under two different temperature profiles. The data were generated using LAVAP and then used in BACKLAVAP for backcalculation of $E(t)$. The AC layer was divided into three equal sublayers with three different temperatures. Pavement section, properties, and temperature used in the forward analysis are shown in table 19.

Table 19. Details of the pavement properties used in single FWD test backcalculation under a known temperature profile.

Property		Asphalt Concrete Layer			Granular Base	Subgrade
		Sublayer 1	Sublayer 2	Sublayer 3		
Thickness (inches)		2	2	2	20	Semi-infinite
Temperature (°F)	Case 1	68	59	50	N/A	N/A
	Case 2	86	77	68	N/A	N/A
Poisson's ratio		0.35			0.4	0.45
Relaxation modulus		$E(t)$ coefficients (c_1, c_2, c_3, c_4) backcalculated			Backcalculated	Backcalculated
Time-temperature shifting coefficients		(a_1, a_2) backcalculated			N/A	N/A
Sensor spacing from the center of load (inches): 0, 8, 12, 18, 24, 36, 48, 60						

N/A = Not applicable.

For the case of backcalculation using a temperature profile, the GA parameters—population size and generation numbers—were again selected after several trials of combinations. It was observed that at population size of 300, improvement in the best solution was marginal after 12 to 15 generations, and the population converged to the best solution at about 45 generations. Similarly, for a population size of 400, improvement in the best solution was marginal after 10 to 15 generations. Figure 114 shows the backcalculation results at the temperature sets given in table 19, where a good match was visible. Error in the backcalculated $E(t)$ was quantified relative to the actual $E(t)$ using $\xi_{AC}(t_i)$, given in figure 87. The $\xi_{AC}(t_i)$ calculation was performed over a reduced time interval from 10^{-8} to 10^{+8} s. Then, the average error (ξ_{AC}^{avg}) was computed using figure 88. The average error level for the first temperature profile was found to be 5.2 percent, and for the second, it was 4.4 percent.

To further investigate the effect of the magnitude of the pavement temperature profile on backcalculation of $E(t)$ master curve, synthetic FWD deflection histories were generated. The synthetic data were then used in backcalculation. The structure was divided into three layers with different temperatures, and $E(t)$ was backcalculated using these data. The pavement section properties used in the study were same as shown in Table 19.

Backcalculation was performed assuming the temperature of the top, middle, and bottom sublayers of the asphalt layer as {68, 59, 50} °F, {86, 77, 68} °F, {104, 95, 86} °F, and {122, 113, 104} °F. It was again observed that the problem converged well with 300 GA populations at 45 GA generations. The results shown in figure 115 did exhibit a trend, suggesting that there was a good potential for backcalculation of $E(t)$ using a single FWD response for the lower temperature ranges, assuming that the temperature profile of the pavement was known.
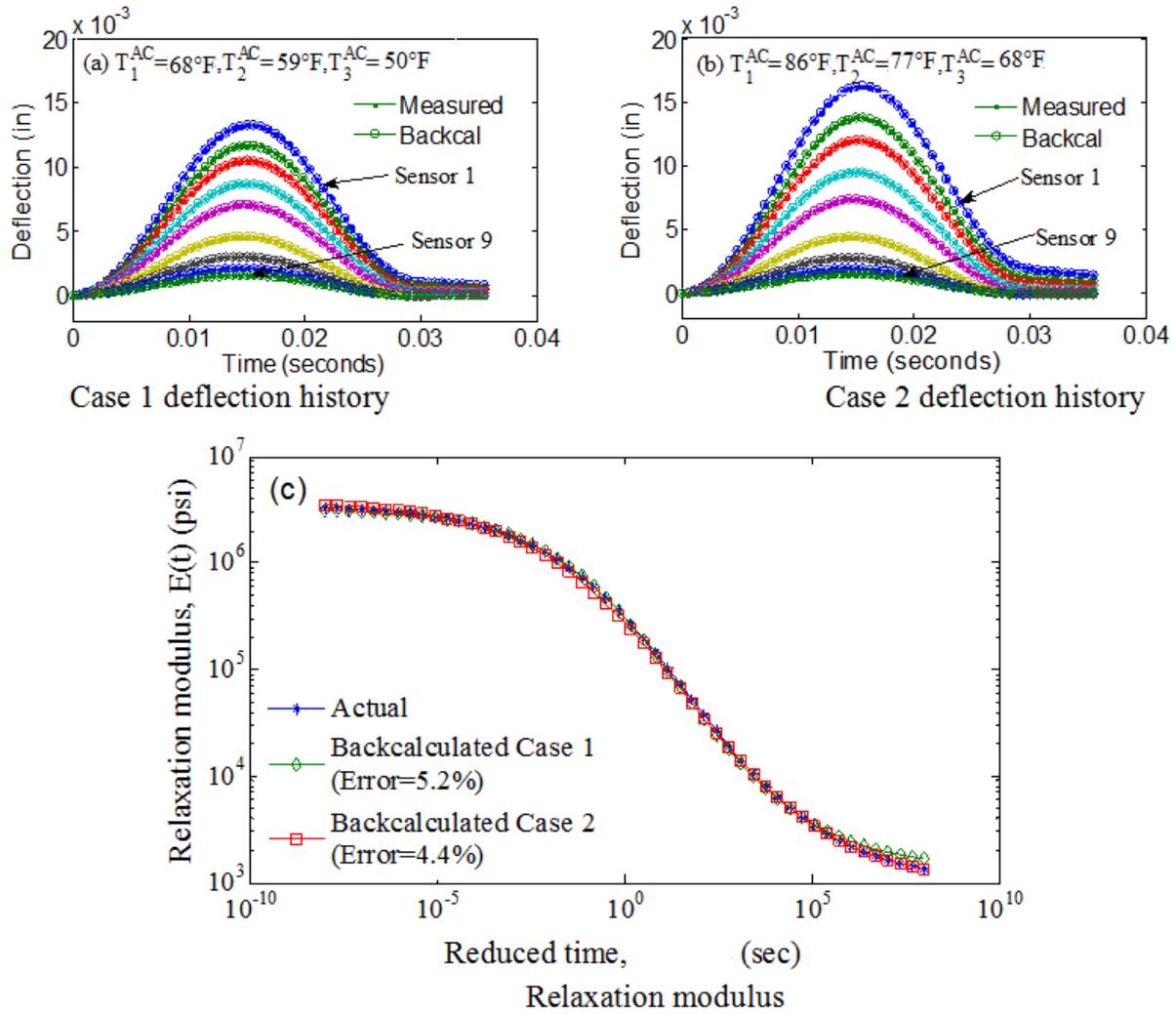
Figure 114. Graphs. Comparison of actual and backcalculated values in backcalculation using temperature profile.
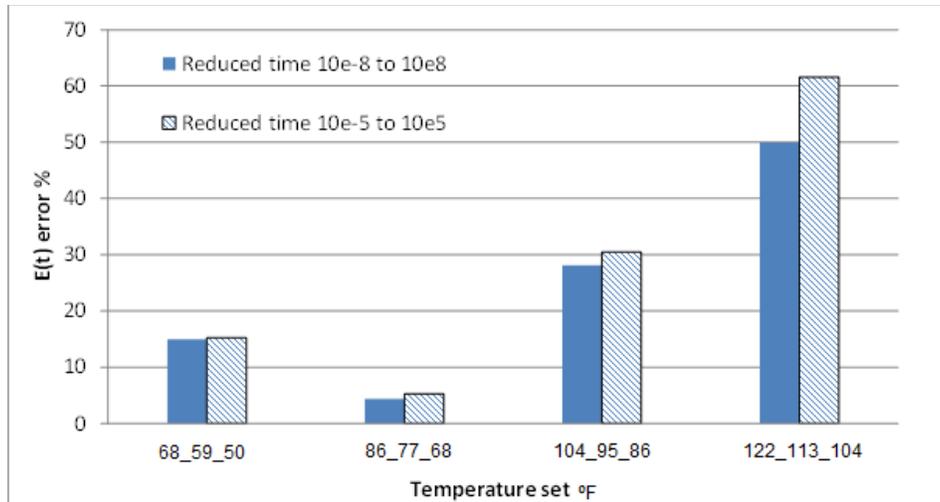
Figure 115. Graph. Error in backcalculated *E*(*t*) curve for a three-temperature profile.

Backcalculation of the Viscoelastic Properties of the LTPP Sections Using a Single FWD Test With Known Temperature Profile

The BACKLAVAP algorithm was next used with field data to backcalculate the viscoelastic properties of nine LTPP sections. With the exception of sections 10101, 300113, and 340801, selection of the sites was done based on the following rules:

- Section comprised three layers with only one AC layer.
- Total number of constructions of the section was one.
- Section was an SPS section type (experiment number 1 and 8)
- Section was flexible pavement.

Table 20 and table 21 contain general and structural information about each selected LTPP site. As shown in table 21, section 10101 had a total of four layers, including two AC layers. However, because the *D*(*t*) of the two AC layers reported in the LTPP database were very close, the section was included in the list, treating the two layers as a single AC layer in the analysis. Section 300113 comprised two AC layers of thickness 0.2 and 5.8 inches. Because the top AC layer of the section was very thin compared with the second AC layer, the AC layers were treated as a single layer. Furthermore, the sectional composition of sections 300113 and 340801 were not changed during various constructions; therefore, they were included in the analysis. However, it is not clear from the LTPP database whether the *D*(*t*) was measured before or after the constructions were done.

Table 20. List of LTPP sections used in the analysis.

State	Section	Year of Construction	Total Number of Constructions	Section Type	Experiment Number
1	0101	4/30/1991	1	SPS	1
6	A805	5/1/1999	1	SPS	8
6	A806	5/1/1999	1	SPS	8
30	0113	9/18/1997	5	SPS	1
34	0801	1/1/1993	2	SPS	8
34	0802	1/1/1993	1	SPS	8
35	0801	9/11/1995	1	SPS	8
35	0802	9/11/1995	1	SPS	8
46	0804	1/1/1992	1	SPS	8

Table 21. Structural properties of the LTPP sections used in the analysis.

State Code	Section	Total Number of Layers	Number of AC Layers	AC Layer Thickness (inches)	Base Layer Thickness (inches)
1	0101	4	2	AC1 = 1.2, AC2 = 6.2	7.9
6	A805	3	1	3.9	8.2
6	A806	3	1	6.8	12.1
30	0113	4	1	AC1 = 0.2, AC2 = 5.8	8.4
34	0801	3	2	3.6	7.8
34	0802	3	1	6.7	11.6
35	0801	3	1	4.2	9.7
35	0802	3	1	7	12.7
46	0804	3	1	6.9	12

In the LTPP Program, each section is tested according to a specific FWD testing plan, which consists of one or more test passes. Both SPS 1 and SPS 8 are tested, along two test passes (test pass 1 and test pass 3) using test plan 4 in LTPP. Test pass 1 data include FWD testing performed along the midlane (ML) whereas test pass 2 data includes FWD testing performed along the OW path. Because testing with the ML test pass represents the axisymmetric assumption better, it was used here in the analysis. Furthermore, for each section, testing was done at several longitudinal locations (in the direction of traffic) in every test pass. Typically, for a 500-ft test section, FWD testing is performed at every 50 ft longitudinally along the test pass. In the LTPP testing protocol, temperature gradient measurements are taken every 30 min, plus or minus 10 min. The necessary temperature profile data were obtained by interpolating the temperature measured during the FWD testing. The AC layer was divided into three equal sublayers, and a constant temperature for each sublayer was estimated. Table 22 shows the interpolated temperatures at the middle of the three sublayers. From the table, it can be seen that the maximum temperature difference (between sublayer 1 and sublayer 3) was 11.2 °F in section 350801 and the minimum 5.3 °F in section 6A805.

Table 22. AC temperature profile during LTPP FWD test.

State Code	Section	Test Date	Temperature Profile (°F)		
			Sublayer 1	Sublayer 2	Sublayer 3
1	0101	04/28/05	100.0	92.5	91.6
6	A805	11/16/11	73.6	69.1	68.2
6	A806	11/16/11	79.2	75.2	71.2
30	0113	07/12/10	84.7	80.1	79.2
34	0801	08/26/98	102.4	98.8	93.6
34	0802	08/26/98	79.3	83.3	86.5
35	0801	04/09/05	74.1	65.1	63.0
35	0802	05/26/00	89.8	84.4	83.3
46	0804	05/02/01	75.9	70.7	67.5

Except for section 350801, the FWD deflection data obtained showed no or minimal waviness at the end of the load pulse, which indicated that there was no shallow stiff layer. The FWD deflection data obtained from section 350801 showed some waviness at the end of the load pulse. This indicated the possibility of a medium-depth stiff layer or high water table. The presence of a stiff layer was further evaluated using a graphical method suggested by Ullidtz.[94] The method involves plotting peak deflections obtained from FWD testing versus the reciprocal of the corresponding sensor location (measured from the center of loading).[95] Depths of stiff layer in each LTPP section estimated using Ullidtz's method are shown in table 23.[94] Note that negative depth to the stiff layer was interpreted as absence of the stiff layer in the method. The results indicate that stiff layers were generally deeper than 18 ft (except section 350801). It was suggested by Lei that if the stiff layer was below 18 ft, the effect of dynamics was not observed on the surface deflections.[96] Section 350801 was also included in the analyses because the depth of the stiff layer was close to the limit of 18 ft.

Table 23. Depths of stiff layer in each LTPP section estimated using Ullidtz's method.

State Code	Section	Depth of Stiff Layer From Surface (ft)			
		Drop 1	Drop 2	Drop 3	Drop 4
1	0101	86.9	32.7	109.8	26.6
6	A805	70.4	No stiff layer	No stiff layer	No stiff layer
6	A806	No stiff layer	No stiff layer	No stiff layer	No stiff layer
30	0113	96.4	45.3	49.9	35.6
34	0801	38.7	38.9	37.9	38.4
34	0802	No stiff layer	No stiff layer	284.5	63.8
35	0801	15.5	15.6	15.5	15.2
35	0802	No stiff layer	No stiff layer	No stiff layer	No stiff layer
46	0804	232.2	183.1	61.2	31.6

Section properties used for elastic and viscoelastic backcalculations were the same (see table 20) except that the modulus of the AC layer in the elastic backcalculation was assumed constant (modulus unknown). For elastic backcalculation, an in-house genetic algorithm was developed. The Poisson's ratio for AC, granular base, and subgrade layers were assumed to be 0.3, 0.4, and 0.45, respectively. As noted above, the results obtained from elastic backcalculation were used to

define bounds for base and subgrade moduli in BACKLAVAP. Table 24 shows the elastic backcalculation results obtained using data from each FWD drop. With the exception of section 350802, the static backcalculated base modulus values varied between 8,425 psi and 64,479 psi, and the subgrade modulus values varied between 16,142 psi and 42,615 psi.

Table 24. Elastic backcalculation results for LTPP sections.

State Code	Section	Drop 1 (psi)		Drop 2 (psi)		Drop 3 (psi)		Drop 4 (psi)	
		E_{base}	$E_{subgrade}$	E_{base}	$E_{subgrade}$	E_{base}	$E_{subgrade}$	E_{base}	$E_{subgrade}$
1	0101	34,129	46,835	29,941	45,478	36,065	42,122	22,264	42,615
6	A805	44,302	19,612	44,985	19,533	44,176	19,707	64,479	19,599
6	A806	32,252	23,219	29,063	23,281	34,932	22,511	43,687	22,636
30	0113	10,908	26,856	10,030	26,754	9,617	27,328	8,425	27,690
34	0801	19,853	20,918	19,446	21,150	26,287	21,392	26,063	22,062
34	0802	59,182	43,534	51,674	42,828	53,932	43,013	56,114	42,112
35	0801	25,508	23,061	20,762	22,567	20,995	21,738	22,113	21,649
35	0802	83,664	35,574	74,723	34,993	83,675	34,619	84,015	34,552
46	0804	19,699	16,142	23,137	16,207	18,359	16,282	13,676	16,545

Next, the viscoelastic backcalculation was performed. The backcalculated unbound layer moduli for the sections obtained from viscoelastic backcalculation are presented in table 25. For the viscoelastic backcalculation, the GA algorithm in BACKLAVAP used 300 populations in each of the 15 generations, except for sections 10101 and 350801, where a 400 population and 15 generations were used. However, Note that, for backcalculation, the search approximately converged after 10 generation for 300 populations. As shown in table 25, with the exception of section 350802, the static backcalculated base modulus values varied between 10,292 and 64,466 psi, and the subgrade modulus values varied between 17,114 and 44,906 psi. Comparing table 24 and table 25, it can be seen that the elastic and viscoelastic backcalculation predict similar modulus values for the unbound layers.

Table 25. Viscoelastic backcalculation results for LTPP sections.

State Code	Section	Drop 1 (psi)		Drop 2 (psi)		Drop 3 (psi)		Drop 4 (psi)	
		E_{base}	$E_{subgrade}$	E_{base}	$E_{subgrade}$	E_{base}	$E_{subgrade}$	E_{base}	$E_{subgrade}$
1	0101	28,799	44,906	26,431	44,035	28,026	42,682	25,621	41,470
6	A805	44,377	17,523	44,929	17,114	44,928	18,234	43,871	18,436
6	A806	26,977	21,273	24,441	20,724	28,809	20,903	29,150	22,615
30	0113	10,491	24,972	10,292	26,127	10,391	26,253	11,257	26,254
34	0801	22,337	20,569	20,282	19,901	18,243	20,569	14,824	22,710
34	0802	64,466	41,648	61,782	38,700	62,967	40,227	48,242	42,904
35	0801	22,337	20,569	20,282	19,901	18,243	20,569	14,824	22,710
35	0802	84,339	37,787	84,338	33,631	84,339	32,521	84,825	32,653
46	0804	26,191	14,746	17,922	14,827	15,427	15,125	12,575	16,373

Figure 116 shows example backcalculated (and measured) deflection time histories for sections 10101 and 350801, where section 10101 exhibited a better match than section 350801. This was attributed to the stiff layer being close to the 18-ft limit in section 350801.

To validate the backcalculated results, creep compliance data available in the LTPP database were converted into relaxation modulus $E(t)$. Creep data were available in tabulated form at three temperatures—14, 41, and 77 °F—and seven different times—1, 2, 5, 10, 20, 50, and 100 s. Assuming the classical power law function for the creep compliance (figure 117), the available data were fitted separately to each temperature.
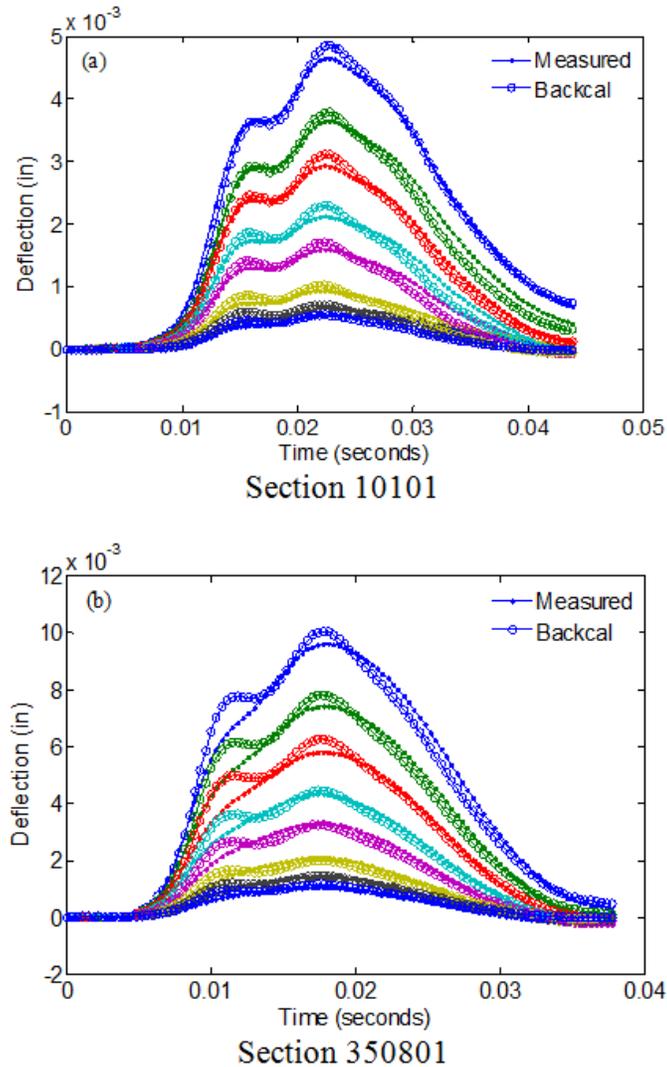
Figure 116. Graphs. Backcalculated and measured deflection time histories for LTPP sections 10101 and 350801.

$$D(t) = D_1 t^n$$

Figure 117. Equation. Creep compliance power law.

The associated relaxation modulus was then obtained using the mathematically exact formula given in figure 118.[85]

112

$$E(t)D(T) = \frac{\sin n\pi}{n\pi}$$

Figure 118. Equation. Relaxation modulus and creep compliance relationship.

Where D_1 and n are the power function coefficients of $D(t)$. The discrete relaxation modulus functions were then shifted to obtain a relaxation modulus master curve. Two different relaxation master curves were calculated. The first relaxation modulus master curve approximation was obtained when the time-temperature shift factors determined from the measured creep data were used to develop the relaxation master curve (labeled as "Measured 1"). The second relaxation modulus master curve approximation was obtained when the time-temperature shift factors determined from backcalculation were used to develop the relaxation master curve (labeled as "Measured 2"). This was done because laboratory creep compliance tests are usually not reliable in determining time-temperature superposition properties because a perfect stress-step function is very difficult to achieve in the laboratory and also because the results are contaminated with viscoplasticity, especially at the high temperatures and long creep times. Finally, for comparison, dynamic modulus and phase angle master curves were calculated from the relaxation modulus via interconversion.[65] For further verification, the estimated dynamic modulus obtained from ANN-based model ANNACAP was also compared. In the present work, all the estimated dynamic modulus master curve and time-temperature shift factors obtained from ANNACAP were based on the M_R model in ANNACAP.[97] From the results, it was found that the dynamic modulus curves estimated using the ANNACAP model, especially at higher frequencies, agreed well with the dynamic modulus curves obtained through interconverted creep data. Backcalculated $E(t)$ and $a_T(T)$ for the sections are shown in figure 119 to figure 127, and backcalculated dynamic modulus and phase angle are shown in figure 128 to figure 136. It can be seen from the figures that in general, the independent test drops within each section resulted in very similar predicted curves. Note that each FWD drop had a different load level and load history. Although the results were encouraging, backcalculated curves for sections 06A806, 350801, and 350802 showed noticeable disagreement with values derived from creep. However, although the dynamic modulus master curve predicted by ANNACAP matched well at the higher frequencies, it typically predicted higher values at reduced frequencies of less than 10^{-2} Hz.

Relaxation modulus   Shift factor
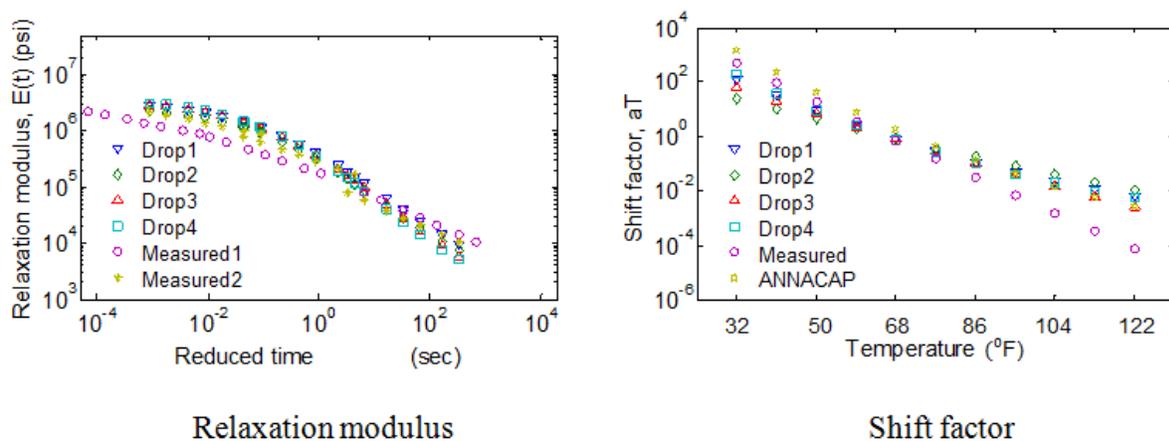
Figure 119. Graphs. Comparison of measured and backcalculated $E(t)$ and $aT(T)$ for LTPP section 10101.
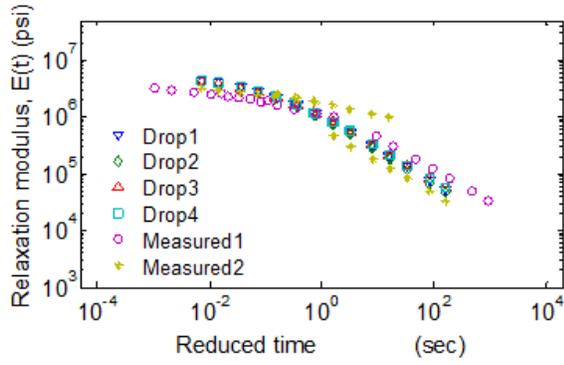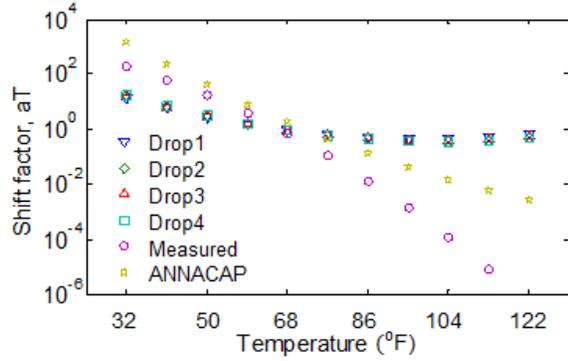
Relaxation modulus   Shift factor

Figure 120. Graphs. Comparison of measured and backcalculated $E(t)$ and $aT(T)$ for LTPP section 6A805.
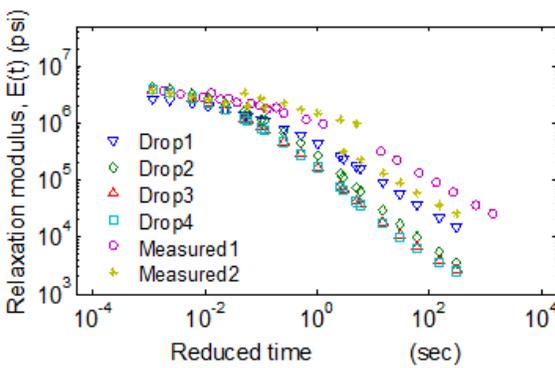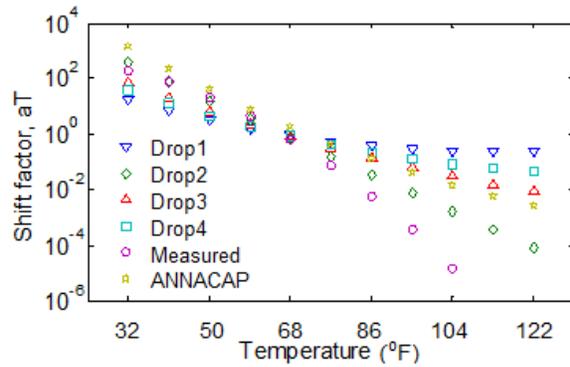
Relaxation modulus   Shift factor

Figure 121. Graphs. Comparison of measured and backcalculated $E(t)$ and $aT(T)$ for LTPP section 06A806.
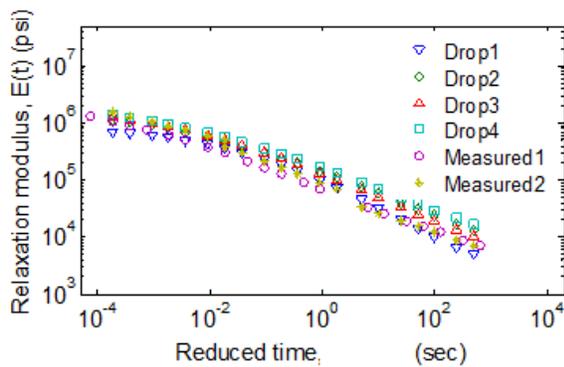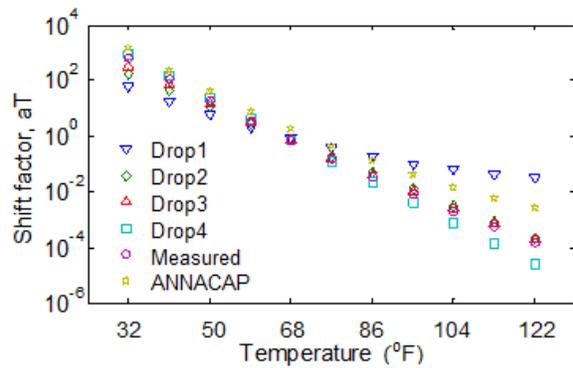
Relaxation modulus   Shift factor

Figure 122. Graphs. Comparison of measured and backcalculated $E(t)$ and $aT(T)$ for LTPP section 300113.

114
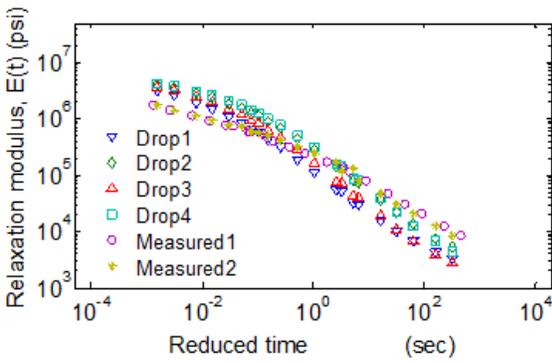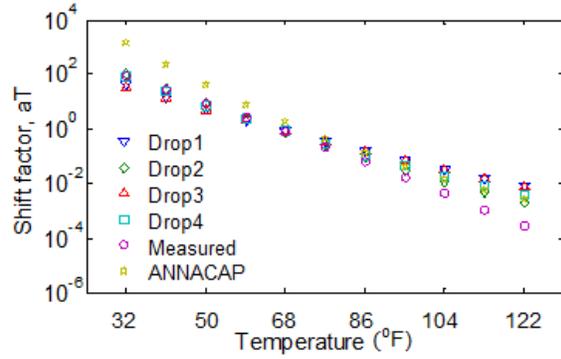
Figure 123. Graphs. Comparison of measured and backcalculated *E*(*t*) and *aT*(*T*) for LTPP section 340801.
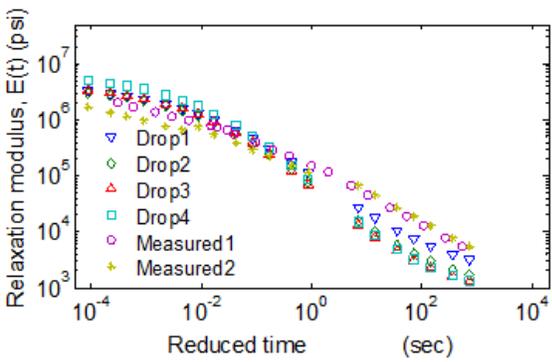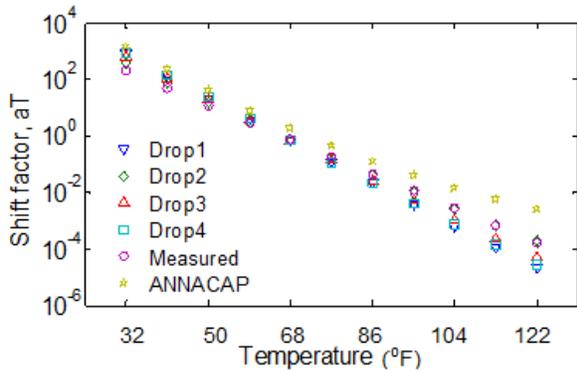
Figure 124. Graphs. Comparison of measured and backcalculated *E*(*t*) and *aT*(*T*) for LTPP section 340802.
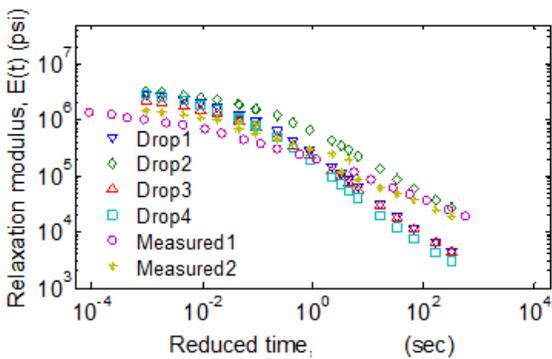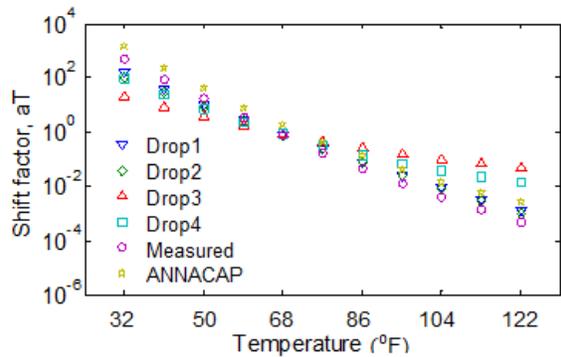
Figure 125. Graphs. Comparison of measured and backcalculated *E*(t) and *aT*(*T*) for LTPP section 350801.

115

Relaxation modulus   Shift factor
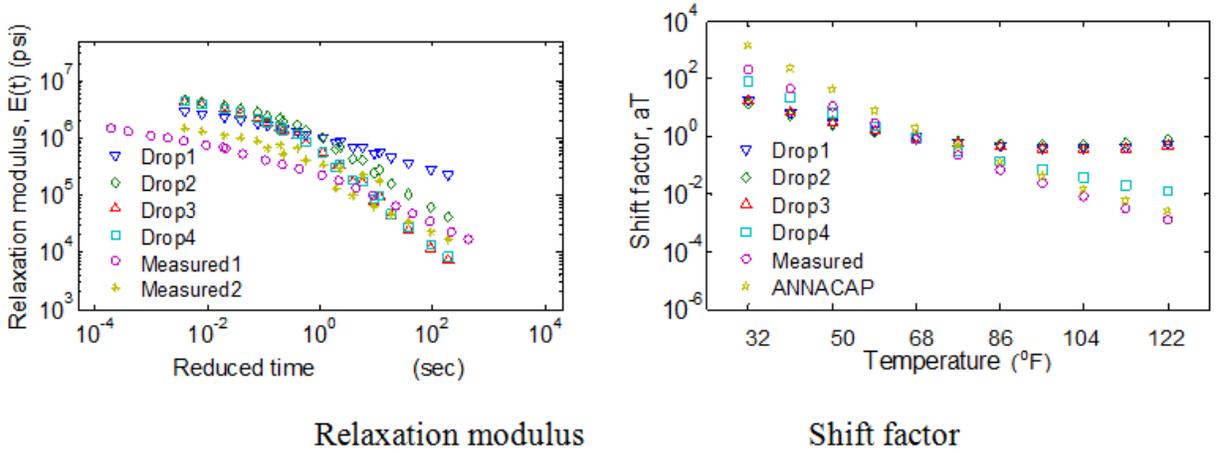
Figure 126. Graphs. Comparison of measured and backcalculated $E(t)$ and $aT(T)$ for LTPP **section 350802.**

Relaxation modulus   Shift factor
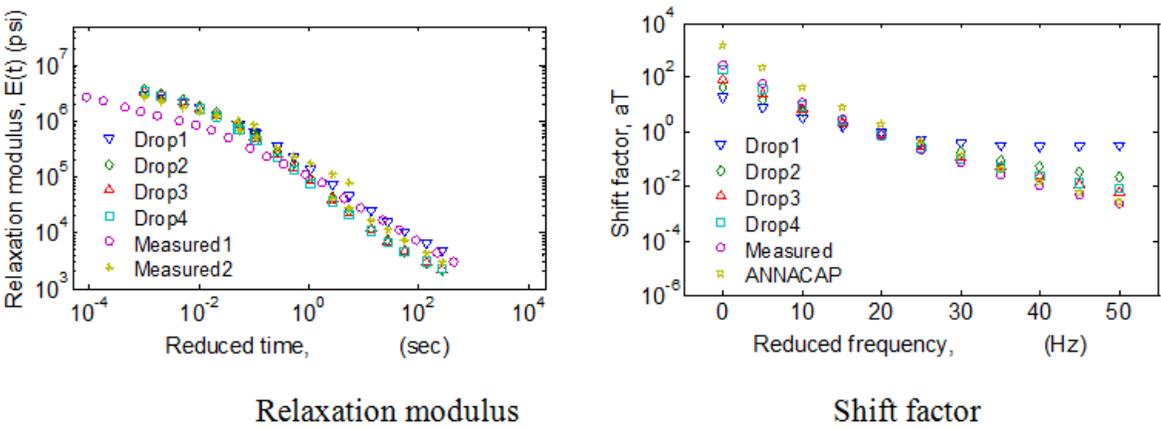
Figure 127. Graphs. Comparison of measured and backcalculated $E(t)$ and $aT(T)$ for LTPP **section 460804.**

Dynamic modulus   Phase angle
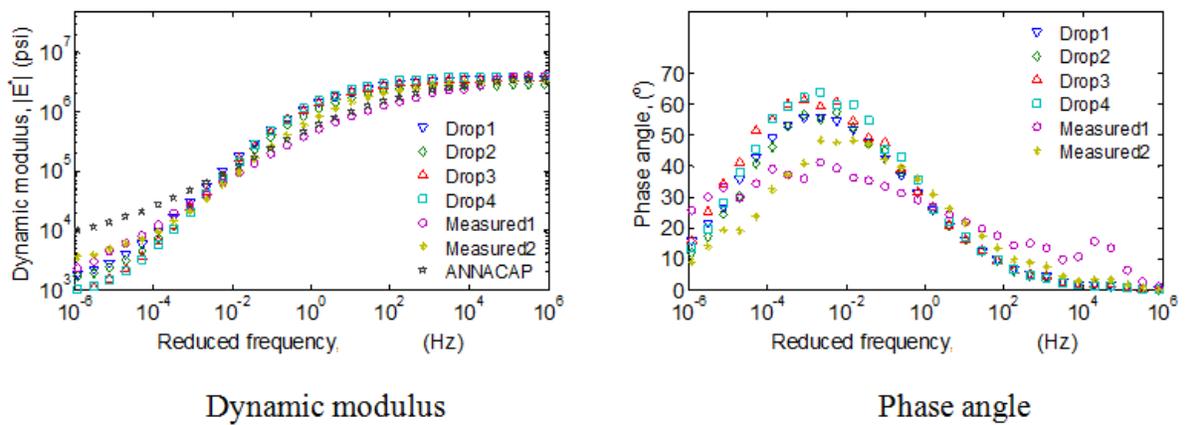
Figure 128. Graphs. Comparison of measured and backcalculated |$E*$| and phase angle for LTPP **section 10101.**

116
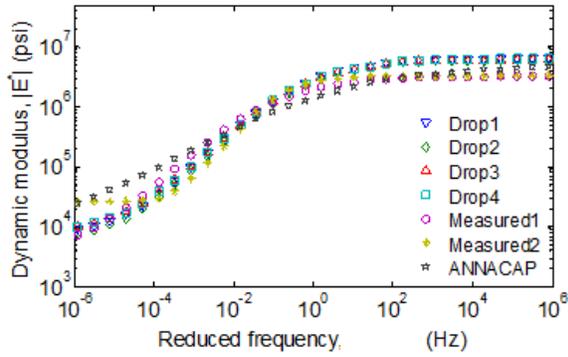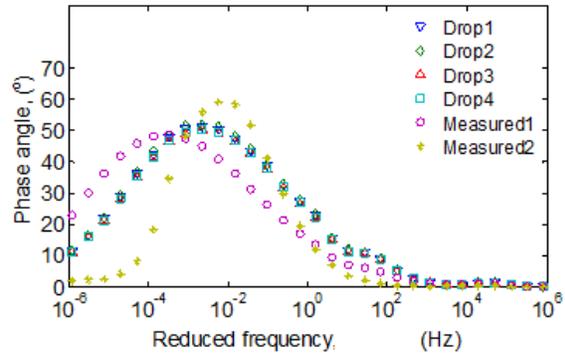
Dynamic modulus

Phase angle

Figure 129. Graphs. Comparison of measured and backcalculated |*E**| and phase angle for LTPP section 6A805.
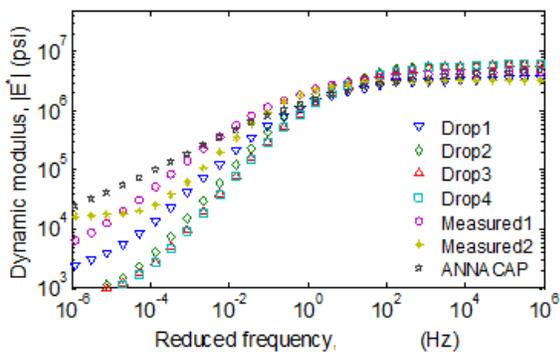
Dynamic modulus
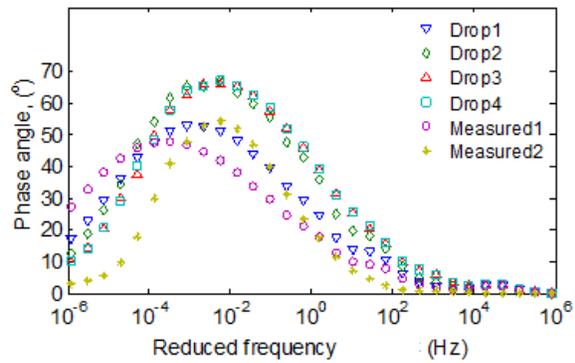
Phase angle

Figure 130. Graphs. Comparison of measured and backcalculated |*E**| and phase angle for LTPP section 6A806.
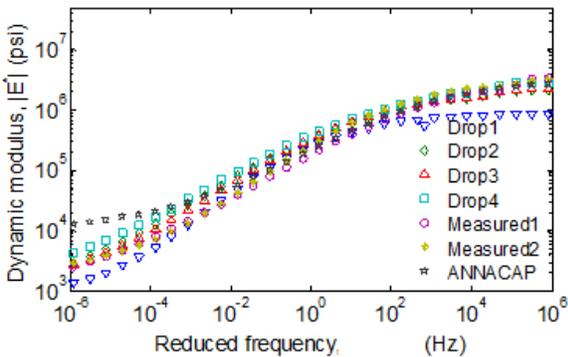
Dynamic modulus
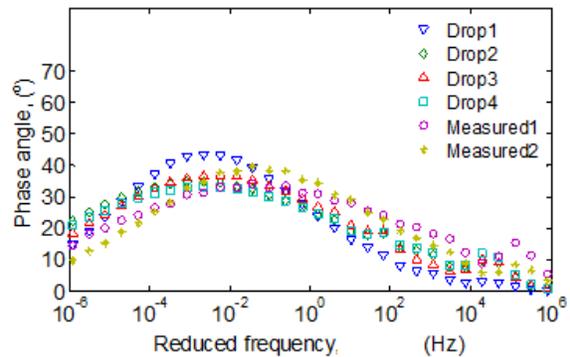
Phase angle

Figure 131. Graphs. Comparison of measured and backcalculated |*E**| and phase angle for LTPP section 300113.

117
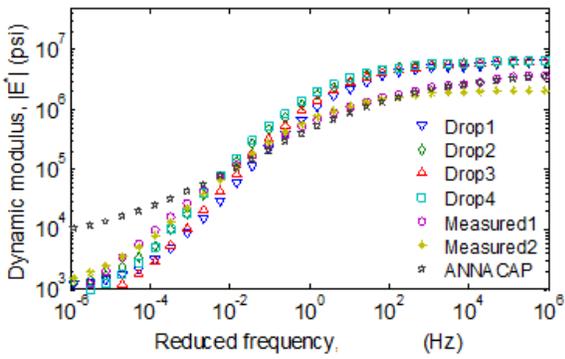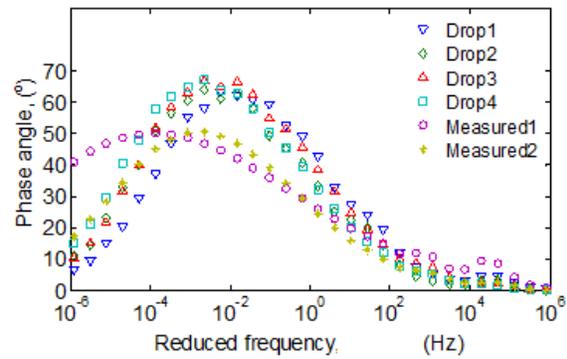
Figure 132. Graphs. Comparison of measured and backcalculated |*E**| and phase angle for LTPP section 340801.
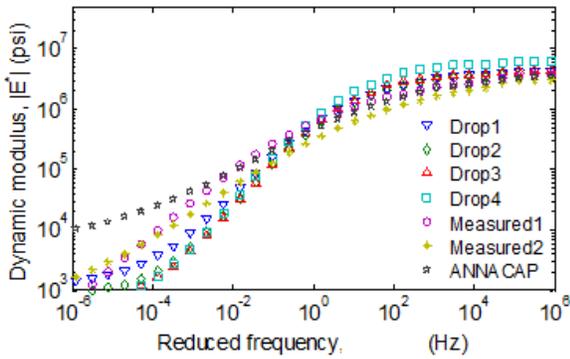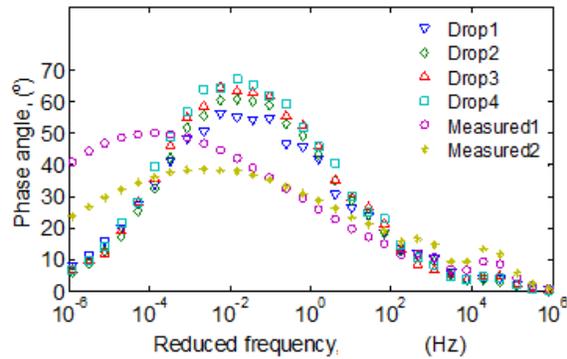
Figure 133. Graphs. Comparison of measured and backcalculated |*E**| and phase angle for LTPP section 340802.
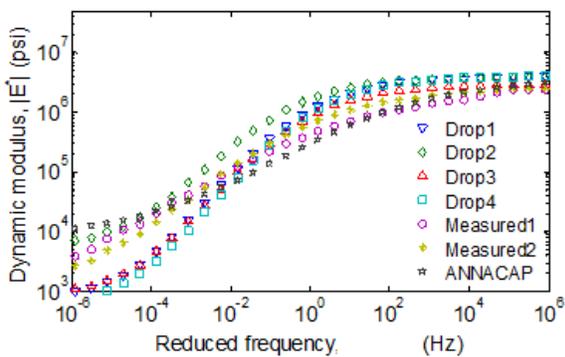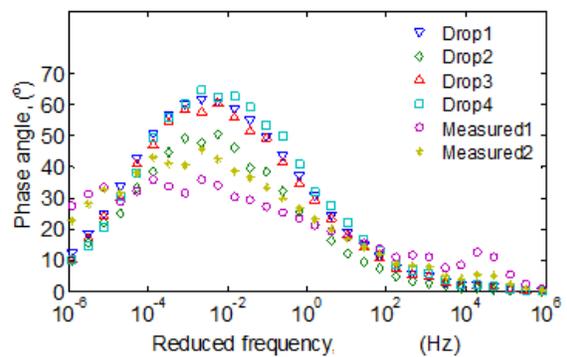
Figure 134. Graphs. Comparison of measured and backcalculated |*E**| and phase angle for LTPP section 350801.

Dynamic modulus   Phase angle
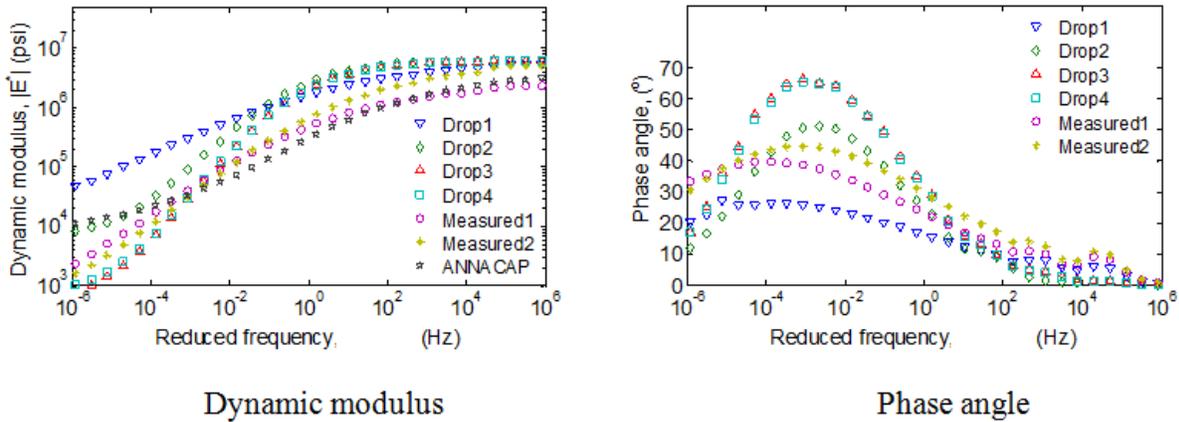
Figure 135. Graphs. Comparison of measured and backcalculated |E*| and phase angle for LTPP section 350802.

Dynamic modulus   Phase angle
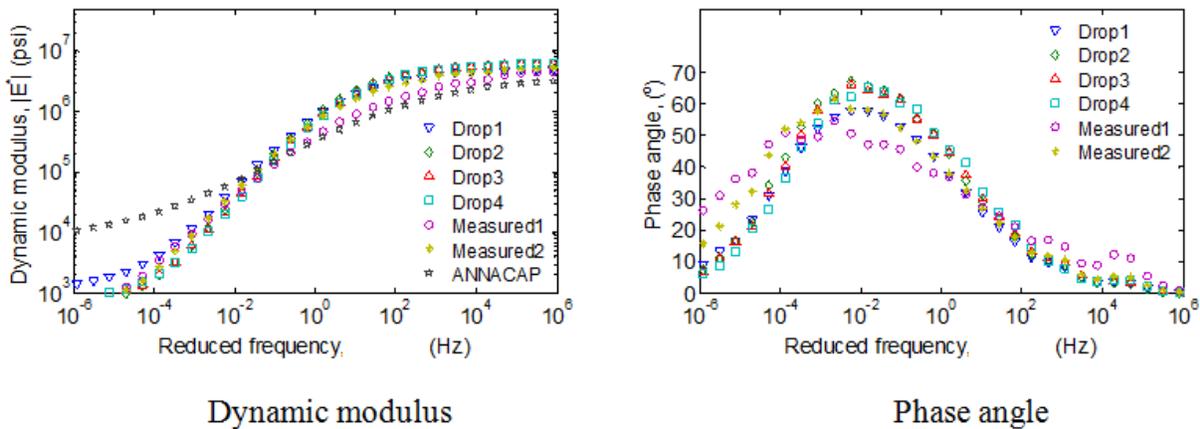
Figure 136. Graphs. Comparison of measured and backcalculated |E*| and phase angle for LTPP section 46804.

As shown in figure 119, for section 10101, the relaxation modulus master curves matched very well when the time-temperature shift factor obtained from backcalculation was used (to shift the discrete relaxation modulus functions obtained through LTPP creep data) to develop a measured master curve (labeled as "Measured 2" in figure 119 (left)). On the other hand, when the time-temperature shift factors were determined from the measured creep data to develop the relaxation master curve (labeled as "Measured 2" in figure 119 (left)), there was a change from the backcalculated curves. The backcalculated time-temperature shift factors were compared with creep and ANNACAP-computed results in figure 119 (right). It can be seen from the figure that the backcalculated time-temperature shift factor functions for all the drops showed a good match over the temperature range of 50 to 131 °F. As shown in figure 128 (left), the backcalculated and measured dynamic modulus curve obtained from Measured 2 also matched well over the entire frequency range. The backcalculated phase angles were compared with measured results in figure 128 (right). The phase angles showed some deviation at frequencies less than 10^{-2} Hz. This was further verified by the dynamic modulus master curve estimated using ANNACAP, which showed a good match over a reduced frequency greater than 10^{-2} Hz.

119

For section 6A805, the backcalculated relaxation modulus master curves were compared with those measured in figure 120 (left). As shown in the figure, a better match with the backcalculated curves was found when the time-temperature shift factor obtained from the measured creep data was used to develop the measured master curve (labeled as "Measured 1" in figure 120 (left)). On the other hand, when the time-temperature shift determined from the backcalculation data was used to develop the relaxation master curve (labeled as "Measured 2" in figure 120 (left)), there was a change from the backcalculated curves. This disagreement in the time-temperature shift can also be seen in the time-temperature shift factors in figure 120 (right) and dynamic modulus and phase angle curves in figure 129.

Relaxation modulus and time-temperature shift factor curves for section 6A806 were compared in figure 121 (left) and figure 121 (right), respectively. For this section, the measured relaxation modulus master curves predicted higher values compared with the backcalculated results, which increased with reduced time. Both the predicted $a_T(T)$ curved obtained from ANNACAP and backcalculation deviated from the measured results. From figure 130 (left) and figure 130 (right), it can be seen that the deviation in relaxation modulus values with time was reflected in dynamic modulus and phase angle curves at lower frequencies.

Relaxation modulus and time-temperature shift factor curves for section 06A806 were compared in figure 122 (left) and figure 122 (right), respectively. Although the predicted $a_T(T)$ curve at drop 1 for section 300113 showed some deviation after 86 °F, both the backcalculated $E(t)$ and $a_T(T)$ curves showed good agreement with laboratory results as well as ANNACAP data. Although the dynamic modulus predicted for drop 1 (see figure 131) showed lower values at frequencies greater than 10^2 Hz, an agreement in backcalculated relaxation modulus curves was also reflected in the dynamic modulus and phase angle curves.

Relaxation modulus and time-temperature shift factor curves for sections 340801 and 340802 were compared in figure 123 and figure 124, respectively. Although the predicted $E(t)$ curves for sections 340801 and 340802 showed some deviation at reduced time greater than 10 s, in general, the two curves showed good agreement with the measurement. Comparison of the backcalculated $a_T(T)$ curves for both sections 340801 and 340802 (see figure 123 (right) and figure 124 (right)) show a good agreement with ANNACAP and measured curves over the temperature range of 50 to 104 °F. Further, it can be seen from figure 132 and figure 133 that although the dynamic modulus and phase angle curves predicted by individual drops were the same, deviation at reduced time greater 10^1 s in relaxation modulus was reflected at frequencies greater than 10^{-1} Hz.

Figure 125 shows the backcalculated $E(t)$ and $a_T(T)$ functions for section 350801. Similar results were obtained using drops 1, 3, and 4, whereas $E(t)$ from drop 2 deviated from the other drops. The reason for this deviation may be the relatively low base modulus (20,241 psi) backcalculated using this drop, as seen in table 25. The average of base moduli in drops 1, 3, and 4 was 28,468 psi, which is about 40-percent higher than the above base modulus value of drop 2. As shown in figure 126 (left) and figure 126 (right), comparison of backcalculated $E(t)$ and $a_T(T)$ curves with measured and ANNACAP results for section 350802 showed complete disagreement. As shown in figure 135 (left) and figure 135 (right), similar discrepancies were reflected in the dynamic and phase angle curves.

For section 46804, the backcalculated relaxation modulus master curves were compared with measured results in figure 127 (left). It can be seen from the figure that the relaxation modulus master curves matched very well when the time-temperature shift factor obtained from backcalculation was used to develop the measured master curve (labeled as "Measured 2" in figure 127 (left)). On the other hand, when the time-temperature shift determined from the measured creep data was used to develop the relaxation master curve (labeled as "Measured 1" in figure 127 (left)), the backcalculated modulus values at reduced time less than 10^{-1} s were found to be low. Further, although the predicted $a_T(T)$ curve for drop 1 showed some deviation after 86 °F, the curves showed good agreement with laboratory as well as ANNACAP data. A comparison of backcalculated and measured dynamic modulus and phase angle for section 460804 is shown in figure 136 (left) and figure 136 (right), respectively. Dynamic modulus values predicted using backcalculation were higher at frequencies greater than 1 Hz, and a better prediction was observed with a frequency greater than 1 Hz.

Note that although measured creep data were used for comparison in the present study, it is not clear from the LTPP database whether $D(t)$ was measured before or after the FWD tests were conducted.

Backcalculation of Linear Viscoelastic Pavement Properties Using Two-Stage Method

In the previous backcalculation process, viscoelastic and unbound properties were calculated during the same step; however, in this section, a two-stage linear viscoelastic backcalculation scheme is presented. The first stage was to perform linear elastic backcalculation of unbound material properties, which was followed by linear viscoelastic backcalculation (using BACKLAVA/BACKLAVAP) of AC layer viscoelastic properties ($E(t)$ sigmoid coefficients c_1, c_2, c_3, and c_4 and shift factor $a_T(T)$ coefficients a_1 and a_2). Details of stage 1 and stage 2 steps are presented in the following sections.

Stage 1: Elastic Backcalculation for Unbound Layer Properties

It is important to verify that the elastic backcalculation (stage 1) gives unbound granular modulus values close to the actual values. If this is verified, the backcalculated $E_{unbound}$ values can be fixed in viscoelastic backcalculation (stage 2) and only the six unknowns of the AC layer can be backcalculated. Known and unknown variables in the first and second stages of backcalculation are listed in table 26. In stage 1, elastic backcalculation was performed assuming the AC layer was linear elastic. In the stage 2, viscoelastic backcalculation was performed keeping the unbound granular layer modulus values obtained in the first stage fixed.

To perform the verification, first, various synthetic deflection time histories were obtained by running LAVA on the structure shown in table 27 at various temperature profiles (also shown in table 27). These synthetic deflections were used in stage 1, which computed $E_{unbound}$ values. Then these backcalculated $E_{unbound}$ values were compared with the original $E_{unbound}$ values used in the original layered viscoelastic forward computation.

Table 26. Variables in two-stage linear viscoelastic backcalculation analysis.

Stage	Known Parameters	Unknown (Backcalculated) Parameters
1	Thickness and Poisson's ratio of each layer	E_{ac}, elastic modulus of AC layer
	FWD parameters (contact radius, pressure, locations of the sensors, etc.)	$E_{unbound\,(i)}$, unbound layer moduli, $i = 1...N_L$, N_L = number of unbound layers
2	Thickness and Poisson's ratio of each layer and FWD parameters	$E(t)$ sigmoid coefficients: c_1, c_2, c_3, and c_4
	$E_{unbound\,(i)}$, unbound layer moduli backcalculated in stage 1	Shift factor $a_T(T)$ coefficients a_1 and a_2

Table 27. Pavement properties in two-stage linear viscoelastic backcalculation analysis.

Property	Values
Thickness (AC followed by granular layers) (inches)	6, 20, infinite
Poisson ratio {layer 1, 2, 3…}	0.35, 0.3, 0.45
$E_{unbound}$ {layer 2, 3…} (psi)	25,560, 11,450
$E(t)$ sigmoid coefficient {layer 1}	0.841, 3.54, 0.86, -0.515
$a_T(T)$ shift factor polynomial coefficients {layer 1}	4.42E-04, -1.32E-01
Total number of sensors	8
Sensor spacing from the center of load (inches)	0, 8, 12, 18, 24, 36, 48, 60
AC layer temperature profile {T1-T2} or {T1-T2-T3} (°F)	{50-32}, {59-50}, {68-50}, {68-59}, {77-68}, {86-68}, {86-77}, {95-86}, {59-50-141}, {68-59-50}, {77-68-59}, {86-77-68}, {95-86-77}, {104-95-86}

Figure 137 and figure 138 show the average base and subgrade modulus values obtained by elastic backcalculation of two- and three-step temperature profile, respectively. Error bars in the figures represent the standard deviation of 10 GA runs performed for each temperature set.
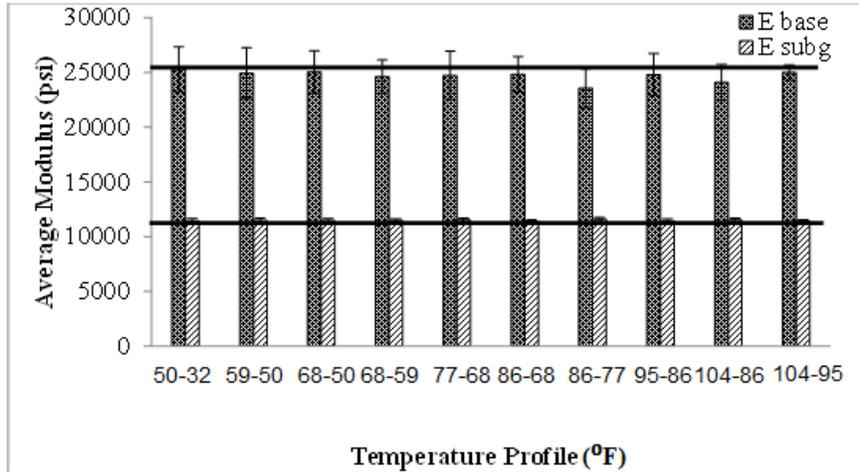
subg = subgrade.

Figure 137. Graph. Elastic backcalculation of two-step temperature profile FWD data, assuming AC as a single layer in two-stage backcalculation.
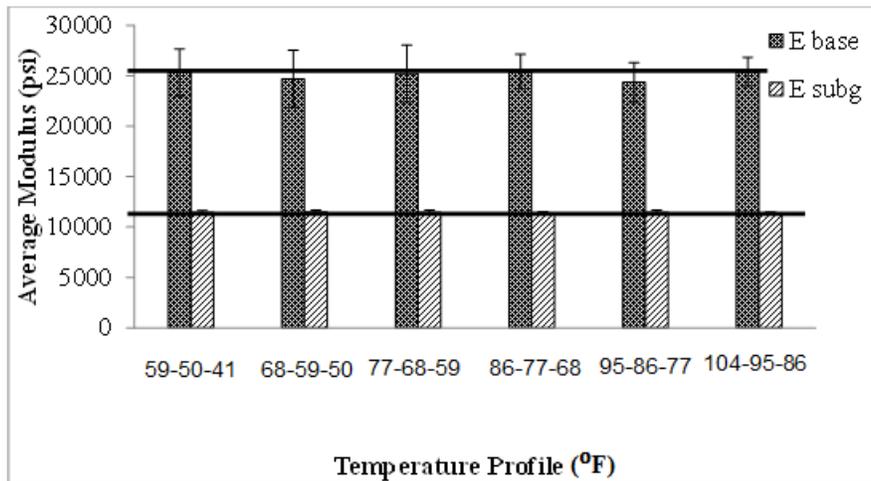
subg = subgrade.

Figure 138. Graph. Elastic backcalculation of three-step temperature profile FWD data, assuming AC as a single layer in two-stage backcalculation.

The analysis results shown in figure 137 and figure 138 were based on elastic backcalculations that assume a single AC layer. However, in the LAVA forward computations, because of different temperatures with depth, multiple layers of AC (two layers for Figure 137 and three layers for Figure 138 analysis) were used. To investigate whether selection of the number of AC layers affected the results for the elastic backcalculation, the computations were repeated assuming the AC layer consisted of two or three independent elastic layers. Average backcalculated base and subgrade modulus values for two-step and three-step temperature profiles are shown in figure 139 and figure 140, respectively. Comparing figure 137 with figure 139 and figure 138 with figure 140, it can be seen that assuming single or multiple AC layers did not significantly affect backcalculation of base and subgrade elastic modulus. From these analyses (figure 137 through

123

figure 140), it can be concluded that it is possible to first perform elastic backcalculation (stage 1) for the unbound layer properties and fix these in stage 2.
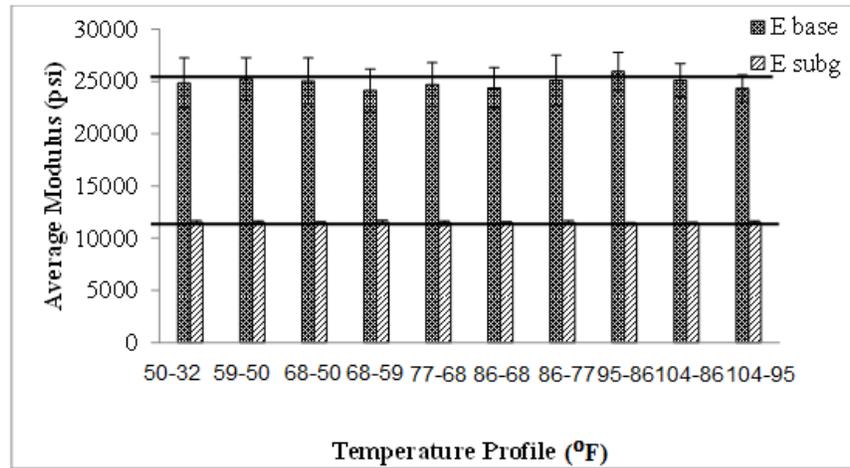
subg = subgrade.

Figure 139. Graph. Elastic backcalculation of two-step temperature profile FWD data, assuming two AC sublayers in two-stage backcalculation.
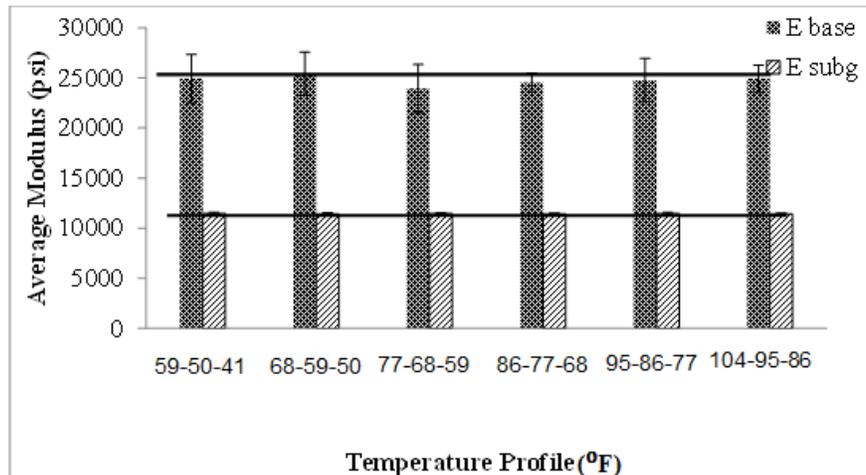
subg = subgrade.

Figure 140. Graph. Elastic backcalculation of three-step temperature profile FWD data, assuming three AC sublayers in two-stage backcalculation.

Stage 2: Viscoelastic Backcalculation for E(t) of AC Layer

After fixing the unbound layer modulus values, the AC layer properties ($E(t)$ sigmoid coefficients: c_1, c_2, c_3, and c_4 and shift factor $a_T(T)$ coefficients a_1 and a_2) were backcalculated using the viscoelastic backcalculation algorithm (BACKLAVA). Note that for viscoelastic backcalculation, as done earlier, a set of FWD test data at different temperature can be used for backcalculation. This is because even though the temperatures are different, the characteristic

properties of the AC layer ($E(t)$ or $|E^*|$ master curves) remain the same. In this stage, viscoelastic backcalculation was performed on a set of temperature profiles keeping the actual unbound modulus values constant.

Average errors (over reduced times from 10^{-8} to 10^8 s) in the $E(t)$ master curve, obtained from a set of two two-step and two three-step temperature profiles, are shown in figure 141 and figure 142, respectively. It can be observed from figure 141 that, for all the cases of the presented two-step temperature profile sets, average error in backcalculated $E(t)$ was below 10 to 12 percent except for the FWD test at {86-68} and {104-86} °F. It can be observed from figure 142 that, for all the cases presented for the three-step temperature profile sets, average error in backcalculated $E(t)$ was below 5.5 percent except for the FWD test at {86-77-68} and {77-68-59}°F. Subfigures in each of the figures were included to illustrate how the given percent error relates to the actual $E(t)$ curves that were being compared. These results indicate that the two-stage algorithm worked well in backcalculating the $E(t)$ of the AC layer. From figure 141 and figure 142, it can be observed that $E(t)$ errors obtained in the two-stage backcalculation are less when compared with single-stage backcalculation (figure 120). However, note that results presented in figure 141 and figure 142 are from backcalculation using a set of two FWD test data each obtained at different temperature profiles, whereas results in figure 120 are from backcalculation using single FWD datum. However, the result does indicate that backcalculation using a set of FWD test data each obtained under a different temperature profile may improve the accuracy.
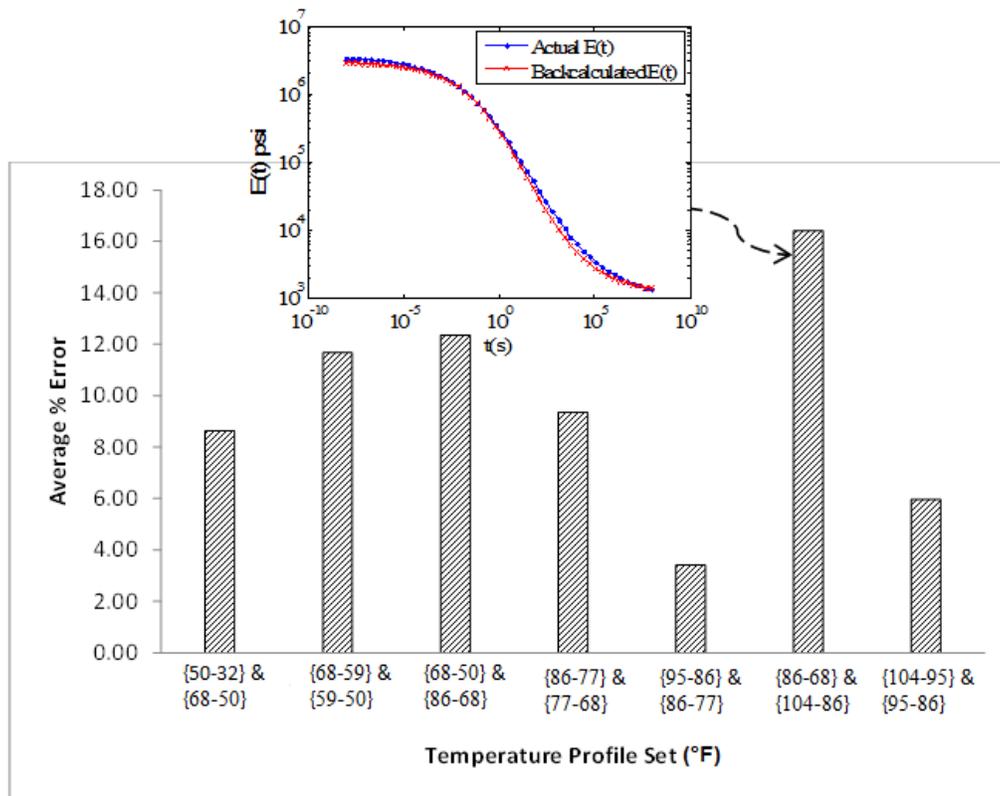
Figure 141. Graphs. Error in backcalculated $E(t)$ curve from two-step temperature profile FWD test data in two-stage backcalculation.
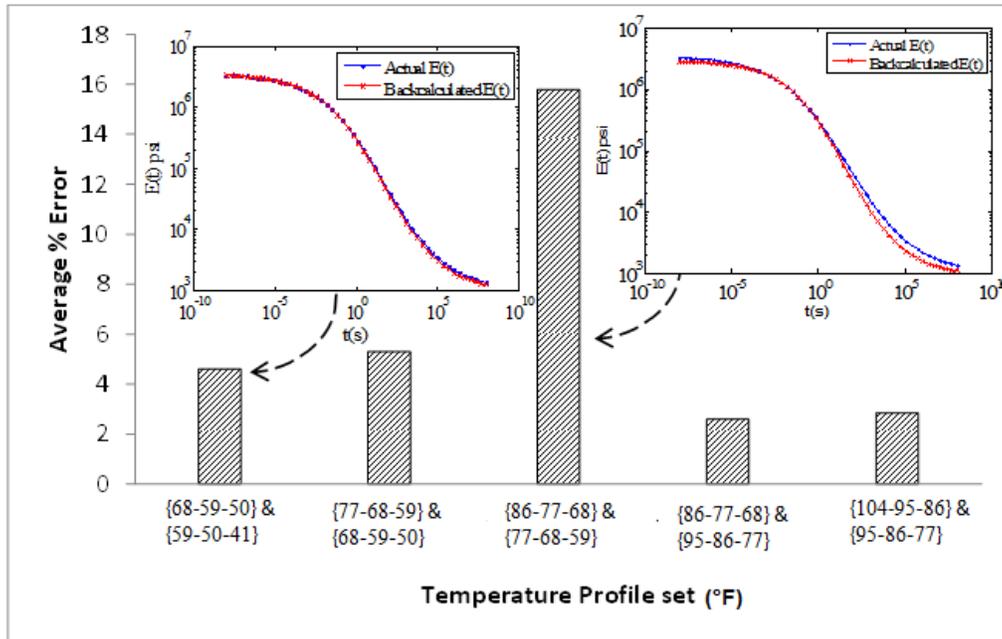
Figure 142. Graphs. Error in backcalculated *E*(*t*) curve from three-step temperature profile FWD test data in two-stage backcalculation.

DEVELOPMENT OF A BACKCALCULATION ALGORITHM TO DERIVE VISCOELASTIC PROPERTIES OF AC AND NONLINEAR PROPERTIES OF UNBOUND LAYERS

In the previous sections, the backcalculation scheme and results were developed for a viscoelastic multilayer pavement model consisting of a linear viscoelastic AC layer and linear elastic unbound layers. This section describes a backcalculation scheme (called BACKLAVAN) that was developed for the layered viscoelastic-nonlinear pavement model consisting of a linear viscoelastic AC layer and nonlinear elastic unbound layers. Because of computational limitations of the current version of the LAVAN algorithm, it can take a very long time to compute all the parameters (i.e., c_1, c_2, c_3, and c_4 of the AC and k_1, k_2, and k_3 of the unbound layer) during the backcalculation stage. Therefore, a two-stage backcalculation scheme was proposed to backcalculate viscoelastic as well as nonlinear unbound layer properties of the pavement layers. The two-stage nonlinear backcalculation model was very similar to the two-stage linear backcalculation model discussed in the earlier section. In the nonlinear model, the first stage involved nonlinear elastic backcalculation of the properties (i.e., k_1, k_2, and k_3) of the unbound granular layer. In the second stage, the backcalculated unbound properties (i.e., k_1, k_2, and k_3) were fixed, and the layered viscoelastic-nonlinear model (LAVAN) was used to backcalculate the linear viscoelastic properties of AC layer. Details of known and unknown properties used during these two stages are shown in table 28. Note that the current forward algorithm (LAVAN) can easily be extended to include the nonlinearity of subgrade layers. However, when such forward solution was used in a backcalculation algorithm, computational efficiency decreased significantly. Typically, the effect of surface stress in the subgrade was limited (stress "bulb" effect) and assumption of linear elastic subgrade, with increasing E (due to geostatic stress) with depth may be sufficient for most design purposes.

Table 28. Pavement properties and test inputs in two-stage nonlinear viscoelastic backcalculation.

Property	Stage 1: Nonlinear Elastic	Stage 2: Nonlinear Viscoelastic
Thickness (inches)	Known (AC), known (BASE), infinite (SUBGRADE)	Known (AC), Known (BASE), infinite (SUBGRADE)
Poisson ratio	Known (AC), known (BASE), known (SUBGRADE)	Known (AC), Known (BASE), Known (SUBGRADE)
E_{base} (psi)	Unknowns (k_1, k_2, k_3)	Obtained from stage 1
$E_{gsubgrade}$(psi)	Unknown	Obtained from stage 1
$E(t)_{AC}$ (psi)	Unknown ($E(t)$ = constant)	Unknown (sigmoid coefficient)
Test Inputs		
Surface loading (psi)	Known peak stress	Known load history
Surface deflection (inches)	Known peak deflection	Known deflection history

The algorithm was used to backcalculate two HMA mixes, namely, Control and CRTB (for mix properties, refer to table 29), on a 35-ms haversine load (synthetic FWD pulse load). The section properties were as shown in table 29. Stresses at distance $r = 0$ (center of loading) and layer mid-depth were used in calculating unbound base modulus value for both forward calculation and backcalculation of synthetic data.

Table 29. Pavement geometric and material properties in two-stage nonlinear viscoelastic backcalculation.

Property	Value
Thickness (inches)	5.9 (AC), 9.84 (base), infinite (subgrade)
Poisson ratio (v)	0.35 (AC), 0.4 (base), 0.4 (subgrade)
Density (pci)	0.0752 (AC), 0.0752 (base), 0.0752 (subgrade)
Nonlinear E_{base} (psi)	K_o = 0.6; k_1 = 3,626; k_2 = 0.5; k_3 = -0.5
$E_{subgrade}$ (psi)	10,000
AC: $E(t)$ sigmoid coefficient (psi) (c_i)	Control: 1.598, 2.937, -0.272, -0.562 CRTB: 0.895, 3.411, 0.634, -0.428
Shift factor coefficients (a_i)	Control: 5.74E-04, -1.55E-01 CRTB: 4.42E-04, -1.32E-01
Haversine stress 35 ms (psi)	Peak stress = 137.79 psi
Sensor spacing from the center of load (inches): 0, 8, 12, 18, 24, 36, 48, 60	

Stage 1: Nonlinear Elastic Backcalculation

Nonlinear elastic model is based on the assumption that the structure is time independent, with the AC layer assumed to be elastic and the unbound base layer assumed to be a stress-dependent nonlinear material. Each FWD test was generally composed of four independent test drops, where each drop corresponded to a different stress level. Typical ranges of stress levels in each drop are shown in table 30.

Table 30. Typical FWD test load levels.

Load Level	Allowable Range for 11.81-inch Diameter Plate (psi)	Used Surface Load (psi)
Drop 1	49–60	55
Drop 2	74–96	80
Drop 3	99–120	110
Drop 4	132–161	137.8

In stage 1, peak stress and deflection values during all the test drops (drop 1 through 4) were used as input. Peak stress values in each drop (drops 1 through 4) for synthetic haversine FWD loading used in the present analysis were 55, 80, 110, and 138 psi, respectively (refer to table 30). The AC layer modulus and unbound layer properties (k_1, k_2, and k_3) backcalculated from synthetic deflection at different temperatures are shown in figure 143 and figure 144, respectively.
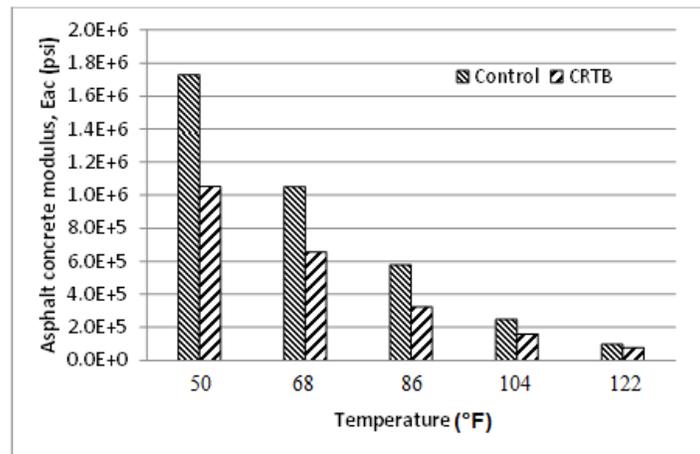
Figure 143. Graph. Nonlinear elastic backcalculated AC modulus for control and CRTB mixes using FWD data at different test temperatures.
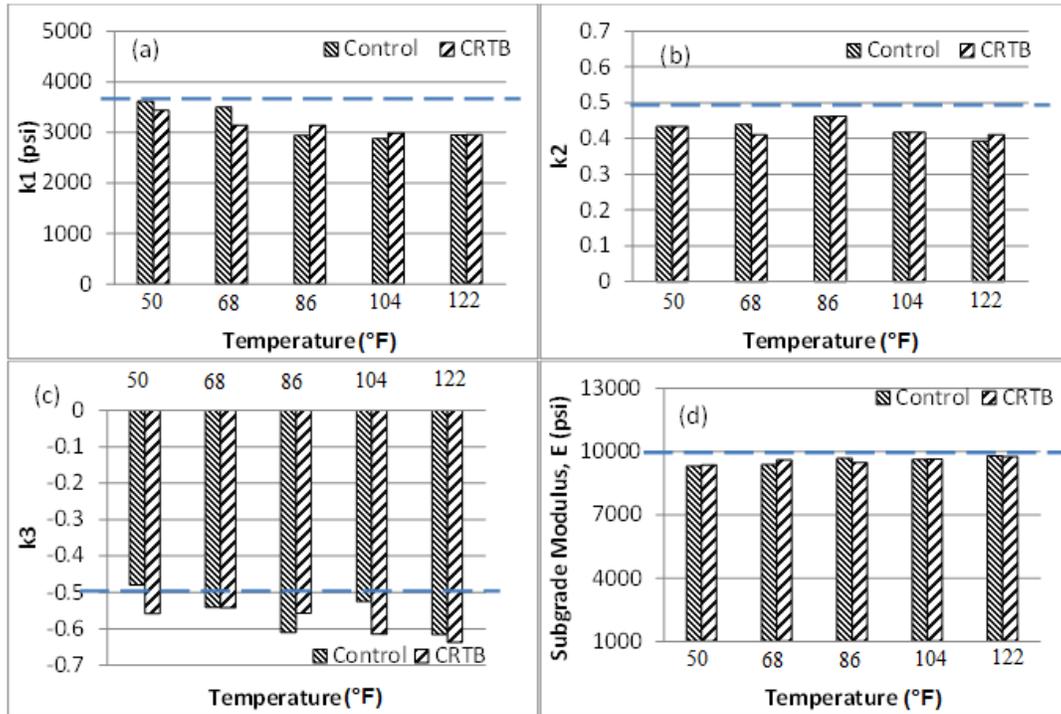
Figure 144. Graphs. Nonlinear elastic backcalculated unbound layer properties for control and CRTB mixes, using FWD data at different test temperatures.

As expected, for both control and CRTB mixes, the backcalculated elastic AC modulus values dropped with increase in temperature. Note that the forward solutions for the FWD surface deflections were computed using the LAVAN (layered viscoelastic-nonlinear) algorithm. The horizontal dashed lines in figure 144 show the actual inputs used in the LAVAN forward computation. As shown, the coefficients were close to the actual values but they were generally underpredicted by the backcalculation algorithm.

Stage 2: Nonlinear Viscoelastic Backcalculation

In stage 2, the backcalculated unbound layer properties from stage 1 were used as known fixed values, and the viscoelastic layer properties of the AC layer were obtained using viscoelastic-nonlinear backcalculation. The performance of the backcalculation algorithm was checked for the set of FWD data at temperatures ({50, 68}, {68, 86}, {86, 104}, {104, 122}°F) to determine the effect of different temperature ranges on the backcalculated $E(t)$ values. The backcalculated unbound layer properties obtained in stage 1 at each independent temperature were averaged when a set of temperatures was used in viscoelastic backcalculation. Average error in the backcalculated $E(t)$ master curve (refer to figure 145 and figure 146), (backcalculated in the second step) were calculated using figure 87. The error was calculated over four time ranges: (1) 10^{-5} to 10^{+1} s, (2) 10^{-5} to 10^{+2} s, (3) 10^{-5} to 10^{+3} s, (4) and 10^{-5} to 10^{+5} s. From figure 145 and figure 146, it can be seen that for lower temperatures, the backcalculated $E(t)$ master curve showed some deviation at higher reduced time, whereas, for higher temperatures, the backcalculated $E(t)$ master curve showed some deviation at lower reduced time. The

129

backcalculated results for the mixes showed good predictability of the $E(t)$ master curve using the two-stage nonlinear backcalculation scheme.
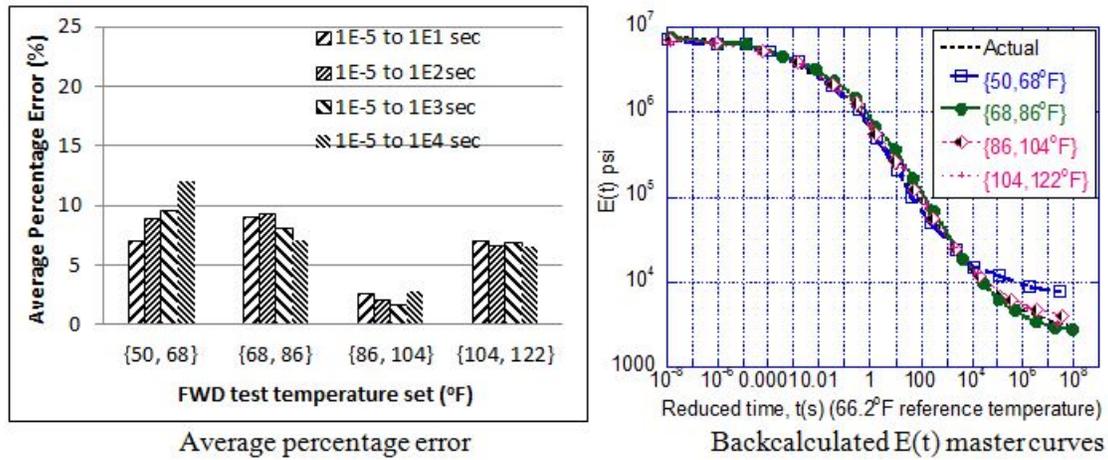
Figure 145. Graphs. Control mix backcalculation results from two-stage nonlinear viscoelastic backcalculation.
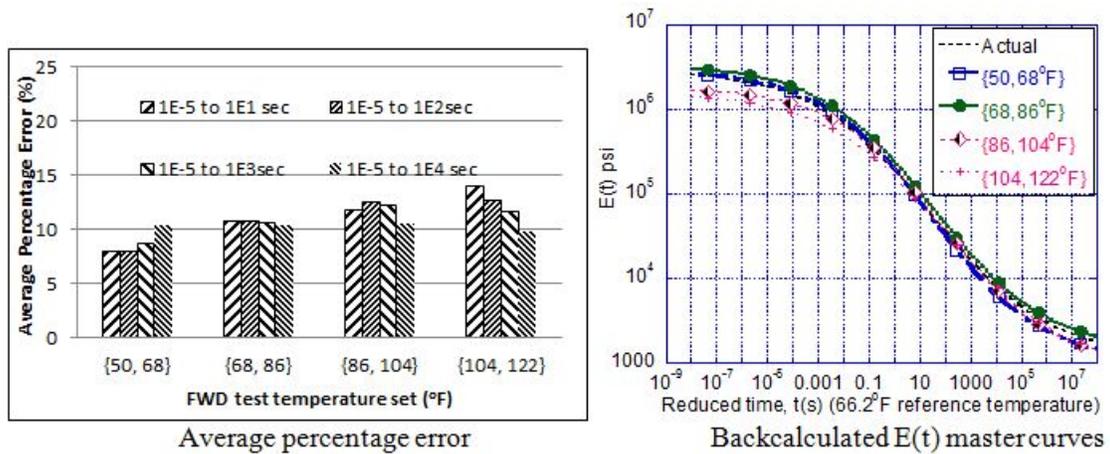
Figure 146. Graphs. CRTB mix backcalculation results from two-stage nonlinear viscoelastic backcalculation.

BACKCALCULATION OF LTPP SECTION USING TWO-STAGE NONLINEAR VISCOELASTIC BACKCALCULATION METHOD

The developed two-stage backcalculation algorithm was next used with field data to backcalculate the viscoelastic properties of the LTPP section 0101 from State 1 (Alabama). Section 10101 was tested consecutively in 2004–2005, with the two tests separated by more than 68 °F (refer to table 31 and table 32). Further, because the section was not modified between the two tests, it was selected for the analysis.

Table 31. FWD test data from LTPP section 10101 for 2004–2005.

Test Date	Drop Level	Peak Stress (psi)	Deflection (mil)						
2/23/2004	1	54.1	5.00	4.25	3.70	2.99	2.44	1.57	1.10
	2	83.5	8.11	6.93	6.10	4.92	4.06	2.56	1.81
	3	113.3	11.65	10.00	8.82	7.13	5.87	3.78	2.60
	4	148.7	16.14	13.90	12.17	9.92	8.19	5.24	3.62
4/28/2005	1	52.2	8.90	6.46	5.04	3.54	2.48	1.46	0.94
	2	80.2	13.98	10.47	8.50	5.83	4.17	2.40	1.73
	3	111.2	20.20	15.55	12.91	8.90	6.38	3.74	2.76
	4	139.1	26.06	20.28	16.93	11.81	8.39	4.84	3.50

Stage 1: Nonlinear Elastic Backcalculation

In stage 1, peak stress and deflection values during all the test drops in table 31 were used as inputs in nonlinear elastic backcalculation. The backcalculation results in table 32 show that the unbound base properties (k_1, k_2, and k_3) were found to be very close; it also shows that although the AC was affected by the temperature of the test, the effect on the unbound layer was not significant. As expected, the backcalculated elastic AC modulus values dropped with increase in temperature.

Table 32. Nonlinear elastic backcalculation results for LTPP section 10101.

Results		FWD Test Year	
		2004	2005
Average AC temperature (°F)		53.4	95.4
Properties	AC modulus (psi)	941,526	227,346
	k_1	17,984	15,972
	k_2	0.16	0.17
	k_3	-0.59	-0.58
	E_{subg}	29,832	26,097

Stage 2: Nonlinear Viscoelastic Backcalculation

Unbound layer material properties may vary depending on environmental factors (seasons). However, because the unbound layer properties obtained for the two tests in stage 1 were found to be very close, they were used in the second stage of the backcalculation without any correction. Stage 2 uses the nonlinear viscoelastic forward algorithm during backcalculation of the $E(t)$ of the AC layer. Note that viscoelastic backcalculation requires the entire time history for backcalculation. For the LTPP section test in year 2004, the entire deflection history was available only for drop 1, hence the backcalculation was performed using only drop 1. Figure 147 and figure 148 show results obtained by two independent backcalculation attempts using data from 2 years of field testing. As shown, a very good match was seen in $E(t)$, and a reasonable match was seen in the shift factor function. The measured viscoelastic properties in the figures were obtained using $D(t)$ data available in the LTPP database (refer to figure 117 and figure 118). As explained earlier (refer to figure 101 through figure 104), the dynamic modulus and phase angle master curve for the backcalculated $E(t)$ were calculated at 66 °F.

Relaxation modulus

Shift factor
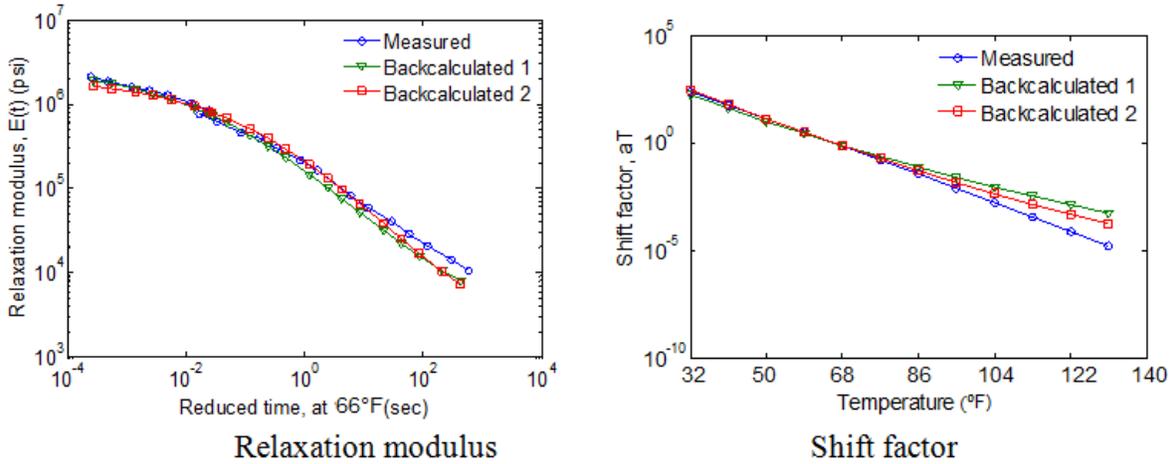
Figure 147. Graphs. Comparison of nonlinear viscoelastic backcalculated and measured $E(t)$ and $a_T(T)$ for LTPP section 10101.

Dynamic modulus
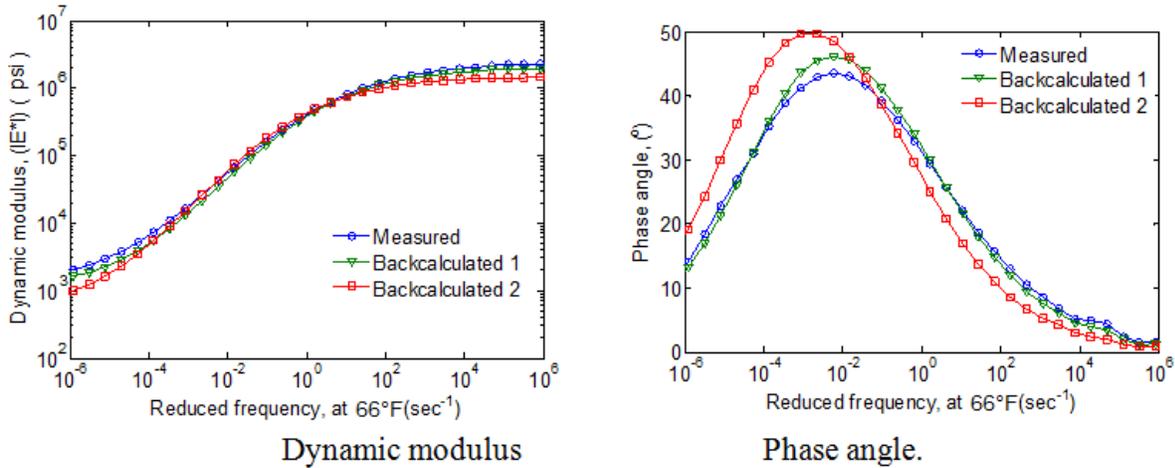
Phase angle.

Figure 148. Graphs. Comparison of nonlinear viscoelastic backcalculated and measured $|E^*|$ and phase angle for LTPP section 10101.

SUMMARY AND CONCLUSIONS

This chapter presented two methodologies for determining the $E(t)/|E^*|$ master curve and unbound material properties of in-service pavements. As part of this effort, two multilayered viscoelastic algorithms were developed. The first algorithm, called LAVA/LAVAP (LAVA can consider constant AC layer temperature, and LAVAP can consider a temperature profile for the AC layer), assumed the AC layer was a linear viscoelastic material and the unbound layers was linear elastic. The second algorithm (called LAVAN) also assumed the AC layer was a linear viscoelastic material; however, it can consider the nonlinear (stress-dependent) elastic moduli of the unbound layers. These two models were used to develop two genetic algorithm-based backcalculation algorithms (called BACKLAVA/BACKLAVAP for the linear model and BACKLAVAN for the nonlinear model) for determining $E(t)/|E^*|$ master curve of AC layers and unbound material properties of in-service pavements.

132

The following conclusions can be drawn regarding the FWD data collection:

- Careful collection of FWD deflection data is crucial. The accuracy of the deflection time history needs to be improved. As a minimum, a highly accurate deflection time history at least until the end of the load pulse duration is needed for $E(t)$ or $|E^*|$ master curve backcalculation. The longer the duration of the deflection time history, the better.

- The temperature of the AC layer needs to be collected during the FWD testing. Preferably, temperatures should be collected at every 2 inches of depth of the AC layer.

- Either a single FWD run on AC with a large temperature gradient or FWDs run at different temperatures can be sufficient to compute the $E(t)/|E^*|$ master curve of AC pavements.

- For backcalculation using multiple FWD test datasets, tests should be conducted at a minimum of two different temperatures, preferably 18 °F or more apart. FWD data collected at a set of temperatures between 68 and 104 °F will maximize the accuracy of the backcalculated $E(t)/|E^*|$ master curve up to less than a 10-percent error.

- For backcalculation using a single FWD test dataset at a known AC temperature profile, the FWD test should be conducted under a temperature variation of preferably ± 9 °F or more.

- An FWD configuration composed of multiple pulses (as presented in the appendix B) will improve the accuracy of the $E(t)$ master curve prediction. However, to obtain the time-temperature shift factor coefficients, either temperature variation with depth needs to be measured (and included in the analysis) or the FWD test (with multiple pulses) needs to be run at different pavement temperatures (e.g., different times of the day).

- Study of the effect of FWD sensor data on backcalculation indicates that the influence of unbound layer properties increases with incorporation of data from farther sensors and with increase in test temperature. Further, it can be concluded that all sensors in the standard FWD configuration are needed for accurate backcalculation of the viscoelastic AC layer and unbound layers.

The following conclusions can be drawn for the backcalculation procedure:

- Viscoelastic properties of AC layer can be obtained using a two-stage scheme. The first stage is an elastic backcalculation to determine unbound layer properties, which is followed by viscoelastic backcalculation of $E(t)$ of the AC layer while keeping the unbound layer properties fixed.

- The examples presented in this study show that, in the case of the presence of considerable dynamic effects, the algorithms (BACKLAVA/BACKLAVAP and BACKLAVAN) should be used with caution. The algorithms presented in this chapter predict the behavior of flexible pavement as a viscoelastic damped structure, assuming it to be massless.

- For the GA-based backcalculation procedures, the following population and generation sizes are recommended:

  o For the BACKLAVA model, use a set of FWD tests run at different (but constant) AC layer temperatures with a population size of 70 and 15 generations.

  o For the BACKLAVAP model, use a single FWD test with a known AC temperature profile and a population size of 300 and 15 generations.

  o For the BACKLAVAN (nonlinear) model, use FWD tests run at different (but constant) AC layer temperatures and a population size of 100 and 15 generations.

CHAPTER 5. DYNAMIC VISCOELASTIC TIME-DOMAIN ANALYSIS

The prevalence of dynamic conditions shown in the LTPP database, as discussed in chapter 3 and in the FWD tests conducted on Waverly Road (near Lansing, MI) as part of this project, emphasized the necessity of using a time-domain based dynamic solution that could also model the viscoelastic response of the HMA layer(s). A new forward dynamic viscoelastic time-domain solution was implemented based on the solution developed by Lee.[98] The new code was written in-house by the research team using the MATLAB® environment and coded for parallel processing to achieve better computational efficiency. This new version of the program is referred to as ViscoWave-II. In addition, a dynamic backcalculation program using ViscoWave-II as its forward engine was developed with GA as its search core. This was done to ensure uniqueness of the backcalculated solution from the search algorithm. This new dynamic backcalculation program with viscoelastic AC layers and damped elastic unbound layers is called DYNABACK-VE.

This chapter first describes in detail the mathematical development of the dynamic viscoelastic time-domain algorithm. It then presents the verification results for the developed algorithm by comparing the simulation results from the developed algorithm to some of the other existing solutions. Later, this chapter describes different backcalculation schemes using the new forward solution developed in this research. Finally, this chapter reports on the backcalculation algorithms tested using theoretically generated deflection time histories and field-measured FWD data collected as part of this project. Note that the current forward solution (ViscoWave-II) can be extended to include nonlinearity of unbound layers. However, when such a forward solution was used in the backcalculation algorithm, computational efficiency decreased significantly and became unreasonable. Therefore, although nonlinearity of unbound layers was considered in chapter 4, it was not investigated in the dynamic analysis for two reasons: (1) unreasonable computational time and (2) lack of development time.

NEW TIME-DOMAIN DYNAMIC (FORWARD) SOLUTION (VISCOWAVE-II)

The time-domain dynamic solution (ViscoWave) developed by Lee was selected as the forward solution.[98] The theoretical development for the proposed methodology followed steps similar to those of the spectral element method, which uses the discrete transforms for solving the wave equations.[2,40] However, the new solution used continuous integral transforms (namely Laplace and Hankel transforms) that were more appropriate for transient, nonperiodic signals in the time domain.[3] The new algorithm code was written in both MATLAB® and C++ and coded for serial and parallel processing with and without multithreading to achieve better computational efficiency. This new version of the program is referred to as ViscoWave-II. The new algorithm represents the master curve using Prony series of 14 elements, not including E_∞, instead of the power law used in ViscoWave. The algorithm also was changed so that it accepts the input of temperature profile along the viscoelastic layer. Appendix C describes in detail the mathematical development of the new algorithm.

Implementation and Preliminary Validation of Algorithm

The algorithm was first implemented in MATLAB® so that the computation would run serially. Then, to speed up the computations, two different parallelization schemes were coded and tested using: (1) a local cluster of 8 and 12 cores and (2) a cluster of 60 computers in the High Performance Computing Center (HPCC) network of Michigan State University using the Message Passing Interface (MPI). Subsequently, as is described later in this chapter, the code was rewritten in C++ to speed the computations even further.

The algorithm was used to simulate the behavior of elastic and viscoelastic structures subjected to an FWD loading. In addition, other available solutions were used to simulate the response of the same pavement structures for validation of the ViscoWave-II algorithm. The results of these numerical simulations and the preliminary validation efforts are presented. For viscoelastic simulation, the master curve was fitted using a Prony series of 14 elements, not including E_∞.

Simulation of an Elastic Pavement Structure

The properties of the pavement layers used for the elastic analysis are shown in table 33. The FWD loading was idealized to be a half-sine load distributed over a circular area of with a radius of 6 inches, a peak magnitude of 9,000 lb, and a duration of 26 ms. The surface deflections were calculated at radial distances of 0, 8, 12, 18, 24, 36, and 60 inches from the center of the loading plate.

To verify the results from ViscoWave-II, the elastic simulation was also conducted using the axisymmetric spectral element algorithm LAMDA, which was already verified through a comparison with the 3-D FEA solution.[2] A summary of the theory behind LAMDA is presented in chapter 2. The time histories for the resulting surface deflections are shown in figure 149. The figure indicates that ViscoWave-II and LAMDA showed almost identical results, validating the algorithm behind ViscoWave-II.

Table 33. Layer properties for elastic simulation using LAMDA and ViscoWave-II.

Layer	Elastic Modulus (ksi)	Poisson's Ratio	Thickness (inches)	Unit Weight (pcf)
Asphalt	145	0.35	6	145
Base	30	0.4	10	125
Subgrade	15	0.45	Infinity	100
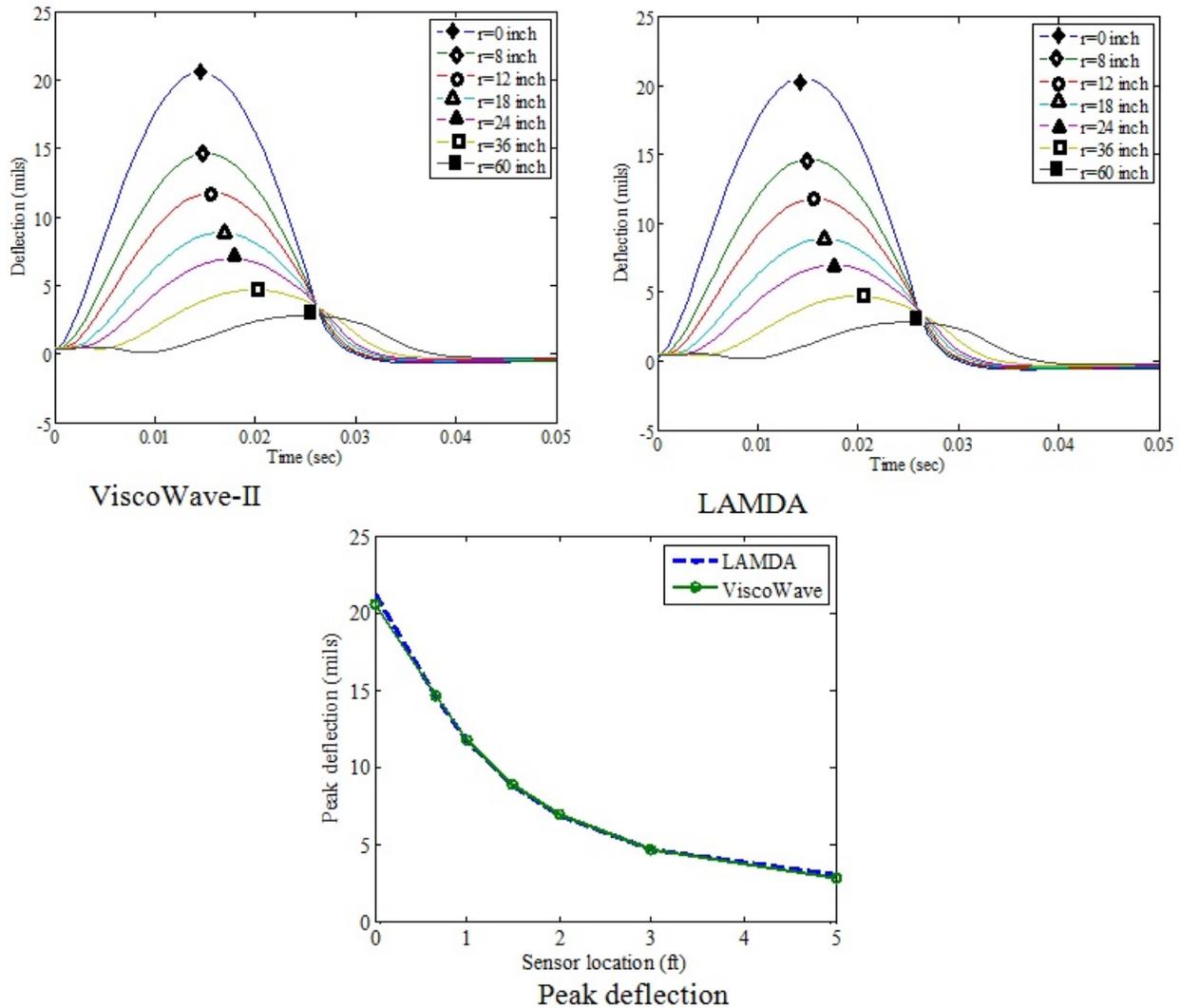
Figure 149. Graphs. Comparison of surface deflections of a layered elastic structure using ViscoWave-II and LAMDA.

Simulation of Viscoelastic Pavement Structures

The viscoelastic simulation was carried out for thin, medium, and thick pavement structures. The layer parameters considered/assumed are presented in table 34. The FWD loading used in this simulation is presented in figure 150, and it was assumed to be uniformly distributed over a circular area with a radius of 6 inches, a peak magnitude of 9,000 lb, and a duration of 35 ms. The surface deflections were calculated at radial distances of 0, 8, 12, 18, 24, 36, 48, 60, and 72 inches from the center of the loading plate. The viscoelasticity of the AC layer was modeled using a Prony series of the simulated master curve presented in figure 151. The results are shown in figure 152.

137

Table 34. Layer properties for viscoelastic simulation using ViscoWave-II.

Layer	Thickness (inches)	Modulus (ksi)	Poisson Ratio	Unit Weight (pcf)
AC (thin)	3	Master Curve	0.35	145
AC (medium)	6			
AC (thick)	10			
Base	15	25.0	0.40	125
Subgrade	Infinity	7.0	0.45	100
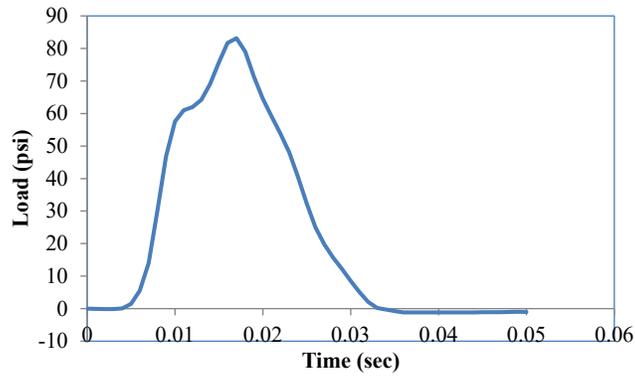
Figure 150. Graph. Simulated FWD load.
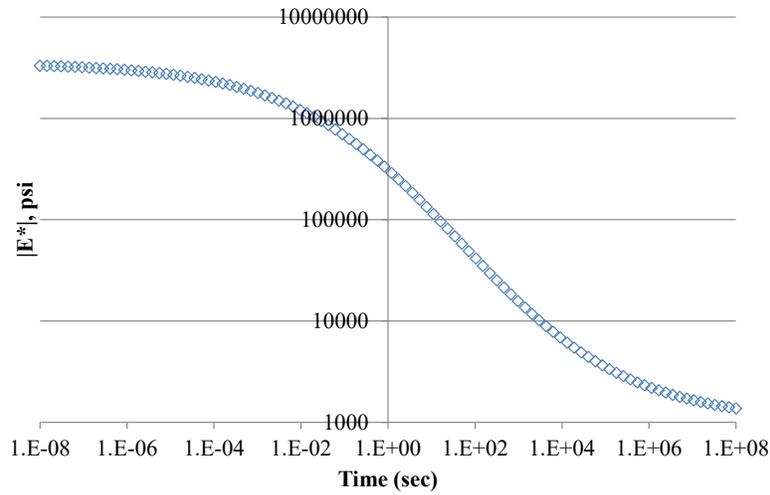
Figure 151. Graph. AC layer master curve for viscoelastic simulation.

138
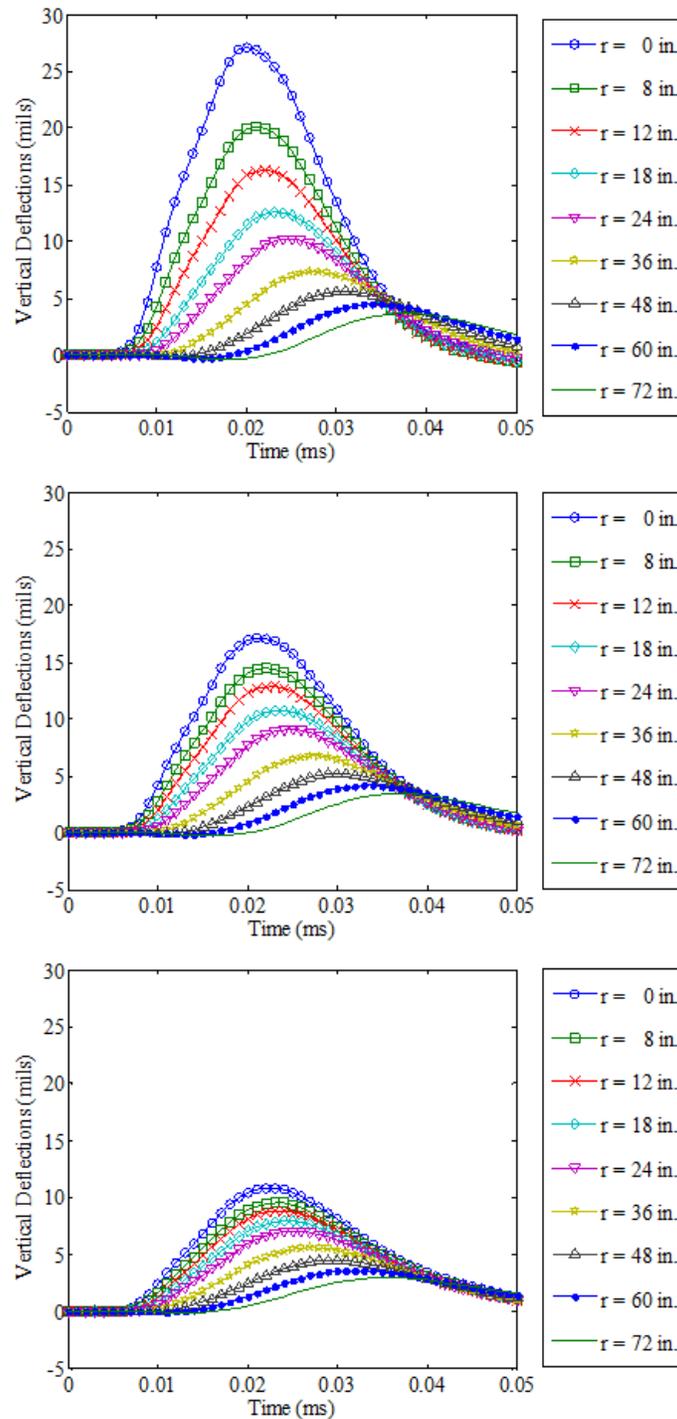
Figure 152. Graphs. Results from ViscoWave-II for viscoelastic simulations of thin (top), medium (middle), and thick (bottom)pavements.

Another viscoelastic simulation was carried out using the same pavement structure that was used for the previous elastic simulation (table 33) with a couple of exceptions. The viscoelasticity of the AC was modeled using two different creep compliance functions: one that represents

139

low-temperature behavior (figure 153 (left)) and the other representing high-temperature behavior in which the viscoelastic effects are more pronounced (figure 153 (right)). In addition, for each of the creep compliance functions shown in figure 153, the subgrade layer was first modeled to be a half-space (infinite thickness) and then with a shallow bedrock (infinite stiffness) located 10 ft below the pavement surface (figure 154). To verify the results of the viscoelastic simulation from ViscoWave-II, a commercially available FEA package, ADINA, was used to simulate the dynamic response of the viscoelastic pavement subjected to the FWD loading. Figure 155 shows the geometry and the FEA mesh that was used for the analysis. The simulations using ADINA were reported by Lee.[98] Although the elements in ViscoWave-II assumed that the elements extend to infinity in the horizontal direction and also in the vertical direction for the one-noded element, the FEA simulation was inevitably conducted with a finite geometry. More specifically, the FEA model only extended to 20 ft in the horizontal direction and 41.3 ft in the vertical direction for the simulation of the half-space (figure 155 (top)).
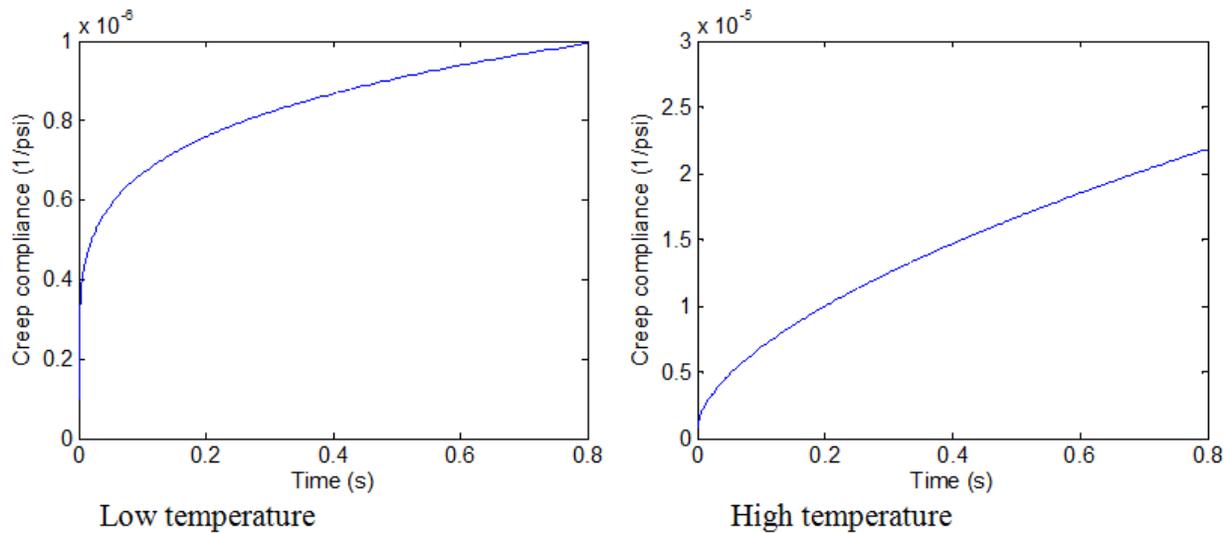
Figure 153. Graphs. Low- (left) and high- (right) temperature AC creep compliance curves used for ViscoWave-II simulation.
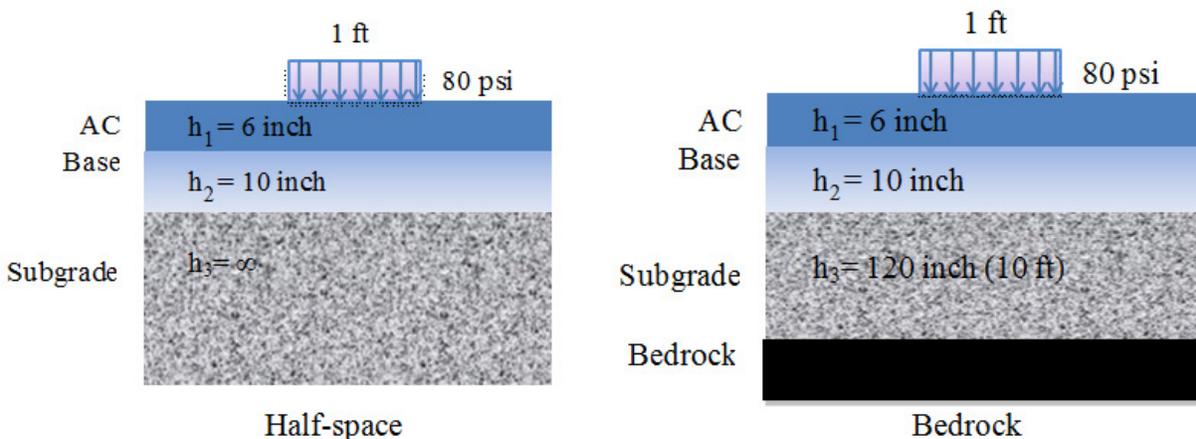
Figure 154. Diagrams. Schematic of the pavement structure with half-space (left) and bedrock (right).

140
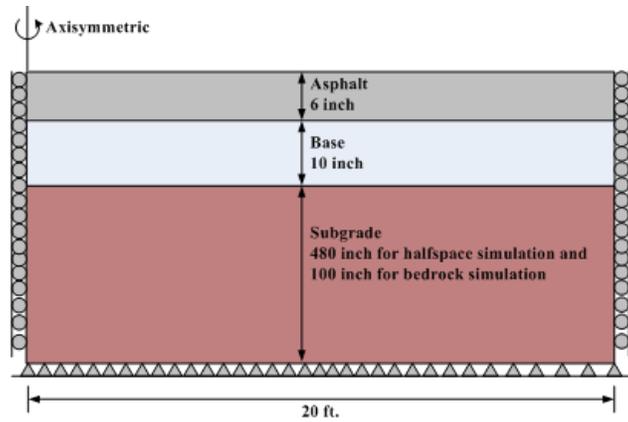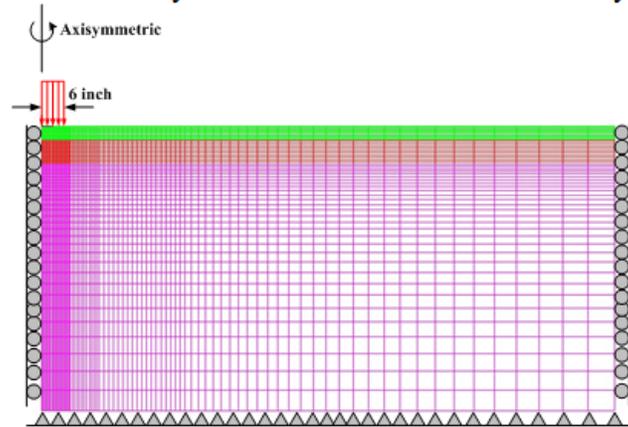
Figure 155. Diagrams. Axisymmetric FEM geometry (top) and FEM mesh (bottom) used for simulation of pavement response under FWD loading.

The FEA mesh was generated in such a way that finer meshes were used near the loaded area, and coarser meshes were used near the geometric boundaries. A total of approximately 8,600 axisymmetric elements, each consisting of 9 nodes, were consistently used for all FEA simulations. The results of the simulations are presented in figure 156 through figure 159. This further verified the implementation of the ViscoWave-II program.
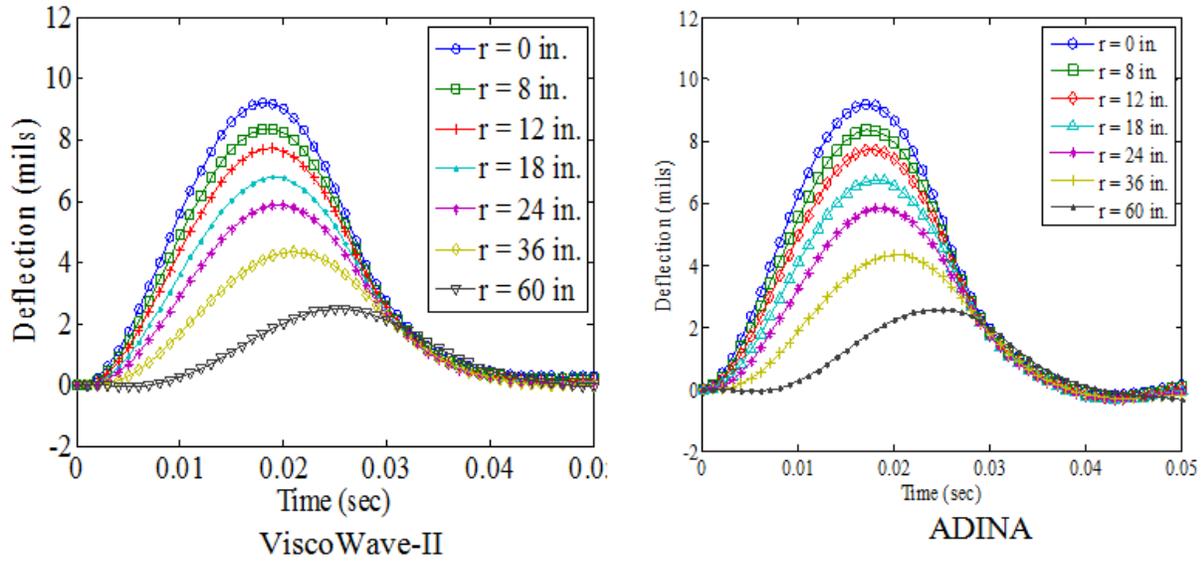
Figure 156. Graphs. Surface deflections of a layered viscoelastic structure with a half-space at low temperature simulated using ViscoWave-II and ADINA.
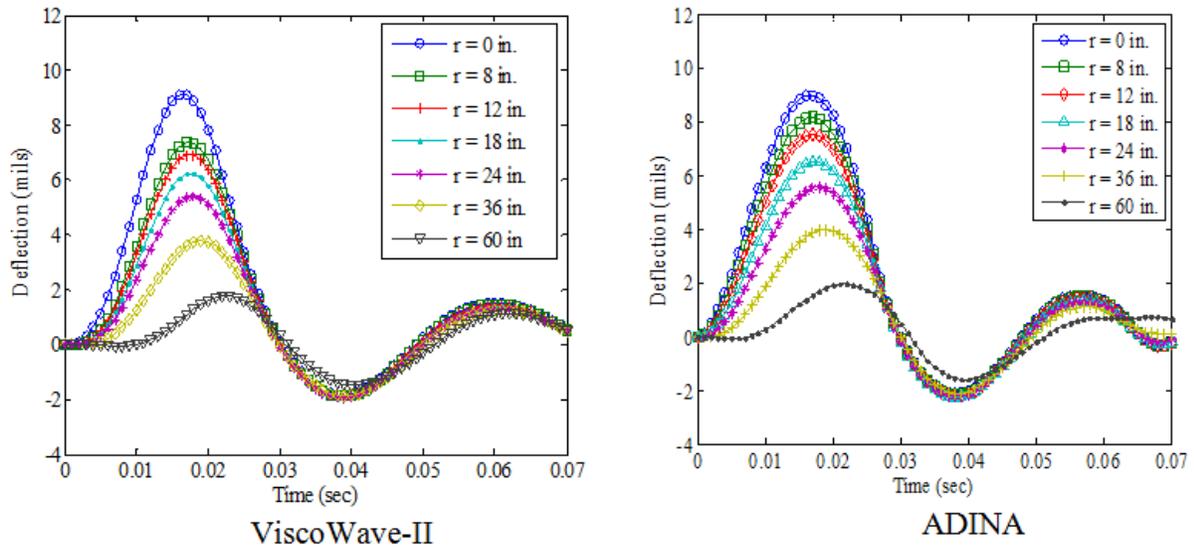
Figure 157. Graphs. Surface deflections of a layered viscoelastic structure with a bedrock at low temperature simulated using ViscoWave-II and ADINA.
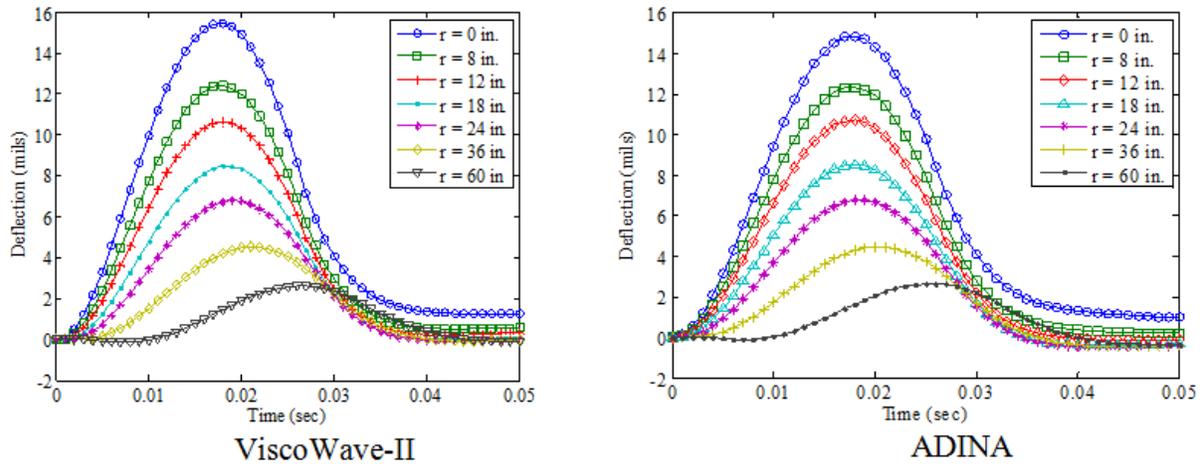
Figure 158. Graphs. Surface deflections of a layered viscoelastic structure with a half-space at high temperature simulated using ViscoWave-II and ADINA.
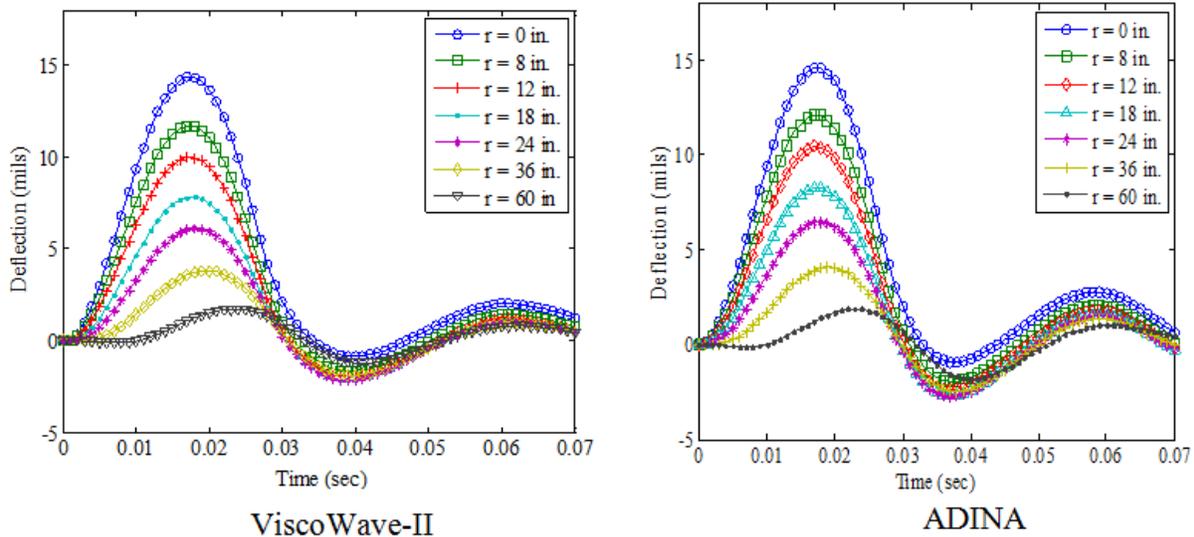
Figure 159. Graphs. Surface deflections of a layered viscoelastic structure with a bedrock at high temperature simulated using ViscoWave-II and ADINA.

Simulation of Viscoelastic Pavement Structures With Stiff Soils

The analyses in chapter 3 showed a prevalence of dynamic behavior (in the form of free vibrations of deflection sensor time histories) observed in a large pool of LTPP FWD test data. A sensitivity analysis was then conducted to show that the stiff layer condition did not necessarily correspond to the presence of shallow bedrock, which often lies at much greater depths. Instead, the stiff layer condition can manifest anytime the soils below the subgrade layer are stiffer than that subgrade layer. In this section, the research team describes the investigation using an increasing subgrade modulus with depth instead of a single stiff layer at a fixed depth. The rationale behind this analysis was that in reality, soil profiles generally exhibited increasing soil modulus with depth. This can be due to increased confinement with depth for sands or

consolidation level with depth in clay—these situations are very common in any soil profile. This is a commonly observed behavior in the geotechnical engineering profession.

The viscoelastic simulation was carried out using the pavement structure presented in table 35. The FWD loading used in this simulation was assumed to be uniformly distributed over a circular area with a radius of 6 inches, a peak magnitude of 9,000 lb, and a duration of 35 ms. Two cases of stiff soils modeling were simulated. The subgrade layer was first modeled to be with a shallow stiff layer (2,000,000 psi) located at about 9 ft below the pavement surface (base case scenario), and then with soils having E-values increasing with depth (figure 160). The surface deflections were calculated at radial distances of 0, 8, 12, 18, 24, 36, 48, 60, and 72 inches from the center of the loading plate. The viscoelasticity of the AC was modeled using a Prony series of the master curve presented in figure 161 (top). The AC layer was divided into two layers with different temperatures as shown in figure 161 (bottom). In addition, the roadbed soil was divided into 11 sublayers of 50 ft total depth (a 2-ft top layer representing the compacted subgrade layer and 10 sublayers of 4.8 ft each with stiffness increasing as a function of depth). The results of the simulations are presented in figure 162. The results indicate that (1) the deflection amplification was higher when a stiff layer modulus was fixed as a high value as opposed to increasing with depth, and (2) the free vibrations (at the tail of the deflection pulses) were lower when the soil modulus was gradually increasing with depth.

Table 35. Layer properties for viscoelastic simulation of structure with stiff soils.

Layer	Elastic Modulus (psi)	Poisson's Ratio	Thickness (inches)	Unit Weight (pcf)
Asphalt	Master curve	0.35	4	145
Base	20,000	0.4	6	125
Subgrade	13,500	0.45	600	100
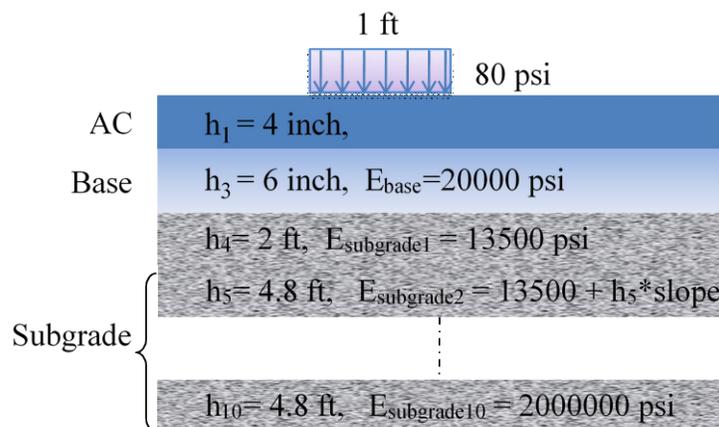
Figure 160. Diagram. Pavement structure with soils having *E*-values increasing with depth.
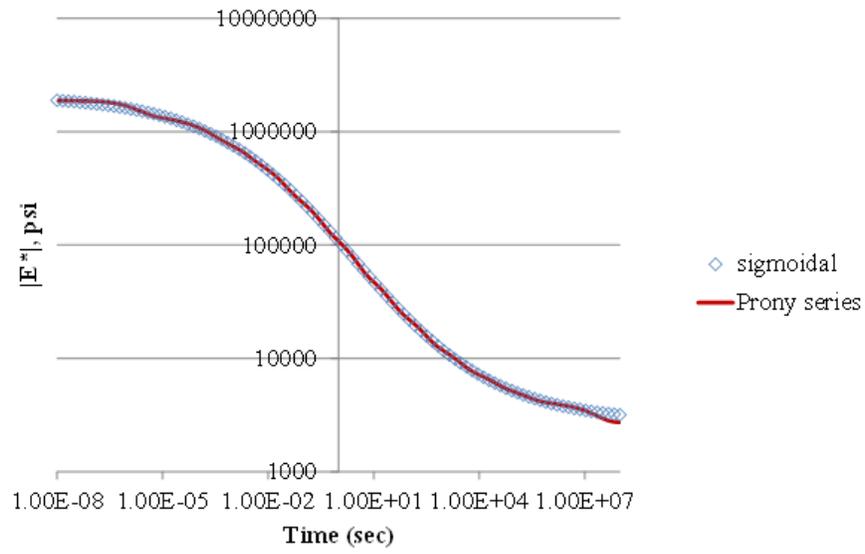
Master curve
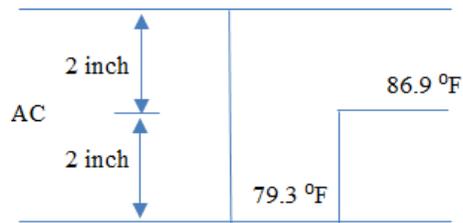
Temperature profile

Figure 161. Graph and Diagram. AC layer parameters.
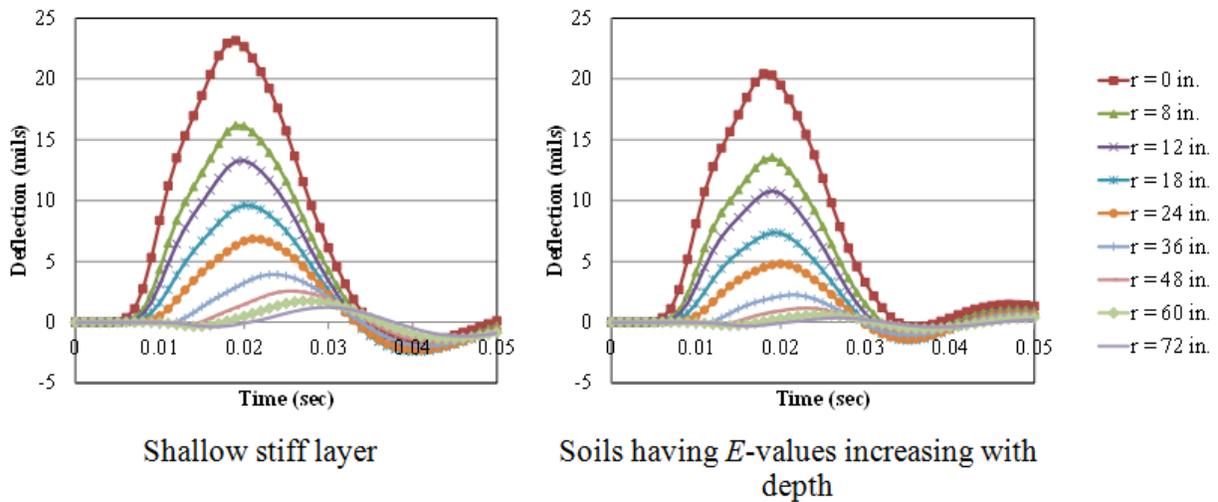
Figure 162. Graphs. Surface deflections of pavement structure with shallow stiff layer and soils having *E*-values increasing with depth.

Computational Efficiency of the New Algorithm

All the simulations previously described in this chapter were run both serially (ViscoWave) and using parallel computing (ViscoWave-II). Note that the efficiency of ViscoWave-II using the MPI parallelization scheme was only an estimate. Because the program was written in MATLAB®, the parallelization relied totally on the MATLAB® distributed computing server, which was known to have problems with long jobs. To overcome this problem, the research team re-implemented the algorithm using a low-level programming language (C++). The new code was tested on a four-core centraol processing unit (CPU) computer, and the runtime with $\Delta t = 0.2$ ms was reduced from 9 min (540 s) to 0.5 min (30 s) in serial (CPU) computing. This represented an 18-fold reduction in computational time. Table 36 presents the computation time for each simulation. It is clear that significant computational savings were achieved when using parallel computation. ViscoWave-II is 8 times faster when using 8 cores, 12 times faster when using 12 cores, and 60 times faster when using 60 cores (available only through the HPCC housed in the Michigan State University College of Engineering). Also, the reduction in computation time by using the code written in C++ language and rather than MATLAB® is significant (almost half). Computation time could be further reduced by using a 64-bit machine. The computational efficiency went from 5 min (300 s) to 2.5 min (153 s) in a two-core CPU machine without multithreading.

Table 36. ViscoWave-II computational efficiency.

Time Step (ms)	Simulation	Serial Computation[1] (s)	Parallel Computation (s)								
			MATLAB®			C++ With Multicore			C++ With Multithreading		
			2 cores[2]	4 cores[3]	8 cores[3]	2 cores[2]	4 cores[3]	8 cores[3]	2 cores[4]	4 cores[4]	8 cores[4]
0.1	Elastic	1,800	900	450	225	500	75	38	250	38	20
	Viscoelastic three-layer system	2,100	1,050	525	262	584	88	45	295	45	22.5
	Viscoelastic with shallow stiff layer	2,593	1,297	649	325	720	108	53	360	54	27
	Viscoelastic with soils stiffening with depth	3,342	1,670	836	418	928	139	70	465	70	35
0.2	Elastic	840	420	210	105	230	35	19	115	17	8.5
	Viscoelastic three-layer system	1,080	540	270	135	300	45	22.5	150	22.5	11.5
	Viscoelastic with shallow stiff layer	1,210	605	304	153	336	50	25	169	26	13
	Viscoelastic with soils stiffening with depth	1,560	780	390	195	435	66	34	218	33	17

[1]Only MATLAB® was used for serial computation.
[2]Intel core 2 duo CPU with 2.5 GHz (32-bit CPU).
[3]Intel core 4 duo CPU with 3.5 GHz (32-bit CPU).
[4]Two threads per core.

Dynamic Analysis of Waverly Test Section

As part of this project, FWD tests were conducted at Waverly Road test sections. The FWD was provided by FHWA. Testing included the following:

1. **Morning set**: Four different sections and four different load levels.
2. **Afternoon set**: Four different sections and four different load levels.
3. **Evening set**: Four different sections and four different load levels.

The top AC layer configurations of the four different sections selected for FWD are presented in table 37.

Table 37. Waverly Road pavement section information.

Station Number	Layer 1 (Thickness)	Layer 2 (Thickness)
1	Crumb rubber modified asphalt (4E03[a]—CRTB) (2 inches)	Crumb rubber modified asphalt (4E03—CRTB) (2 inches)
2	Crumb rubber modified asphalt (4E03—CRTB) (2 inches)	Control 4E03 (2 inches)
3	Control 4E03 (2 inches)	Control 4E03 (2 inches)
4	Control LVSP[b] (2 inches)	Control LVSP[b] (2 inches)

[a]4E03 = MDOT 4E03 Superpave mix
[b]LVSP = Low-Volume Superpave mix.

During the test, different loads were dropped, and deflection histories at each load level were measured. To measure deflection histories, sensors were kept at specified spacing measured from the loading unit. The FWD test loading system and deflection sensors are shown in figure 163.

Figure 163. Photos. FWD used during the field tests.

Temperature in pavements typically varies with depth, which may significantly affect pavement response. Holes at depths 2, 4, 6, 8, and 10 inches were drilled to measure temperature. The drills

were made close to the testing location as shown in figure 164. Temperature measurements were taken each time the test was run. The test load levels, deflection sensor locations, temperature profile, and the peak FWD deflection measurements at stations 1 and 3 are given in appendix D. The research team used only stations 1 and 3 because stations 2 and 4 have an asphalt base with a different mix. Use of the latter would cause a problem for the backcalculation algorithm because it was not designed to backcalculate the modulus of more than one AC layer in the pavement structures with different mixes. The same is true if there were multiple subgrade layers with similar modulus values.

Figure 164. Photo. Illustration of temperature measurement at different depths of the pavement.

Comparison of Theoretical and Measured Deflection Time Histories

In this analysis, the ViscoWave-II program was used to analyze the response under the FWD test for the Waverly Road site (stations 1 and 3). The purpose of the exercise was to verify the observations from measurements with theory. To minimize the trials for a reasonable match, the AC dynamic modulus curves from laboratory tests on cores obtained from the field (and presented in appendix D in the section entitled Laboratory-Measured Results for Waverly Road) were used. The corresponding relaxation modulus curves were fitted with appropriate Prony series. The average AC layer temperature measured in the field was used. The depth to the stiff layer was estimated at 8 ft using the Ullidtz analysis procedure (described in chapter 4 in the section entitled Backcalculation of the Viscoelastic Properties of the LTPP Sections Using a Single FWD Test With Known Temperature Profile).[94] Initially, the stiff layer modulus was set at 2 million psi, which was the value used for the static and viscoelastic backcalculation described earlier. The moduli of the unbound layers were varied until a reasonable match was obtained. Table 38 and table 39 show the final pavement stations used in the analysis for stations 1 and 3, respectively. The same pavement cross sections with identical layer properties were then used for running the program LAVA for comparison purposes.

Table 38. Pavement properties used in dynamic analysis of station 1 with ViscoWave-II.

Layer	Modulus (psi)	Poisson's Ratio	Mass Density (pcf)	Thickness (inches)
HMA	Master curve	0.35	145	4
Base	20,000	0.4	125	6
Subgrade	13,500	0.45	100	96
Stiff Layer	2,000,000	0.2	125	Infinity

Table 39. Pavement properties used in dynamic analysis of station 3 with ViscoWave-II.

Layer	Modulus (psi)	Poisson's Ratio	Mass Density (pcf)	Thickness (inches)
HMA	Master curve	0.35	145	4
Base	15,000	0.4	125	6
Subgrade	12,500	0.45	100	96
Stiff Layer	2,000,000	0.2	125	Infinity

Figure 165 and figure 166 show the predicted deflection time histories from ViscoWave-II and LAVA together with measured ones for stations 1 and 3, respectively. Figure 167 shows comparisons of ViscoWave-II and LAVA solutions with measured deflections for station 1 in terms of peak deflections (top graph); ratio of predicted to measured deflections (bottom graph).

The following useful observations were made:

- The theoretical predictions from ViscoWave-II show very good agreement with the measured deflection time histories. In particular, it is worthwhile noting that both theory and measurement show very clearly that the most distant sensors (6 through 8) indicated a slight rebound at the beginning of the signal (inside the dashed circle). The fact that both theory and measurement showed the same behavior was proof that these observations were physically real. While this might be construed as a detail and may not be ultimately critical in the practical implications of the backcalculation exercise, it is an important fact that reinforces the belief that (1) a comprehensive model that takes into account viscoelasticity of the AC layer, damping in the unbound layers, and dynamics in terms of inertial and wave propagation effects, can explain the measured data with all its complexities; and (2) the FWD sensor measurements appear to be quite reliable in showing the physical behavior for most of the time range, with the exception of the drift problems at the tail of the records (previously mentioned in chapter 3).

- The layered viscoelastic solution (LAVA program) cannot simulate the true deflection time histories because it cannot account for inertial and wave propagation effects. As such, it cannot predict the time delays in the response, the initial rebounds of the farther sensors, and the free vibrations after the load is applied. Also, the viscoelastic solution mostly follows the shape of the applied load (typical waviness observed in the Dynatest® load signal). In terms of peak response, the solution will significantly underestimate the deflections when a stiff layer is presented. This is because it cannot account for the dynamic amplification due to the wave energy trapped in the unbound layers when a stiff

layer condition exists. In fact, it will further reduce the deflection because the stiff layer has a very high modulus (similar to a static solution). Therefore, in the context of backcalculation when a stiff layer condition exists, using the layered viscoelastic program as a forward solution will force the backcalculation algorithm to compensate by either overestimating the depth to the stiff layer, or if the user fixes this depth to a more reasonable estimate it will underestimate layer moduli.
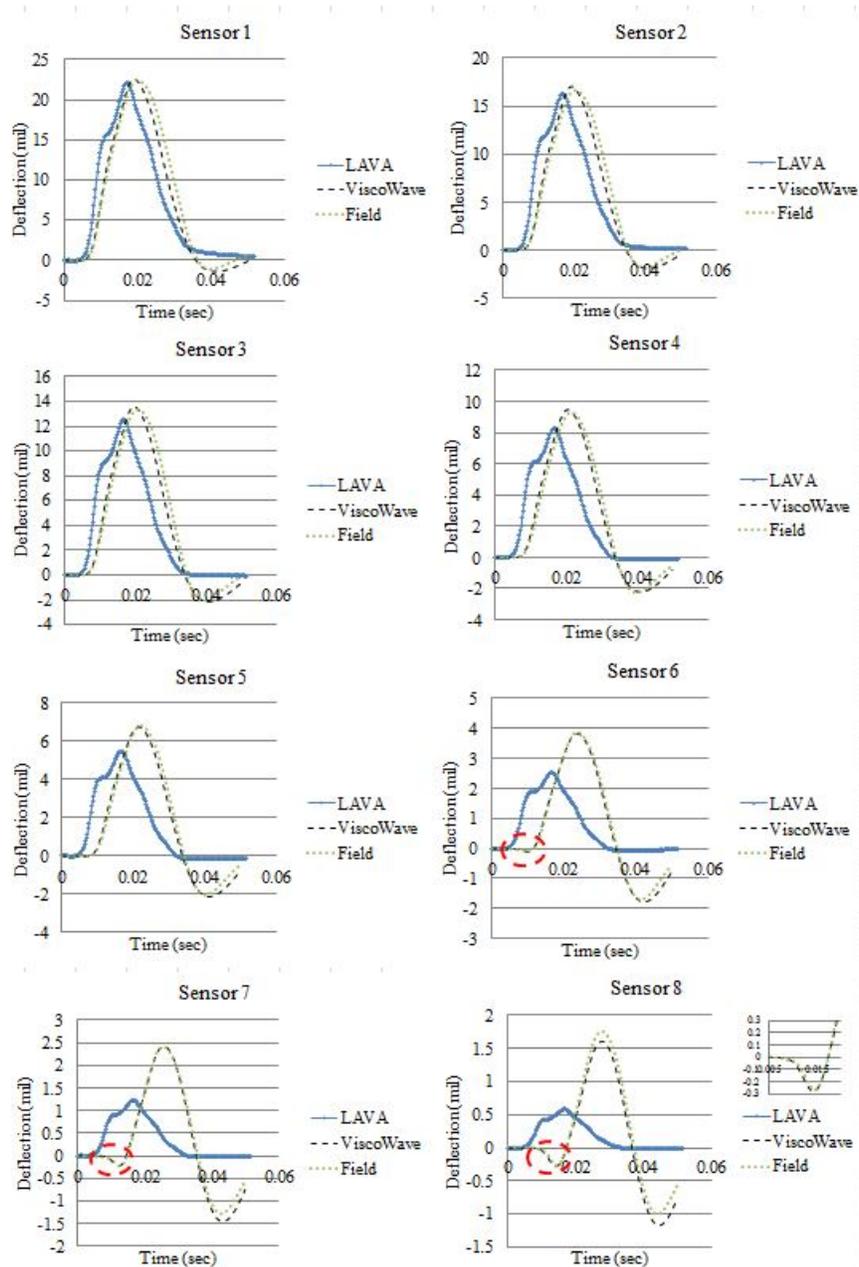
Figure 165. Graphs. Comparison of deflection response from ViscoWave-II and LAVA predictions for station 1.

151
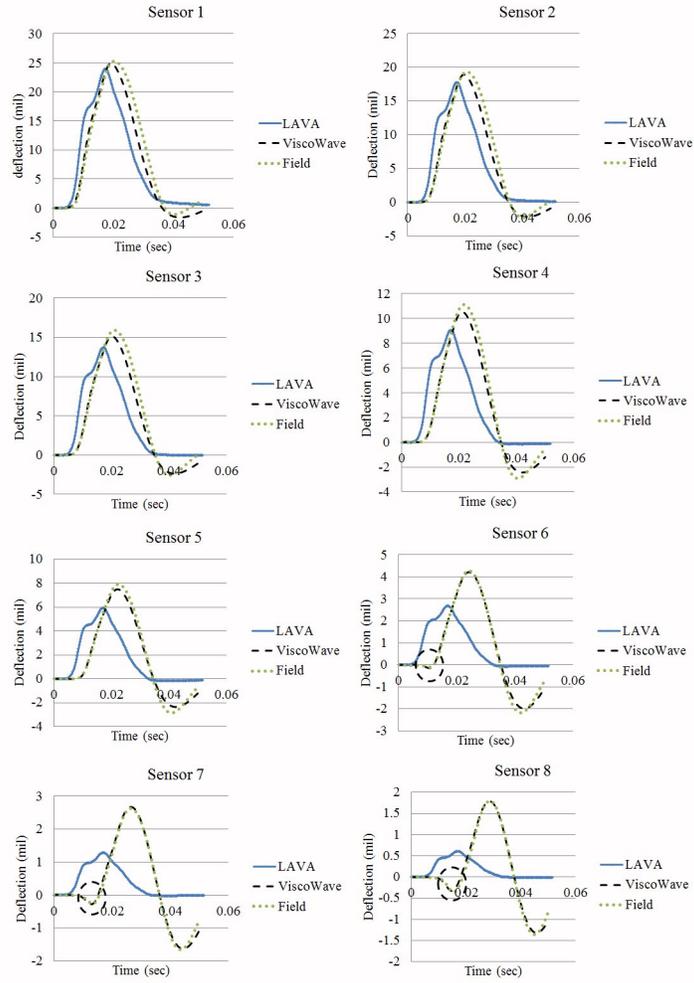
Figure 166. Graphs. Comparison of deflection response from ViscoWave-II and LAVA predictions for station 3.
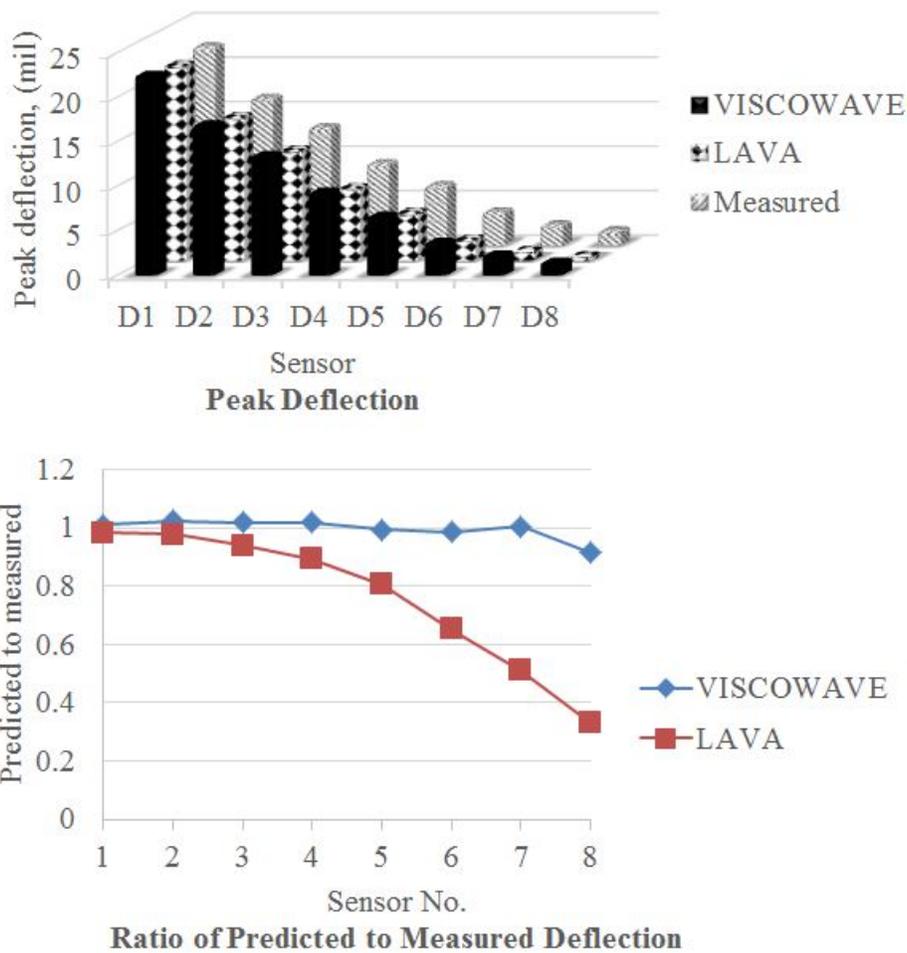
Figure 167. Graphs. Comparison of ViscoWave-II and LAVA solutions with measured deflections for station 1.

Sensitivity Analysis on the Effect of Stiff Layer Modulus Value

Because of the prevalence of dynamic behavior (in the form of free vibrations of deflection sensor time histories) observed in the large sample of LTPP FWD test data (as shown in chapter 3 of this report), it was hypothesized that in the great majority of the cases, the stiff layer condition may not correspond to the presence of shallow bedrock. Such bedrock would be highly unlikely given that it typically lies at much greater depths. Instead, the stiff layer condition could manifest anytime the soils below the subgrade layer are stiffer than the subgrade layer itself. This could be caused by increased confinement with depth, overconsolidation, or existence of a shallow groundwater table for example; these situations are very common in any soil profile. This would explain the high percentage of sections from the LTPP database that showed dynamic behavior.

Given that argument, the research team decided to conduct a small sensitivity analysis on the value of the stiff layer modulus. This value was reduced from the initial value of 2 million psi, first in 200,000-psi increments (i.e., 1.8 million, 1.6 million psi, etc.), then in 20,000-psi

153

increments below 200,000 psi (i.e., 180,000, 160,000 psi, etc.), and finally used a minimum value of 10,000 psi, which was lower than the subgrade modulus (taken as 13,500 psi).

Figure 168 shows example deflection time histories with the stiff layer modulus decreasing from 2 million to 10,000 psi. The figure shows that the sensors close to the load were mostly not affected by the stiff layer modulus value while those farther from the load were. Free vibrations, while decreasing in magnitude and delayed further, will occur even at low values of the stiff layer modulus, as long as this value is higher that the subgrade modulus value.

Figure 169 and figure 170 summarize the sensitivity analysis results for all sensors in terms of (1) the ratio of predicted to measured peak deflection values and (2) the amplification factor relative to the base case of 2 million psi. The figures show that only the farther sensors (6 through 8) were affected by the stiff layer modulus value and that the effect became visible when the stiff layer modulus was 200,000 psi or lower (compared with the base case of 2 million psi). The effect is significant for the farther sensors, with up to a 50-percent error in the ratio of predicted to measured value and up to a factor of 2 for the amplification ratio, for the lower stiff layer modulus values. Even though these observations used one structure, they could be generalized.

Summary of Findings From Dynamic Analyses

The results of the above analyses clearly showed the superiority of a fully dynamic solution with a viscoelastic AC layer modulus in predicting deflection responses that were in line with the physical reality, as evidenced by the close match in the details of the deflection time histories between theory and observation.
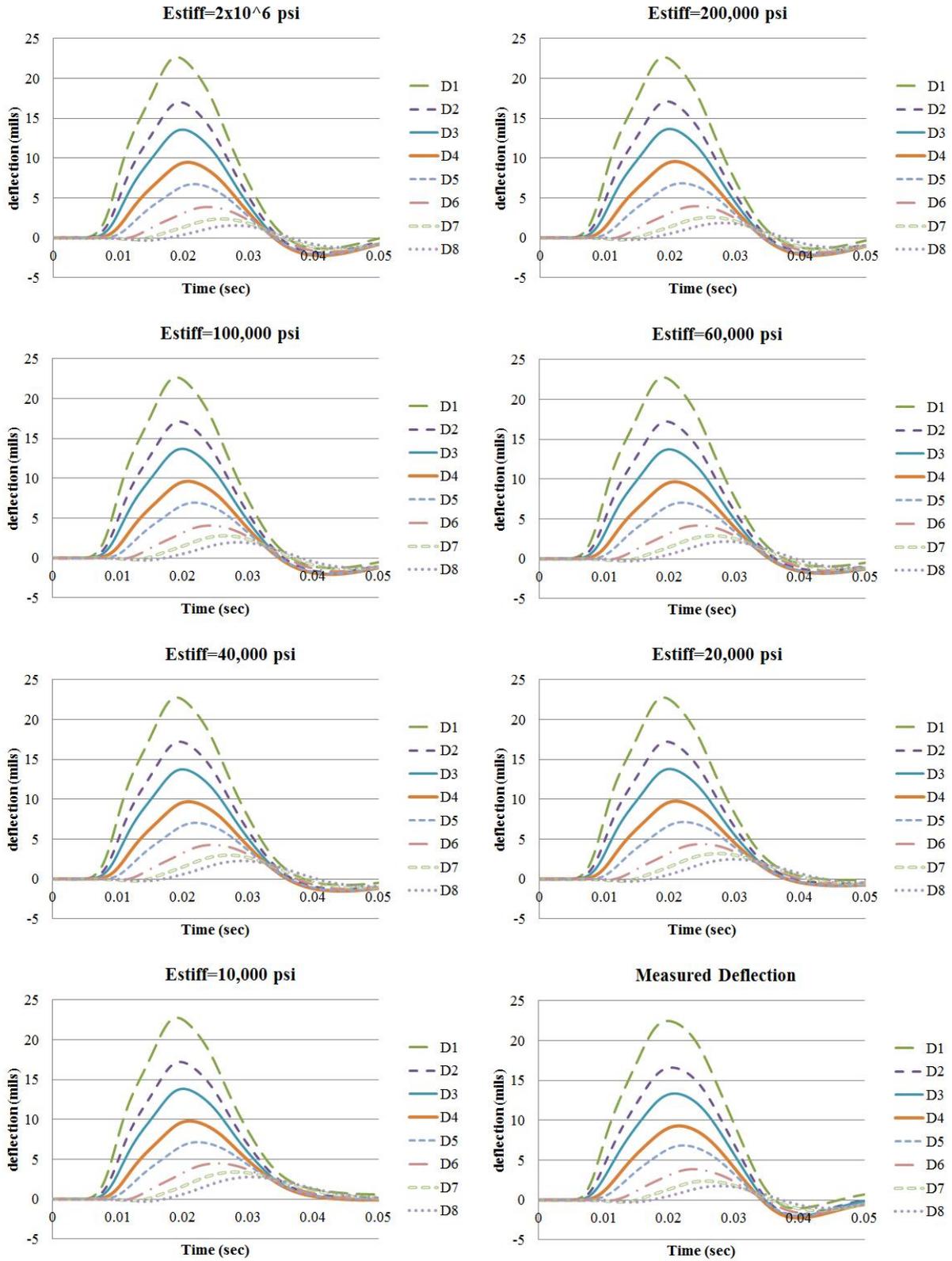
Figure 168. Graphs. Example time histories from ViscoWave-II with decreasing stiff layer modulus and measured sensor deflections for station 1.

155
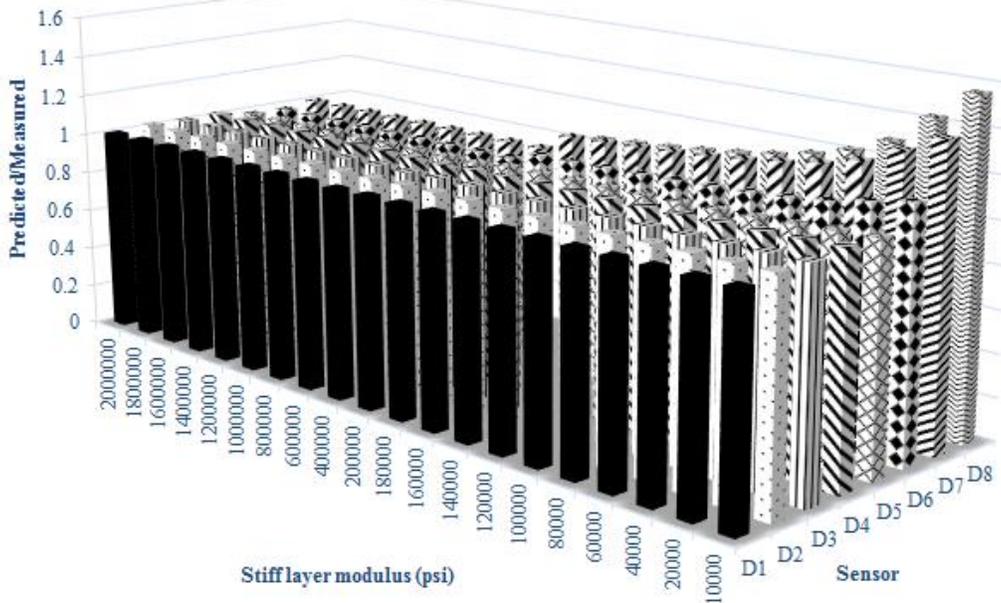
Figure 169. Graph. Effect of stiff layer modulus on ratio of predicted to measured sensor deflections for station 1.
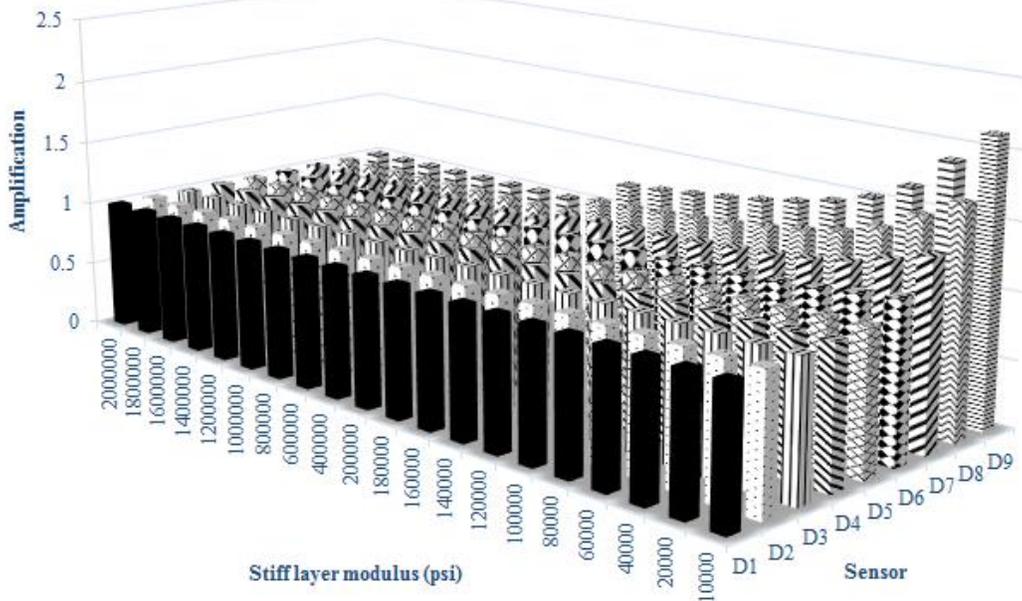
Figure 170. Graph. Effect of stiff layer modulus on predicted sensor deflection amplification for station 1.

BACKCALCULATION USING GA

As discussed in chapter 4, one of the problems with gradient-based methods is that the multidimensional surface represented by the objective function may have many local minima. As a result, the program may converge to different solutions for different sets of seed moduli, as is discussed later in this chapter. The key disadvantages of gradient-based methods are precisely the strengths of the other two categories. In principle, GAs and direct search methods find a global optimum. The key disadvantage is that they can converge very slowly, especially near an optimum, requiring numerous calls to the dynamic forward solution. A second weakness is that determining a termination criterion is not straightforward.

These strengths and weaknesses are considered in choosing an optimization algorithm. A key tradeoff is between the possibility of converging to a local minimum using gradient-based methods and the high computational cost of the GA. The more frequently the algorithm is to be used, the more beneficial the gradient-based algorithm becomes. Therefore, the research team decided to use a hybrid approach—use GA to obtain a good set of seed values that would then be used by the modified LM gradient-based algorithm to backcalculate the master curve of HMA layers and the layer properties for base and subgrade.

The forward solution used a Prony series with 14 coefficients to model the master curve in the Laplace domain. Considering the Prony coefficients as unknown parameters during the backcalculation increased the search domain; thus, it may take a longer time to converge. Therefore, during the backcalculation, Prony series was first fitted to a sigmoidal function using nonlinear least squares optimization. The equation shown in figure 171 presents the fitting steps.[98] Using this approach, the research team had 6 unknowns instead of 17 for the master curve. Table 40 identifies the type of variables for the backcalculation. The equation shown in figure 172 presents the formulation of the optimization problem.

$$\text{Step 1: } \log(E(t_n)) = c_1 + \frac{c_2}{1 + e^{-c_3 - c_4 \times log(t_n)}}, n = 1, \ldots, N$$

$$\text{Step 2: } log(t_n) = log(t) - log(aT)$$

$$\text{Step 3: } log(aT) = a_1 \times T^2 + a_2 \times T + a_3$$

$$\text{Step 4: } \underbrace{E(t_n) - E_\infty}_{\{A\}} = \underbrace{\sum_{m=1}^{14} e^{\left(-\frac{t_n}{TK_m}\right)}}_{[B]} \underbrace{E_m}_{\{C\}}, n = 1, \ldots, N$$

$$\text{Step 5: } minimize \; |[B]\{C\} - \{A\}| \quad such \; that \; \{C\} \geq 0$$

Figure 171. Equation. Fitting steps of the Prony series.

Table 40. Known and unknown parameters.

Known Parameters	Backcalculated Parameters
Thickness of each layer	Master curve coefficients (c_1, c_2, c_3, c_4)
Poisson's ratio of each layer	Master curve shift factors (a_1, a_2)
FWD load and setup	Moduli of base, subbase, subgrade, stiff layer
Mass density of each layer	Thickness of subgrade if stiff layer exists

Objective function

$$Er = \sum_{k=1}^{m} 100 \sum_{i,o=1}^{n} \frac{\left| \left(d_i^k - d_o^k \right) \right|}{\left\{ d^k \right\}_{\max}}$$

Bound constraints

$$\begin{cases} c_1^l \le c_1 \le c_1^u \\ c_2^l \le c_2 \le c_2^u \\ c_3^l \le c_3 \le c_3^u \\ c_4^l \le c_4 \le c_4^u \end{cases} \qquad \begin{cases} a_1^l \le a_1 \le a_1^u \\ a_2^l \le a_2 \le a_2^u \\ a_3^l \le a_3 \le a_3^u \end{cases} \qquad \begin{cases} E_b^l \le E_b \le E_b^u \\ E_{sg}^l \le E_{sg} \le E_{sg}^u \end{cases}$$

Figure 172. Equation. Optimization problem.

Where:

m = Number of sensors
d_i = Input deflection information obtained from field at sensor k.
d_o^k = Output deflection information obtained from forward analysis at sensor k.
n = Total number of deflection data points recorded by a sensor.
c_i = Sigmoid coefficients.
E_b and E_{sg} = Base and subgrade moduli.
a_i = Shift factor polynomial coefficients.

The superscript l represents the lower limit, and u superscript represents the upper limit. Table 41 presents bounds of the variables used as input to the backcalculation algorithm.

Table 41. Bounds of the variables.

Variable	Lower Limit	Upper Limit
c_1	0.045	2.155
c_2	1.800	4.400
c_3	-0.523	1.025
c_4	-0.845	-0.380
a_1	-0.00053801	0.00113610
a_2	-0.159792	-0.077
a_3	1.656202	2.763
E_{base} (psi)	10,000	30,000
$E_{subgrade}$ (psi)	5,000	20,000

Theoretical Verification of DYNABACK-VE

To check the accuracy and robustness of the backcalculation using the new dynamic forward solution, the research team first used only GA and did not focus on the computational efficiency of the algorithm. The verification and evaluation of the new backcalculation program DYNABACK-VE was carried out for the following:

- Simulated deflections using ViscoWave-II.
- Field FWD test data from Waverly Road stations and LTPP sections.

158

Backcalculation Using Simulated Deflections

This section describes the results of backcalculation using simulated deflections.

Sensitivity Analysis: Sensitivity analysis was conducted to assess the optimal number of populations and generations to be used for backcalculation. The pavement structure used in that sensitivity analysis is presented in table 42. The population-generation combinations used were 30/15, 70/15, 100/15, 200/15, and 300/15. Figure 173 and table 43 summarize the results of the backcalculation. Based on the sensitivity analysis, the optimal population/generation combination was 200/15. Therefore, all the following backcalculations were performed using a population size of 200 with 15 generations. Because the optimal numbers of populations and generations were affected by the number of unknown variables and how smooth the objective function was, the recommendation to use a population size of 200 with 15 generations held true for all cases with 10 or fewer unknowns.

Table 42. Layer properties for the simulated pavement structure.

Layer	Elastic Modulus (psi)	Poisson's Ratio	Thickness (inches)	Unit Weight (pcf)
Asphalt	Master curve (figure 161 (top)) (86.9 °F, 79.3 °F)	0.35	4	145
Base	20,000	0.4	6	125
Subgrade	13,500	0.45	96	100
Stiff layer	2,000,000	0.25	Infinity	125
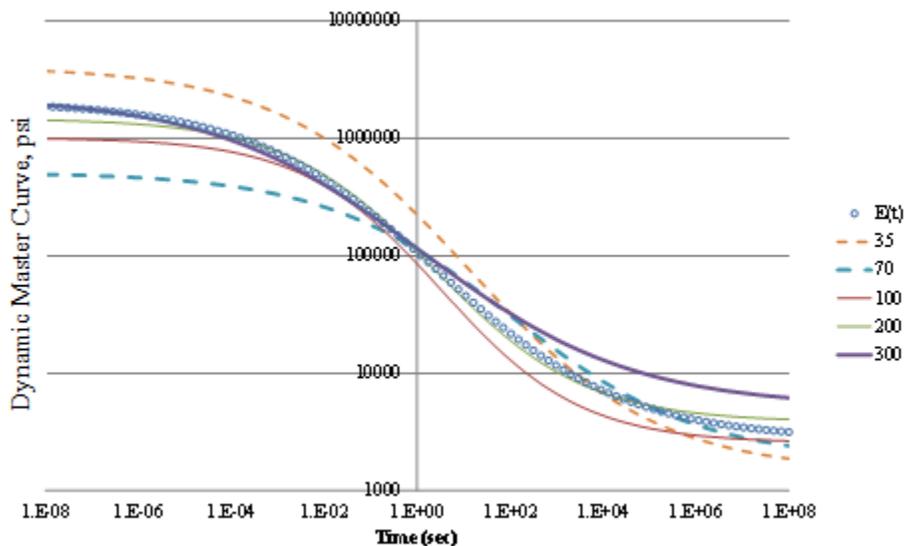
Figure 173. Graph. Backcalculated master curve for different population-generation combinations optimization problem.

159

Table 43. Backcalculated layer moduli.

Layer	Elastic Modulus (psi)	Backcalculated Moduli (psi) for Various Population Sizes				
		35	70	100	200	300
Base	20,000	13,857	15,315	16,281	16,736	20,246
Subgrade	13500	6,886	11,027	13,928	13,548	13,559
Stiff layer	2,000,000	1,381,454	1,473,155	1,573,994	1,824,154	1,591,451

Backcalculation of Layer Moduli Only: The viscoelastic simulation was carried out using the same pavement structure presented in table 42. The FWD loading used in all simulations was assumed to be uniformly distributed over a circular area with a radius of 6 inches, a peak magnitude of 9,000 lb, and a duration of 35 ms (same pulse as figure 150). Two cases of stiff soils modeling were simulated. The subgrade layer was first modeled to be with a shallow stiff layer (2 million psi) located at about 8 ft below the pavement surface (figure 174 (left)) and then with subgrade having E-values increasing with depth (figure 174 (right)). The surface deflections were calculated at radial distances of 0, 8, 12, 18, 24, 36, 48, 60, and 72 inches from the center of the loading plate. The viscoelasticity of the AC was modeled using a Prony series of the master curve presented in figure 175 (left). The AC layer was divided into two layers with different temperatures as shown in figure 175 (right). In the backcalculation, the two AC layers were considered to have the same master curve coefficients but different shift factors (computed using the same shift factor coefficients and different temperatures). In addition, for the case where E-values are increasing with depth (figure 174 (right)), the subgrade layer was divided into 11 sublayers of 50-ft total depth (a 2-ft top layer representing the compacted subgrade layer and 10 sublayers of 4.8 ft each with stiffness increasing as a function of depth). The semi-infinite layer in the case where the subgrade had E-values increasing with depth was a half-space. Therefore, the modulus of the half-space was the same as the lowest sublayer.
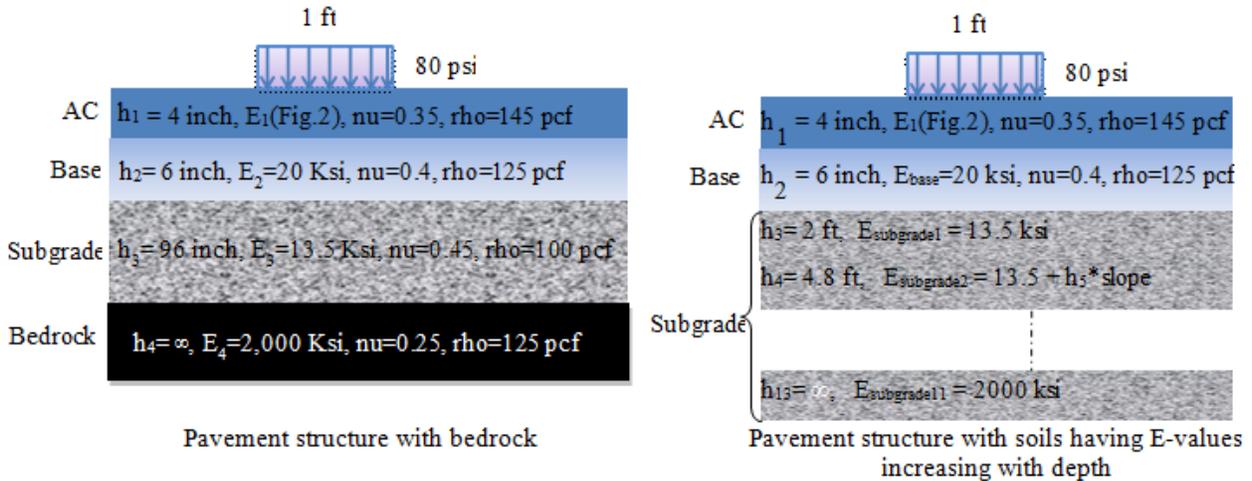
Figure 174. Diagrams. Schematic of the pavement structure with stiff soils.

Master curve   Temperature profile
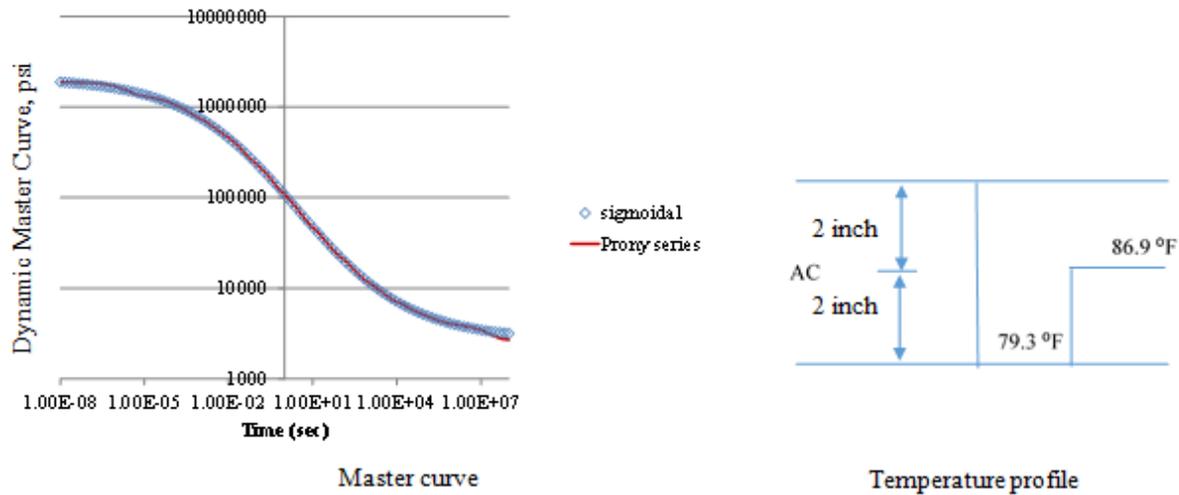
Figure 175. Graph and Diagram. AC layer master curve and temperature profile.

Table 44 shows the viscoelastic dynamic backcalculation results of the pavement structure presented in table 42. Figure 176 shows the errors in deflection time histories. Figure 177 shows the backcalculated relaxation modulus master curve and the corresponding error. Note that the symbols in the plot show the useful range of reduced time for the temperatures in the upper and lower halves of the AC layer. The results were quite reasonable, except for the tail end of the $E(t)$ curve (longer reduced time range). Note that the next section of this chapter describes the results when the research team ran a second backcalculation using the best 100 populations from run 1 as seed values in run 2—the backcalculation of the AC relaxation modulus curve greatly improved.

Table 44. Backcalculated layer moduli.

Parameter	Simulation	Backcalculated
c_1	1.271	1.55083
c_2	2.883	2.64494
c_3	0.22	0.04296
c_4	-0.497	-0.441535
a_1	0.000442	0.000483158
a_2	-0.132	-0.139815
a_3	2.34	2.68989
E_{base} (psi)	20,000	20,246
$E_{subgrade}$ (psi)	13,500	13,559
E_{stiff} (psi)	2,000,000	1,591,450

161
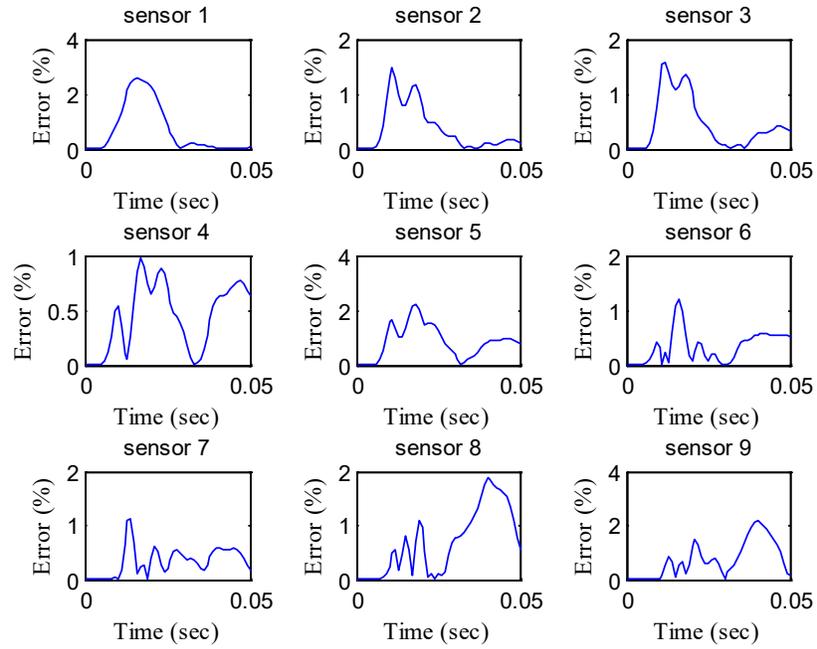
Figure 176. Graphs. Error in the backcalculated time histories by sensor—backcalculation of layer moduli only.
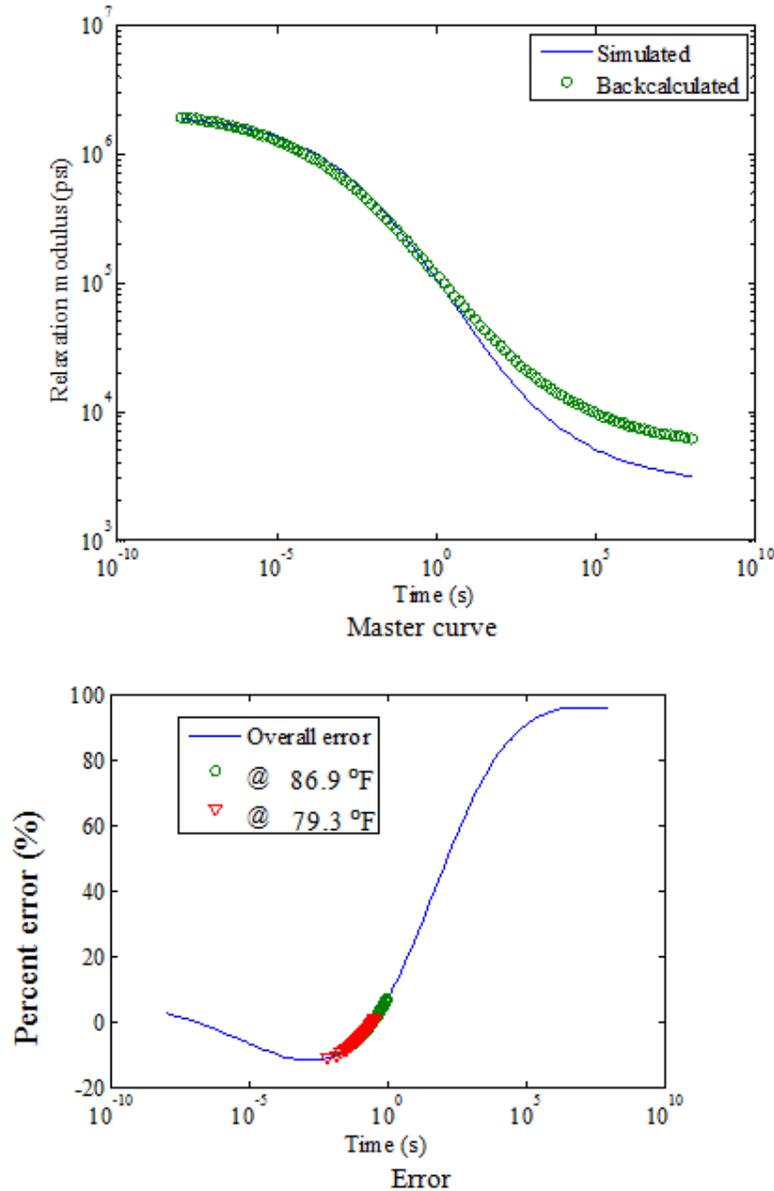
Figure 177. Graphs. Backcalculation results of the master curve—backcalculation of layer moduli only.

Backcalculation of Layer Moduli and Subgrade Thickness: This section presents the results of the team's effort to backcalculate the depth to the stiff layer in addition to the stiff layer modulus. The previous profile was used with similar input parameters with the exception of the subgrade thickness, which was unknown and needed to be backcalculated. The backcalculation algorithm was run twice. The final population of the last run was input as the initial population for the second run. Table 45 shows the viscoelastic dynamic backcalculation results. Figure 178 shows the percent error of the deflection time histories. Figure 179 shows the backcalculated relaxation modulus master curves and the corresponding percent error. It was clear that running a second backcalculation using the results from the first run as seed populations led to a much improved backcalculated AC modulus master curve. Note that the curves with circular and

163

triangular symbols in figure 177 show the useful range of reduced time for the temperatures in the upper and lower halves of the AC layer.

Table 45. Backcalculated layer moduli and subgrade thickness.

Parameter	Simulation	Backcalculated
c_1	1.271	1.304318
c_2	2.883	2.950314
c_3	0.22	0.107608
c_4	-0.497	-0.40963
a_1	0.000442	0.000489292
a_2	-0.132	-0.15225078
a_3	2.34	2.948735039
E_{base} (psi)	20,000	20,568
$E_{subgrade}$ (psi)	13,500	13,372
$h_{subgrade}$ (inches)	96	95.5
E_{stiff} (psi)	2,000,000	2,281,374
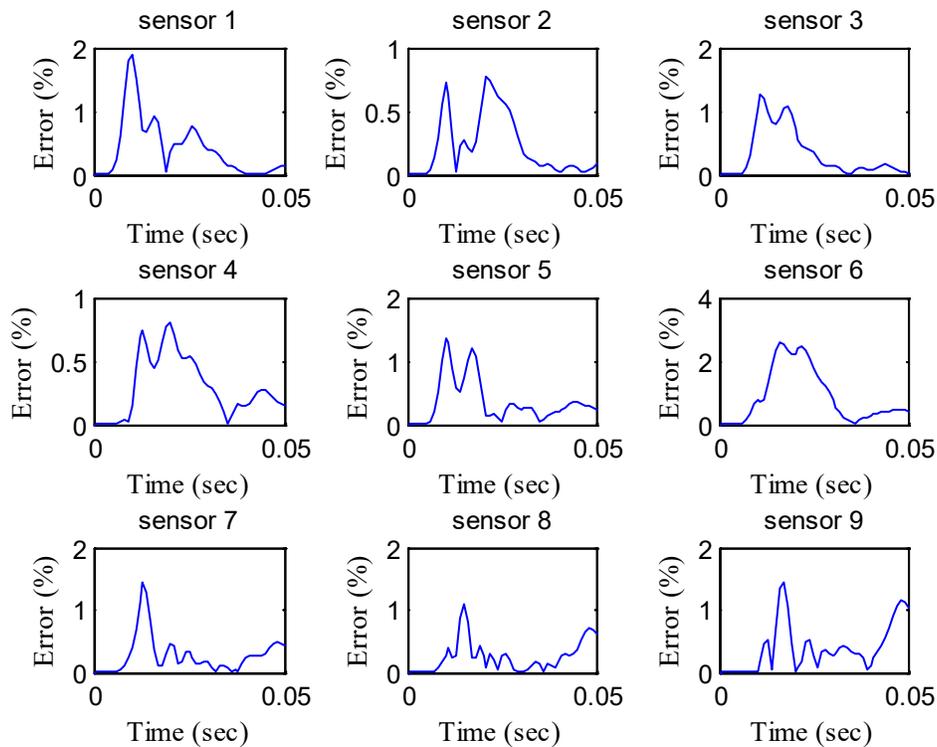
Figure 178. Graphs. Error in the backcalculated time histories by sensor—backcalculation of layer moduli and subgrade thickness.
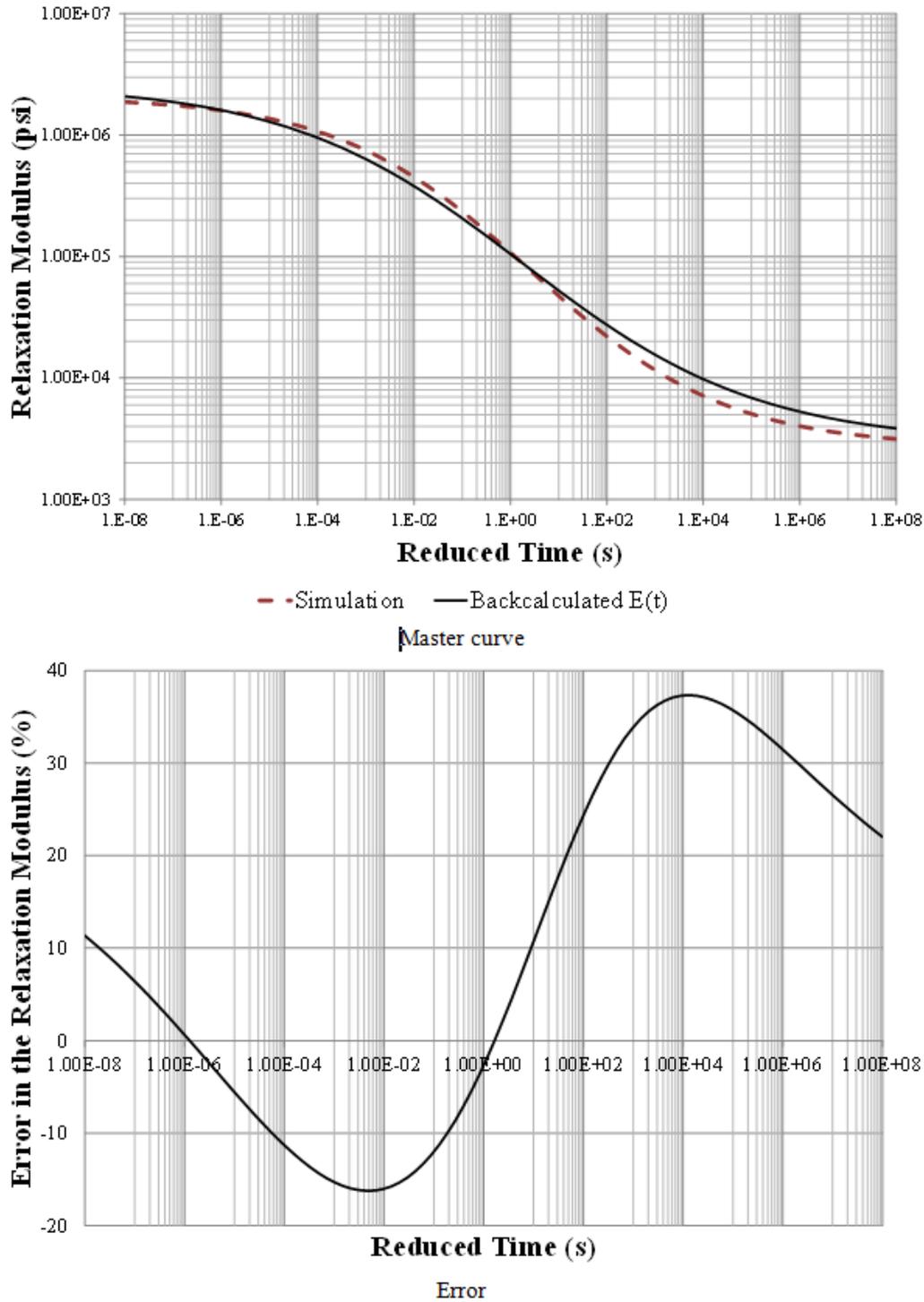
Figure 179. Graphs. Backcalculation results of the AC master curve—backcalculation of layer moduli and subgrade thickness.

Backcalculation Using Field Data

This section provides an evaluation of the new dynamic viscoelastic backcalculation program DYNABACK-VE using the field FWD test results from the Waverly Road tests conducted as

165

part of this study and from two LTPP sections. As discussed previously, the forward solution used a Prony series with 14 coefficients to model the master curve in the Laplace domain. To reduce the number of backcalculated variables, it was decided to reduce the number of coefficients for the shift factor by one using a simple mathematical transformation.[99] The equations in figure 180 show the old and new equations for shift factor. Figure 180 shows the formulation of the optimization problem.

$$\text{Old shift factor: } log(aT) = a_1 \times T^2 + a_2 \times T + a_3$$
$$\text{New shift factor: } log(aT) = a_1 \times (T - Tref)^2 + a_2 \times (T - Tref)$$

Figure 180. Equation. New and old shift factor equations.

For figure 181, it was decided to constraint the sum of the first two coefficients of the master curve instead of constraining the two coefficients to reduce the search domain as explained in chapter 4.

Objective function

$$Er = \sum_{k=1}^{m} 100 \sum_{i,o=1}^{n} \frac{\left| \left(d_i^k - d_o^k \right) \right|}{\left\{ d^k \right\}_{max}}$$

Bound constraints

$$\begin{cases} c_1^l \leq c_1 \leq c_1^u \\ C^l \leq C = c_1 + c_2 \leq C^u \\ c_3^l \leq c_3 \leq c_3^u \\ c_4^l \leq c_4 \leq c_4^u \end{cases} \quad \begin{cases} a_1^l \leq a_1 \leq a_1^u \\ a_2^l \leq a_2 \leq a_2^u \end{cases} \quad \begin{cases} E_b^l \leq E_b \leq E_b^u \\ E_{sg}^l \leq E_{sg} \leq E_{sg}^u \end{cases}$$

Figure 181. Equation. New optimization problem.

Where:

m = the number of sensors.
d_i = the input deflection information obtained from the field at sensor k
d_o^k = the output deflection information obtained from forward analysis at sensor k.
n = the total number of deflection data points recorded by a sensor.
c_i = the sigmoid coefficients.
E_b and E_{sg} = base and subgrade modulus.
a_i = the shift factor polynomial coefficients.

The superscript l represents the lower limit, and u represents the upper limit. Table 46 presents the bounds of the variables used as input to the backcalculation algorithm.

Table 46. Bounds of the variables.

Variable	Lower Limit	Upper Limit
c_1	0.045	2.155
$c_1 + c_2$	3.239	4.535
c_3	-0.523	1.025
c_4	-0.845	-0.380
a_1	-0.000536829	0.00113638
a_2	-0.140735	-0.097358
E_{base} (psi)	10,000	30,000
$E_{subgrade}$ (psi)	5,000	20,000

Waverly Road: The pavement structure used in the backcalculation is presented in table 47. The AC layer was assumed to have a two-step piecewise temperature profile. Figure 182 shows the two-step temperature profile assumed along the AC layer at station 1 (based on measurement in the field). The field data collected for drop 2 section 1 at 9 a.m. and 1 p.m. were used as input to the GA algorithm in DYNABACK-VE to search for the layer moduli as well as the subgrade thickness. Figure 183 shows the collected data. Using the morning and afternoon data together increased over-determinacy of the problem. However, trying to fit more data at the same time using GA would require increasing the variability in the initial population of the GA; which would mean increasing the number of populations and generations. This would have led to an increase in the computational time of the backcalculation algorithm. Therefore, the research team decided to use only the morning test data in the first run to obtain a good initial population; then the afternoon test data was input to the GA in DYNABACK-VE during the second run, using the final population of the first run, taking advantage of elitism.

Table 47. Known layer properties for Waverly Road.

Layer	Elastic Modulus (psi)	Poisson's Ratio	Thickness (inches)	Unit Weight (pcf)
Asphalt	—	0.35	4	145
Base	—	0.4	6	125
Subgrade	—	0.45	—	100
Stiff layer	—	0.25	Infinity	125

— Indicates unknown value.
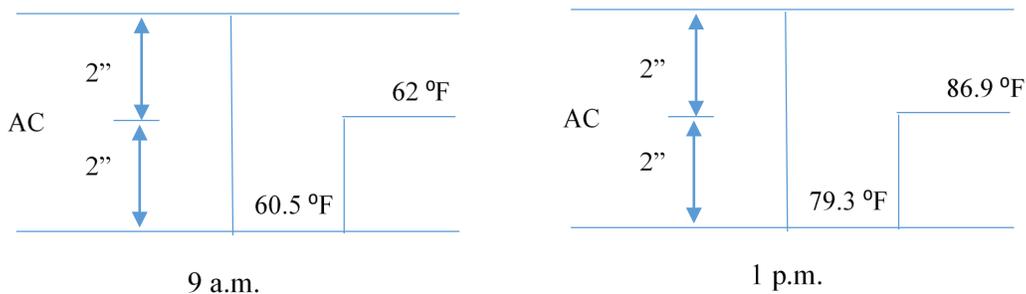
Figure 182. Diagrams. Waverly Road section 1 temperature profile at 9 a.m. and 1 p.m.
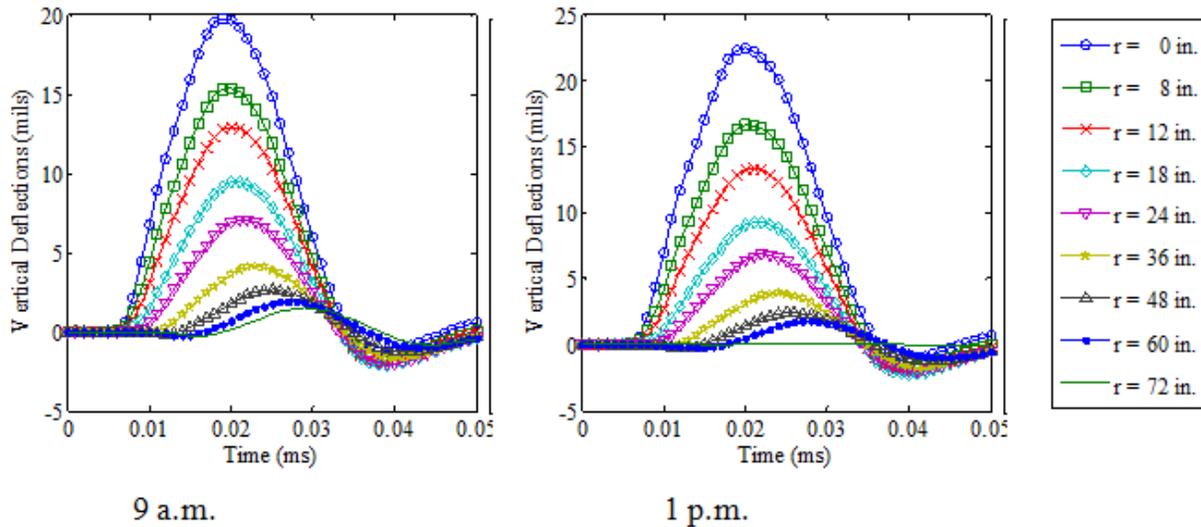
Figure 183. Graphs. Waverly Road FWD time histories for section1 collected at 9 a.m. and 1 p.m.

Table 48 shows the backcalculated layer parameters from the DYNABACK-VE backcalculation. The results were very promising, indicating good stability and realistic values. The following two interesting facts are worth noting:

- The depth to the stiff layer was estimated at about 8 ft using DYNABACK-VE. This agreed with the predictions using the Ullidtz method, which suggested presence of a shallow stiff layer at about 8 to 10 ft.[94]

- The backcalculated stiff layer modulus was 795,304 psi, which was much closer to what would be expected from stiff soils. Also, the results from the described in the Sensitivity Analysis section earlier in this chapter showed that the amplification on the peak deflection was not sensitive to a stiff layer with modulus higher than 200,000 psi.

Table 48. Backcalculated layer parameters for drop 1 section 1—Waverly Road.

Parameter	Laboratory Test/ Estimation	Backcalculated
c_1	1.482	1.58391
c_2	2.642	2.57049
c_3	0.417	0.3894
c_4	-0.569	-0.55199
a_1	-6.85E-05	0.000916
a_2	-1.06E-01	-0.1126
E_{base} (psi)	20,000	20,482
$E_{subgrade}$ (psi)	13,500	12,987
$h_{subgrade}$ (inches)	96 (1/r method)	98.7
E_{stiff} (psi)	—	795,304

— Indicates value was not measured.

168

Figure 184 shows the backcalculated relaxation modulus master curve and the measured laboratory master curve from laboratory testing on field cores. Figure 185 shows the corresponding percent error. Figure 186 and figure 187 show the measured and predicted deflection time histories and the corresponding percent errors for the 1 p.m. test, respectively. The backcalculation results were very good. Running a second backcalculation using the results from the first run as seed populations led to a much improved backcalculated AC modulus master curve.
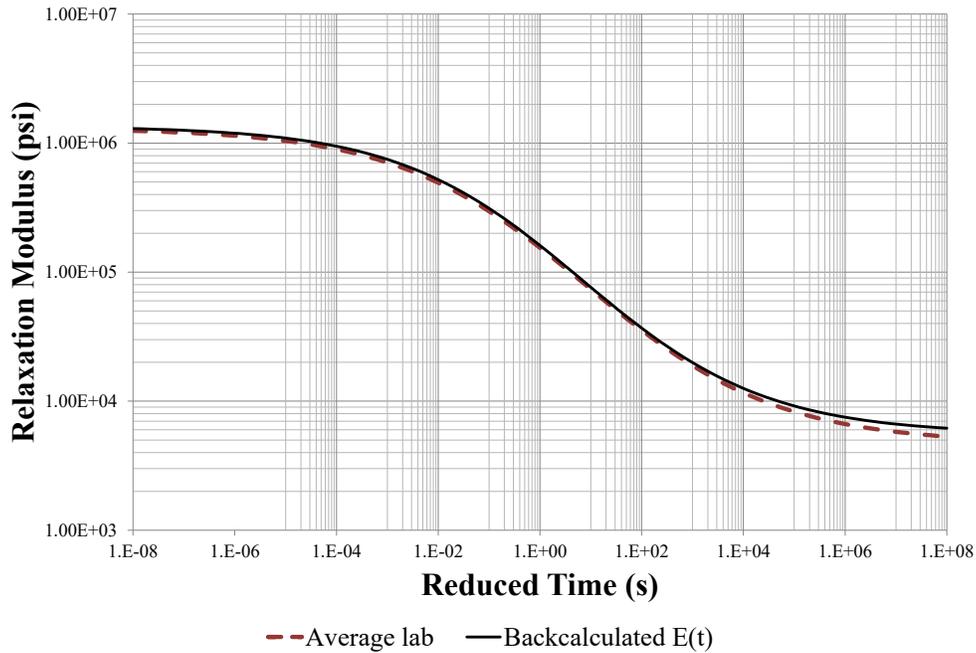
Figure 184. Graph. Backcalculated master curve forWaverly Road.
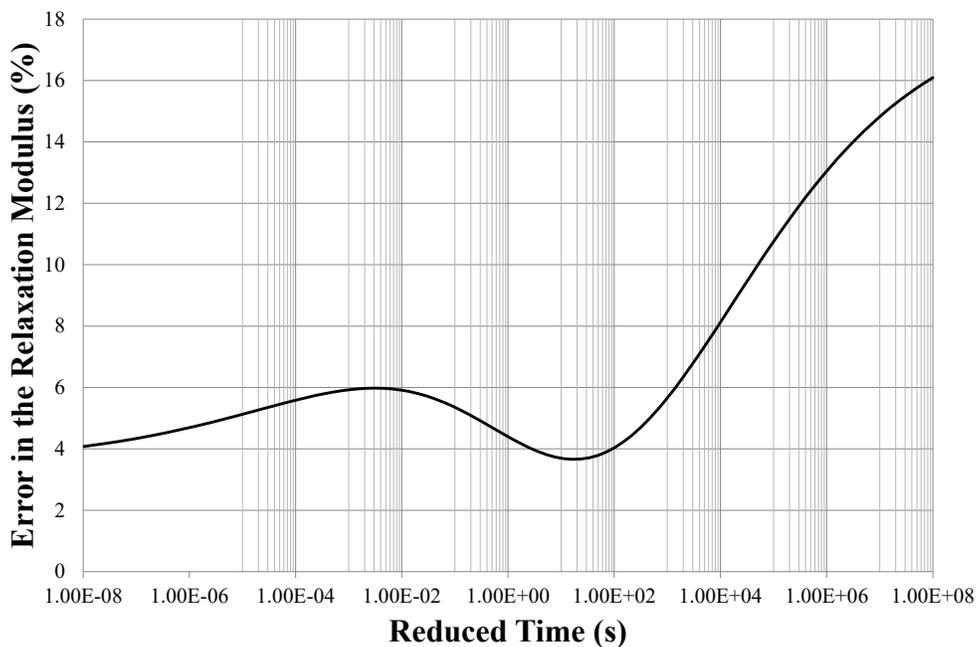
Figure 185. Graph. Error in the backcalculated master curve for Waverly Road.
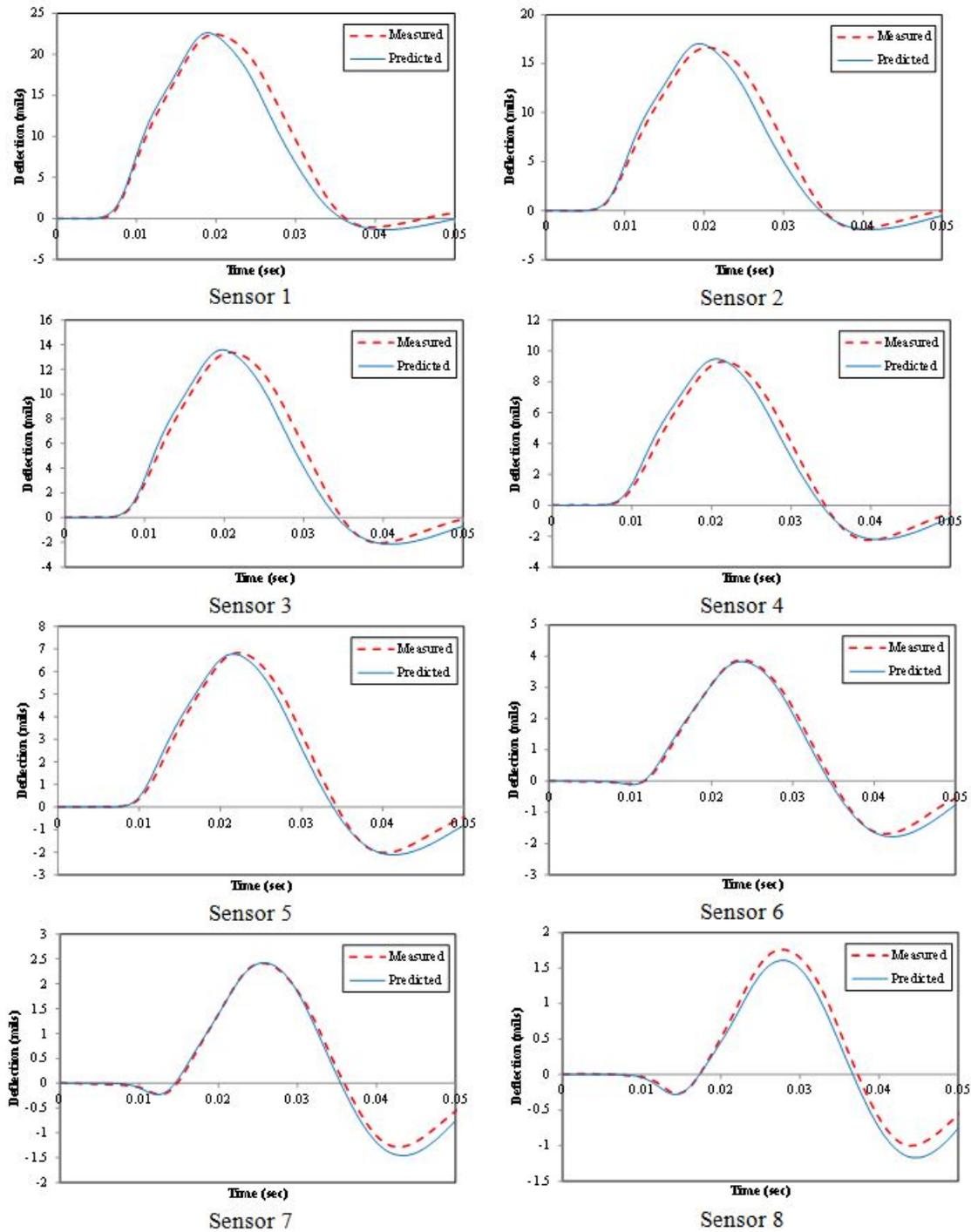
Figure 186. Graphs. Predicted versus measured deflection time histories by sensor for 1 p.m. test for Waverly Road.
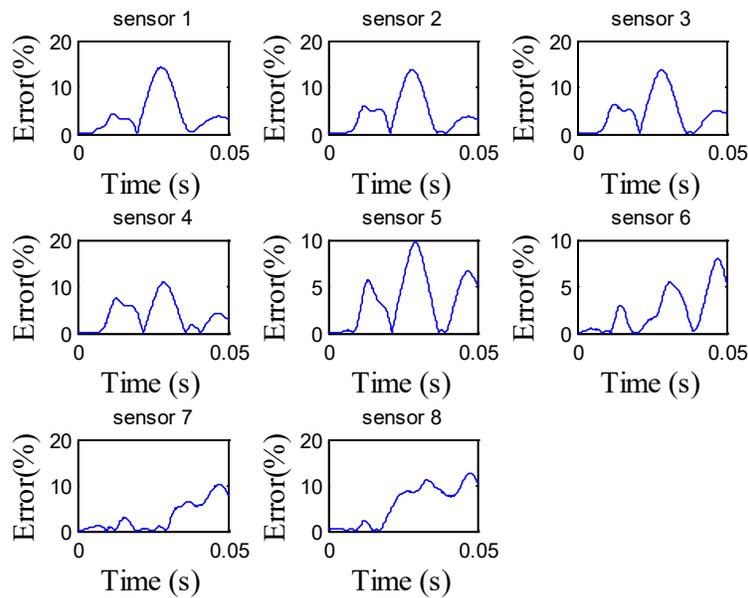
Figure 187. Graphs. Error in the backcalculated deflection time histories by sensor for 1 p.m. tests for Waverly Road.

The significant practical implications from these results are the following:

- Conducting two FWD tests in the field with a pavement temperature difference of 18 to 27 °F between the two tests (in this case one test at 9 a.m. at about 59 to 61°F and a second test at 1 p.m. at about 79 to 86 °F) seemed to be sufficient to backcalculate the damaged AC modulus master curve accurately, without the need to change the FWD load pulse duration; this was possible by conducting two successive dynamic backcalculation runs, where the results from run 1 were used as seed populations for the GA in the second run.

- Inaccuracies at the tail end of the sensor deflection time histories did not appear to compromise the ability of the dynamic viscoelastic backcalculation program DYNABACK-VE to accurately prediction all in situ layer properties, including the damaged AC modulus master curve, the depth to the stiff layer, and the stiff layer modulus.

LTPP Section 350801 Station 1: The Strategic Highway Research Program ID of the selected section is 0801 in New Mexico (State 35). The section was selected because the deflection time histories showed free vibrations at the end of the load pulse, suggesting that there were dynamic effects (the existence of stiff layer) and that the LTPP database included creep data for these sites to allow verification of the backcalculated results. In this analysis, the research team sought to backcalculate the depth to the stiff layer in addition to the stiff layer modulus using DYNABACK-VE. The backcalculation algorithm was run in two steps. The final population of the first step was entered as the initial population to the second step. Table 49 shows the pavement structure of section 350801. The AC layer was assumed to have a two-step piecewise temperature profile, as shown in figure 188. The measured deflection time histories are presented in figure 189. The FWD deflection data obtained from section 350801 showed some waviness at the end of the load pulse

suggesting the existence of a stiff layer. Table 50 shows the backcalculated layer parameters from the DYNABACK-VE backcalculation after all the steps of the algorithm. The results, as shown in figure 190 through figure 192 were very promising, indicating good stability and realistic values.

Table 49. Known layer properties for LTPP section 350801.

Layer	Elastic Modulus (psi)	Poisson's Ratio	Thickness (inches)	Unit Weight (pcf)
Asphalt	—	0.35	4.2	145
Base	—	0.4	9.7	125
Subgrade	—	0.45	—	100
Stiff layer	—	0.25	Infinity	125

— Indicates unknown value.
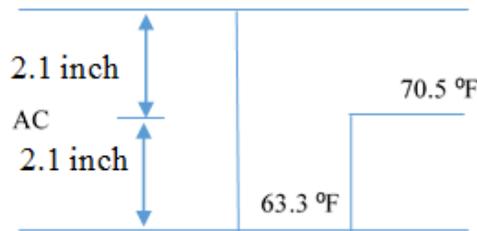
Figure 188. Diagram. Temperature profile for LTPP section 350801.
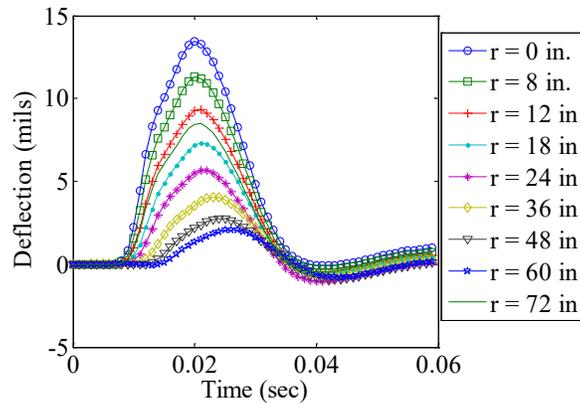
Figure 189. Graph. Measured FWD time histories for LTPP **section 350801.**

Table 50. Backcalculated layer parameters for drop 1, station 1—LTPP section 350801.

Parameters	Backcalculated
c_1	1.09999
c_2	3.401333
c_3	1.024748
c_4	-0.50124
a_1	0.001096
a_2	-0.0926
E_{base} (psi)	20,822.38
$E_{subgrade}$ (psi)	18,857.25
$h_{subgrade}$ (inches)	193.32
E_{stiff} (psi)	236,363.82
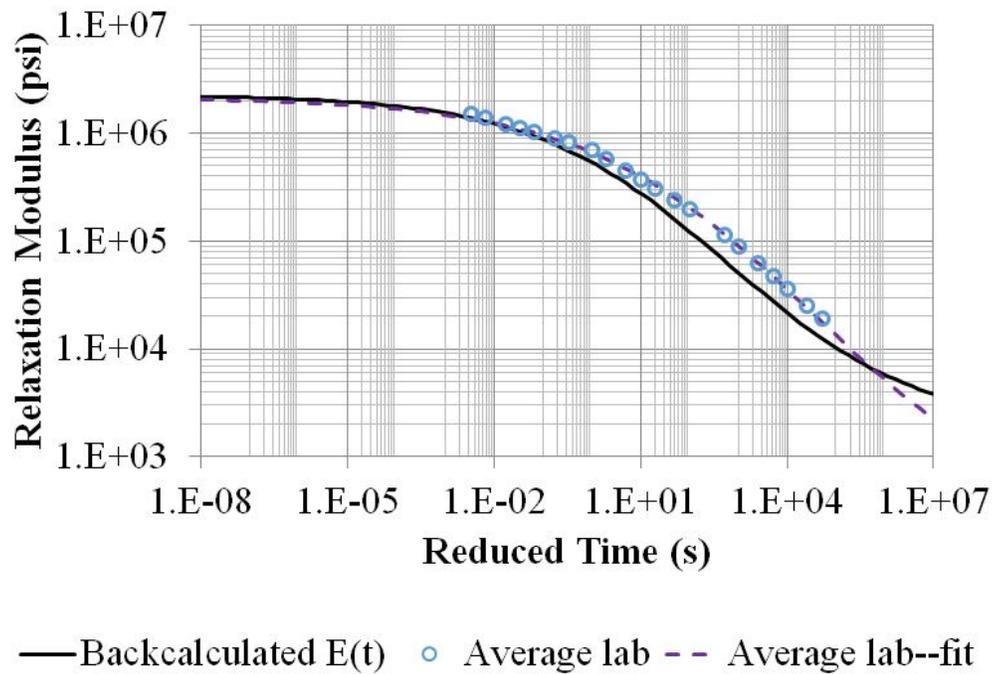
Figure 190. Graph. Backcalculation results of the AC master curve for LTPP section 350801.
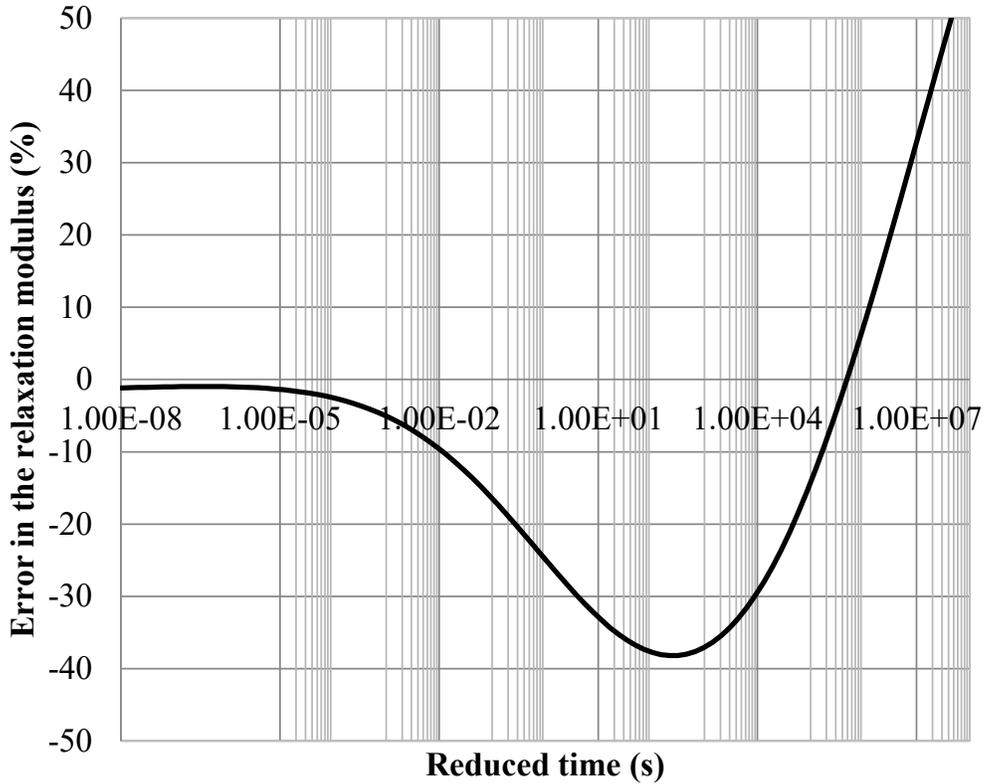
Figure 191. Graph. Error in the backcalculated master curve for LTPP **section 350801.**
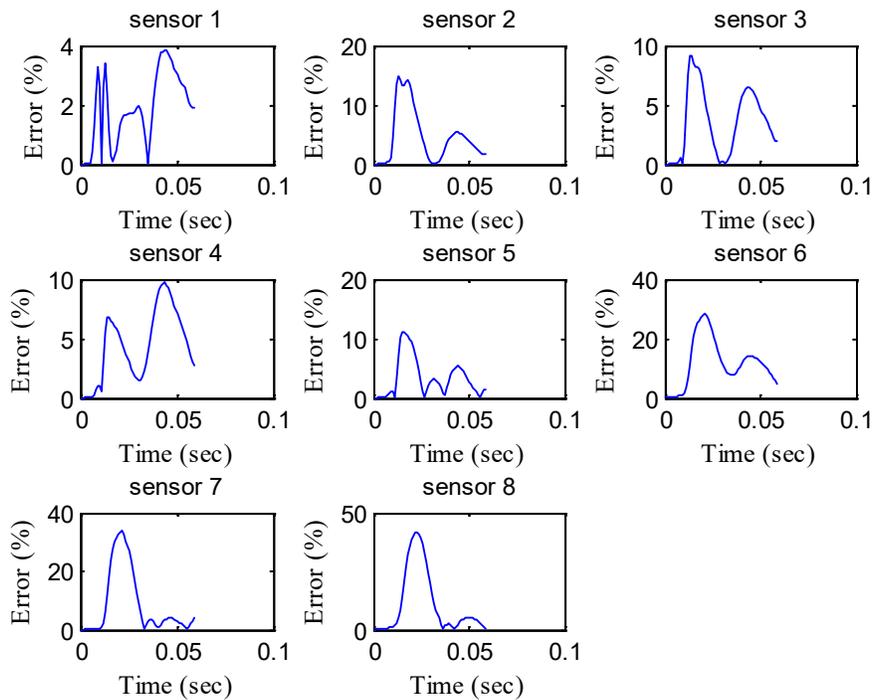
Figure 192. Graphs. Error in the backcalculated time histories by sensor for LTPP **section 350801.**

174

The following two interesting observations are worth noting:

- The depth to the stiff layer is estimated at about 16 ft; this agrees with the predictions from Ullidtz method, which suggested presence of a shallow stiff layer at about 15 ft.[94]

- The backcalculated stiff layer modulus from run 2 is 236,363 psi, which is much closer to what would be expected from stiff soils. Figure 190 shows the backcalculated relaxation modulus master curves. Figure 191 shows the corresponding percent error. It is clear that running a second backcalculation using the results from the first run as seed populations led to a much improved backcalculated AC modulus master curve. Figure 192 and figure 193 show the measured and predicted deflection time histories and the corresponding percent error, respectively. The backcalculation results are good, although relatively large errors are seen in the most distant deflection sensors. Running a second backcalculation using the results from the first run as seed populations leads to a much improved backcalculated AC modulus master curve.
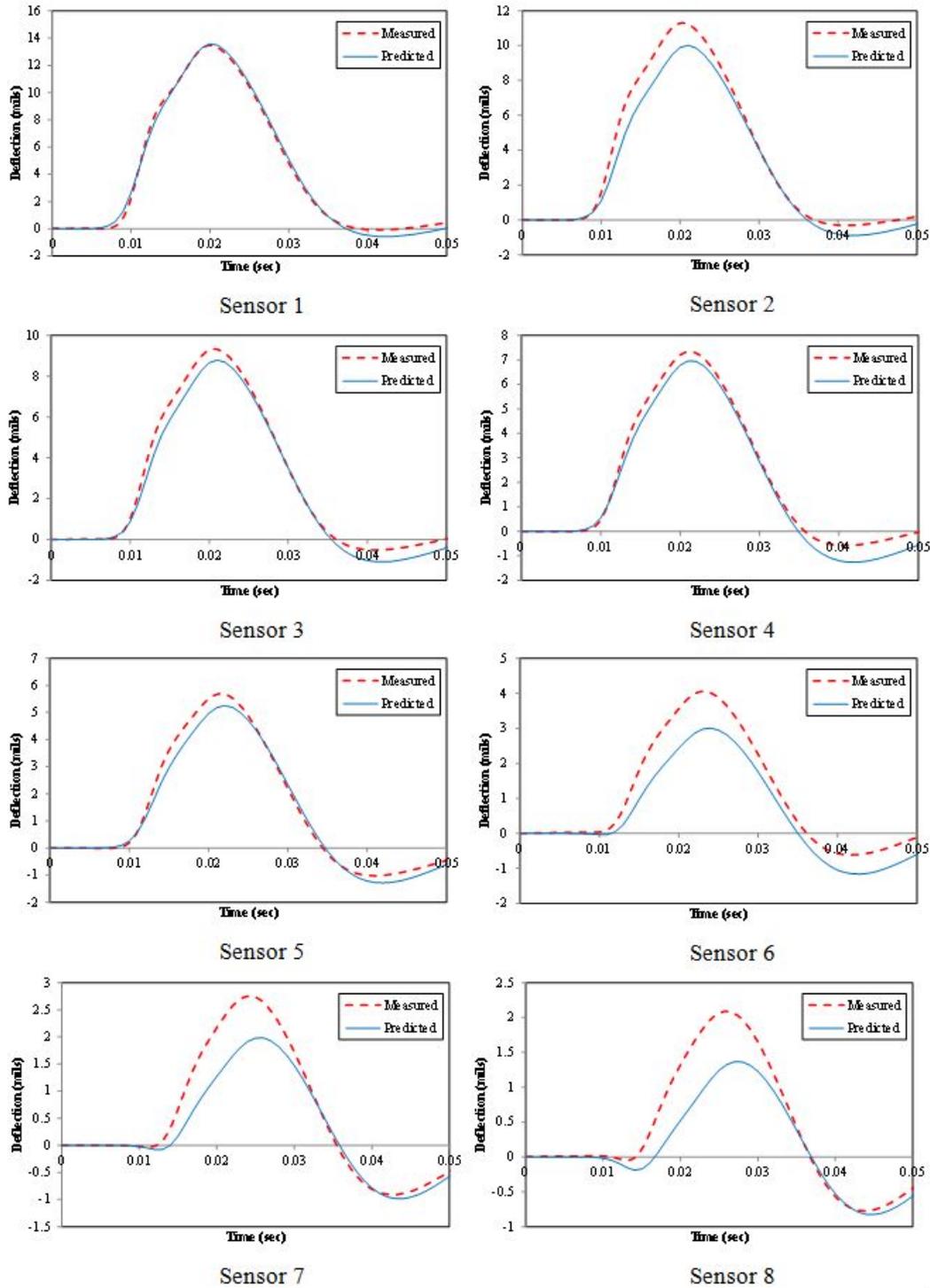
Figure 193. Graphs. Backcalculated versus measured deflection time histories by sensor for LTPP **section 350801, station 1.**

LTPP Section 350801 Station 8: The deflection time histories of section 350801 station 8 also showed free vibrations at the end of the load pulse. The approach described in the previous section was used to backcalculate the master AC master curve, the moduli of the unbound layers,

and the depth to the stiff layer. Table 49 shows the pavement structure of section 350801. For this section, the AC layer was assumed to have a three-step piecewise temperature profile, as shown in figure 194. The measured deflection time histories are presented in figure 195.

Table 51 shows the backcalculated layer parameters from the DYNABACK-VE backcalculation. Recall that the algorithm is minimizing the error on $(c_1 + c_2)$. Therefore, the evaluation of the backcalculation algorithm should be based on $(c_1 + c_2)$. The results were very promising, indicating good stability and realistic values. Figure 196 shows the backcalculated relaxation modulus master curves. Figure 197 shows the corresponding percent error. It was clear that running a second backcalculation using the results from the first run as seed populations led to a much improved backcalculated AC modulus master curve. Figure 198 shows the measured and predicted deflection time histories. The backcalculation results were good, although relatively large errors were seen in the farther deflection sensors. The error results were good compared with the results presented in the previous section for station 1. The backcalculation results for station 8 were significantly better than those for station 1. The error was less than 20 percent for reduced times up to 104 s (laboratory value of 20,000 psi versus backcalculated value of 24,000 psi at 104 s). Figure 198 shows very good agreement between the measured and predicted deflection histories for station 8, although there was a larger time shift for sensors 6 through 8. It is believed that this could be due to a synchronization problem between the load and deflection measurements.

To summarize, the backcalculation results were very promising, indicating good stability and realistic values. The backcalculation results for the LTPP section, while reasonable, were not as good as those for the Waverly Road section because only one temperature profile was available; using the morning and afternoon data in the Waverly test increased the over-determinacy of the optimization problem.
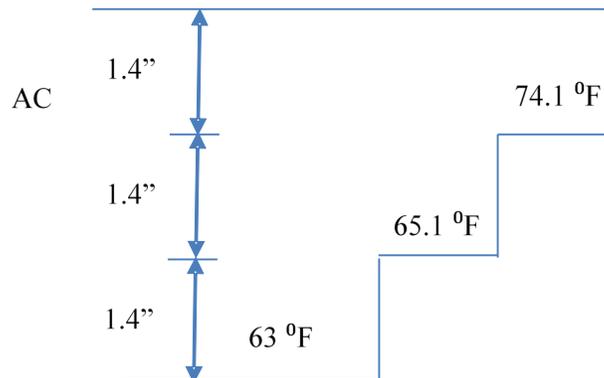
Figure 194. Diagram. Temperature profile for LTPP section 350801.
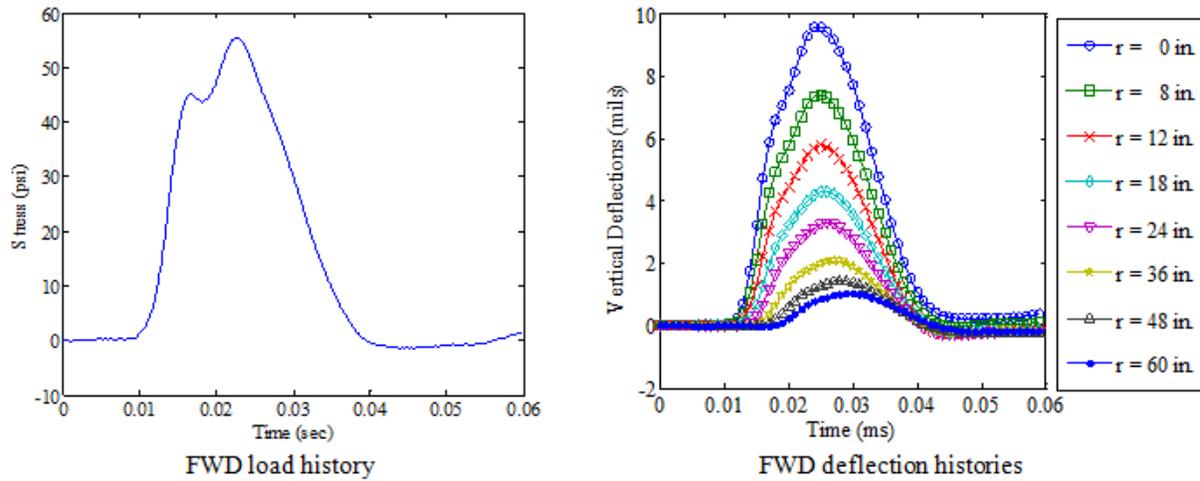
Figure 195. Graphs. Measured FWD load and deflection time histories for LTPP **section 350801.**

Table 51. Backcalculated layer parameters for drop 1 station 8 for LTPP **section 350801.**

Parameter	Laboratory	Backcalculated
c_1	0.120	0.804351
c_2	4.049	3.350811
c_3	1.112	0.905003
c_4	-0.423	-0.48508
a_1	6.66E-05	0.0011361
a_2	-1.41E-01	-0.13538745
E_{base} (psi)	—	26,183
$E_{subgrade}$ (psi)	—	21,579
$h_{subgrade}$ (inches)	180 (1/r method)	185.93
E_{stiff} (psi)	—	714,658

— Indicates data were not available.

178
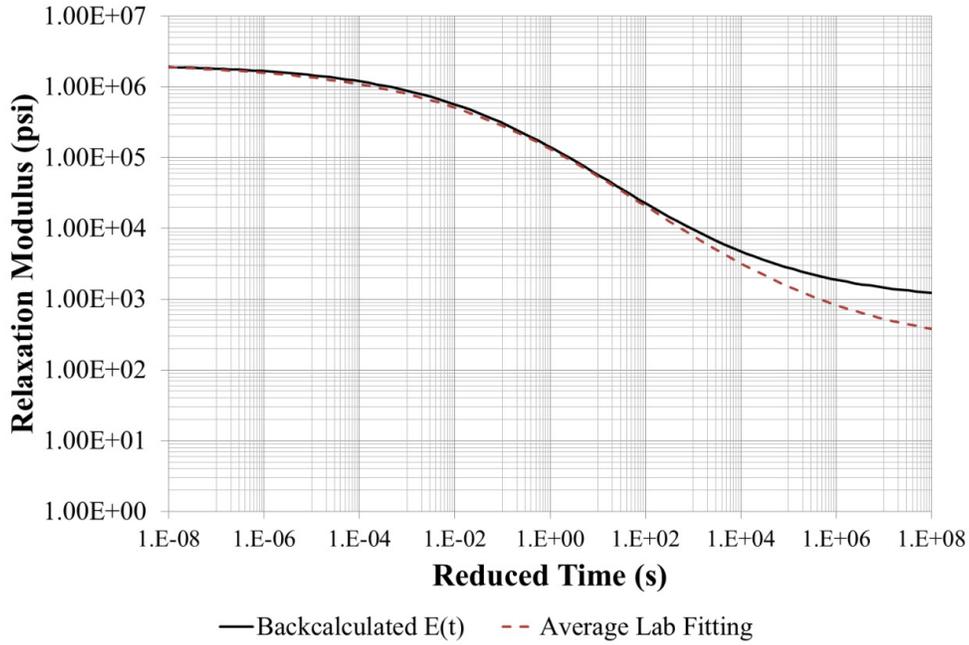
Figure 196. Graph. Backcalculation results of the AC master curve for LTPP **section 350801.**
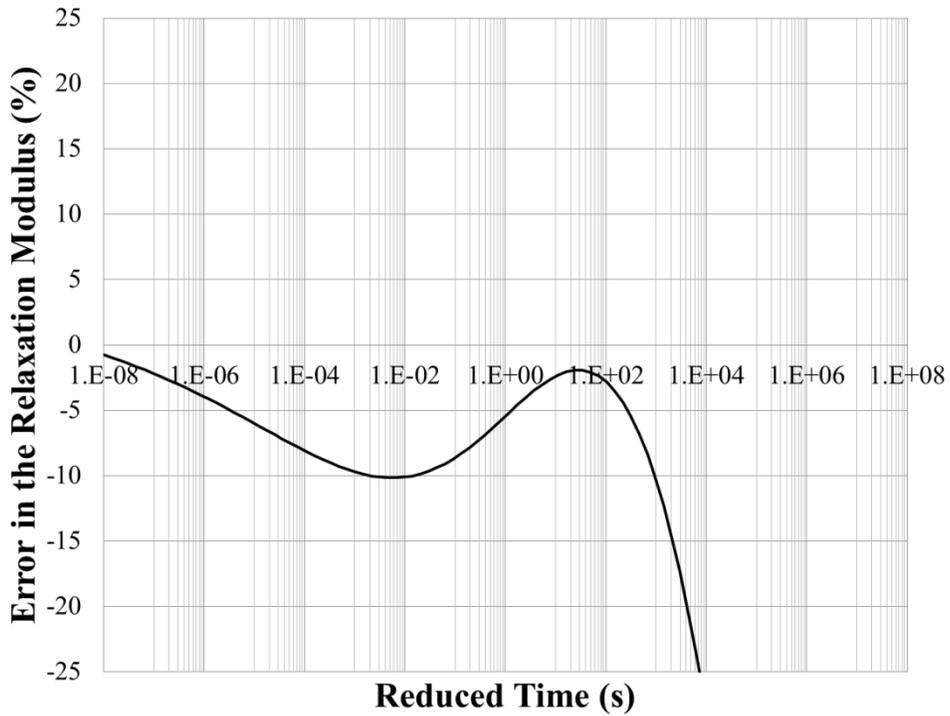
Figure 197. Graph. Error in the backcalculated master curve for LTPP **section 350801.**
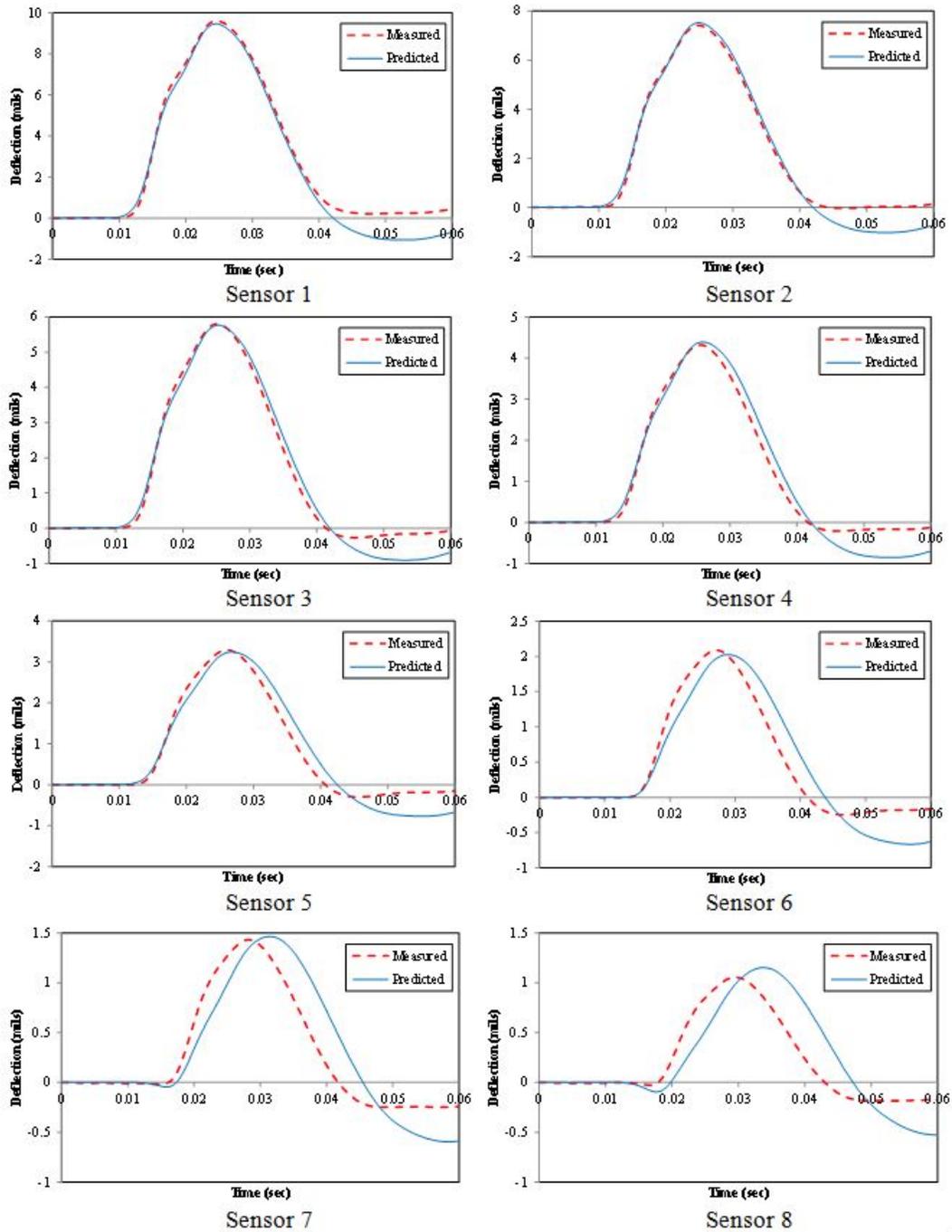
**Figure 198. Graphs. Backcalculated versus measured deflection time histories by sensor for
LTPP section 350801, station 8.**

Effect of Pulse Width on Backcalculation Results

The previous section included a discussion of how conducting two FWD tests in the field with a
pavement temperature difference of 50 to 59 °F between the two tests seemed to be sufficient to
backcalculate the damaged AC modulus master curve accurately without the need to change the
FWD load pulse duration. However, for budgetary and time constraints, it might be impractical

to conduct two FWD tests. For these reasons, the research team investigated the effect of increasing the pulse width to increase the useful time range and improve the backcalculation results. However, the team also considered the temperature profile along the AC layer to be able to backcalculate the shift factor coefficients. The effect of using multiple pulses is discussed in appendix B.

The dynamic viscoelastic simulation was carried out using the pavement structure presented in table 52. The FWD loading used in this simulation was assumed to be uniformly distributed over a circular area of a radius of 6 inches, a peak magnitude of 9,000 lb, and pulse durations of 35, 40, 45, and 50 ms (figure 199). The subgrade layer was modeled to be with a shallow stiff layer (2 million psi) located at about 9 ft below the pavement surface (figure 200). The surface deflections were calculated at radial distances of 0, 8, 12, 18, 24, 36, 48, 60, and 72 inches from the center of the loading plate. The viscoelasticity of the AC was modeled using a Prony series of the master curve presented in figure 201 (left). The AC layer was divided into two layers with different temperatures as shown in figure 201 (right). The results of the simulations are presented in figure 202.

Table 52. Layer properties for dynamic viscoelastic simulation.

Layer	Elastic Modulus (psi)	Poisson's Ratio	Thickness (inches)	Unit Weight (pcf)
Asphalt	Master curve (86.9 °F)	0.35	2	145
Asphalt	Master curve (79.3 °F)	0.35	2	145
Base	20,000	0.4	6	125
Subgrade	13,500	0.45	96	100
Stiff layer	2,000,000	0.25	Infinity	125
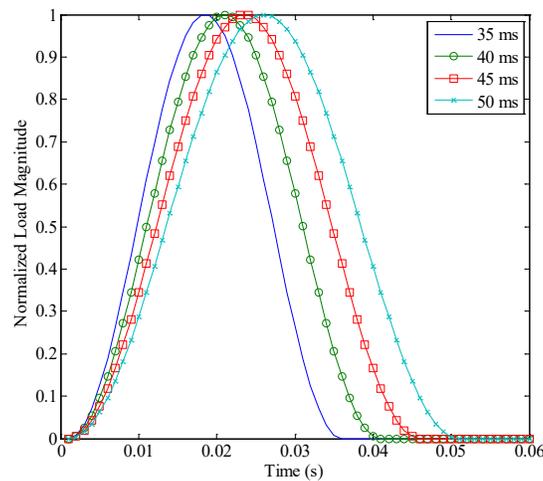
Figure 199. Graph. Simulated FWD load pulses with various durations.
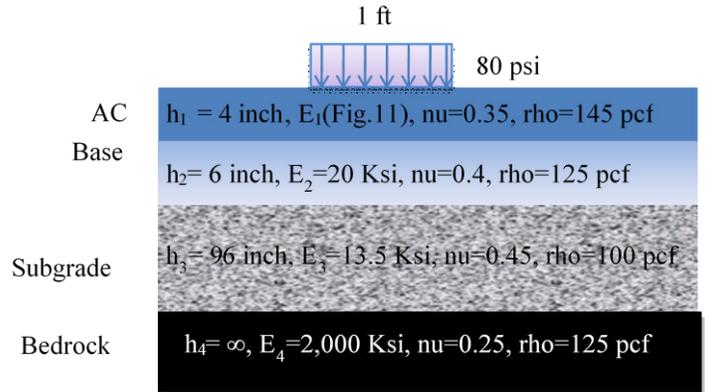
Figure 200. Diagram. Schematic of the pavement structure with bedrock.

AC — $h_1 = 4$ inch, E_1(Fig.11), nu=0.35, rho=145 pcf

Base — $h_2 = 6$ inch, E_2=20 Ksi, nu=0.4, rho=125 pcf

Subgrade — $h_3 = 96$ inch, E_3=13.5 Ksi, nu=0.45, rho=100 pcf

Bedrock — $h_4 = \infty$, E_4=2,000 Ksi, nu=0.25, rho=125 pcf

Master curve

Temperature profile
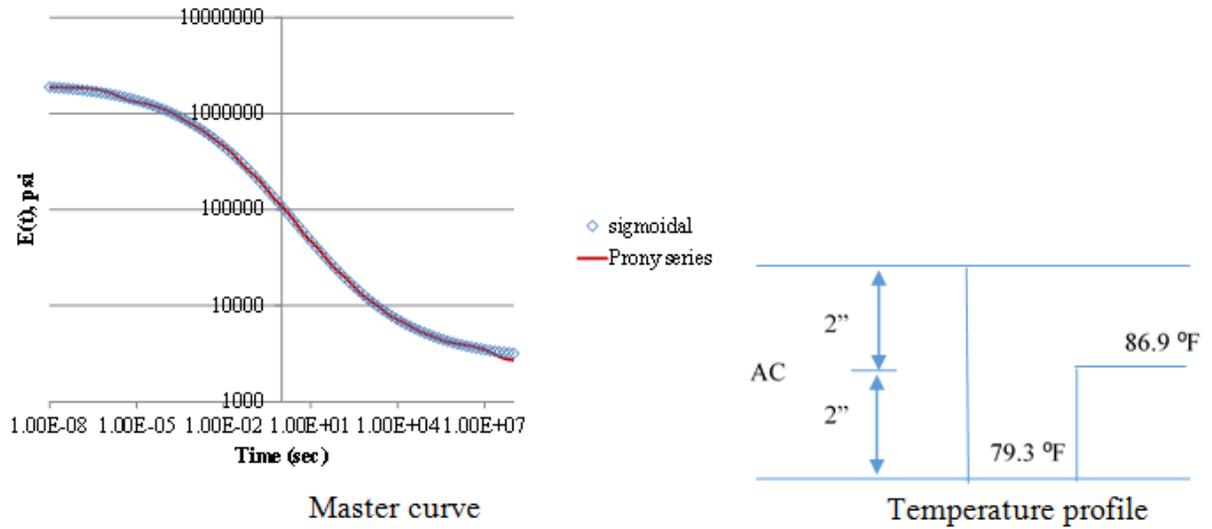
Figure 201. Graph and Diagram. AC layer parameters.
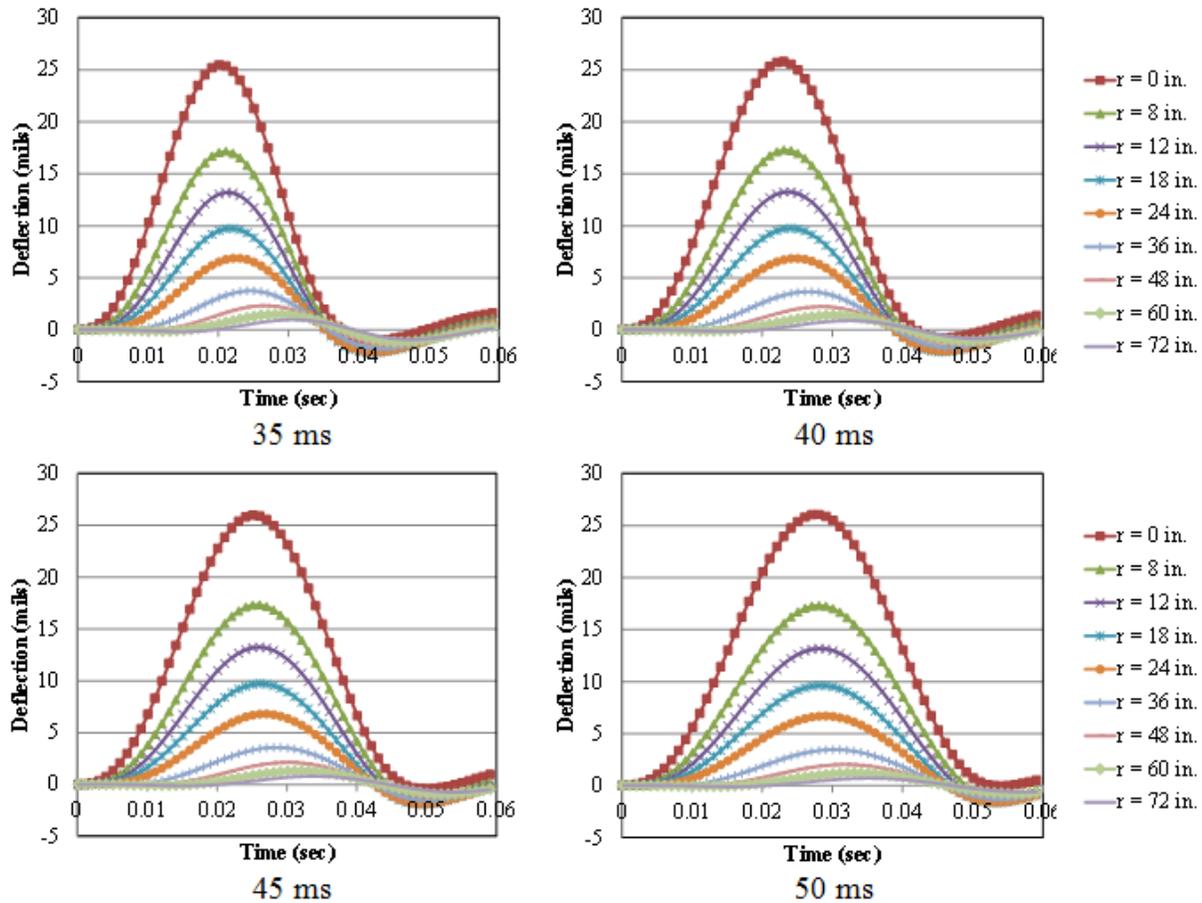
Figure 202. Graphs. Surface deflections of pavement structure for different widths of load pulses.

The analysis shows that increasing the width of the FWD pulse would improve the backcalculation of the master curve. However, it would not improve the backcalculation of unbound layer moduli. In the previous section, it was shown that running a second backcalculation using the results from the first run as seed populations not only led to a much improved backcalculated AC modulus master curve but also to much closer base and subgrade moduli. This was because running the second backcalculation after replacing half of the population with random strings increased not only the diversity of the population but the number of generations. As the number of generation increased, the individuals in the population got closer together and approached the minimum point. For all these reasons, the research team recommends increasing the size of the population to 300 when increasing the pulse width instead of testing at different temperatures. Table 53 shows the viscoelastic dynamic backcalculation results of the pavement structure presented in table 52. Figure 203 through figure 206 show the error in the deflection time histories.

Table 53. Backcalculated layer parameters for different pulse durations.

Parameter	Simulation	Backcalculated			
		35 ms	40 ms	45 ms	50 ms
c_1	1.271	1.606	1.501	1.404	1.359
c_2	2.883	2.405	2.550	2.677	2.796
c_3	0.22	0.323	0.302	0.286	0.152
c_4	-0.497	-0.595	-0.582	-0.574	-0.526
a_1	0.00109568	1.12E-06	0.000163	0.000574	0.001516
a_2	-0.0925978	-0.08675	-0.12647	-0.09447	-0.09126
E_{base} (psi)	20,000	20,373	20,744	20,546	20,386
$E_{subgrade}$ (psi)	13,500	15,235	16,311	17,667	14,289
$h_{subgrade}$ (inches)	96	103.1	110.1	121.4	100.4
E_{stiff} (psi)	2,000,000	773,111	607,944	701,243	898,816
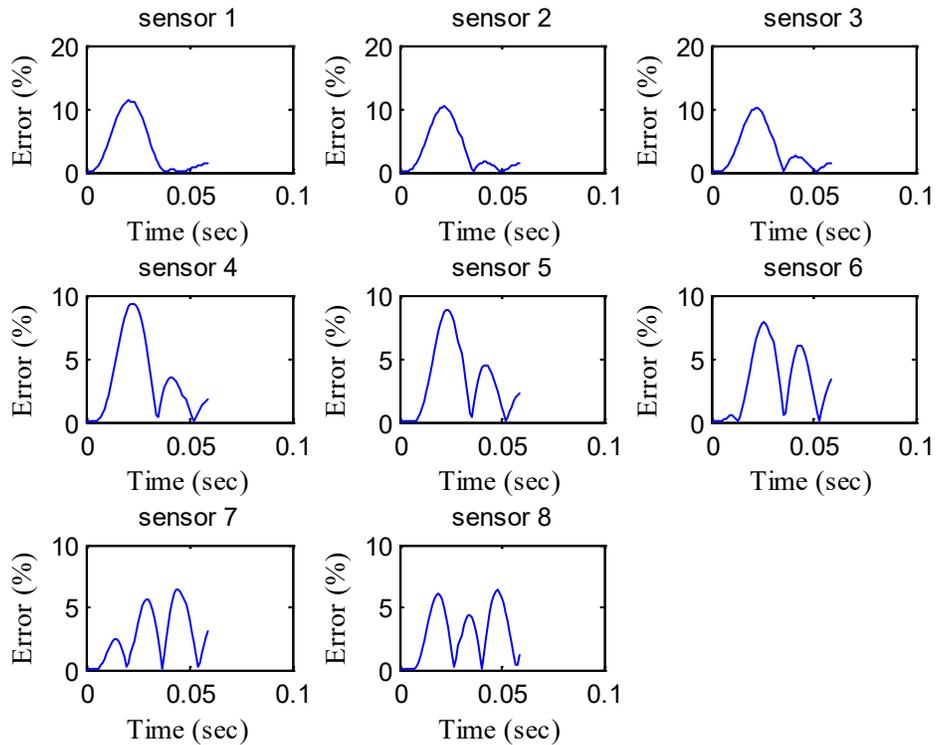
Figure 203. Graphs. Error in the backcalculated time histories by sensor for a pulse width of 35 ms.
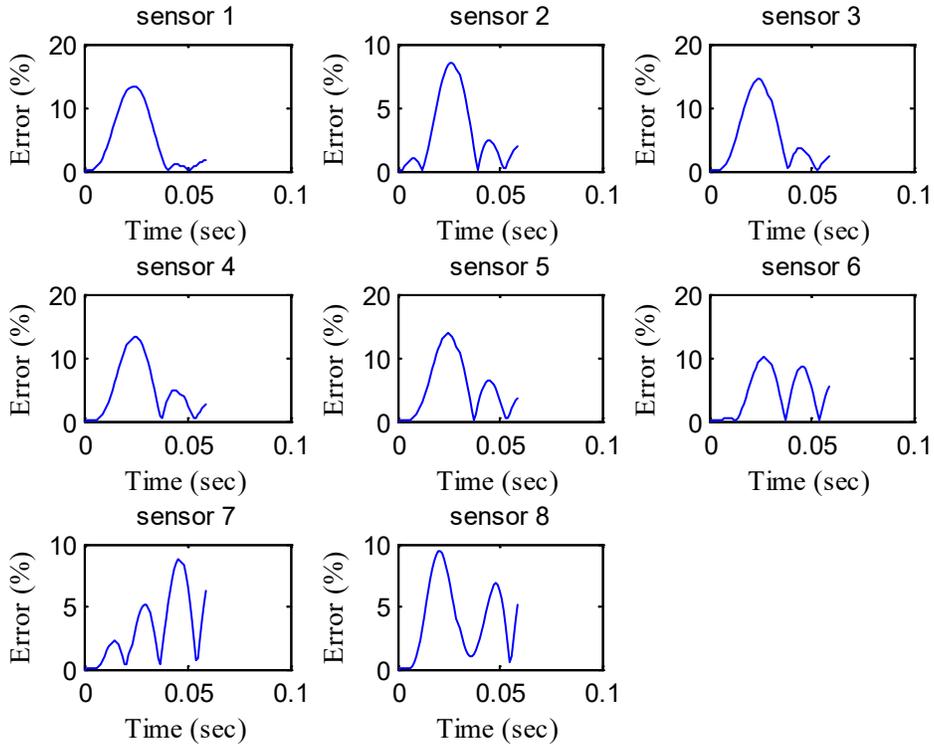
Figure 204. Graphs. Error in the backcalculated time histories by sensor for a pulse width of 40 ms.
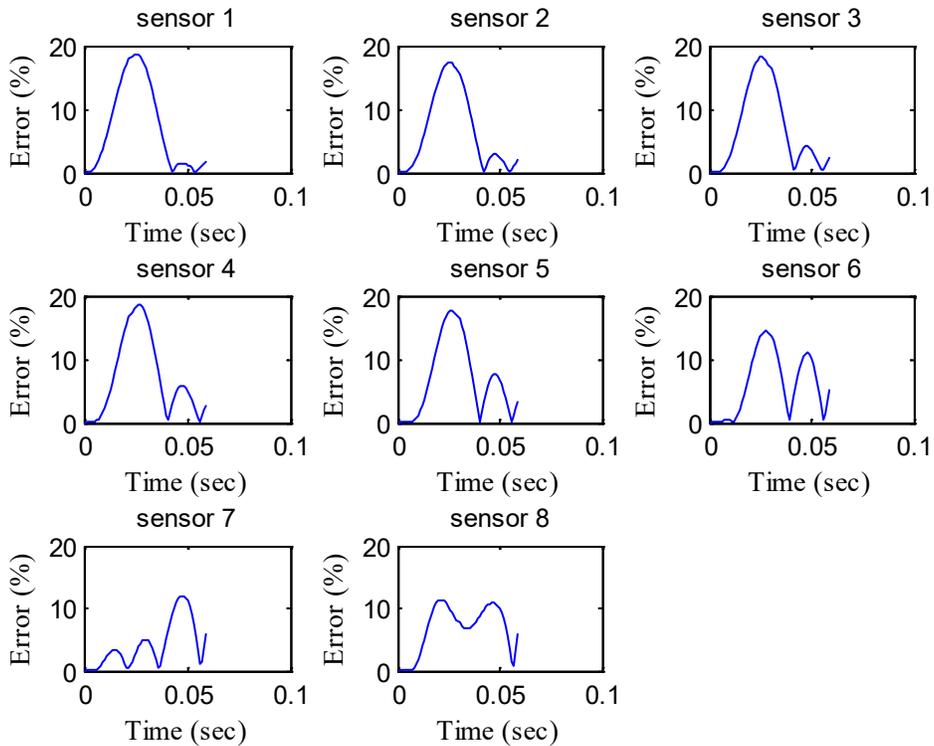
Figure 205. Graphs. Error in the backcalculated time histories by sensor for a pulse width of 45 ms.

185
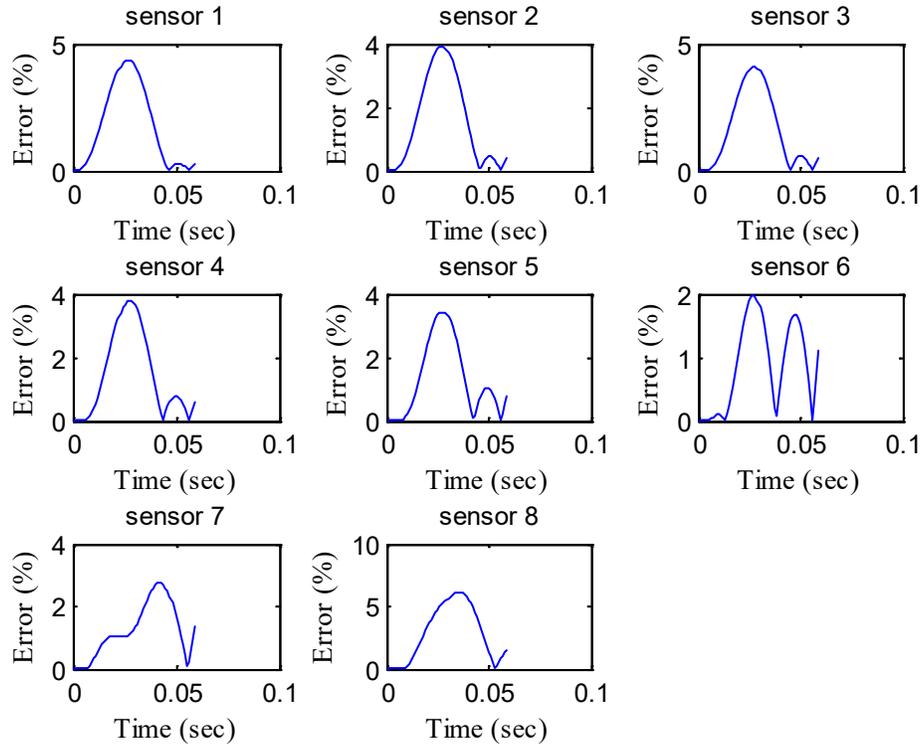
Figure 206. Graphs. Error in the backcalculated time histories by sensor for a pulse width of 50 ms.

Figure 207 shows the backcalculated relaxation modulus master curve. Figure 208 shows the corresponding error using different pulse widths. The results were quite reasonable, except for the tail end of the $E(t)$ curve (longer reduced time range).
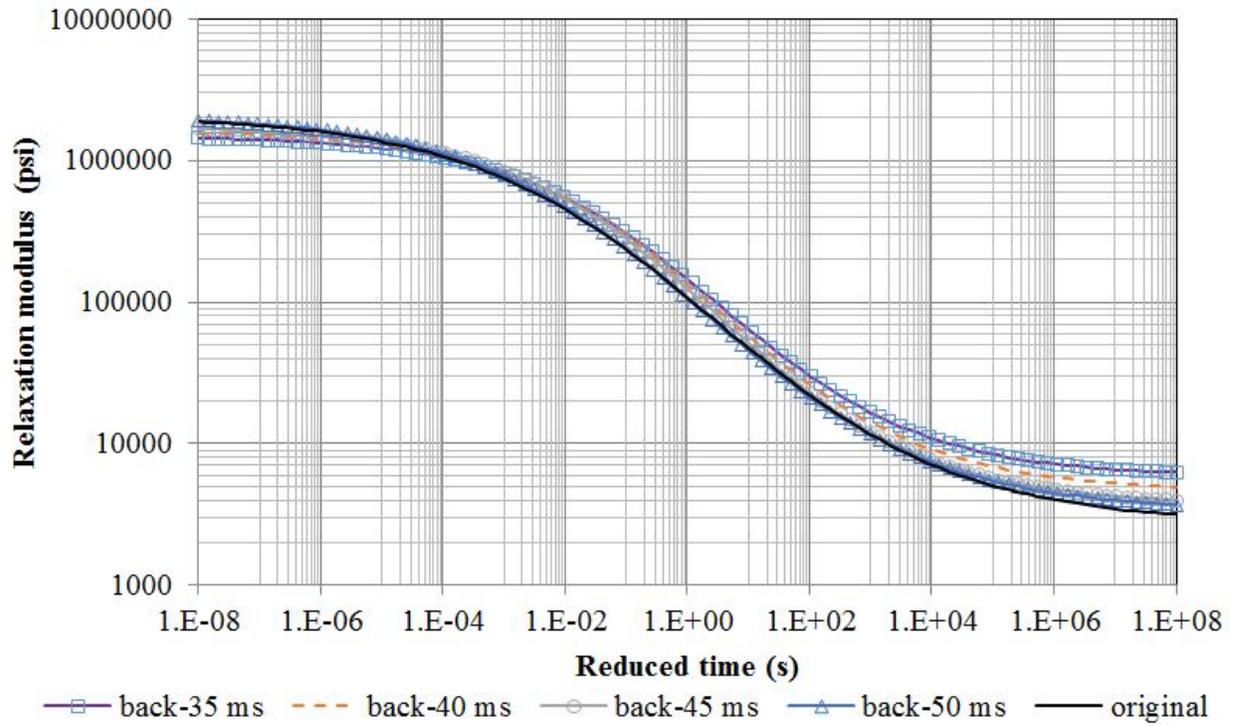
Figure 207. Graph. Backcalculation results of the AC master curve for different pulse widths.
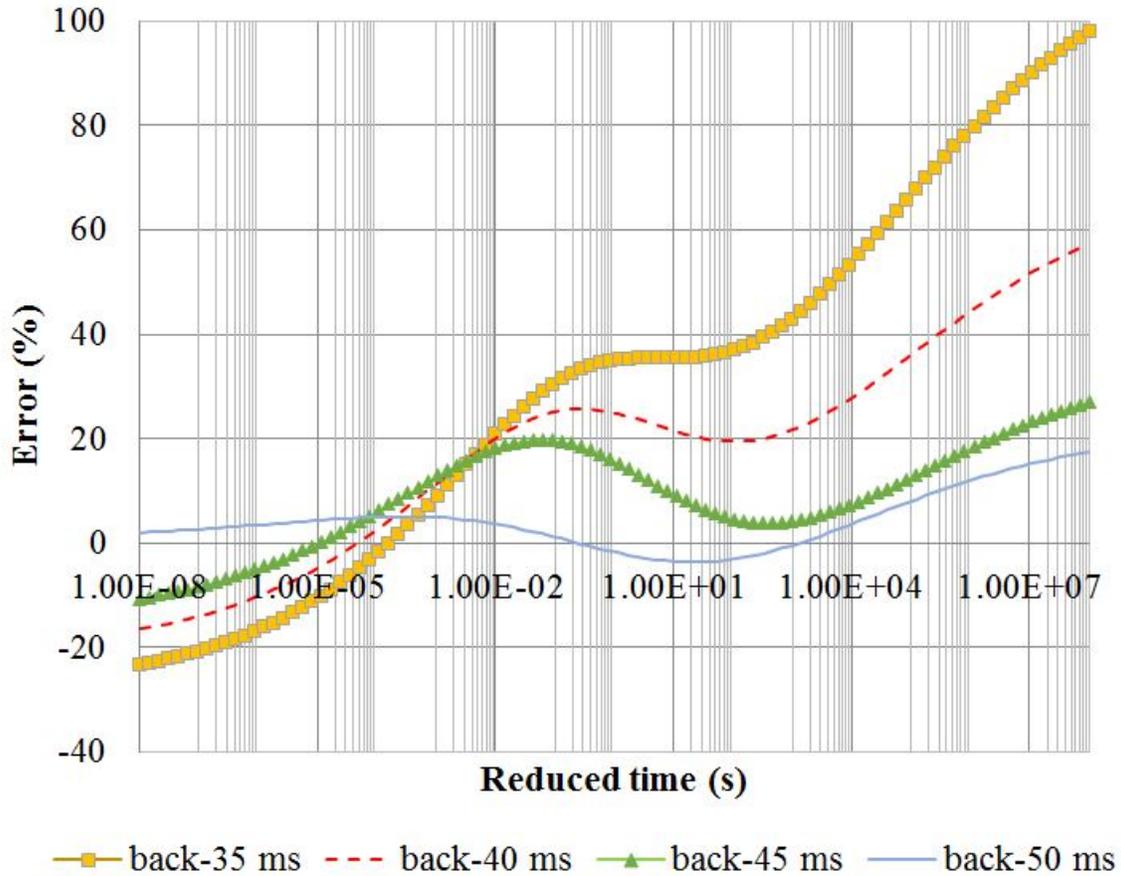
Figure 208. Graph. Error in the backcalculated master curve for different pulse widths.

To conclude, the research team concluded that increasing the pulse width will improve the backcalculation of the master curve, which can be used instead of having to test at multiple temperatures. However, the team also concluded that including a temperature profile is important to be able to backcalculate the shift factors. Two major studies looked at a method to predict the temperature profile using air and pavement surface temperatures. The empirical relationships provided in the LTPP guide and in the Ongel and Harvey study reported errors of 9 and 18 °F, respectively.[5,100] The analysis conducted as part of the current project showed that the temperature gradient in the AC layer is 18 °F at most, which is the same order of magnitude as the error reported by both studies. Therefore, using predicted temperature with depth using such models does not lead to reliable results. It is recommended at this point to use the LTPP manual to manually measure the temperature profile.[5]

Computational Efficiency

Table 54 presents the computation efficiency of the backcalculation algorithm for all the previously discussed analyses. Note that the efficiency of the backcalculation using the MPI parallelization scheme is only an estimate. The algorithm written in MATLAB® was used in all runs.

Table 54. Backcalculation algorithm computational efficiency using GA only.

Backcalculation		Computational Efficiency	
Analysis Type	Characteristics	Eight Cores	MPI[1]
Sensitivity	35/15	5	0.67
	70/15	11.5	1.5
	100/15	17	2.25
	200/15	33	4.4
	300/15	50	6.5
Simulation	Stiffness and thickness run 1	43	5.6
	Stiffness and thickness run 2	44	5.8
	Slope run 1	75	10
	Slope run 2	74.5	9.9
Field data	Waverly run 1	43.5	5.8
	Waverly run 2	44	5.8

[1]Estimated using equal distribution between cores.

BACKCALCULATION USING THE HYBRID APPROACH (DYNABACK-VE)

In this part of the project, the research team first used GA to obtain a good seed value and to make sure that the algorithm did not converge to a local minimum. Then, the team used the gradient-based LM algorithm to obtain the final results.

Evaluation of the Dynamic Backcalculation Scheme (DYNABACK-VE)

Sensitivity Analysis

The research team conducted a sensitivity analysis to select the optimal population/number of generations for the GA and maximum iteration for the LM algorithm. The viscoelastic simulation was carried out using the pavement structure presented in table 55. Figure 209 presents the simulated master curve for the asphalt layer along with the temperature profile. The FWD loading used in all simulations was assumed to be uniformly distributed over a circular area of a radius of 6 inches, a peak magnitude of 9,000 lb, and a duration of 35 ms. Figure 210 (left) presents the simulated FWD load pulse. The subgrade layer was modeled to have a shallow stiff layer (250,000 psi) located at about 8 ft below the pavement surface. The surface deflections were calculated at radial distances of 0, 8, 12, 18, 24, 36, 48, 60, and 72 inches from the center of the loading plate. Figure 210 (right) shows the simulated deflections time histories for all sensors.

Table 55. Layer properties for the simulated pavement structure.

Layer	Elastic Modulus (psi)	Poisson's Ratio	Thickness (inches)	Unit Weight (pcf)
Asphalt	Master curve (86.9 °F)	0.35	2	145
	Master curve (79.3 °F)	0.35	2	145
Base	20,000	0.35	6	125
Subgrade	13,500	0.45	96	120
Stiff layer	250,000	0.30	Infinity	145
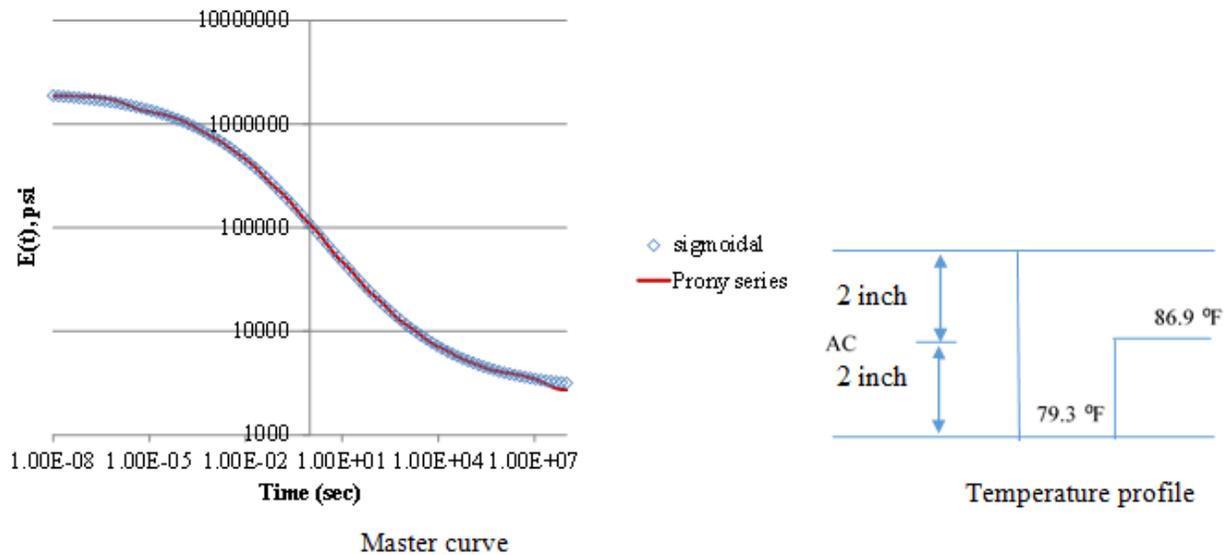
Figure 209. Graph and Diagram. AC layer master curve and temperature profile.
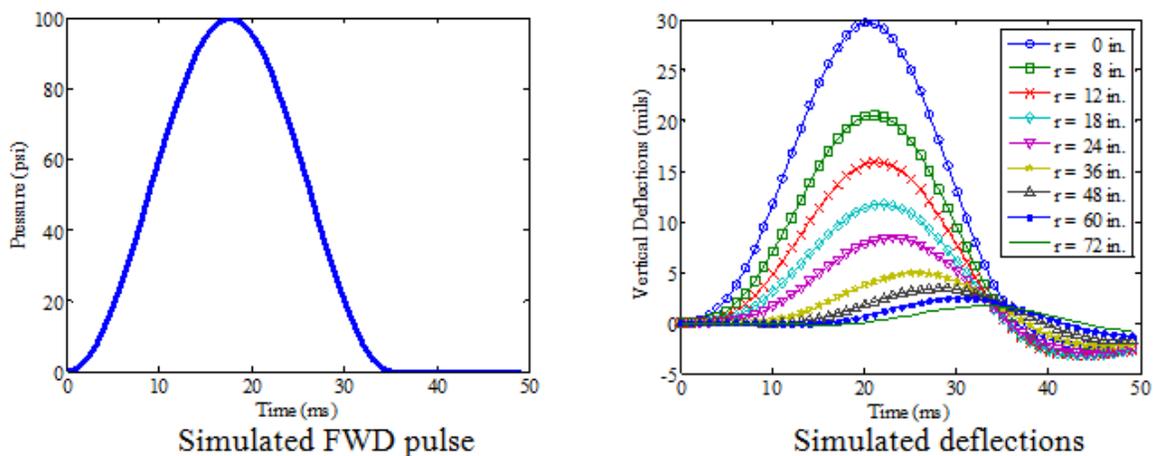
Figure 210. Graphs. Simulated FWD pulse and deflection time histories.

Table 56 presents the information for all 60 runs (19 LM method runs, 25 hybrid method runs, and 16 GA method runs). The last column for each method shows the total number of calls to the forward solution (ViscoWave-II) and hence gives an indication of computational cost, i.e., the higher the number the higher the computational cost.

It was observed during the sensitivity analysis that the convergence of the backcalculation using only the LM algorithm was not guaranteed. The algorithm was very sensitive to the seed values. If the seed values were close to the real values, the algorithm converged very fast (about 25 iterations). However, when the seed values were picked randomly inside the search domain, the algorithm converged fast to a local solution or sometimes it diverged as shown in figure 211.

190

Table 56. Runs information for the sensitivity analysis.

Method	Run Number	Population Size	Number of Generations	Number of Iterations	Number of Calls to ViscoWave-II
LM	1	—	—	100	100
	2	—	—	150	150
	3	—	—	200	200
	4	—	—	250	250
	5	—	—	300	300
	6	—	—	350	350
	7	—	—	400	400
	8	—	—	450	450
	9	—	—	500	500
	10	—	—	550	550
	11	—	—	600	600
	12	—	—	650	650
	13	—	—	700	700
	14	—	—	750	750
	15	—	—	800	800
	16	—	—	850	850
	17	—	—	900	900
	18	—	—	950	950
	19	—	—	1,000	1,000
GA+LM	20	50	5	100	350
	21	50	5	150	400
	22	50	5	200	450
	23	50	5	250	500
	24	50	5	300	550
	25	75	5	100	475
	26	75	5	150	525
	27	75	5	200	575
	28	75	5	250	625
	29	75	5	300	675
	30	100	5	100	600
	31	100	5	150	650
	32	100	5	200	700
	33	100	5	250	750
	34	100	5	300	800
	35	150	5	100	850
	36	150	5	150	900
	37	150	5	200	950
	38	150	5	250	1,000
	39	150	5	300	1,050
	40	200	5	100	1,100
	41	200	5	150	1,150

Method	Run Number	Population Size	Number of Generations	Number of Iterations	Number of Calls to ViscoWave-II
	42	200	5	200	1,200
	43	200	5	250	1,250
	44	200	5	300	1,300
GA	45	35	5	—	175
	46	50	5	—	250
	47	75	5	—	375
	48	100	5	—	500
	49	150	5	—	750
	50	200	5	—	1,000
	51	250	5	—	1,250
	52	300	5	—	1,500
	53	35	15	—	525
	54	50	15	—	750
	55	75	15	—	1,125
	56	100	15	—	1,500
	57	150	15	—	2,250
	58	200	15	—	3,000
	59	250	15	—	3,750
	60	300	15	—	4,500

— Indicates not applicable.
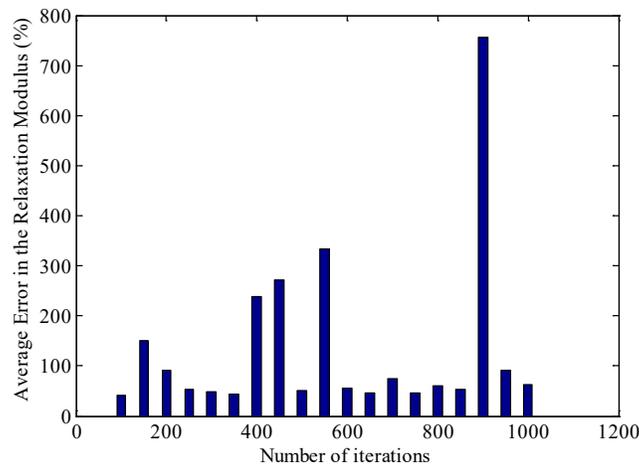
Figure 211. Graph. Average error in the backcalculated AC layer master curve for all runs in LM method.

The average error (over reduced times from 10^{-8} to 10^{8} s) in the $E(t)$ master curve was defined in figure 211. The runs in which the algorithm diverged were repeated. Figure 212 shows the results in terms of average errors in $E(t)$ from the DYNABACK-VE. Figure 213 through figure 216 show the results for base, subgrade, and stiff layer moduli as well as the depth to the stiff layer.
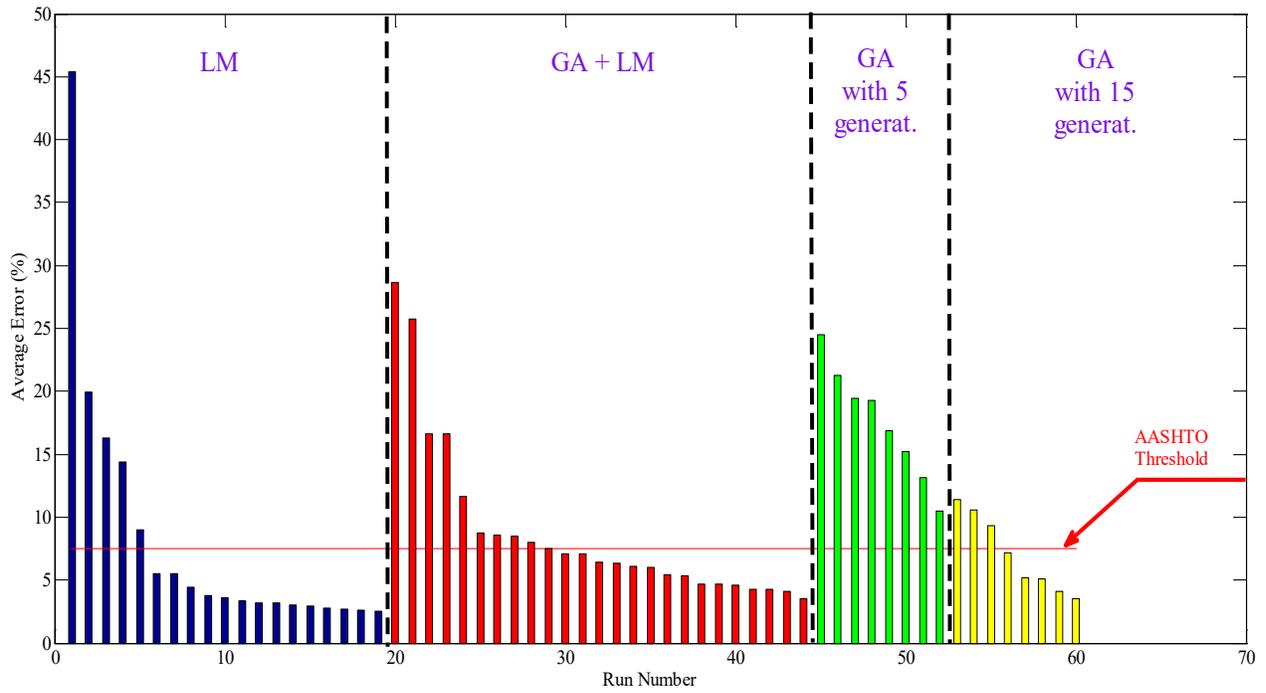
Figure 212. Graph. Average error in the backcalculated AC layer master curve for all runs.
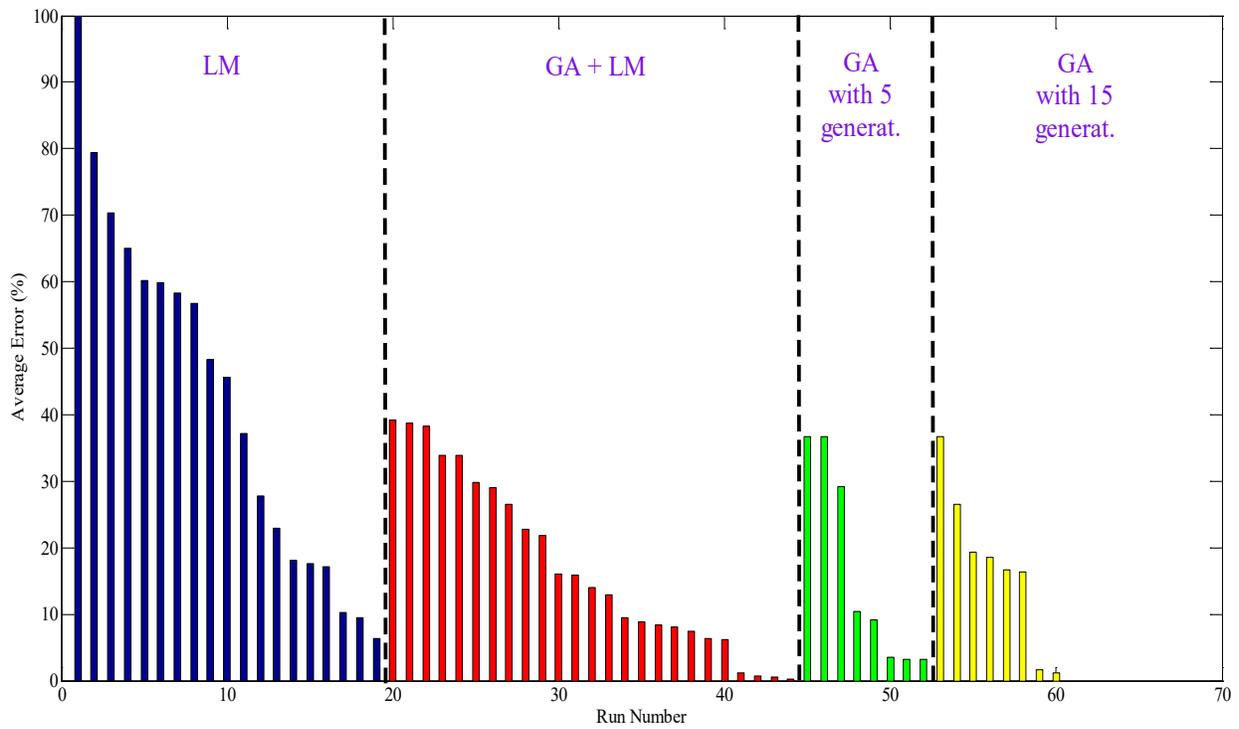
Figure 213. Graph. Average error in the backcalculated base layer modulus for all runs.
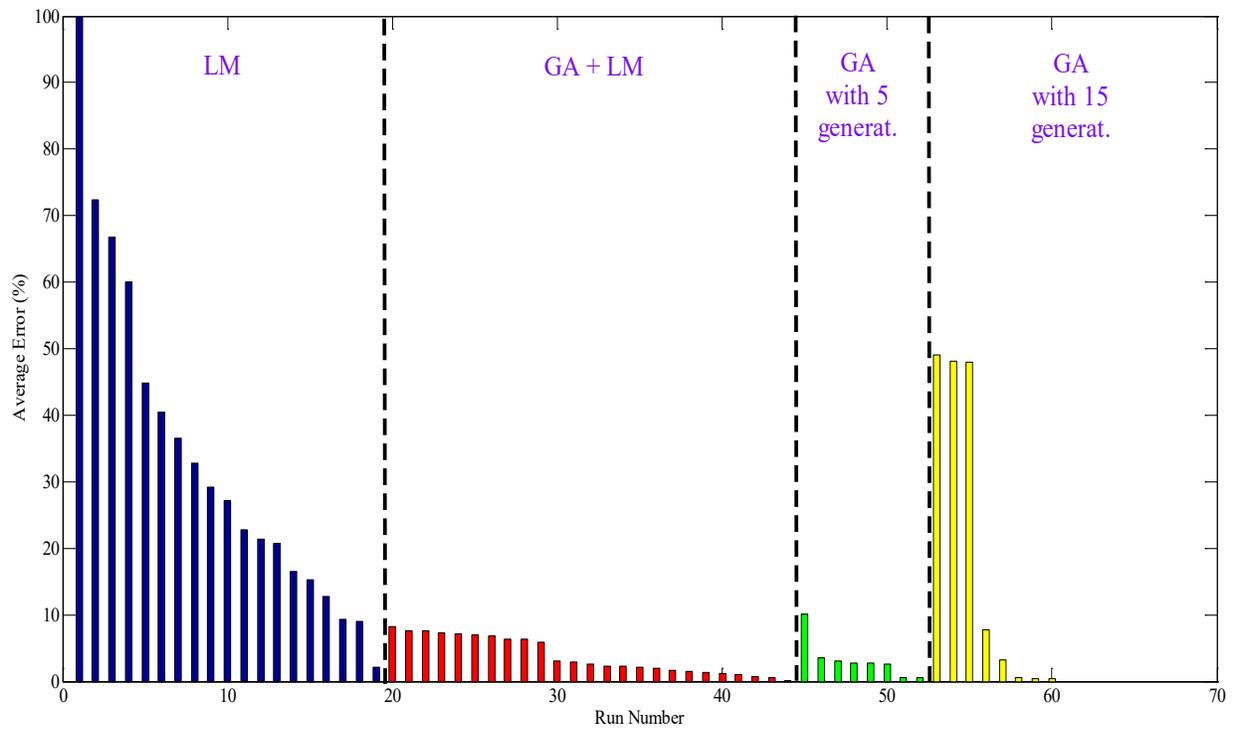
Figure 214. Graph. Average error in the backcalculated subgrade modulus for all runs.
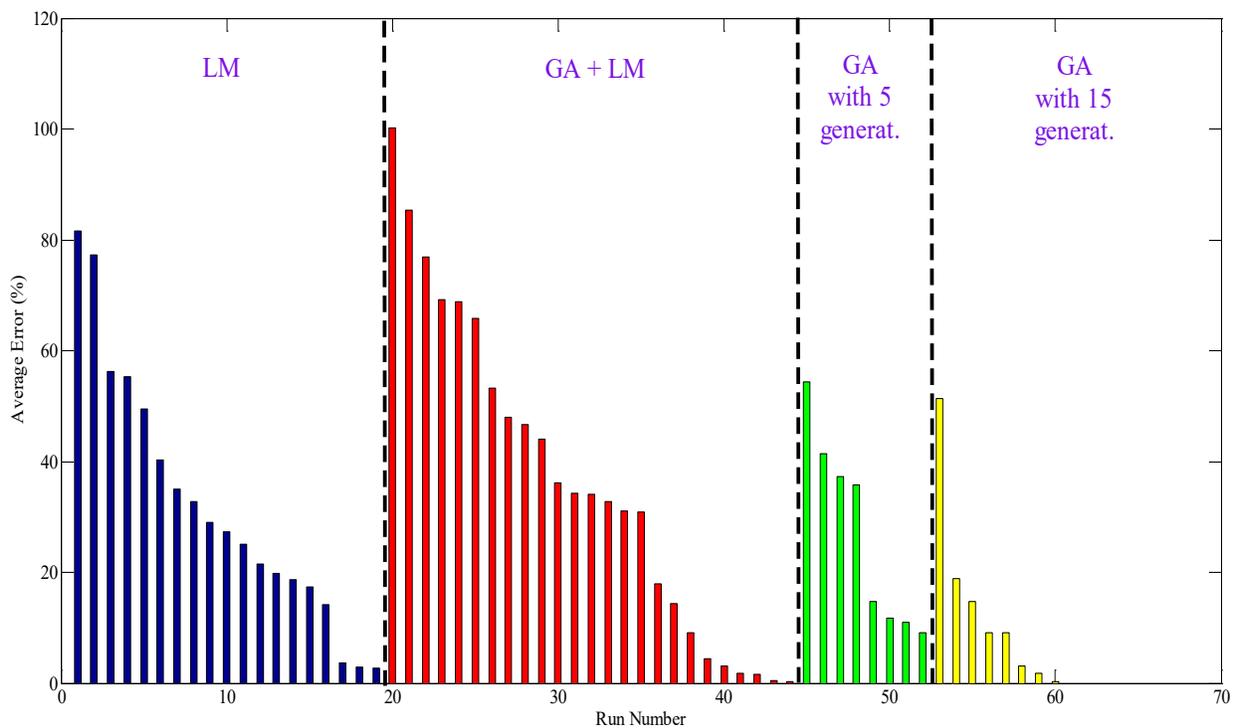
Figure 215. Graph. Average error in the backcalculated stiff layer modulus for all runs.

194
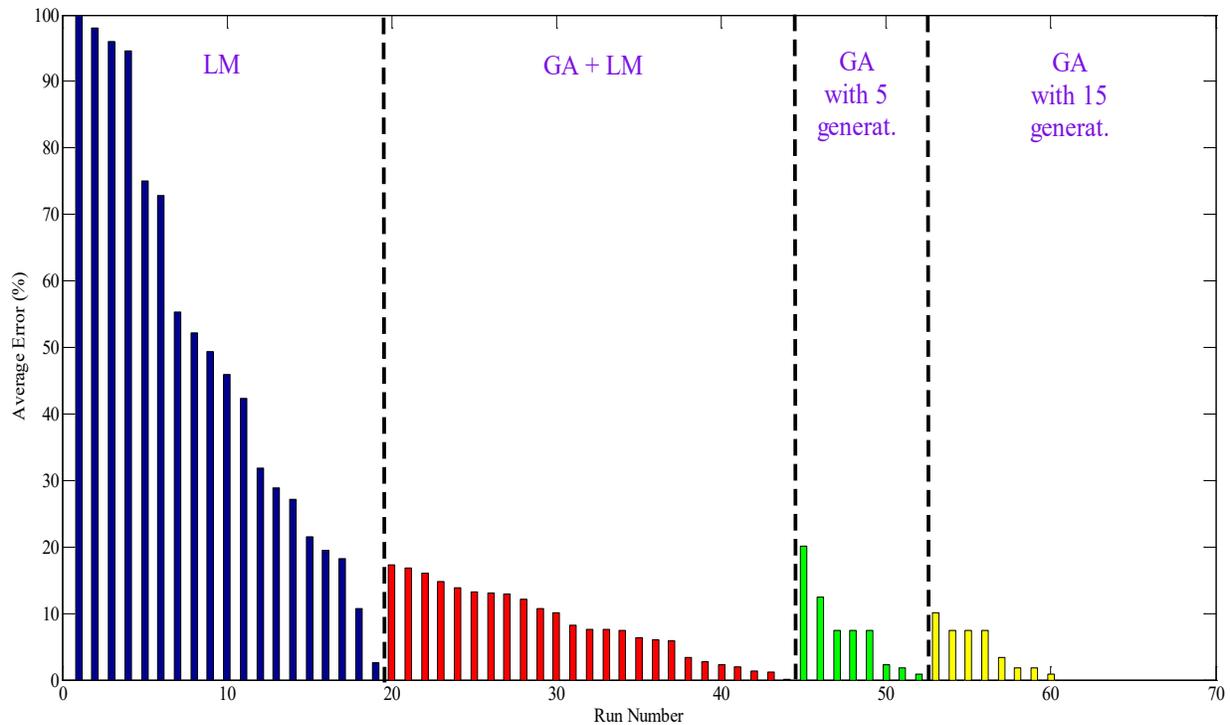
Figure 216. Graph. Average error in the backcalculated depth to the stiff layer for all runs.

It can be observed from figure 212 that the average error in backcalculated $E(t)$ was below the maximum acceptable level (American Association of State Highway and Transportation Officials threshold of 7.5 percent) as defined in figure 87 when any of the following options are true:[1]

- **Option 1**: At least 350 iterations (run 6 and up) using only the LM algorithm.

- **Option 2**: At least 75 populations, 5 generations, and 300 iterations (run 29 and up) when using the hybrid approach.

- **Option 3**: At least 100 populations and 15 generations (run 56 and up) when using the GA algorithm only.

Next, assuming a maximum tolerable error of 20 and 10 percent for the remaining parameters (base and subgrade layer moduli, stiff layer modulus and depth to the stiff layer, as seen in figure 212 through figure 216), the optimal runs and corresponding minimum number of computations to arrive at an acceptable solution for each search method are shown in table 57. It can be seen that the hybrid GA+LM approach is the best approach; it is guaranteed to converge within the search domain and is the most computationally efficient.

Table 57. Optimal runs for the various search methods.

Search Method	10-Percent Error Tolerance		20-Percent Error Tolerance	
	Optimal Run Number	Number of Calls to ViscoWave-II	Optimal Run Number	Number of Calls to ViscoWave-II
LM[a]	17	900	16	850
GA+LM[b]	35	850[c]	30	600[c]
GA[b]	59	3,750	56	1,500

[a]Convergence is not guaranteed (depending on seed values).
[b]Convergence is guaranteed (within the search domain).
[c]Computationally most efficient. The time to run ViscoWave-II depends on the speed and number of processors (cores) used during the backcalculation.

Figure 217 and figure 218 show the measured and predicted deflection time histories for GA+LM runs 30 and 32, respectively, for comparison purposes. Table 58 shows the backcalculation results. The backcalculation results were good, although relatively large errors were seen in the farther deflection sensors. Figure 219 shows the backcalculated relaxation modulus master curves for both combinations. Figure 220 shows the corresponding percent error. Running a GA algorithm along with the LM algorithm led to a much improved backcalculated AC modulus master curve that was achieved faster and more efficiently.
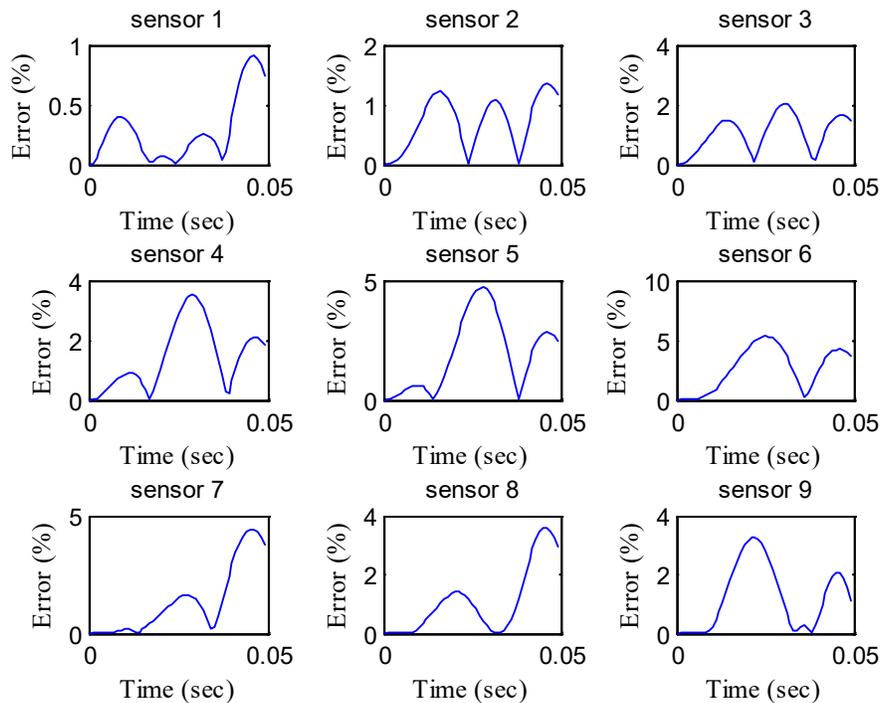
Figure 217. Graphs. Error in the backcalculated deflections for run 30.
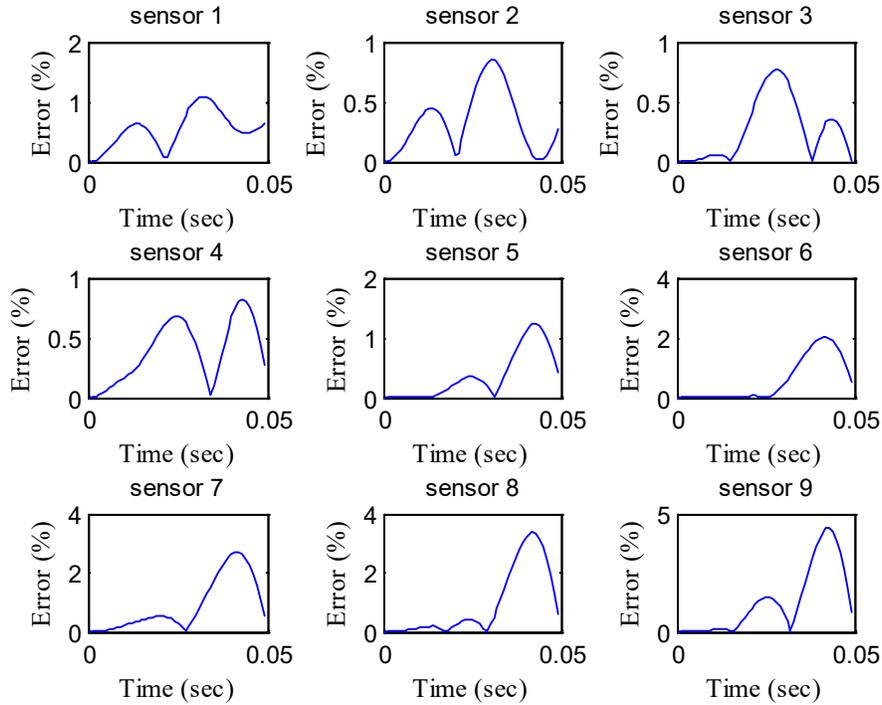
Figure 218. Graphs. Error in the backcalculated deflections for run 35.

Table 58. Backcalculated layer parameters for the simulated structure.

Layer	Simulated	Run 35		Run 30	
AC	**Master Curve Coefficient**	**Master Curve Coefficient**	**Error (Percent)**	**Master Curve Coefficient**	**Error (Percent)**
c_1	1.271	1.296	1.96	1.112	-12.5
c_2	2.883	2.883	0.01	3.085	7.1
c_3	0.22	0.145	-33.9	0.291	32.2
c_4	-0.497	-0.512	3.1	-0.427	-14.2
a_1	0.001096	0.000647	-40.9	0.000448	-59.1
a_2	-0.0926	-0.09686	4.6	-0.1317	42.3
Base, subgrade, and stiff layer	**Elastic Modulus (psi)**	**Elastic Modulus (psi)**	**Error (Percent)**	**Elastic Modulus (psi)**	**Error (Percent)**
E_{base} (psi)	20,000	21,769.7	8.8	23,797	19.0
$E_{subgrade}$ (psi)	13,500	14,464.4	7.1	14,473	7.2
E_{stiff} (psi)	200,000	331,313	32.5	349,894	40.0
$h_{subgrade}$ (inches)	96	103.5	7.8	106.0	10.4
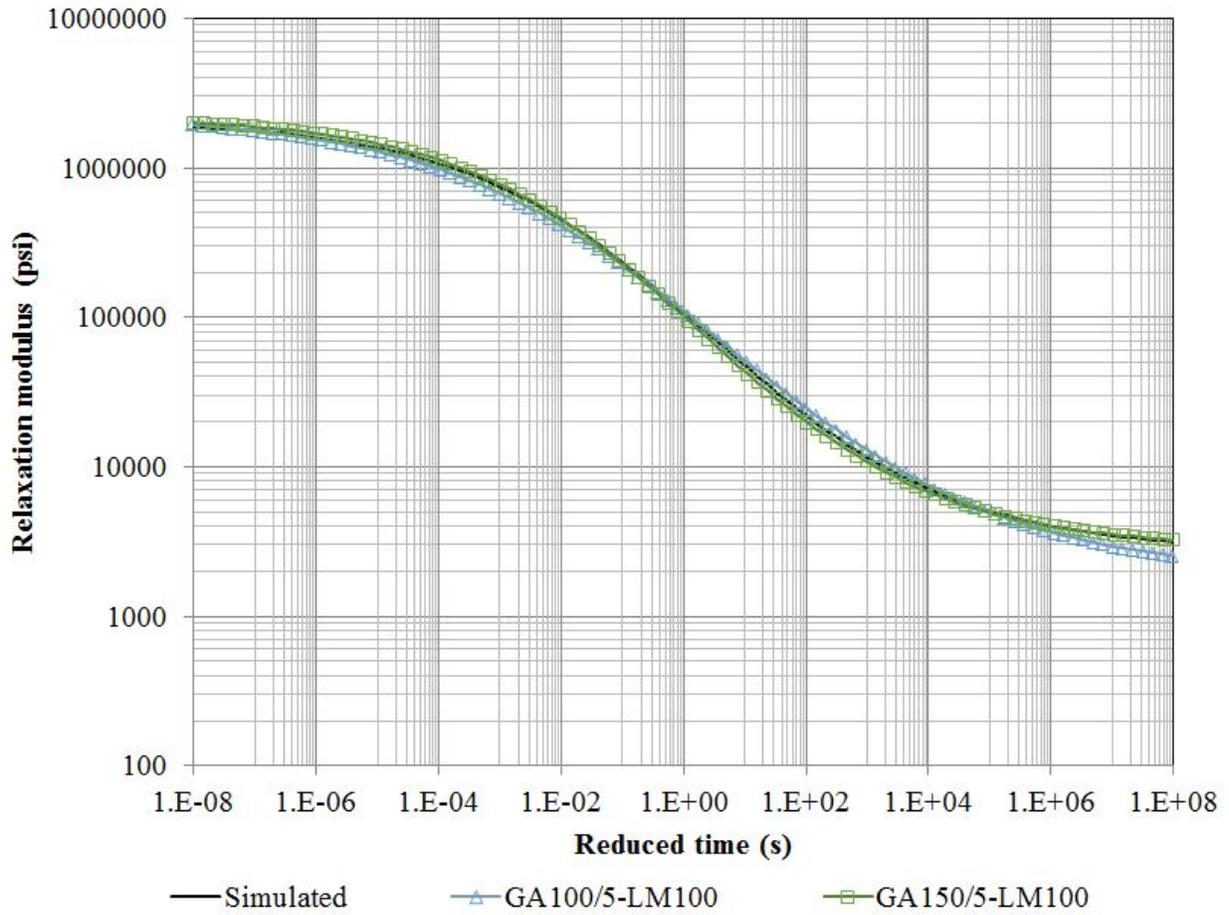
Figure 219. Graph. Backcalculated master curves for runs 30 and 35.
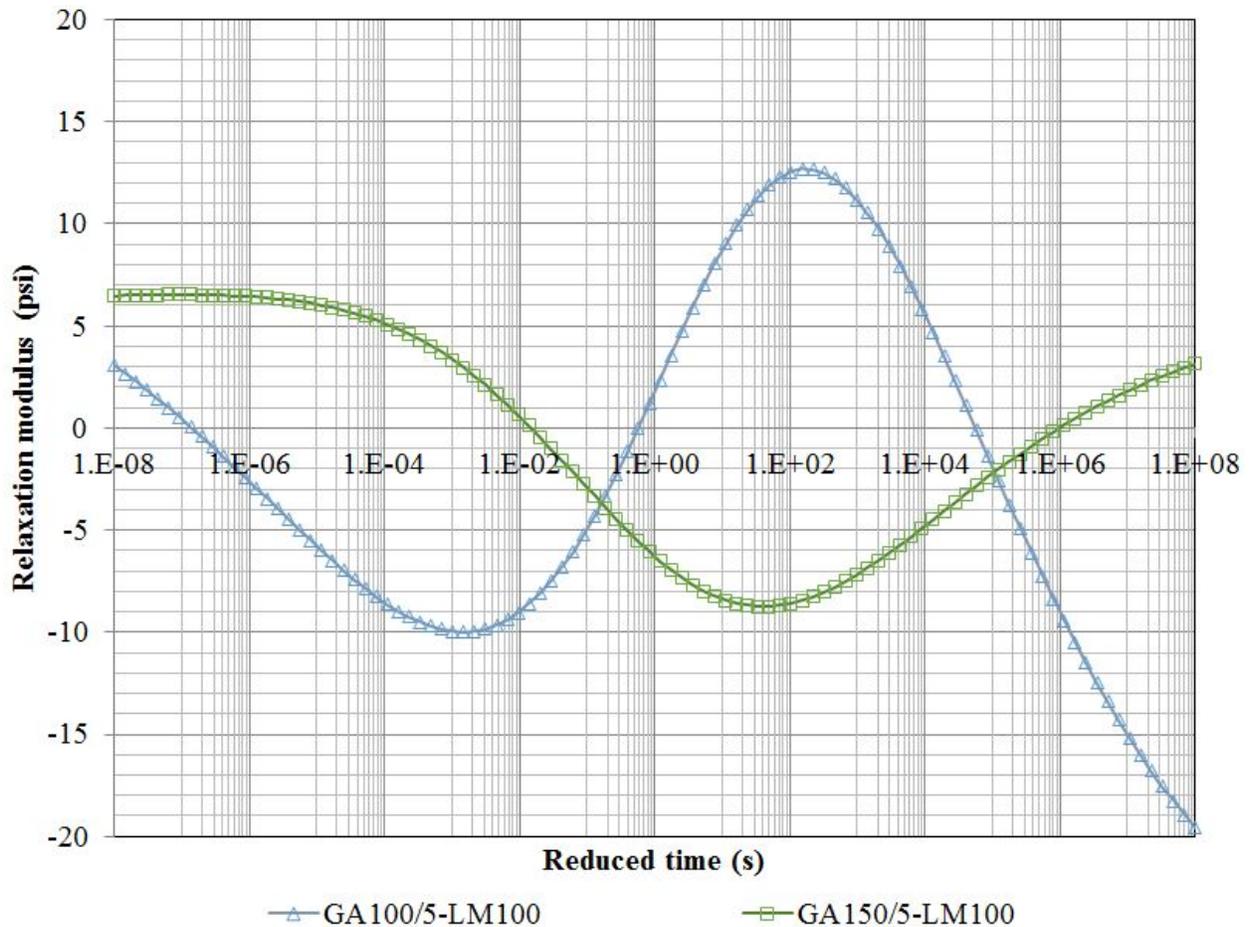
Figure 220. Graph. Percent error in the backcalculated master curves for all combinations.

Backcalculation Using Field Data

This section presents the evaluation of the new dynamic viscoelastic backcalculation program DYNABACK-VE using the field FWD test results from six LTPP sections. The details of the identified sections are presented in table 59. Table 60 shows the pavement structure of all the identified sections. These sections were identified based on the following criteria:

- Creep or E^* master curve data were available in the LTPP database.
- The AC layer was at least 2 inches thick.
- The pavement structure of the section did not include an AC treated base.
- One subgrade layer was present.
- One construction occurred.

Table 59. Identified LTPP sections for the verification of DYNABACK-VE.

State Code	Section	Date of Construction	Total Number of Constructions	Section Type	Experiment Number	Test Date	Test Time
1	0101	04/28/05	1	SPS	1	04/28/05	15:59
6	A805	11/16/11	1	SPS	8	11/16/11	12:23
6	A806	11/16/11	1	SPS	8	11/16/11	13:50
30	0113	07/12/10	5	SPS	1	07/12/10	09:39

Table 60. Layer properties for LTPP sections.

Section	Property	Asphalt Concrete Layer			Granular Base	Subgrade	Stiff Layer
		Layer 1	Layer 2	Layer 3			
10101	Thickness (inches)	2.47	2.47	2.47	6	Semi-infinite	No stiff layer
	Temperature (°F)	100.0	92.5	91.6	N/A	N/A	
	Poisson's ratio	0.35			0.40	0.45	
	Unit weight (pcf)	145			125	100	
	Relaxation modulus	$E(t)$ coefficients (c_1, c_2, c_3, c_4) Backcalculated			Backcalculated	Backcalculated	
	$a(T)$ coefficients	(a_1, a_2)—Backcalculated			N/A	N/A	
6A805	Thickness (inches)	1.3	1.3	1.3	8.2	Backcalculated	Semi-infinite
	Temperature (°F)	73.6	69.1	68.2	N/A	N/A	N/A
	Poisson's ratio	0.35			0.4	0.45	0.2
	Unit weight (pcf)	145			125	100	125
	Relaxation modulus (ksi)	$E(t)$ coefficients (c_1, c_2, c_3, c_4) Backcalculated			Backcalculated	Backcalculated	Backcalculated
	$a(T)$ coefficients	(a_1, a_2) Backcalculated			N/A	N/A	N/A
6A806	Thickness (inches)	2	2	2.8	12.1	Backcalculated	Semi-infinite
	Temperature (°F)	79.1	75.1	71.2	N/A	N/A	N/A
	Poisson's ratio	0.35			0.4	0.45	0.2
	Unit weight (pcf)	145			125	100	125
	Relaxation modulus (ksi)	$E(t)$ coefficients (c_1, c_2, c_3, c_4) Backcalculated			Backcalculated	Backcalculated	Backcalculated
	$a(T)$ coefficients	(a_1, a_2) Backcalculated			N/A	N/A	N/A
300113	Thickness (inches)	2	2	2	No stiff layer	Semi-infinite	No stiff layer
	Temperature (°F)	84.7	80.1	79.2	N/A	N/A	
	Poisson's ratio	0.35			0.4	0.45	
	Unit weight (pcf)	145			125	100	
	Relaxation modulus (ksi)	$E(t)$ coefficients (c_1, c_2, c_3, c_4) Backcalculated			Backcalculated	Backcalculated	
	$a(T)$ coefficients	(a_1, a_2) Backcalculated			N/A	N/A	

N/A = Not applicable.

In this analysis, the research team sought to backcalculate the depth to the stiff layer in addition to the stiff layer modulus using DYNABACK-VE. The backcalculation algorithm was run in two steps. The final population of the first step was input as initial population to the second step. The AC layer was assumed to have a three-step piecewise temperature profile for all the sections, as shown in table 60.

LTPP Section 10101: The measured deflection time histories from all the drops for section 10101 are presented in figure 221. The deflection time histories did not show waviness at the end of the signal, which indicated that there was no stiff layer or that the depth to the stiff layer was greater than 15 ft. The presence of a stiff layer was further evaluated using the graphical method suggested by Ullidtz.[94] The method involves plotting peak deflections obtained from FWD testing versus the reciprocal of the corresponding sensor location (measured from the center of loading). The analysis showed that a stiff layer existed at 86.9, 32.7, 109.8, and 26.6 ft using the deflection histories from drops 1 through 4, respectively. Even though the $1/r$ method suggested that there was no stiff layer, the research team decided to include a stiff layer in the pavement structure. The backcalculation results from all the drops are presented in table 61. Figure 222 shows the backcalculated master curves. Figure 223 shows the backcalculated time-temperature shift factors. For section 10101, the backcalculated relaxation modulus master curves from all the drops matched very well with the measured master curve (figure 222). However, it can be seen from figure 223 that the backcalculated shift factor functions for all the drops showed a good match over the temperature range of 50 to 131 °F, whereas the laboratory-measured values deviated from the backcalculated values. This could be because laboratory creep compliance tests are usually not reliable in determining time-temperature superposition properties because a perfect stress-step function is very difficult to achieve in the laboratory and also because the results are contaminated with viscoplasticity, especially at the high temperatures and long creep times.

Table 61. Backcalculation results for LTPP **section 10101 using DYNABACK-VE.**

Parameter		Laboratory Results	Backcalculated Results			
			Drop 1	Drop 2	Drop 3	Drop 4
c_1		0.304	0.420	0.402	0.431	0.391
c_2		4.160	4.049	4.042	4.009	4.053
c_3		0.684	0.611	0.731	0.711	0.656
c_4		-0.428	-0.442	-0.450	-0.457	-0.418
a_1		3.14E-04	0.0011364	0.0008364	0.0010633	0.0010246
a_2		-1.47E-01	-0.070735	-0.0587358	-0.064368	-0.04627
E_{base} (psi)		—	28,519	23,433	20,121	20,124
$E_{subgrade}$ (psi)		—	48,899	46,669	42,889	45,371
$h_{subgrade}$ (ft)	Drop 1	86.9 (1/r)	25	29	34.5	32.5
	Drop 2	32.7(1/r)				
	Drop 3	109.8(1/r)				
	Drop 4	26.6(1/r)				
E_{stiff} (psi)		—	814,826	922,537	732,145	655,421

— Indicates data were not available.
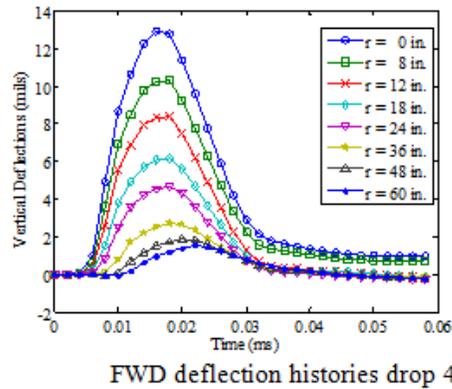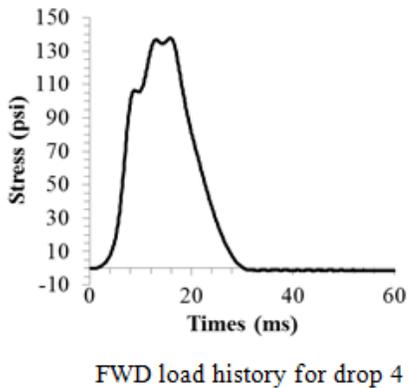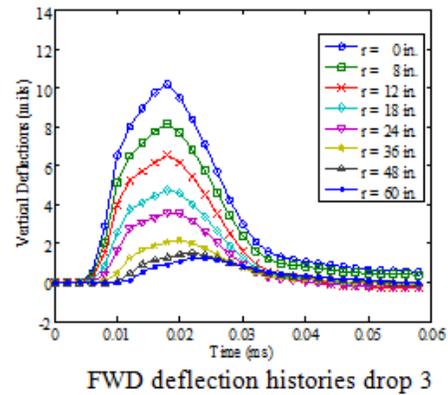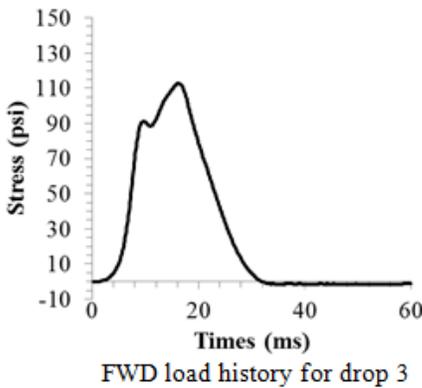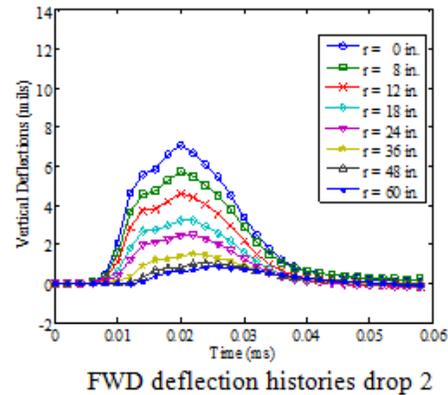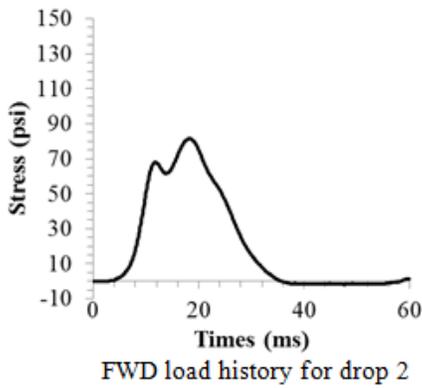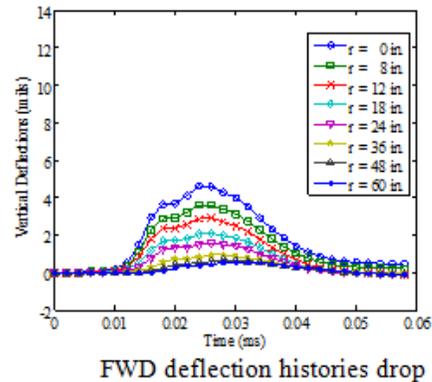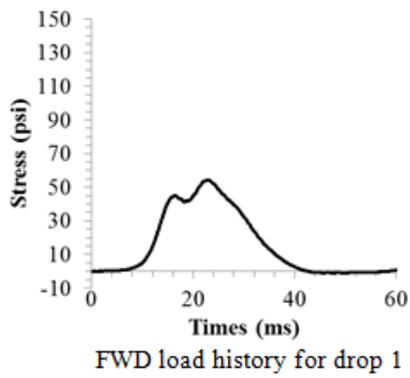
Figure 221. Graphs. Measured FWD load and time histories for LTPP **section 10101.**
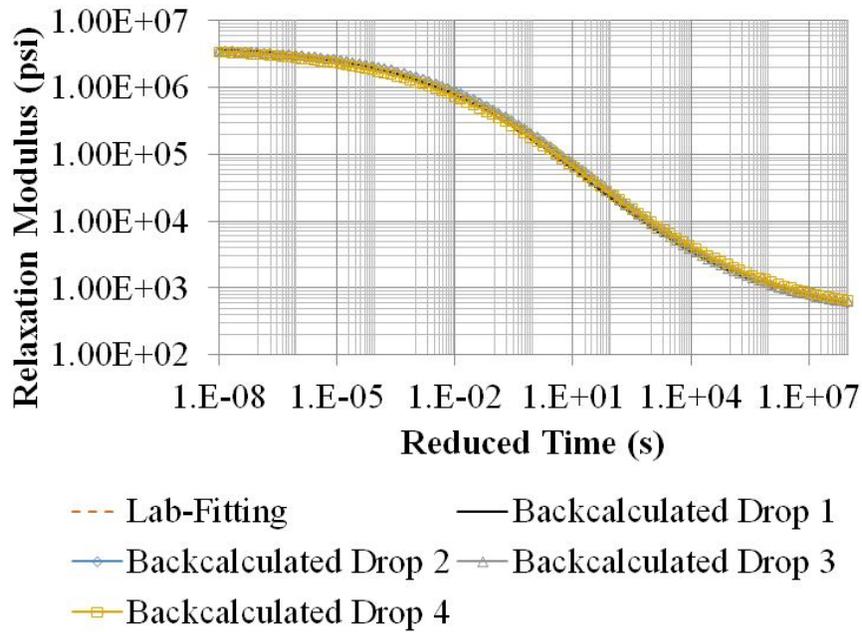
Figure 222. Graph. Backcalculated master curves for LTPP **section 10101 from all the drops.**
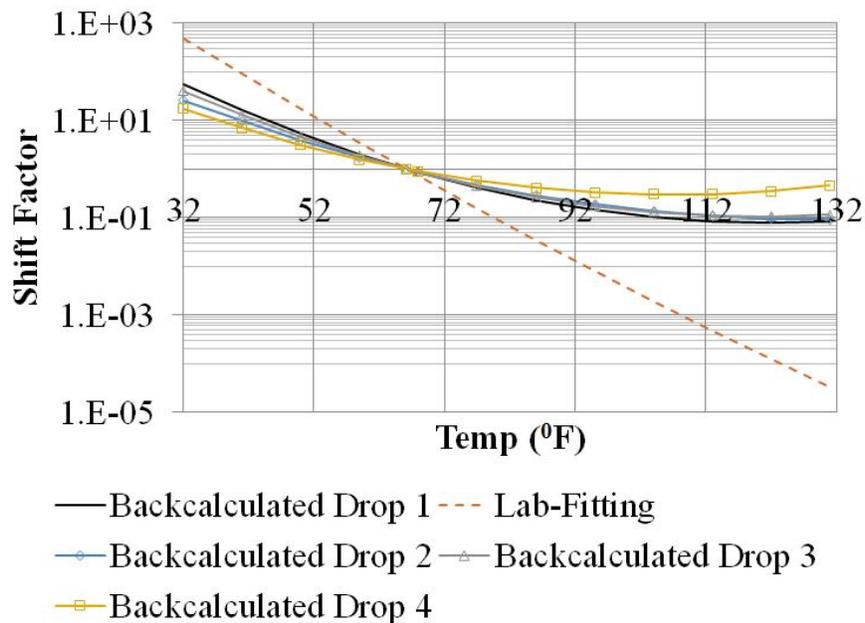
Figure 223. Graph. Backcalculated shift factors for LTPP **section 10101 from all the drops.**

From table 61, the backcalculated moduli for unbound layers from all the drops suggest that the subgrade layer was stiffer than the base layer. Also, it was observed that the backcalculated moduli for the unbound layers were lower as the load level increased, which suggests softening conditions. The same section was used in LTPP data analysis presented in chapter 3. Figure 224 presents the load-to-deflection ratio at each load level. The plots also suggest softening conditions. The practical implication of these observations suggests that one could backcalculate

the moduli for the unbound layers from all the drops to capture the nonlinearity. This could merit discussion for future research.

Load/Def8 = -0.1058*Load + 102.85

Load/Def7 = -0.1133*Load + 87.683

Load/Def6 = -0.0886*Load + 62.319

Load/Def5 = -0.0556*Load + 37.057

Load/Def4 = -0.0404*Load + 27.987

Load/Def3 = -0.0260*Load + 19.944

Load/Def2 = -0.0202*Load + 15.976

Load/Def1 = -0.0142*Load + 12.569
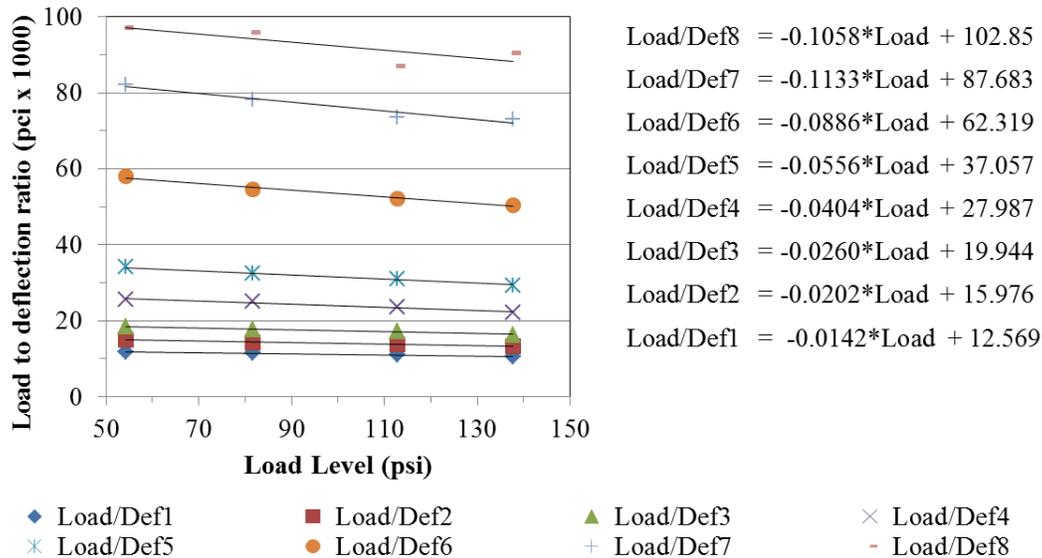
Figure 224. Graph. Softening behavior for LTPP section 10101.

LTPP Section 6A805: The measured deflection time histories from all the drops for section 6A805 are presented in figure 225. The deflection time histories did show waviness at the end of the signal, which indicates that there was a stiff layer. The depth to the stiff layer estimated using Ullidtz method is about 70.4 ft using the deflection histories from drop 1.[94] Even though the 1/r method suggests that there was no stiff layer, the research team also decided to include a stiff layer in the pavement structure. The backcalculation results using drop 1 time histories are presented in table 62. Figure 226 shows the backcalculated and measured master curves. Figure 227 shows the backcalculated and measured time-temperature shift factors. For section 6A805, the backcalculated and the laboratory-measured relaxation modulus master curves matched very well with the measured master curve until reduced time of 10 s (figure 226). However, it can be seen from figure 227 that the backcalculated shift factor functions did not match.
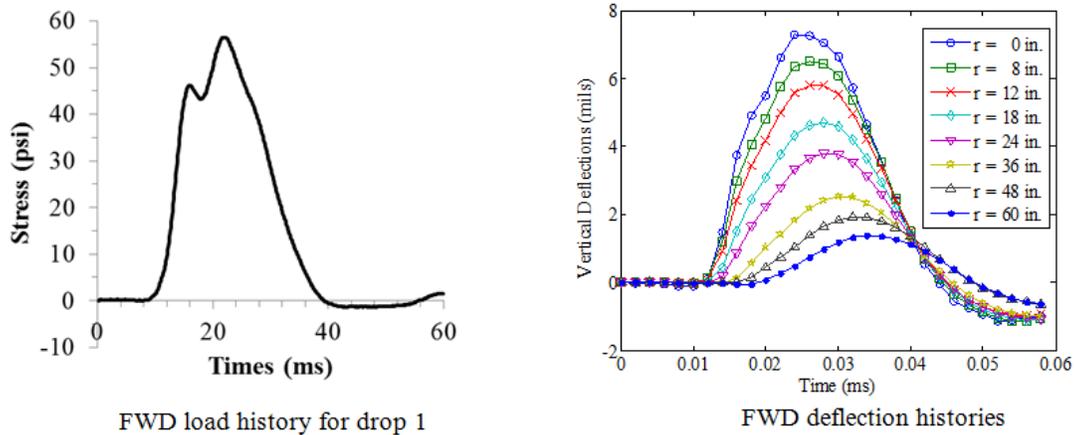
Figure 225. Graphs. Measured FWD load and time histories for LTPP section 6A805.

Table 62. Backcalculation results for LTPP section 6A805 using DYNABACK-VE.

Parameter	Laboratory Results	Drop 1 Backcalculation
c_1	1.381	1.609
c_2	2.983	2.758
c_3	1.625	1.425
c_4	-0.784	-0.845
a_1	-0.00169	0.001
a_2	-0.08729	-0.077
E_{base} (psi)	—	43,546
$E_{subgrade}$ (psi)	—	17,435
$h_{subgrade}$ (ft) drop1	70.4 (1/r)	14
E_{stiff} (psi)	—	315,452

— Indicates data values were not measured.
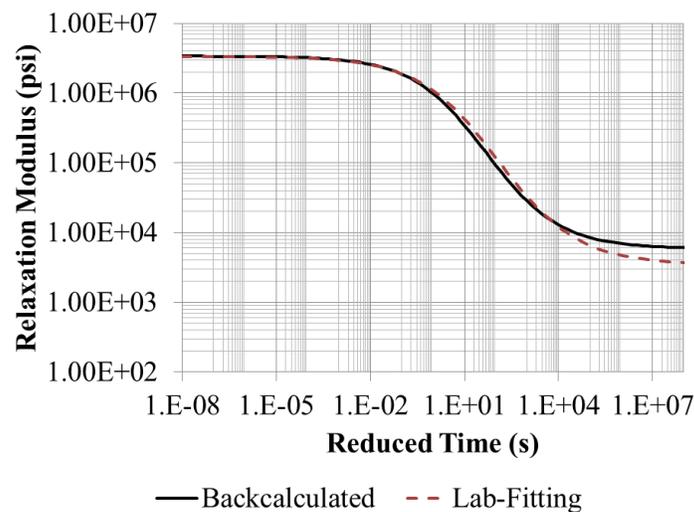
Figure 226. Graph. Backcalculated master curves for LTPP section 6A805.
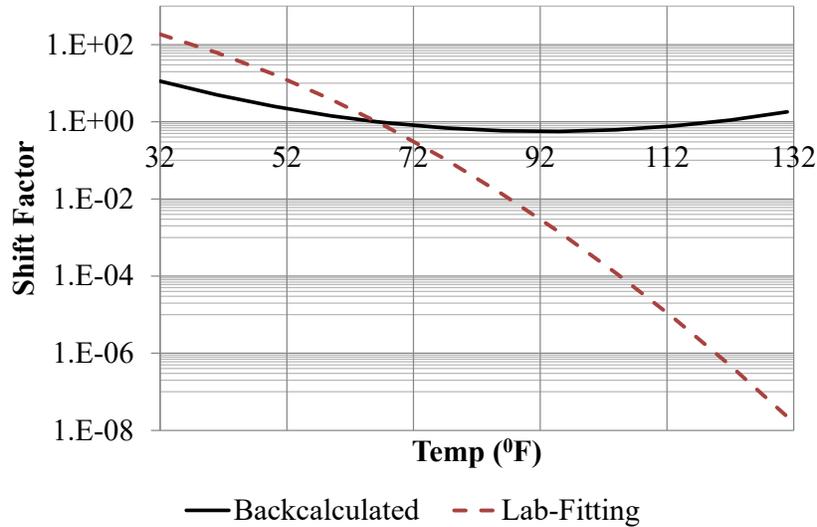
Figure 227. Graph. Backcalculated shift factors for LTPP section 6A805.

In table 62, the backcalculated depth to the stiff layer is about 14 ft, which suggests that there was a stiff layer at a shallow depth. This contradicts the results from the $1/r$ method. However, because this estimated depth is close to the depth to the stiff layer beyond which dynamic effects are insignificant, i.e., 15 ft, the possible existence of a stiff layer could be ignored.[96] The load-to-deflection ratio presented in figure 228 shows a maximum slope of about 4 percent seen for sensor 8, which suggests that nonlinearity can be ignored.

Load/Def8 = -0.0472*Load + 44.174
Load/Def7 = -0.0102*Load + 30.751
Load/Def6 = -0.015*Load + 23.686
Load/Def5 = -0.0011*Load + 15.219
Load/Def4 = 0.0051*Load + 12.085
Load/Def3 = 0.0056*Load + 9.7279
Load/Def2 = 0.0042*Load + 8.7655
Load/Def1 = 0.0014*Load + 7.8761
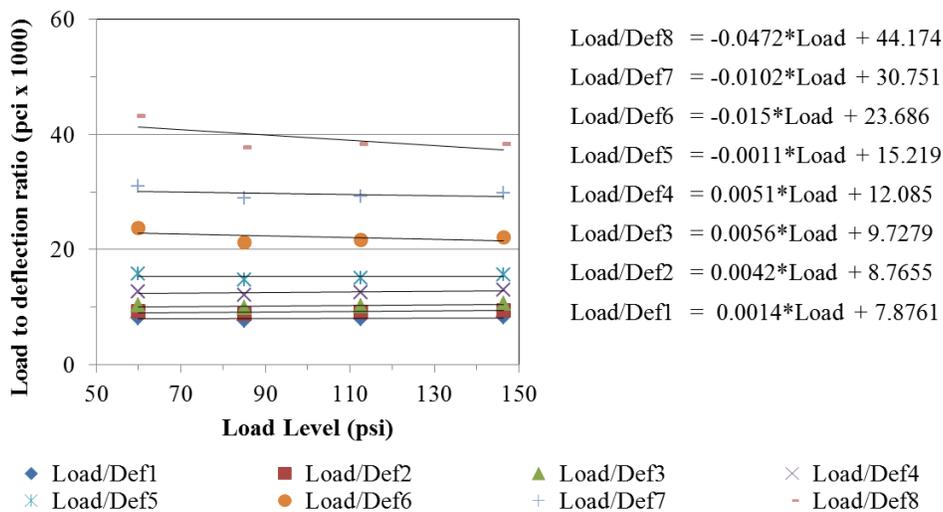
Figure 228. Graph. Load-to-deflection ratio for LTPP section 6A805.

LTPP Section 06A806: The measured deflection time histories from all the drops for section 06A806 are presented in figure 229. The deflection time histories did show waviness at the end of the signal, which indicated that there was a stiff layer. Using the Ullidtz method, the depth to the stiff layer was estimated as a negative value, which was interpreted as the absence of a stiff layer.[94] Even though the $1/r$ method suggests that there was no stiff layer, the research team also

206

decided to include a stiff layer in the pavement structure. The backcalculation results using drop 1 time histories are presented in table 63. Figure 230 shows the backcalculated and measured master curves. Figure 231 shows the backcalculated and measured time-temperature shift factors. For section 6A806, the backcalculated and the laboratory-measured relaxation modulus master curves matched very well with the measured master curve until reduced time of 1 s (figure 230). However, it can be seen from figure 231 that the backcalculated shift factor functions did not match.

FWD load history for drop 1

FWD deflection histories
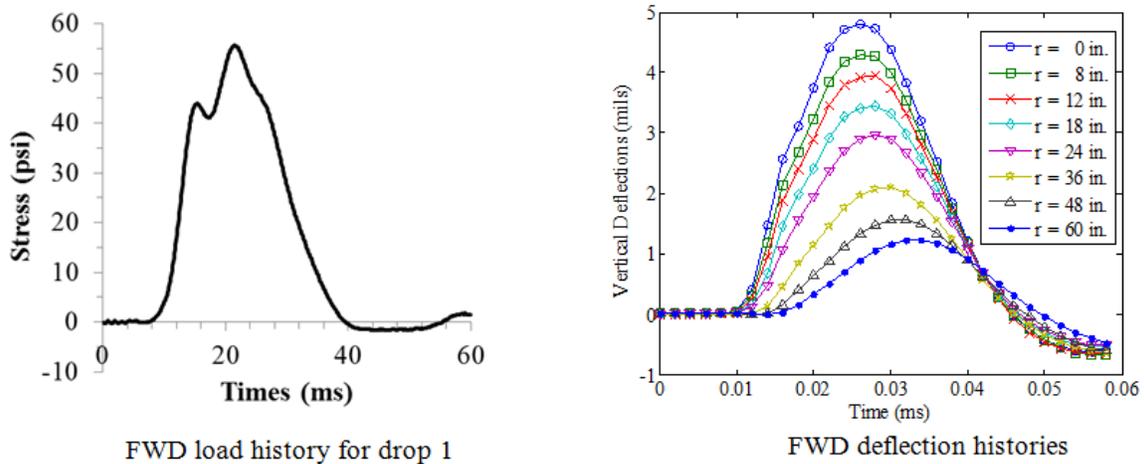
Figure 229. Graphs. Measured FWD load and time histories for LTPP **section 6A806.**

Table 63. Backcalculation results for LTPP **section 6A806 using DYNABACK-VE.**

Parameter	Laboratory Results	Drop 1 Backcalculation
c_1	1.157	1.252
c_2	3.356	3.259
c_3	1.388	1.025
c_4	-0.673	-0.723
a_1	-0.0027	-0.001
a_2	-0.06976	-0.140735
E_{base} (psi)	—	26,546
$E_{subgrade}$ (psi)	—	19,075
$h_{subgrade}$ (ft) drop 1	No stiff (1/r)	13.33
E_{stiff} (psi)	—	316,575

— Indicates data were not available.
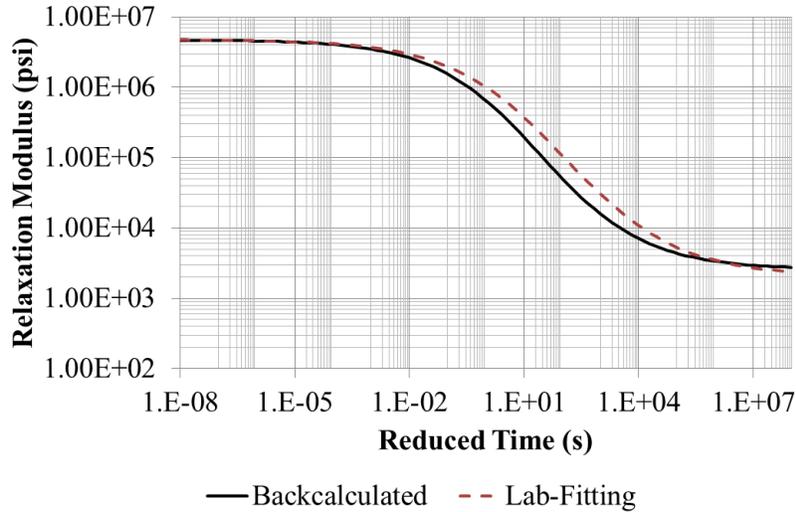
Figure 230. Graph. Backcalculated master curves for LTPP **section 6A806.**
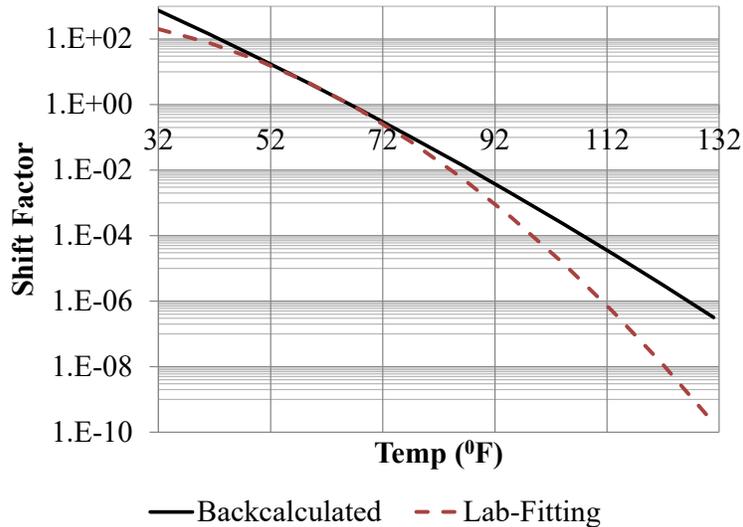
Figure 231. Graph. Backcalculated shift factors for LTPP **section 6A806.**

In table 63, the backcalculated depth to the stiff layer is about 13 ft, which suggests that there was a stiff layer at a shallow depth. This contradicts the results from the $1/r$ method. However, because this estimated depth is close to the depth to the stiff layer beyond which dynamic effects are insignificant, i.e., 15 ft, the possible existence of a stiff layer could be ignored.[95] The load-to-deflection ratio presented in figure 232 shows a maximum slope of about 5 percent seen for only sensor 8, which suggests that nonlinearity can be ignored.

Load/Def8 = -0.0543*Load + 50.843

Load/Def7 = -0.0406*Load + 39.110

Load/Def6 = -0.0206*Load + 28.409

Load/Def5 = -0.0030*Load + 19.809

Load/Def4 = 0.0007*Load + 16.902

Load/Def3 = 0.0007*Load + 14.756

Load/Def2 = 0.0007*Load + 13.590

Load/Def1 = -0.0014*Load + 12.228

◆ Load/Def1   ■ Load/Def2   ▲ Load/Def3   × Load/Def4
＊ Load/Def5   ● Load/Def6   + Load/Def7   - Load/Def8
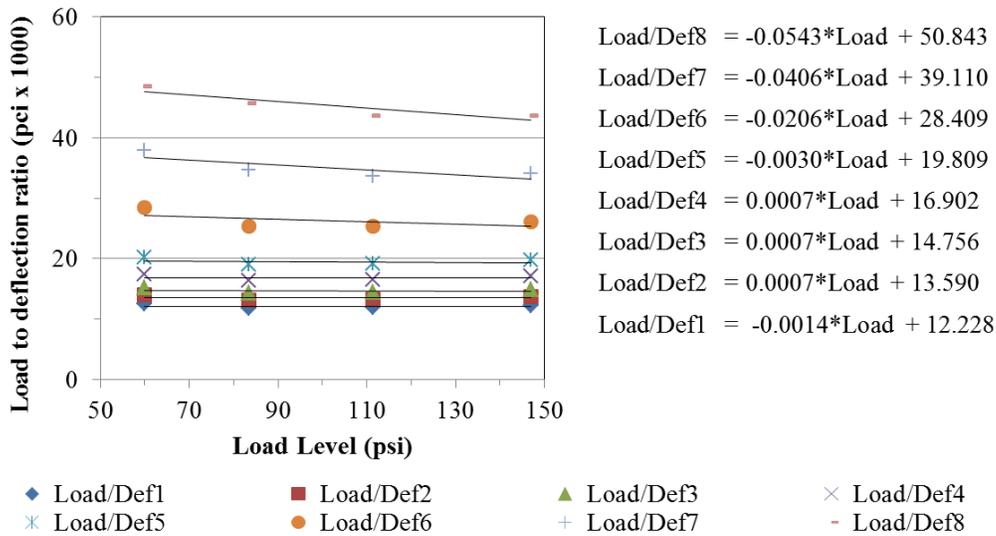
Figure 232. Graph. Load-to-deflection ratio for LTPP **section 6A806.**

LTPP Section 300113: The measured deflection time histories from drop 1 for section 300113 are presented in figure 233. The deflection time histories did not show waviness at the end of the signal, which indicates that there was no stiff layer or that the depth to the stiff layer was greater than 15 ft. Using the Ullidtz method, the depth to the stiff layer was estimated at about 96.4 ft.[94] Even though the $1/r$ method suggests that there was no stiff layer, the research team included a stiff layer in the pavement structure. The backcalculation results using drop 1 time histories are presented in table 64. Figure 234 shows the backcalculated and measured master curves. Figure 235 shows the backcalculated and measured time-temperature shift factors. For section 6A806, the backcalculated and the laboratory-measured relaxation modulus master curves matched very well until reduced time of 1 s (figure 234). However, it can be seen from figure 235 that the backcalculated shift factor functions did not match.

FWD load history for drop 1

FWD deflection histories
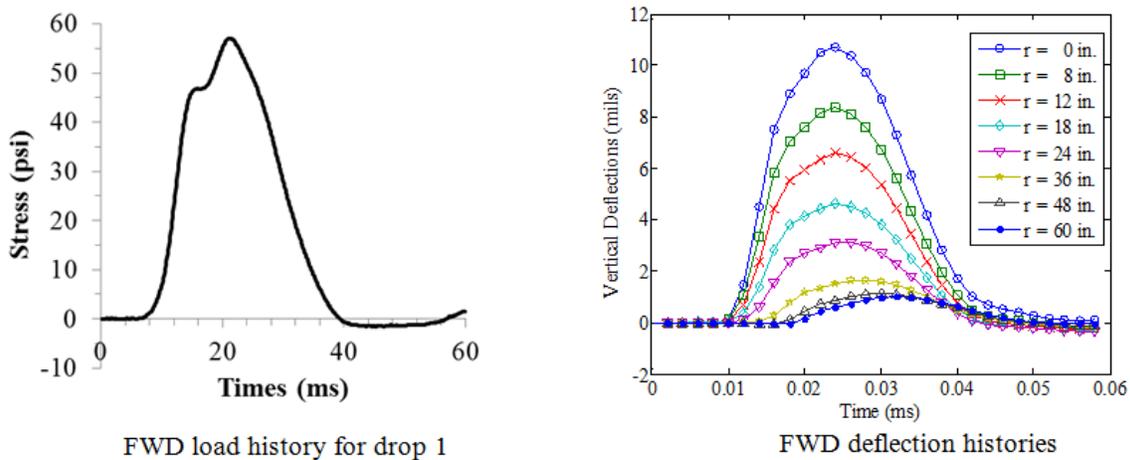
Figure 233. Graphs. Measured FWD load and time histories for LTPP **section 300113.**

Table 64. Backcalculation results for LTPP section 6A806 using DYNABACK-VE.

Parameter	Laboratory Results	Drop 1 Backcalculation
c_1	0.778	1.098
c_2	3.789	3.449
c_3	0.000	-0.081
c_4	-0.400	-0.423
a_1	4.97E-04	0.001
a_2	-1.57E-01	-0.077
E_{base} (psi)	—	10,745
$E_{subgrade}$ (psi)	—	22,995
$h_{subgrade}$ (ft) drop1	96.4 (1/r)	16
E_{stiff} (psi)	—	215,298

— Indicates data were not available.
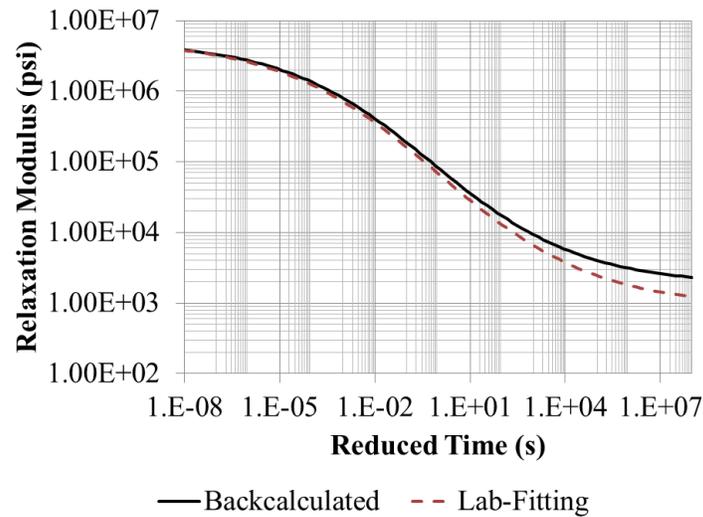
Figure 234. Graph. Backcalculated master curves for LTPP section 300113.
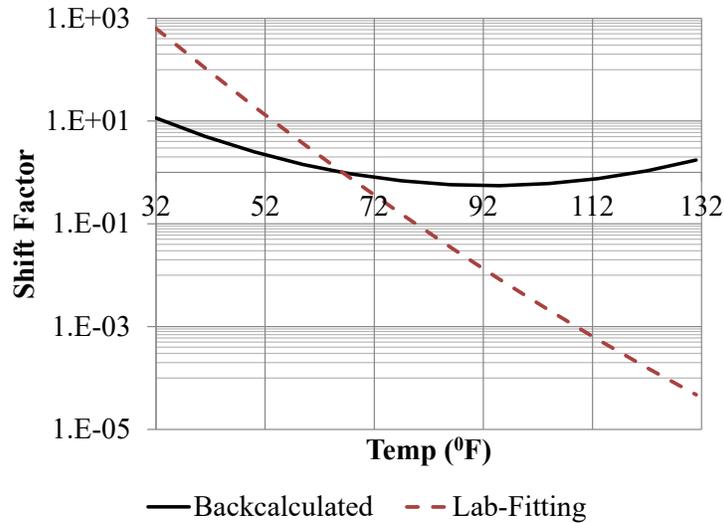
Figure 235. Graph. Backcalculated shift factors for LTPP **section 300113.**

In table 63, the backcalculated depth to the stiff layer is about 16 ft, which is close to the depth to the stiff layer beyond which dynamic effects are insignificant, i.e., 15 ft.[96] Therefore, the possible existence of a stiff layer could be ignored. Figure 236 shows the load-to-deflection ratio for all the sensors. The maximum slope is about 5 percent for only sensor 7, which means that nonlinearity could be ignored.

Load/Def8 $= -0.0206 \cdot \text{Load} + 60.763$

Load/Def7 $= -0.0580 \cdot \text{Load} + 54.648$

Load/Def6 $= -0.0322 \cdot \text{Load} + 37.512$

Load/Def5 $= -0.0106 \cdot \text{Load} + 19.250$

Load/Def4 $= -0.0033 \cdot \text{Load} + 12.939$

Load/Def3 $= -0.0021 \cdot \text{Load} + 9.060$

Load/Def2 $= -0.0021 \cdot \text{Load} + 7.154$

Load/Def1 $= -0.0034 \cdot \text{Load} + 5.7003$
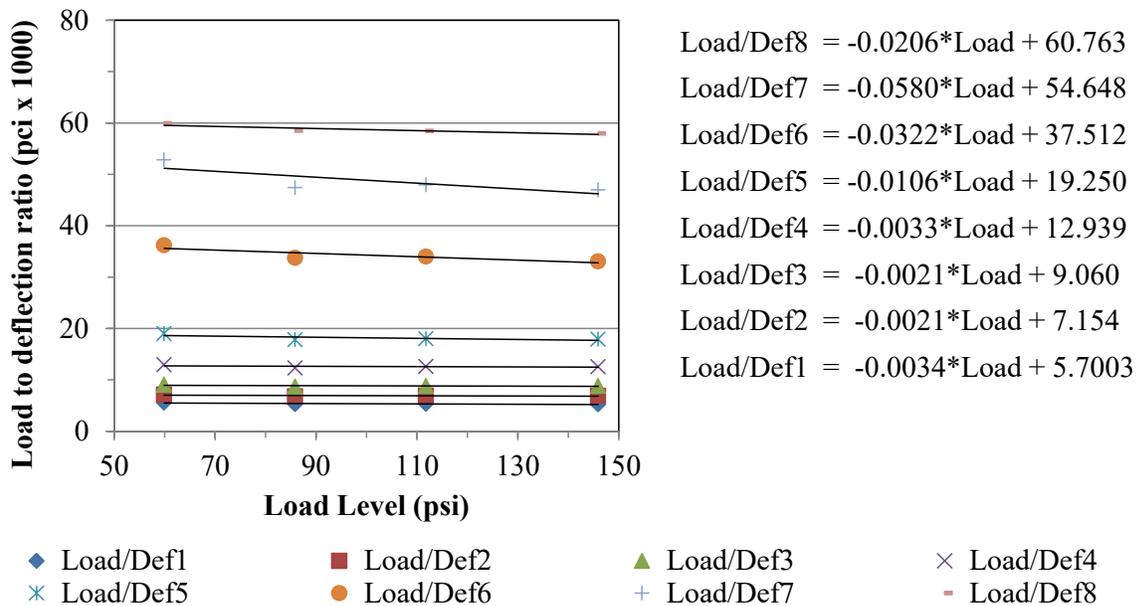
Figure 236. Graph. Load-to-deflection ratio for LTPP **section 300113.**

CONCLUSION

A new solution and its associated computer program were developed for dynamic viscoelastic time-domain backcalculation of multilayered flexible pavement parameters under FWD tests in the time domain. The method uses a time-domain viscoelastic solution as a forward routine (ViscoWave-II) and a hybrid routine (DYNABACK-VE: GA and modified LM method) for backcalculation analysis. For the GA-based backcalculation procedure, the research team recommends using DYNABACK-VE twice with a population of 200 and 15 generations. When increasing the pulse width, the team recommends using a population of 300 and 15 generations. The advantage of the new solution is that it can analyze the response of pavement systems in the time domain and can therefore accommodate time-dependent layer properties and incorporate wave propagation. Also, because the backcalculation is performed in the time domain, the algorithm is not sensitive to truncation in the deflection time histories. The new algorithm is capable of backcalculating layer moduli, including the master curve of the AC layer at every reduced time and depth to the stiff layer, if it exists, and its modulus value. The results using simulated deflection time histories and field FWD data showed excellent stability and accuracy. Note that the backcalculation algorithm is not designed to backcalculate the modulus of more than one AC layer in pavement structures with different mixes or in cases where there are multiple subgrade layers with similar moduli values.

The sensitivity of dynamic backcalculation solutions to signal noise and synchronization problems is high. The remedy to noise is to preprocess the raw data by filtering out the high-frequency content of the signal (anything above 100 Hz) in deflection and load pulse data. Also, in the analysis presented in chapter 5, the percent error between the computed and measured displacement was used as the minimizing error. If percent error were used as the minimizing objective, it could lead to overemphasis of lower magnitudes of deflections at the later portion of the time history, which typically includes noise and integration errors. Hence another fit function was proposed in which the percent error was calculated with respect to the peak of deflection at each sensor. This de-emphasizes the tail data by normalizing them with respect to the peak.

If synchronization problems occur, the dynamic backcalculation algorithm may not work as well, although one could shift the signals similar to what was done in the quasi-static viscoelastic solution (chapter 4). Because the quasi-static solution presented in chapter 4 is already coded to remove the time delay between sensors, the research team recommends the use of BACKLAVA instead of DYNABACK-VE when such a synchronization problem exists and cannot be removed manually.

The results from dynamic analyses clearly showed the superiority of a fully dynamic solution with a viscoelastic AC layer modulus in predicting deflection responses that are in line with what one would expect from soil, as evidenced by the close match in the details of the deflection time histories between theory and observation. The theoretical predictions from ViscoWave-II showed very good agreement with the measured deflection time histories. The fact that theory and measurement showed the same behavior with time was proof that these observations were physically real. This is important in that it reinforces the following: (1) a comprehensive model that takes into account viscoelasticity of the AC layer, damping in the unbound layers, and dynamics in terms of inertial and wave propagation effects can explain the measured data with all their complexities; and (2) the FWD sensor measurements, if properly calibrated, can show

the physical behavior for most of the time range, with the exception of the drift problems at the tail of the records.

In contrast, the layered viscoelastic solution cannot simulate the true deflection time histories because it cannot account for inertial and wave propagation effects. As such, it cannot predict the time delays in the response, the initial rebounds of the farther sensors, and the free vibrations after the load is applied. Also, the layered viscoelastic solution significantly underestimates the deflections when a stiff layer is present. This is because it cannot account for dynamic amplification caused by the wave energy trapped in the unbound layers when a stiff layer condition exists.

CHAPTER 6. ENHANCEMENT TO THE FWD EQUIPMENT

This chapter describes the results from a set of experimental procedures designed to evaluate the performance of FWD measurement systems (seismometers, geophones, and accelerometers). Parameters such as accuracy and sensitivity were considered. Observations were used to help test certain features of the numerical tools presented in chapter 5. A high-precision laser system was used in the experimental setups as a reference system and also to evaluate limitations on potential recommendation of its use in FWD systems.

REVIEW OF FWD EQUIPMENT

In this section, the research team focused on the key issues to address for potential improvements to FWD testing and interpretation. The identified issues were the following: (1) FWD data collection and measurement; and (2) analysis methods, i.e., static versus dynamic, linear versus nonlinear; and viscoelastic behavior of the AC material. A review of the basic mechanisms and characteristics of the measurement systems available in FWD equipment was conducted.

The research team found that FWD systems available in North America used either geophones or seismometers as sensors to measure the deflection basins. Geophones fell between accelerometers and seismometers in function and price. Seismometers were typically larger and more expensive and usually detected extremely small movements at lower frequencies than geophones. The team learned that some seismometers could be very fragile, and calibrating a seismometer was critical to obtaining useful data. Therefore, a geophone or an accelerometer would more likely be used to get a simpler signal. Because accelerometers are nearly solid state, they are good at handling more violent motion.

Because the measurements are done in a moving reference frame (the pavement surface), almost all sensors are based on the inertia of a suspended mass, which tends to remain stationary in response to external motion. The mass is used as the reference in the system. Therefore, the relative motion of the suspended mass and the ground is a function of the pavement's motion. Because the sensor is moving with the ground and there is no fixed, undisturbed reference available means that the displacement cannot be measured directly, and according to the inertia principle, one can observe the motion only if it has an acceleration. The frequency response of the mass-spring system is thus a critical factor that greatly influences the sensitivity and the accuracy of the measurement devices.

The basic principle of a geophone involves use of a moving coil within a magnetic field. This can be implemented by having a fixed coil and a magnet that moves with the mass or a fixed magnet and the coil moves with the mass. The output from the coil is proportional to the velocity of the mass relative to the frame. This kind of electromagnetic geophone is called a velocity transducer. Therefore, the measured output from a geophone is related to ground movement through a two-stage transfer function—first a second-order differential transformation describing the mechanical system movement, followed by the electrical system relation obeying the Faraday's law and describing the generated current in the coil, which is theoretically proportional to velocity. Figure 237 shows an example of the frequency response characteristics for the two stages. Even though the mechanical system exhibited a relatively flat response at low

frequencies, the performance of the overall combined response for an in-series configuration fell considerably for low frequencies.
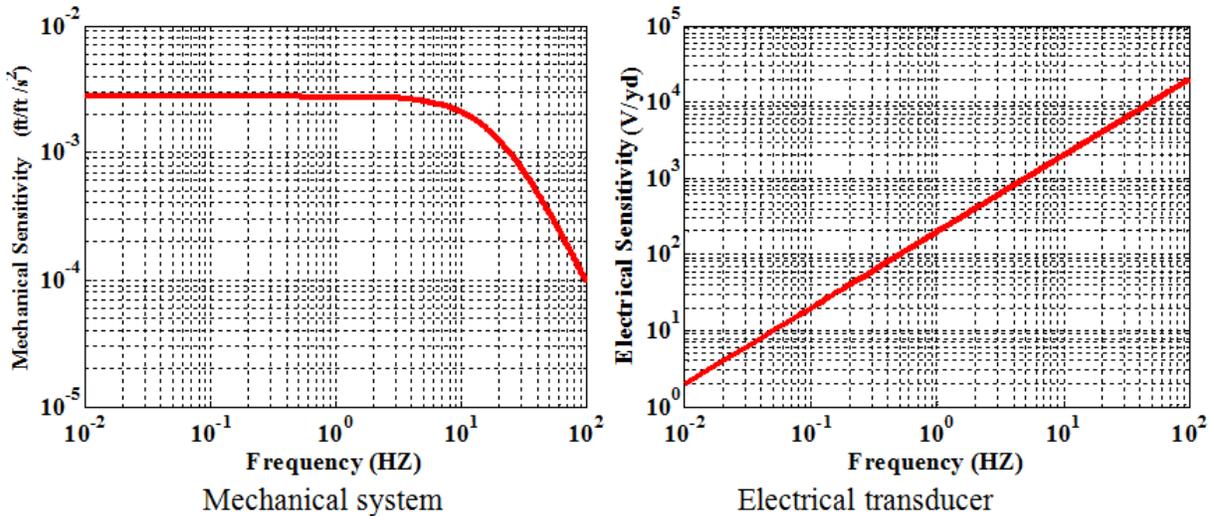
Figure 237. Graphs. Frequency response of geophone components.

For a seismometer, the relative motion of the mass with respect to the casing of the sensor is measured directly using LVDTs. The natural frequency of the mass-spring system and the damping must be tuned to control the sensitivity of the module. The sensitivity (of a seismometer) is defined as the ratio of the maximum motion of the mass to the maximum ground motion during steady-state motion; it is a measure of magnification developed directly at the transducer.

Figure 238 shows the amplitude response of a sensor with a natural period of 1 s and damping ranging from 0.25 to 4 h. As can be seen, low damping resulted in a peak in the response function that occurred for ratio values less than 1. If damping was equal to 1, the seismometer mass returned to its rest position in the least possible time without overshooting, the response curve had no peak, and the seismometer is said to be critically damped. From the shape of the curve, it can be seen that the seismometer could be considered a second-order high pass filter for ground displacement. Seismometers perform optimally at damping close to critical. When the damping increases above 1, the sensitivity decreases and the response approaches that of a velocity sensor.

If the ground displacement frequency were near the resonance frequency, a larger relative motion would be induced (depending on damping). If the damping was low, the mass could get a push at precisely the right time such that the mass would move with a larger and larger amplitude, thus the gain would be larger than 1. For this to occur, the push from the ground would have to occur when the mass was at an extreme position (top or bottom) and there must be a phase shift of $-\pi/2$.

Below the resonance frequency, the relative displacement due to ground displacement would decrease. With the ground moving very slowly, the mass would have time to follow the ground motion; in other words, there would be little relative motion and less phase shift. Thus the gain

would be low. Therefore, for small frequencies, the relative displacement of the mass would be directly proportional to the ground acceleration. The sensitivity of the sensor to low frequency ground acceleration would be inversely proportional to the squared natural frequency of the sensor.

Strictly speaking, none of the sensors are linear—in the sense that an arbitrary waveform of ground motion can be exactly reproduced at scale—for any kind of response.
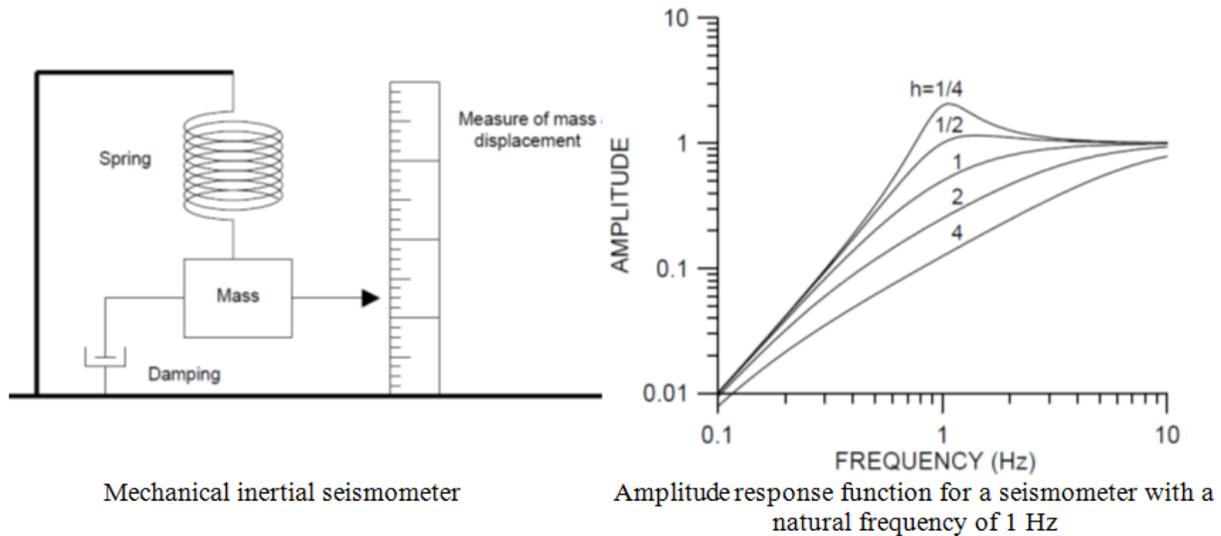
Figure 238. Diagram and Graph. A mechanical inertial seismometer with a natural frequency of 1 Hz.

Based on the collected information concerning the frequency behavior of the different measuring devices, a time-frequency analysis was conducted. Measured real field signals were analyzed in the time and frequency domains. The objective was to determine the location, with respect to the signal peak, of frequencies that were artificially filtered by the mechanical spring-mass system, which reduces the accuracy of the sensors (figure 239 through figure 244). The spectrograms, or time-frequency representations of a signal shown in these figures, are 2-D visual representations of the spectrum of frequencies in a signal as they vary with time. The colors illustrate the distribution of the energy contained in the signal as a function of time (x-axis) and frequency (y-axis). The spectrogram is equivalent to a tracing of the frequency response of the analyzed signal in a moving time window. The unit is the decibel, which is a logarithmic unit commonly used to express the ratio between a reference value and the value of a physical quantity measured in units of power or intensity.

As discussed in the previous paragraph, the different measuring instruments eliminate certain frequencies because of poor performance in some specific ranges. Therefore, it is important to know in what time window (before or after the peak) the eliminated frequencies occur. Also, the comparison between the time-frequency contents of the load and the response from the sensors help in determining the effect of time synchronization.

Figure 239. Graphs. Time-frequency content of the load for LTPP section 60565.

Figure 240. Graphs. Time-frequency content of the load for LTPP section 320101.
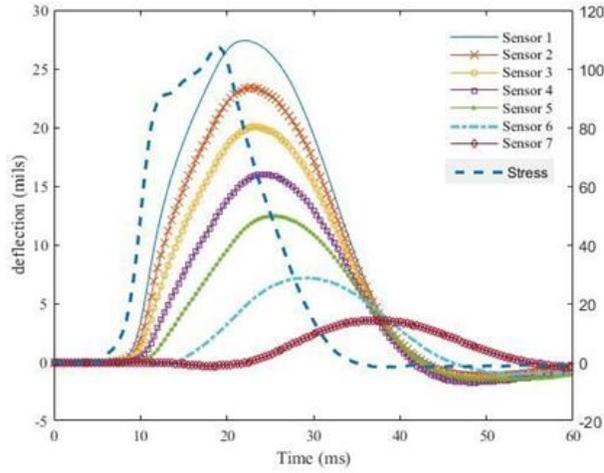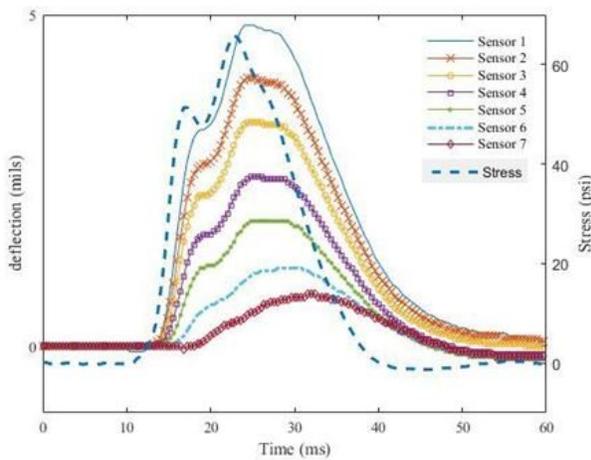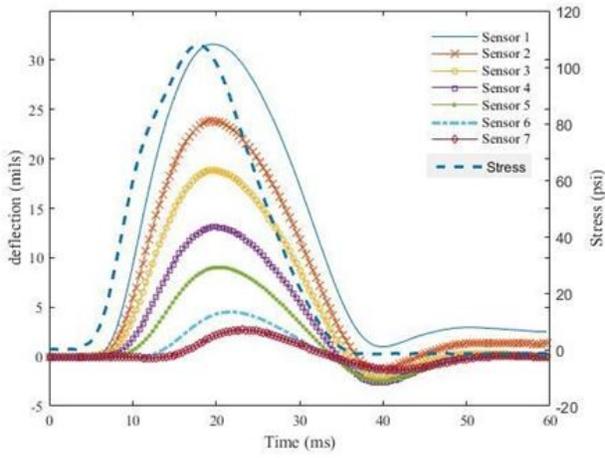
Load and deflection time histories
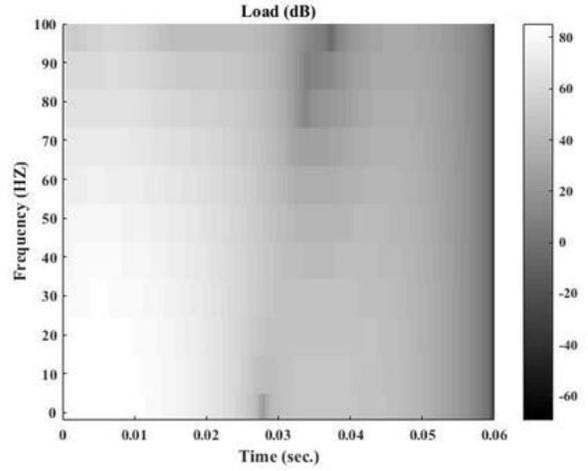
Time-frequency representation of the load

Figure 241. Graphs. Time-frequency content of the load for LTPP **section 400113.**
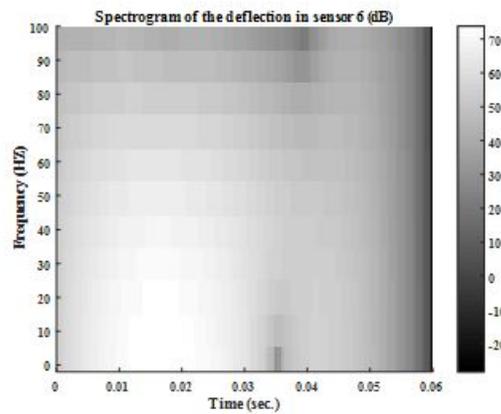
Figure 242. Graphs. Spectrum of deflection at each sensor for LTPP section 60565.
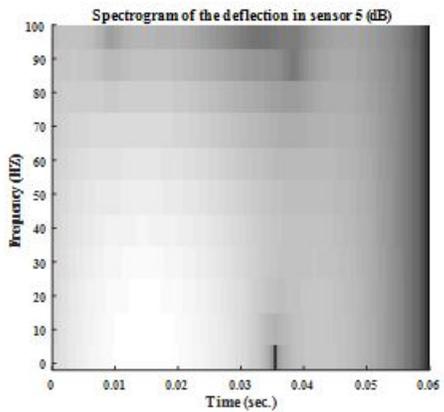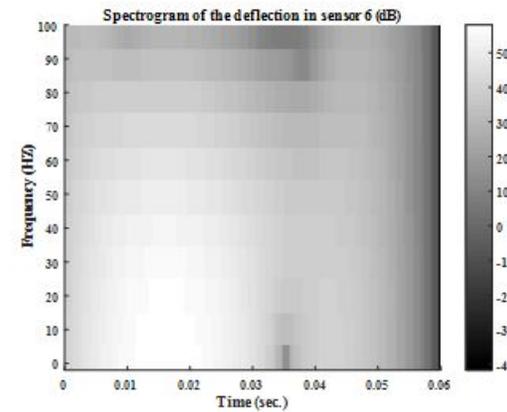
Figure 243. Graphs. Spectrum of deflection at each sensor for LTPP **section 320101.**
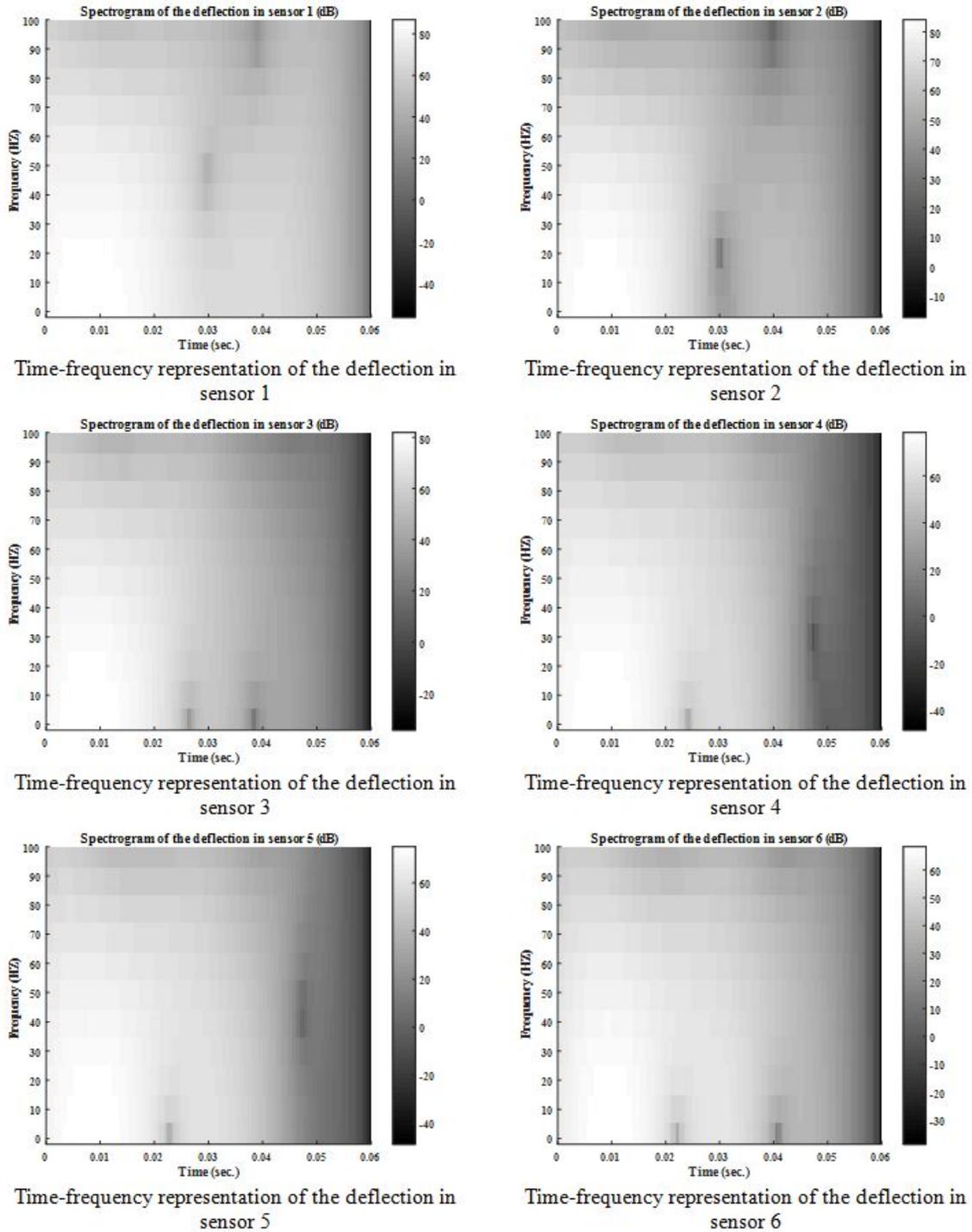
Figure 244. Graphs. Spectrum of deflection at each sensor for LTPP **section 400113.**

In light of the literature review of the FWD equipment and the above interpretations, the following issues and observations were identified:

- Key issue 1: Accuracy

  - o A fixed reference system is needed.
  - o For seismometers, "fixed mass" is not easy to achieve (highly sensitive to calibration).
  - o For geophones, relying on external corrections for the displacement of the sensor bar is very susceptible to numerical errors (double integration, etc.).

- Key issue 2: Sensitivity

  - o The ideal is to have the same sensitivity over the entire frequency content of the motion.
  - o Both seismometers and geophones have problems at low frequency (especially geophones), which is crucial when measuring pavement deflections.

EXPERIMENTAL TESTING

Preliminary Field Evaluations

Different sensor types were identified and acquired. A seismometer, a geophone, and an accelerometer were tested. Figure 245 shows the acquired systems. An in-house data acquisition module was built to extract the raw unfiltered data from all the measurement sensors.

Figure 245. Photos. Geophone (left), seismometer (center), and high-accuracy piezoelectric accelerometer (right).

A laser head capable of noncontact measurement of deflections was also tested. Preliminary evaluations of the laser under simulated real field conditions were conducted at the testing facility at FHWA's Turner-Fairbank Highway Research Center (TFHRC) (see figure 246).

Figure 246. Photos. Setup attached to the FWD system at TFHRC.

The objective was to determine the induced errors (noise) in the recorded signal from the laser in a non-controlled environment. A sample of the obtained signal and its frequency content are shown in figure 247.
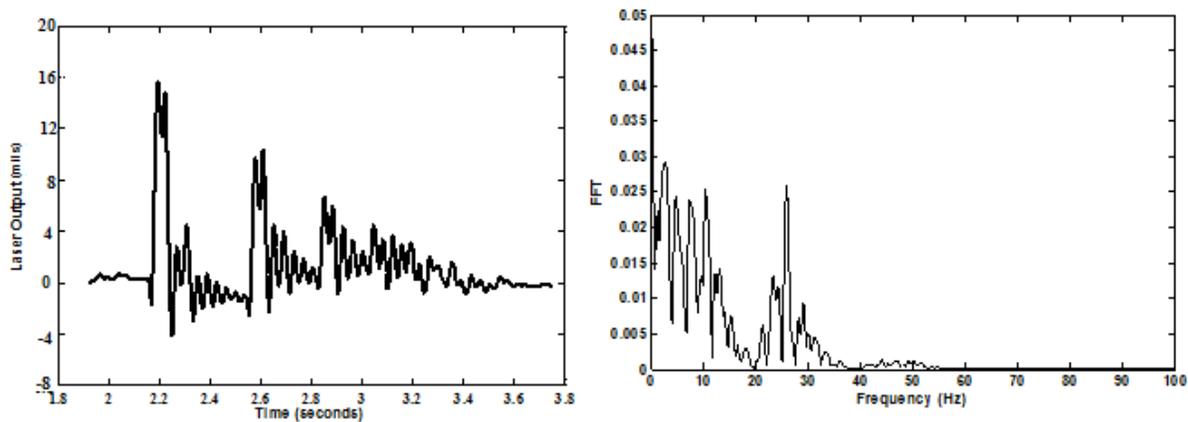
Figure 247. Graphs. Sample measured signal (left) and frequency content (right).

The signal-to-noise ratio (SNR) was calculated as 122 for the recording shown in figure 247. This high SNR factor indicated that most of the power in the signal was useful information, and there was very little background noise, which can be identified and filtered. A variation of ±10 percent was observed in the calculated ratios for all measured signals. In addition, the accuracy was evaluated to be on the order of 10^{-5} mil.

The recorded deflection was not compared with the output of the FWD system because of the unavailability of the control laptop computer for the machine during the testing.

To improve the accuracy of the laser measurements, a new more accurate system was acquired. The system and the properties of the new laser head are shown in figure 248. Furthermore, observations during the testing showed that vibrations in the mounting device were a major cause

of induced noises. Specific fixtures were built to attach to different models of FWD machines. Figure 249 shows the design for the fixture.

Figure 248. Photos. LK-H008 laser head for deflection measurement .
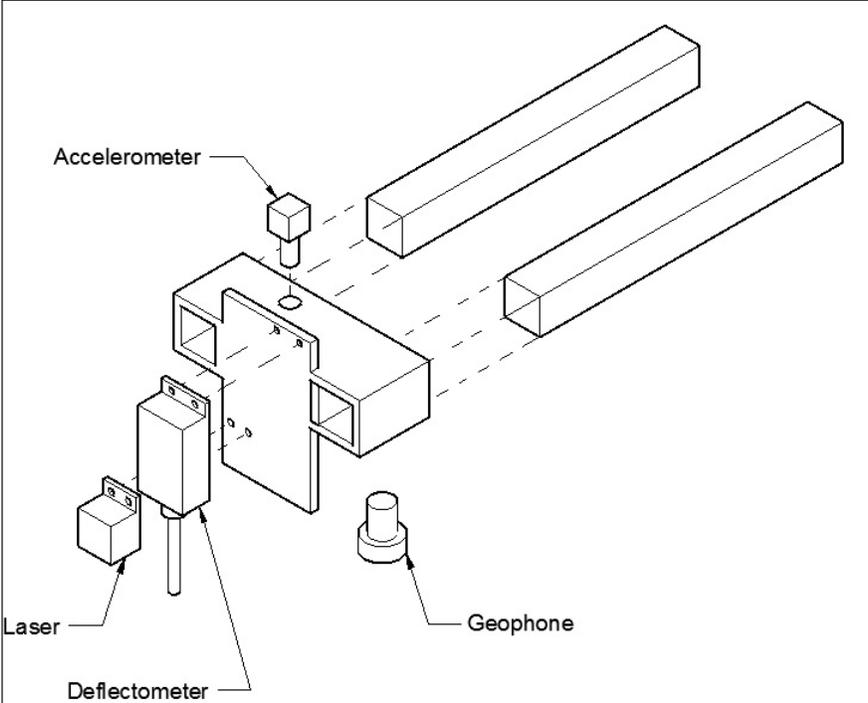
Figure 249. Diagram. Schematic of the designed fixture.

Laboratory Evaluation of Geophones—Accuracy and Sensitivity

A set of laboratory tests were conducted to evaluate the performance of the geophone sensor. Two series of tests were conducted: First, the research team placed the geophone directly on the beam and side by side with the laser sensor (see figure 250). Then the geophone was placed in its encasement provided by the manufacturer and situated symmetrically opposite to the laser sensor relative the MTS® load actuator (see figure 251). For this second set of tests, the team also introduced noise on the system by independently vibrating the test setup while placing an accelerometer on the MTS® system so that the noise could be filtered out of the signal.

Figure 252 shows an example of raw velocity signal data from the geophone, and figure 253 shows the filtered velocity data. The figures show that the velocity signal was not symmetrical about zero and that some cyclic behavior occurred post loading time.

Figure 254 shows multiple replications of the laser displacement readings. The data show that the laser was capable of producing a faithful and repeatable deflection signal.

Figure 250. Photo. Geophone placed directly on beam next to laser sensor.
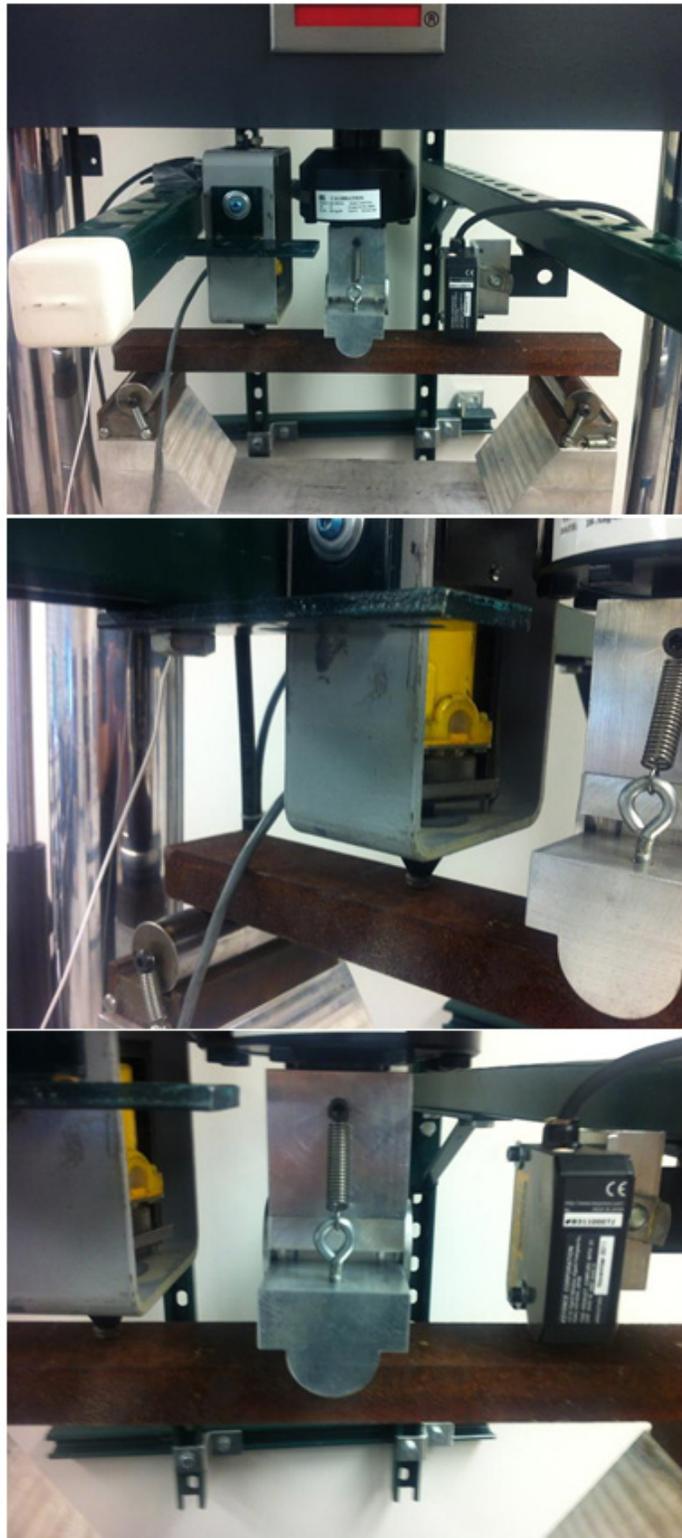
Figure 251. Photos. Test setup for mounted geophone and laser sensor.
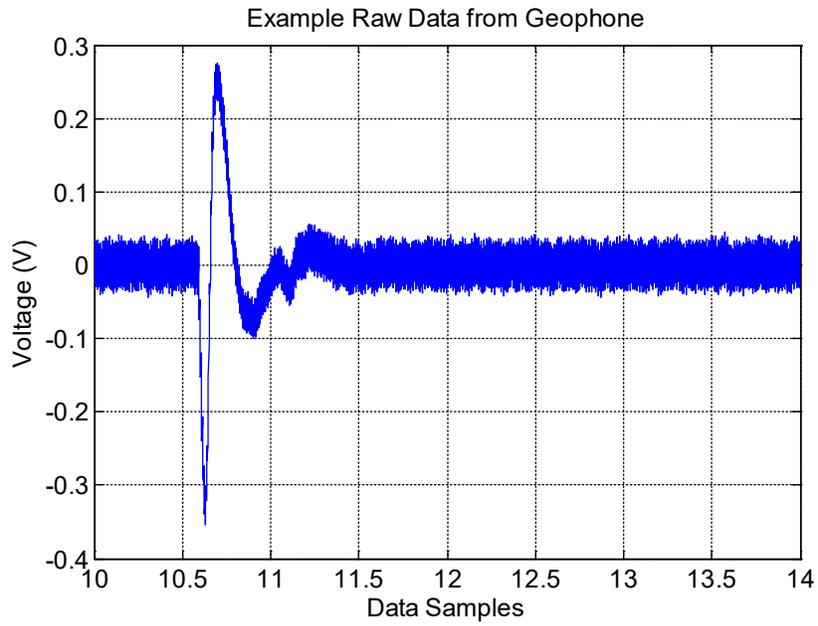
Figure 252. Graph. Example of raw data from geophone.
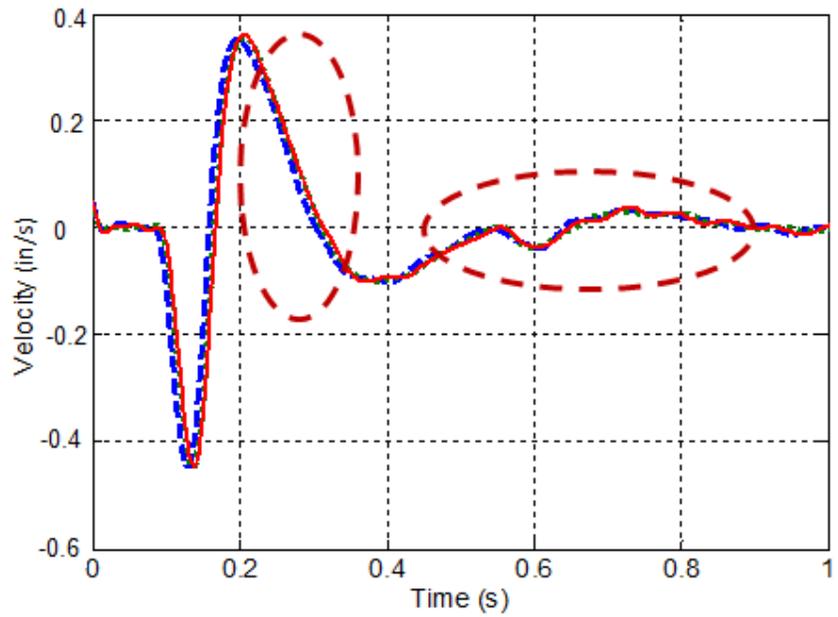
Figure 253. Graph. Filtered geophone data with multiple replications.
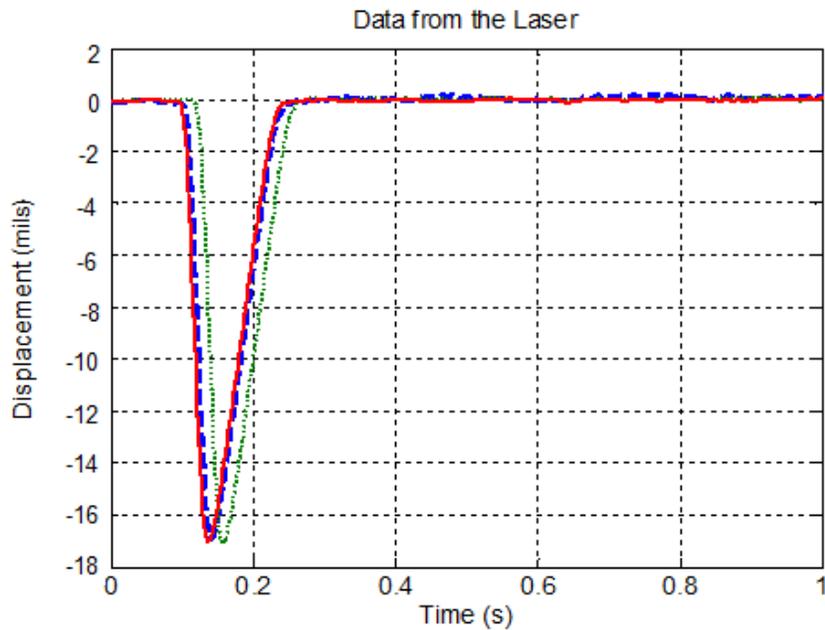
Figure 254. Graph. Laser data with multiple replications.

Figure 255 and figure 256 show comparisons between the geophone and laser data for the first test series. When comparing velocity measurements, laser displacement signal was differentiated with respect to time. When comparing deflection measurements, geophone measurements were integrated with respect to time. The measurements showed some significant differences between the two systems, especially after the load returned to zero.

Figure 257 shows similar behavior for the second test series. From the conducted tests, it was clear that numerical errors played a significant role in altering the recorded signals. A set of tests was devised to illustrate the effect of numerical integrations on the collected data to be used in the tools introduced in chapter 5.
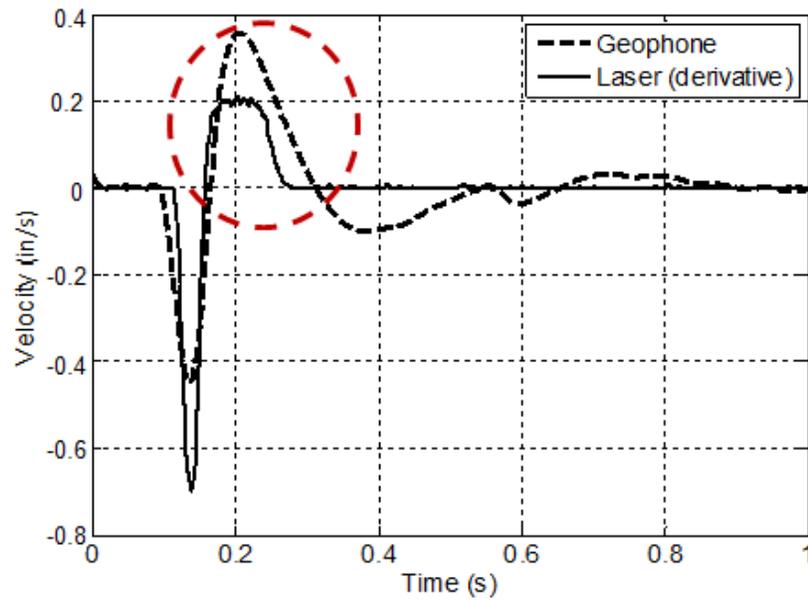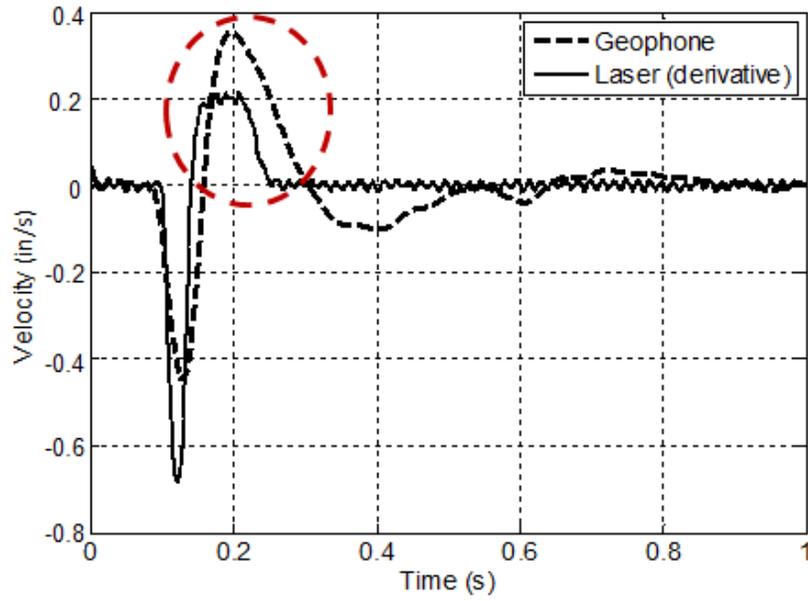
Figure 255. Graphs. Comparison of filtered geophone velocity data with the laser derivative output for test series 1.
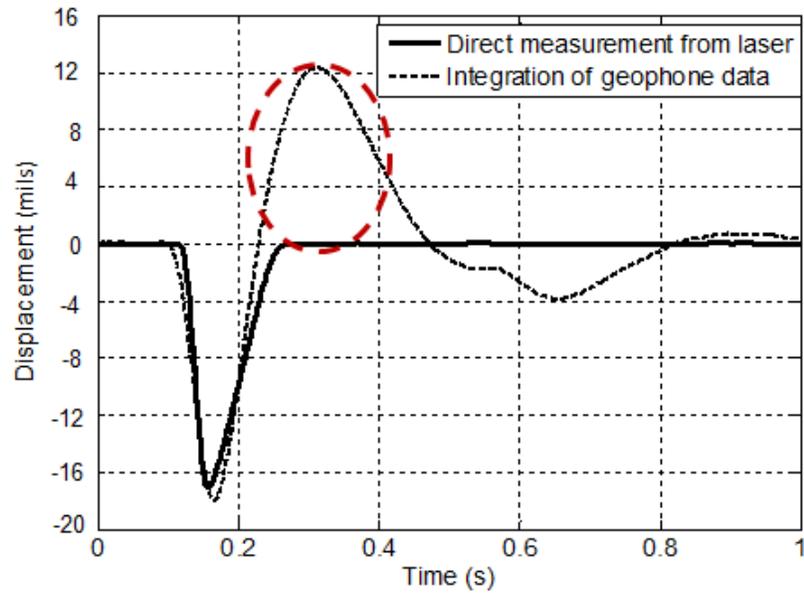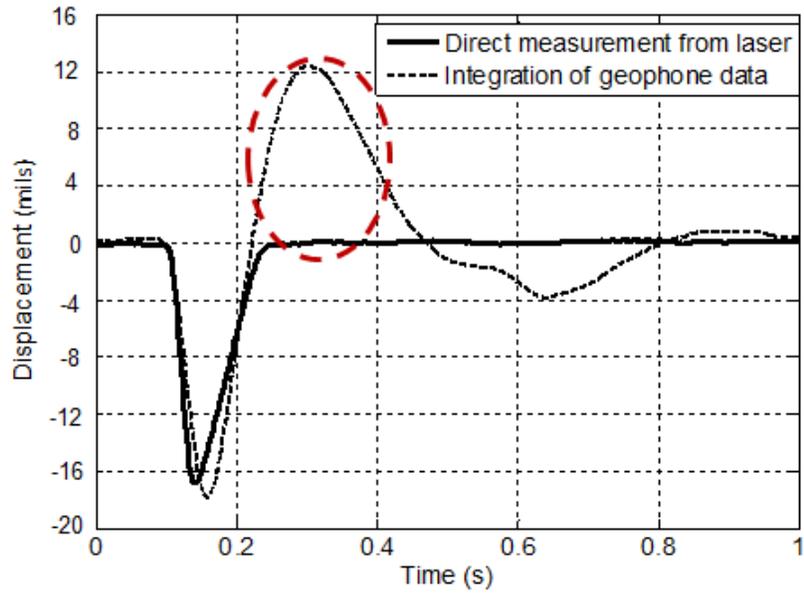
Figure 256. Graphs. Comparison of integrated geophone data with direct laser displacement output for test series 1.
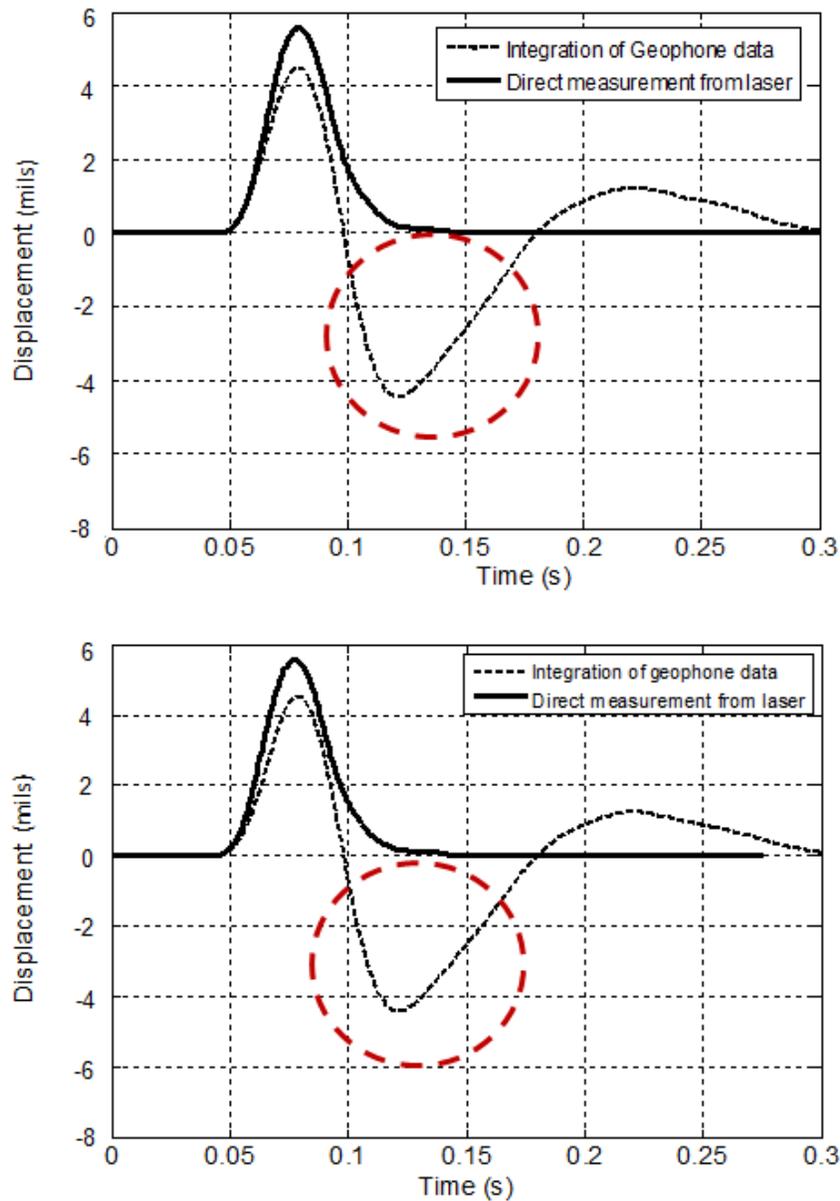
Figure 257. Graphs. Comparison of integrated geophone data with direct laser displacement output for test series 2.

Effects of Numerical Errors and Drifts

A series of field tests were performed with the objective of illustrating the effects of drifts and errors induced by numerical integrations and filtering/treatment of raw data collected from inertial sensors (geophones). A KUAB FWD system (owned by the Michigan Department of Transportation (MDOT)), which uses seismometers, was outfitted with a geophone (see figure 258). Loading tests, at four different load levels, were performed on a thin asphalt layer covering a granular structure. Raw data were collected directly from the sensors and compared with the output rendered by the device software (see figure 259).

Figure 258. Photos. Test setup.
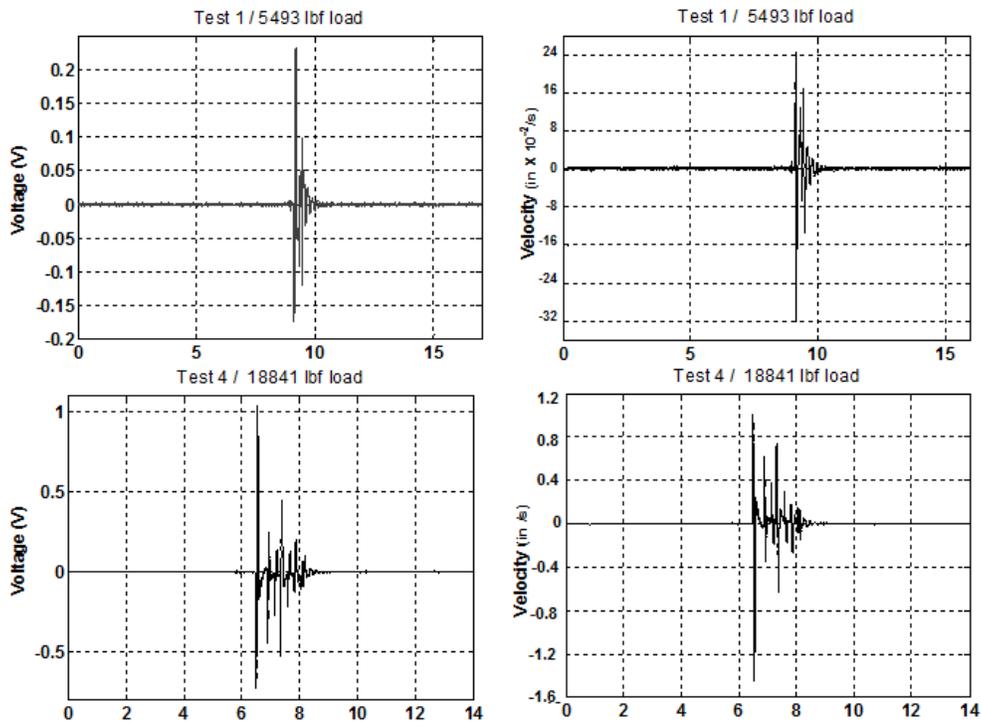
Figure 259. Graphs. Sample of recorded raw geophone data.

The use of numerical integration of acceleration or velocity information from inertial sensors to obtain position information inherently causes errors to grow with time, commonly known as "integration drift." The main problem is that integrating a signal contaminated with noise and drift leads to an output that has an RMS value that increases with integration time even in the absence of any motion of the sensor. For a single integration, the errors are a function of the duration of the signal. For that reason, estimation of deflections using inertial sensors is usually performed with the help of externally reference-aided sensors or sensing systems, or prior knowledge about the motion to correct for the drift. With aided sensors or sensing systems, KFs or EKFs are commonly used to fuse different sources of information in an attempt to correct for the drift.

233

For real-time compensation, zero-phase adaptive filtering algorithms are employed. These algorithms are based on truncated Fourier series such as weighted-frequency Fourier linear combiner (WFLC) or band-limited multiple Fourier linear combiners (BMFLCs), which can detect periodic or quasi-periodic signals. These algorithms can estimate desired periodic signals from a mixture of desired periodic signals and undesired signals without altering the phase and magnitude of the desired periodic signal. However, to achieve satisfactory accuracy of the estimate, the WFLC and the BMFLC have limitations—the magnitude of the undesired signals compared with that of the desired periodic signal cannot be too large. Because the magnitude of the integration drift is too large compared with that of the periodic signal, the algorithms are not well suited for the problem of drift.

For the tests performed, the research team needed to obtain drift-free deflection estimates of the quasi-periodic motion using the geophone sensor without employing other aided sensors or sensing systems. An example of the effects induced by the numerical integration is shown in figure 260. The methods used to obtain the test results are based on linear high-pass filtering of drifted position by selecting a cutoff frequency between the frequencies of low-frequency drift signals and that of the periodic motion, which had relatively high frequency (the effect of the cutoff frequency selection is shown in figure 261). A specific cutoff frequency was selected for each dataset. Optimal values were used to obtain the final result shown in figure 262 and figure 263. One of the issues observed was that linear filtering inherently introduced phase shift and attenuation, resulting in inaccurate deflection-amplitude estimates. A combination of linear filtering and WFLC was used. The integrated signal was filtered using a high-pass linear filter. The filtered signal, which was the phase-shifted and amplitude-modified version of the actual desired signal, was then estimated using WFLC algorithms. The estimate of the actual periodic signal was recovered from the phase-shifted and modified estimate by compensating for the phase-shift and amplitude alteration introduced by the filter.
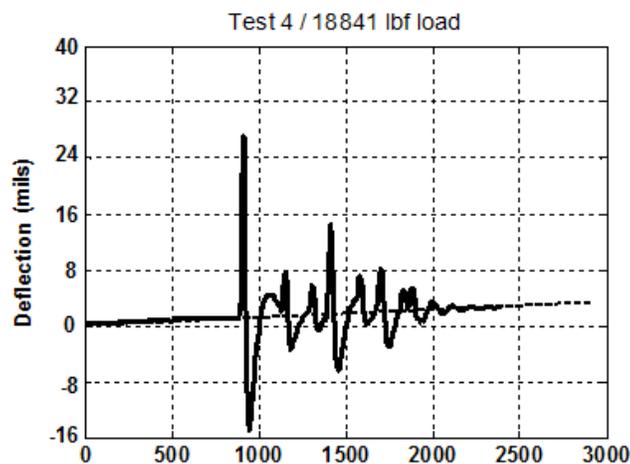
Figure 260. Graph. Example of numerical drift resulting from integration of raw geophone data.
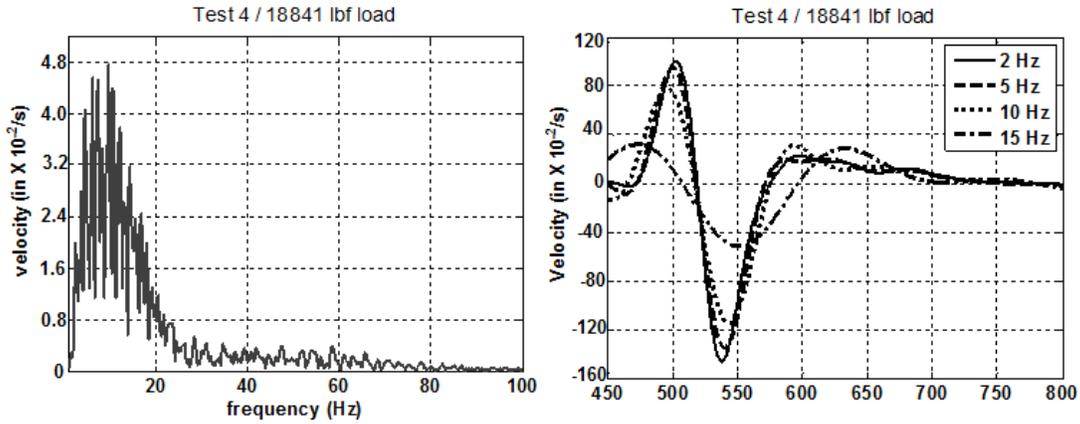
Figure 261. Graphs. Illustration of the windowing and filtering procedure and the observed effects on the raw velocity data: frequency content of the velocity signal (left) and effect of the selected cutoff frequency on the signal magnitude as a source of errors (right).
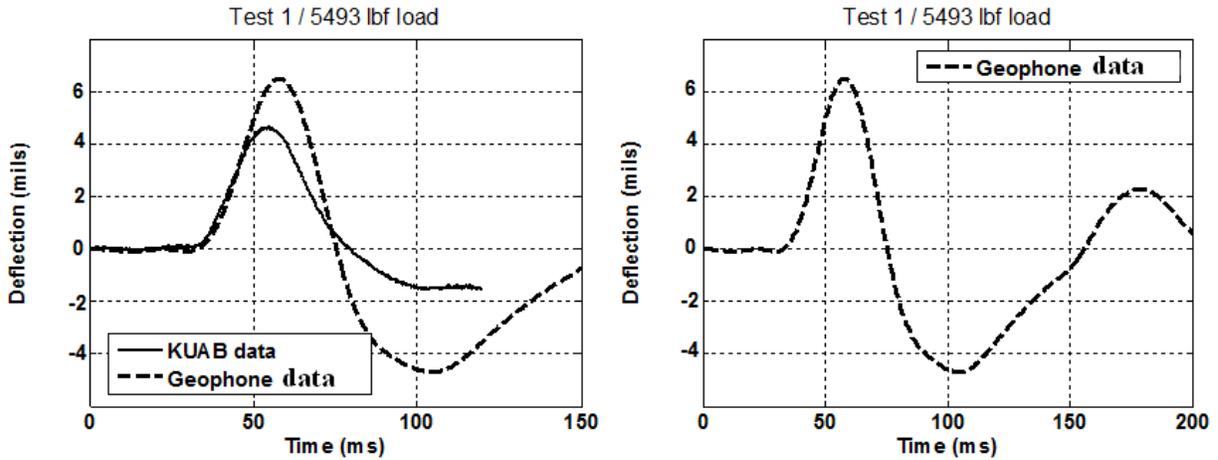
Figure 262. Graphs. Comparison between the filtered and treated seismometer data rendered by the device software and the integrated unfiltered geophone data (left); and integrated and filtered geophone data showing post-peak effects due to propagation of cumulative errors (right).
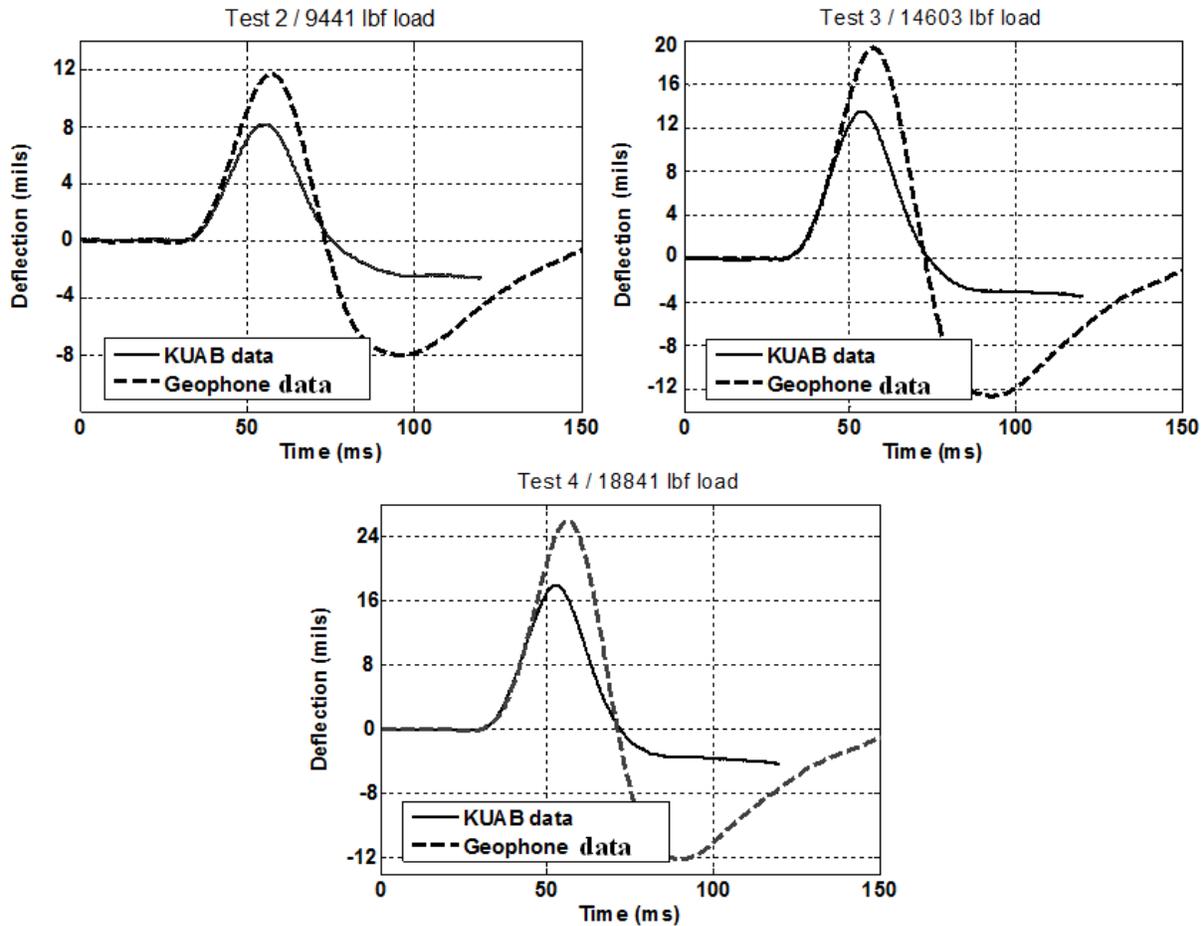
Figure 263. Graphs. Comparison between the filtered and treated seismometer data rendered by the device software and the integrated unfiltered geophone data at different load levels.

Seismometer—Field Evaluation

The FWD system (owned by the MDOT), which uses seismometers, was outfitted with a laser for direct deflection measurements. Loading tests, at four different load levels, were performed on a section of a local road. Raw data were collected directly from the laser and compared with the output rendered by the commercial software used.

The laser was mounted on a beam that was attached to the ground on the roadside (see figure 264). The objective was to isolate the beam from the effects of the vibrations in the pavement.

Given the high accuracy of the laser system, even small vibrations are picked up in the signal. For the tests performed, a poor SNR was observed. The measurements from the laser had to be filtered and adjusted. An example is shown in figure 265.

As figure 265 shows, the post peak fluctuations rendered in the laser signal were not included in the KUAB signal, which was cut off at 120 ms. More important, the difference in deflection time

236

histories seemed to be much larger in the post peak region. This would seem to confirm anecdotal assertions made by FWD specialists over the years.

Figure 264. Photos. FWD test setup: view of the beam used for mounting the laser (top left), close-up view of mounted laser(top right), and view of laser sensor setup (bottom).
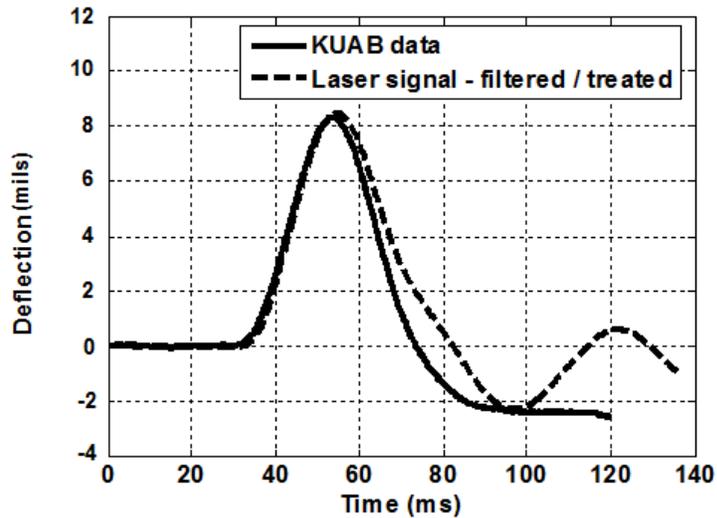
Figure 265. Graph. Comparison between the seismometer data rendered by the KUAB software and the filtered and treated laser data measured for a 9,500-lbf load.

CONCLUSION

This chapter describes a set of experimental procedures conducted both in the laboratory and in the field using seismometers, geophones, and accelerometers. The experiments were designed to evaluate the performance of the sensors in term of accuracy and sensitivity, with the objective of including the effects of these parameters in the tools described in previous chapters.

Based on the observations, the following issues were discussed:

- The need for a fixed reference system.

- The difficulty of achieving a "fixed mass" for seismometers, which are highly sensitive to calibration.

- The reliance of geophones on external corrections for the displacement of the sensor bar, which is very susceptible to numerical errors (double integration, etc.).

- Maintenance of sensitivity over the entire frequency content of the motion, which cannot be done.

- The problems that both seismometers and geophones have at low frequency (especially geophones), which is crucial when measuring pavement deflections.

In addition, a study was presented to illustrate the effects of numerical integrations and drifts, confirming their significant influence on the output results.

For all the tests presented, a high-precision laser system was used in the experimental setups as a reference system and also to evaluate limitations on potential recommendation of its use in FWD systems. Even though the laser system performed flawlessly under laboratory conditions and was successfully used as a reference for characterizing the other devices, it was much more difficult to use in the field. Given the high accuracy of the laser, even small vibrations were picked up in the signal. Therefore, field measurements from the laser also had to be filtered and adjusted. The advantages of using a laser were mainly that it eliminated all the undesirable effects from numerical artifacts because it directly measured the deflection. This is similar to seismometers but with the added advantage that it was a noncontact method so there were no seating errors. The main disadvantage was that lasers still need a fixed reference in the system to extract the pavement's true surface motion. This could be achieved by either disconnecting the rigid bar that holds the sensors away from the FWD machine frame, thus isolating the frame from the vibration noise, or by placing an external reference mechanism away from the influence of the deflection basin induced by the load drop. The external reference could be position sensors that track the movement of the beam holding the sensors. This was previously done using accelerometers but would not solve the problem because it would require a double integration for the accelerometer data.

Geophones have the advantage of not requiring an added reference, but it was shown in the studies reported in this chapter that data were relatively less reliable post-peak. Geophones are based on the inertia of a suspended mass, which means they have performance issues at low

frequencies. Furthermore, the requirement for a numerical integration induces several numerical artifacts such as errors in post-peak amplitude and drifts.

The issue with time synchronization between the load and the measurements output was an easy technological fix. The focus of existing FWD systems has been to determine the response peaks, which are not affected by the synchronization problem. This becomes important when the whole time response is of interest. This issue could be resolved by adding a position sensor that records the exact position of the dropping mass. The position sensor should be connected to the same data acquisition system as all the sensors so that it uses the same timer.

CHAPTER 7. CONCLUSIONS

SUMMARY OF FINDINGS

LTPP Data Analysis

A detailed sensitivity analysis on a relatively large sample of FWD test results from the LTPP database was conducted to determine the following: (1) prevalence of dynamics, (2) how prevalence of nonlinear behavior, and (3) measurement issues based on apparently erroneous deflection sensor time histories. The data covered all climatic zones, seasons, and temperature ranges. It was observed that dynamics were present in about 65 percent of the cases, while nonlinearity could be prevalent in a range from as low as 24 percent of the cases to as high as 65 percent of the cases, depending on severity level and sensor location. Nonlinearity was more prevalent for the sensors that were far from the center of the load. Because of the prevalence of dynamic behavior (in the form of free vibrations of deflection sensor time histories) observed in the large sample of LTPP FWD test data, it was hypothesized that in the great majority of the cases, the stiff layer condition might not correspond to the presence of shallow bedrock. Such bedrock would be highly unlikely given that it typically lies at much greater depths. Instead, the stiff layer condition could manifest anytime the soils below the subgrade layer are stiffer than the subgrade layer itself. This could be caused by increased confinement with depth, overconsolidation, or existence of shallow groundwater table for example; these situations are very common in any soil profile. This would explain the high percentage of sections from the LTPP database that showed dynamic behavior.

Viscoelastic Approach

As part of this effort, two multilayered viscoelastic algorithms were developed. The first algorithm (called LAVA/LAVAP) assumes the AC layer as a linear viscoelastic material and unbound layers as linear elastic. The second algorithm (called LAVAN) also assumes the AC layer as a linear viscoelastic material; however, it can consider the nonlinear (stress-dependent) elastic moduli of the unbound layers. These two models were used to develop two GA-based backcalculation algorithms (called BACKLAVA/BACKLAVAP and BACKLAVAN) for determining the $E(t)$ or $|E^*|$ master curve of AC layers and unbound material properties of in-service pavements.

The research team drew the following conclusions:

- Viscoelastic properties of AC layer can be obtained using a two-stage scheme. The first stage is an elastic backcalculation to determine unbound layer properties, which is followed by viscoelastic backcalculation of $E(t)$ of the AC layer while keeping the unbound layer properties fixed.

- The examples presented in this study show that, in the case of the presence of considerable dynamic effects, the algorithms (BACKLAVA and BACKLAVAN) should be used with caution or use the dynamic backcalculation algorithm (DYNABACK-VE). The algorithms presented in chapter 4 predict the behavior of flexible pavement as a viscoelastic damped structure, assuming it to be massless.

- For the GA backcalculation procedures, the following population and generation sizes are recommended:

  o For the BACKLAVA model, use a set of FWD tests run at different (but constant) AC layer temperatures with a population size of 70 and 15 generations.

  o For the BACKLAVAP model, use a single FWD test with a known AC temperature profile and a population size of 300 and 15 generations.

  o For the BACKLAVAN (nonlinear) model, use FWD tests run at different (but constant) AC layer temperatures and a population size of 100 and 15 generations.

Dynamic Viscoelastic Approach

A new solution and its associated computer program were developed for dynamic viscoelastic time-domain backcalculation of multilayered flexible pavement parameters under FWD tests in the time domain. The method uses a time-domain viscoelastic solution as a forward routine (ViscoWave-II) and a hybrid routine (DYNABACK-VE: GA and modified LM method) for backcalculation analysis. For the GA-based backcalculation procedure, the research team recommends using DYNABACK-VE with a population size of 300 and a number of generations of 15. The advantage of the new solution is that it can analyze the response of pavement systems in the time domain and can therefore accommodate time-dependent layer properties and incorporate wave propagation. Also, because the backcalculation is performed in the time domain, the algorithm is not sensitive to truncation in the deflection time histories. The new algorithm is capable of backcalculating layer moduli, including the master curve of the AC layer at every reduced time and the depth to the stiff layer and its modulus value, if it exists. The results using simulated deflection time histories and field FWD data show excellent stability and accuracy.

The sensitivity of dynamic backcalculation solutions to signal noise and synchronization problems is high. The remedy to noise is to preprocess the raw data by filtering out the high-frequency content of the signal (anything above 100 Hz) in deflection and load pulse data. Also, in the analysis presented in chapter 5, the percent error between the computed and measured displacement was used as the minimizing error. If percent error were used as the minimizing objective, it could lead to overemphasis of lower magnitudes of deflections at the later portion of the time history, which typically includes noise and integration errors. Hence another fit function was proposed in which the percent error was calculated with respect to the peak of deflection at each sensor. This de-emphasized the tail data by normalizing them with respect to the peak.

If synchronization problems occur, the dynamic backcalculation algorithm may not work as well, although one could shift the signals similar to what was done in the quasi-static viscoelastic solution (chapter 4). Because the quasi-static solution presented in chapter 4 is already coded to remove the time delay between sensors, the research team recommends the use of BACKLAVA instead of DYNABACK-VE when such a synchronization problem exists.

The results from dynamic analyses clearly showed the superiority of a fully dynamic solution with a viscoelastic AC layer modulus in predicting deflection responses that are in line with the physical reality, as evidenced by the close match in the details of the deflection time histories

between theory and observation. The theoretical predictions from ViscoWave-II showed very good agreement with the measured deflection time histories. The fact that theory and measurement showed the same behavior with time was proof that these observations were physically real. This is important in that it reinforces the following: (1) a comprehensive model that takes into account viscoelasticity of the AC layer, damping in the unbound layers and dynamics in terms of inertial and wave propagation effects can explain the measured data with all their complexities; and (2) the FWD sensor measurements, if properly calibrated, can show the physical behavior for most of the time range, with the exception of the drift problems at the tail of the records.

In contrast, the layered viscoelastic solution cannot simulate the true deflection time histories because it cannot account for inertial and wave propagation effects. As such, it cannot predict the time delays in the response, the initial rebounds of the farther sensors and the free vibrations after the load is applied. Also, the layered viscoelastic solution significantly underestimates the deflections when a stiff layer is presented. This is because it cannot account for dynamic amplification caused by the wave energy trapped in the unbound layers when a stiff layer condition exists.

Practical Implications and Recommendations

The research team makes the following recommendations regarding FWD data collection, based on both viscoelastic and dynamic analyses conducted in this study:

- Careful collection of FWD deflection data is crucial. The accuracy of the deflection time history needs to be improved. As a minimum, a highly accurate deflection time history at least until the end of the load pulse duration is needed for the $E(t)$ or $|E^*|$ master curve backcalculation. The longer the duration of the deflection time history, the better.

- The temperature of the AC layer needs to be collected during the FWD testing. Preferably, temperatures should be collected at every 2 inches of depth of AC layer.

- Either a single FWD run on an AC with a large temperature gradient or FWDs run at different temperatures can be sufficient to compute the $E(t)$ or $|E^*|$ master curve of asphalt pavements. Moreover, in chapter 5, in the subsection Effect of Pulse Width on Backcalculation Results, it was shown that increasing the pulse duration will improve the backcalculation results and therefore, there is no need to run FWDs at different temperatures. However, a temperature profile is still needed to be able to backcalculate the shift factors for the master curve.

- For backcalculation using multiple FWD test datasets, tests should be conducted at a minimum of two different temperatures, preferably 18 °F or more apart. FWD data collected at a set of temperatures between 68 and 104 °F will maximize the accuracy of backcalculated $E(t)$ or $|E^*|$ master curve up to less than a 10-percent error.

- For backcalculation using single FWD test dataset at a known AC temperature profile, the FWD test should be conducted under a temperature gradient of preferably ±9 °F or more.

- An FWD configuration composed of multiple pulses will improve the accuracy of the $E(t)$ master curve prediction. However, to obtain the time-temperature shift factor coefficients, either temperature variation with depth needs to be measured (and included in the analysis) or the FWD test (with multiple pulses) needs to be run at different pavement temperatures (e.g., different times of the day). While testing using multiple pulses or elongated pulses allows calculation of $E(t)$ at longer durations, testing at lower or higher temperatures (with respect to the reference temperature) essentially means shrinking or elongating the loading pulse in reduced time domain and hence may be sufficient.

- The influence of unbound layer properties increases with incorporation of data from farther sensors and with increase in test temperature. All sensors in the standard FWD configuration are needed for accurate backcalculation of the viscoelastic AC layer and unbound layers.

FWD Equipment Analysis

A set of experimental procedures, conducted both in the laboratory and in the field, were performed using seismometers, geophones, and accelerometers. The experiments were designed to evaluate the performance of the sensors in term of accuracy and sensitivity, with the objective of including the effects of these parameters in the tools studied in earlier chapters of this report.

Based on the observations, the following issues were discussed:

- The need for a fixed reference system.

- The difficulty of achieving a "fixed mass" for seismometers, which are highly sensitive to calibration.

- The reliance of geophones on external corrections for the displacement of the sensor bar, which is very susceptible to numerical errors (double integration, etc.).

- Maintenance of the sensitivity over the entire frequency content of the motion, which cannot be done.

- The problems that both seismometers and geophones have at low frequency (especially geophones), which is crucial when measuring pavement deflections.

In addition, a study was presented to illustrate the effects of numerical integrations and drifts, confirming their significant influence on the output results.

For all the tests presented, a high-precision laser system was used in the experimental setups as a reference system and also to evaluate limitations on potential recommendation of its use in FWD systems. Even though the laser system performed flawlessly under laboratory conditions and was successfully used as a reference for characterizing the other devices, it was much more difficult to use it in the field. Given the high accuracy of the laser, even small vibrations were picked up in the signal. Therefore, field measurements from the laser also had to be filtered and adjusted. The advantages of using a laser were mainly that it eliminated all the undesirable effects from

numerical artifacts because it directly measured the deflection. This is similar to seismometers but with the added advantage that it was a noncontact method so there were no seating errors. The main disadvantage was that lasers still need a fixed reference in the system to extract the true pavement's surface motion. This could be achieved by either disconnecting the rigid bar that holds the sensors from the FWD machine frame, thus isolating the frame from the vibration noise, or by placing an external reference mechanism away from the influence of the deflection basin induced by the load drop. The external reference could be position sensors that track the movement of the beam holding the sensors. This was previously done using accelerometers but would not solve the problem because it would require a double integration for the accelerometer data.

Geophones have the advantage of not requiring an added reference, but it was shown in studies reported in chapter 6 that data were relatively less reliable post-peak. Geophones are based on the inertia of a suspended mass, which means that they have performance issues at low frequencies. Furthermore, the requirement for a numerical integration induces several numerical artifacts such as errors in post-peak amplitude and drifts.

The issue with time synchronization between the load and the measurements output was an easy technological fix. The focus of existing FWD systems has been to determine the response peaks, which are not affected by the synchronization problem. This becomes important when the whole time response is of interest. This issue could be resolved by adding a position sensor that records the exact position of the dropping mass. The position sensor should be connected to the same data acquisition system as all the sensors so that it uses the same timer.

IMPLEMENTATION RECOMMENDATIONS AND FUTURE RESEARCH

The tools developed in this project are standalone applications that could be used on most computers. The following four time-domain backcalculation software products were developed:

- **BACKLAVA**: Backcalculation algorithm for a constant AC layer temperature.

- **BACKLAVAP**: Backcalculation algorithm for a temperature profile in an AC layer.

- **BACKLAVAN**: Backcalculation algorithm for a viscoelastic AC layer and nonlinear base layer.

- **DYNABACK-VE**: Backcalculation algorithm for a viscoelastic AC layer (with temperature profile).

All these tools are engineering software applications that allow the user to backcalculate the master curve of the AC layer (four sigmoidal coefficients and two time-temperature shift factors) and the resilient moduli for the unbound base/subbase and subgrade materials. DYNABACK-VE could also backcalculate the modulus of the stiff layer and the depth to the stiff layer, if one is present.

With good seed values for the moduli (e.g., previous information about the moduli), one could also implement a simple gradient-based method along with LAVA, LAVAP, LAVAN, and ViscoWave-II as forward routines. If the measured deflections are reasonably free from errors, a simple RMS objective function can be selected; otherwise, it is better to first apply any remedies

as discussed in chapter 2, (subsection Review of Status of FWD Data Collection, Analysis, and Interpretation) before running the program.

Owing to the searching method used, DYNABACK-VE could take more time to run compared with current backcalculation programs. Thus, continued study is needed on reducing the runtime of the program. For example, the current version of DYNABACK-VE takes approximately the following times on various computers:

- Three min on a 2-core processor with 64-bit operating system.
- Forty-five s on a 4-core processor with 64-bit operating system.
- Twenty-two s on an 8-core processor with 64-bit operating system.
- Six s on a 60-core processor with 64-bit operating system.

These translate to backcalculation runs of approximately the following times and costs:

- Forty-three h on a 2-core processor with 64-bit operating system (approximately $200).
- Eleven h on a 4-core processor with 64-bit operating system (approximately $1,000).
- Six h on an 8-core processor with 64-bit operating system (approximately $2,000).
- Two h on a 60-core processor with 64-bit operating system (approximately $2,800).

As shown in this study, the influence of the parameters in the GA (size of population, number of generations, mutation rate, etc.) on the backcalculation procedure is significant, which could be an interesting topic for future study. Recently, a variety of optimization techniques have been developed with several advantages and disadvantages. A comparative study of these techniques could help better understand the moduli optimization and improve the backcalculation method. In addition, while the approach in this effort has assumed the layer thickness is known, DYNABACK-VE could be extended in the future to reliably backcalculate layer thicknesses as well. Also, the current DYNABACK-VE program assumes linear elastic pavement layers. The nonlinearity of unbound layers should be considered in the backcalculation procedure, especially under high surface loads. The algorithm could also be improved to consider the thermal effect in future versions.

APPENDIX A. DEVELOPMENT OF NONLINEAR VISCOELASTIC MODEL USING k-θ NONLINEARITY

DEVELOPMENT OF A LAYERED ELASTIC ALGORITHM WITH NONLINEAR UNBOUND LAYERS

Introduction

Unbound layers typically exhibit nonlinearity, i.e., their responses are affected by the state of stress. This stress includes the induced stress due to the applied load on the surface and the geostatic stress. Software programs such as KENLAYER and MICHPAVE consider the constitutive equation between resilient modulus and stress invariants as that shown in figure 266.

$$E = k_1 \theta^{k_2}$$

Figure 266. Equation. Relationship between resilient modulus and stress invariants..

Where:
$\theta = \sigma_1 + \sigma_2 + \sigma_3 + \gamma z(1 + 2K_0)$.
k_1 and k_2 = material constants.
K_0 = the coefficient of earth pressure at rest.
σ_1, σ_2, and σ_3 = principle stresses.

MICHPAVE is a FEM-based software program and hence can consider both the radial and vertical nonlinearity in calculations, whereas KENLAYER (being a "layered" algorithm) can consider only the vertical nonlinearity. In KENLAYER, the elastic nonlinearity is solved iteratively assuming an initial set of elastic moduli. The developed algorithm used in this section is similar to KENLAYER in that the evaluated stresses obtained using the current values of moduli are used to evaluate a new set of moduli using the equation in figure 266 iteratively. Note that the appropriate stress adjustments were made because unbound granular material cannot take tension. This means that in such a case, a residual stress would be generated that should make the stress zero or such that it would obey the yield criterion.

The algorithm developed to obtain response in nonlinear system was compared with the more robust nonlinear FEM software program MICHPAVE. Two cases were considered. In the first case, the unbound layer was considered as a single layer for nonlinearity calculations (algorithm 1), and in the second case, the layer was divided into two sections (algorithm 2). The pavement section used in the analysis is described in table 65.

Table 65. Pavement section used in the nonlinear comparison analysis.

Physical Layer	Modulus	Thickness (inches)	Poisson's Ratio	Density (pcf)	K_0
AC (Elastic)	$E(t)$ psi	6	0.45	138	0.6
Base (Nonlinear)	Nonlinear: k_1=11,450, k_2=0.33	20	0.35	121	0.6
Subgrade (Elastic)	25,500 psi	Infinity	0.45	130	0.6

Results and Discussion for Layered Elastic Algorithm With Nonlinear Unbound Layer

Results for surface deflection at the center of the load ($r = 0$ inches) at contact pressures of 10, 30, 60, and 80 psi are shown in figure 267. From the figure, it can be seen that the deflections obtained from the developed algorithms 1 and 2 match well at all the load values. This means that subdividing the 20-inch base layer into two layers and computing the nonlinear deflections on the surface did not produce an improvement in the results.
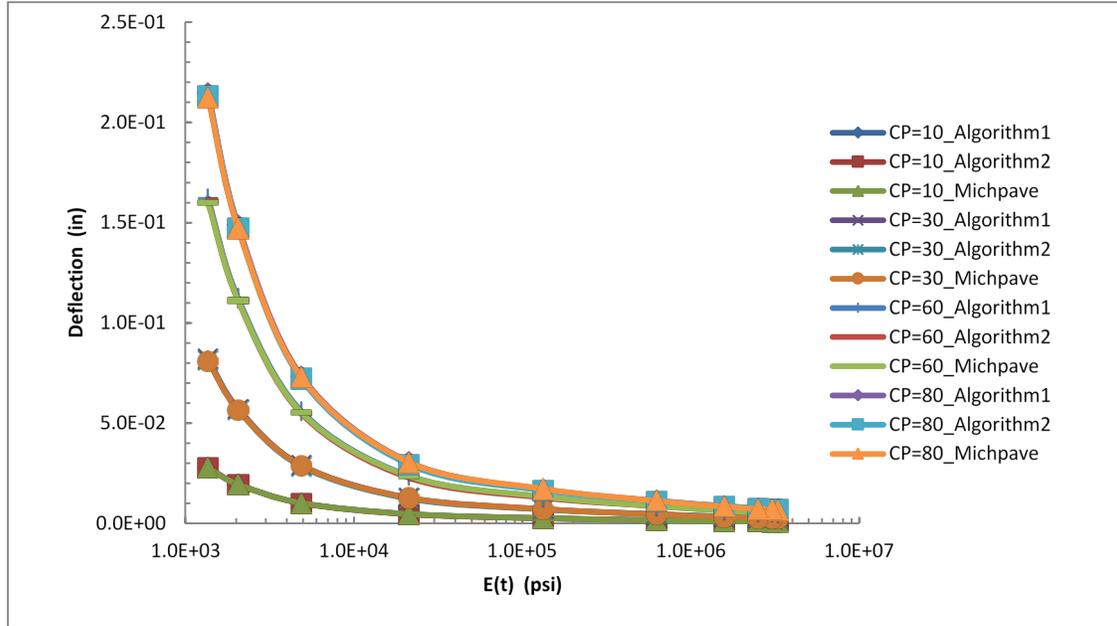
Figure 267. Graph. Results for multilayer nonlinear structure surface deflection at the center of the load ($r = 0$ inches).

NONLINEAR VISCOELASTIC ANALYSIS USING k-θ MODEL

Introduction

For the multilayered viscoelastic nonlinear pavement model to follow Fung's QLV nonlinearity model, it should satisfy figure 63 through figure 66. However, it was shown that these conditions are not satisfied for k-θ-τ type of nonlinearity. Subsequently, a generalized form of QLV model was used to develop a nonlinear viscoelastic pavement response model for k-θ-τ type nonlinearity.

In this section, the same analysis is presented for the k-θ model, shown as in figure 268.

$$M_R = k_1 \left(\frac{\theta}{p_a} \right)^{k_2}$$

Figure 268. Equation. Resilient modulus.

248

As the first step it was shown that Fung's model of nonlinear viscoelasticity was not applicable for this type of nonlinearity. Subsequently, the LAVA algorithm was modified to implement the granular base nonlinearity using the iterative solution for the pavement properties shown in table 66.

Table 66. Pavement section used in the nonlinear viscoelastic validation of k-θ model.

Physical Layer	Modulus	Thickness (inches)	Poisson's Ratio	Density (pcf)	K_0
AC (viscoelastic)	$E(t)$ sigmoid constants: 1.598,2.937,0.512,-0.562	5.9	0.35	130	0.6
Base (nonlinear)	Nonlinear: $k_1 = 3,626$, $k_2 = 0.5$	9.84	0.4	130	0.6
Subgrade (linear)	10,000 psi	Infinity	0.4	130	0.6

Figure 269 shows the variation of $g(\sigma)$ calculated using the procedure already explained in the section in chapter 4 entitled Layered Viscoelastic Nonlinear (LAVAN) Pavement Model. From the figure, it can be seen that similar to the results obtained for k-θ-τ nonlinearity, the $g(\sigma)$ values decreased with increasing stress (σ). This shows that $g(\sigma)$ was not solely based on the stress, and Fung's model cannot be used in a layered pavement structure.
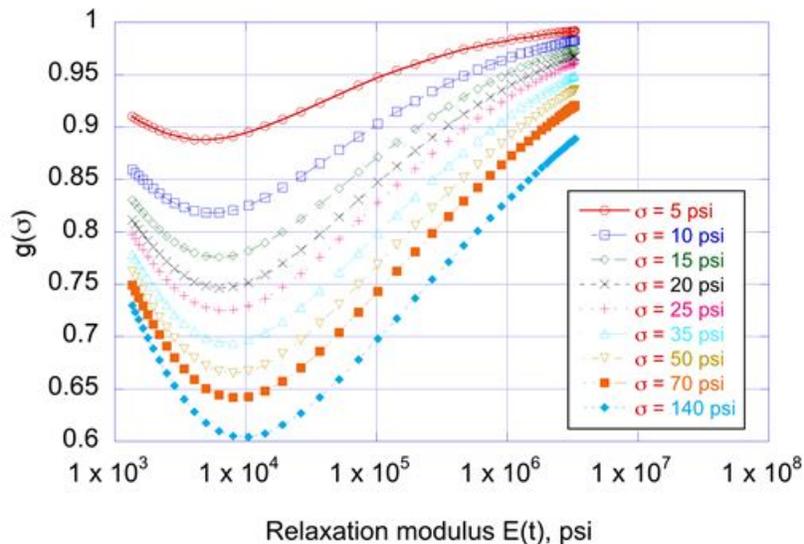
Figure 269. Graph. Variation of $g(\sigma)$ with stress and $E(t)$ of AC layer.

Subsequently, similar to the k-θ-τ model, the k-θ model was also implemented in the proposed generalized QLV algorithm and was analyzed on a 35-ms haversine load (synthetic FWD pulse load). As shown in table 58, the section properties were kept the same as used for k-θ-τ model. Two HMA mix properties were considered: control and CRTB (for mix properties refer to figure 73). Again stresses at two radial distance $r = 0$ and $3.5a$ within the center of the layer (vertically) were used in calculating unbound base modulus value. In the first trial, the modulus value of unbound granular material in LAVA was calculated using stress state at $r = 0$. In the second trial, the modulus value of unbound granular material in LAVA was calculated using stress state at $r = 3.5a$.

Results and Discussion for Nonlinear Viscoelastic Model Using k-θ Nonlinearity

Figure 270 (top) and figure 271 (top) show the results when $r = 0$ was used in LAVAN, whereas Figure 270 (bottom) and figure 271 (bottom) show the results when $r = 3.5a$ was used in LAVAN. The difference between the ABAQUS and LAVAN was quantified using the two variables PE_{peak} and PE_{avg} defined earlier for k-θ-τ model in figure 78 and figure 79, respectively. Because the model integrated both viscoelastic and nonlinear material properties, both peak deflection as well as creeping of deflection should be predicted with accuracy. PE_{avg} was used to examine the model performance in creeping.
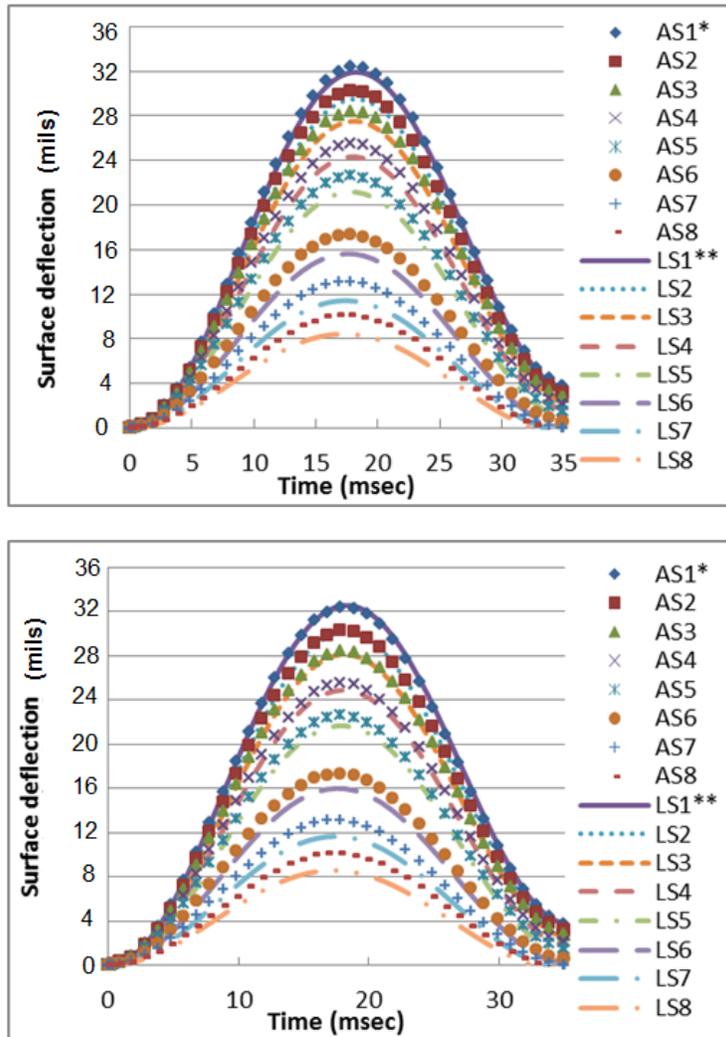
Figure 270. Graphs. Comparison of ABAQUS and LAVAN for nonlinear viscoelastic structure for the control mix where (top) LAVAN uses stress at $r = 0$, and (bottom) LAVAN uses stress at $r = 3.5a$.
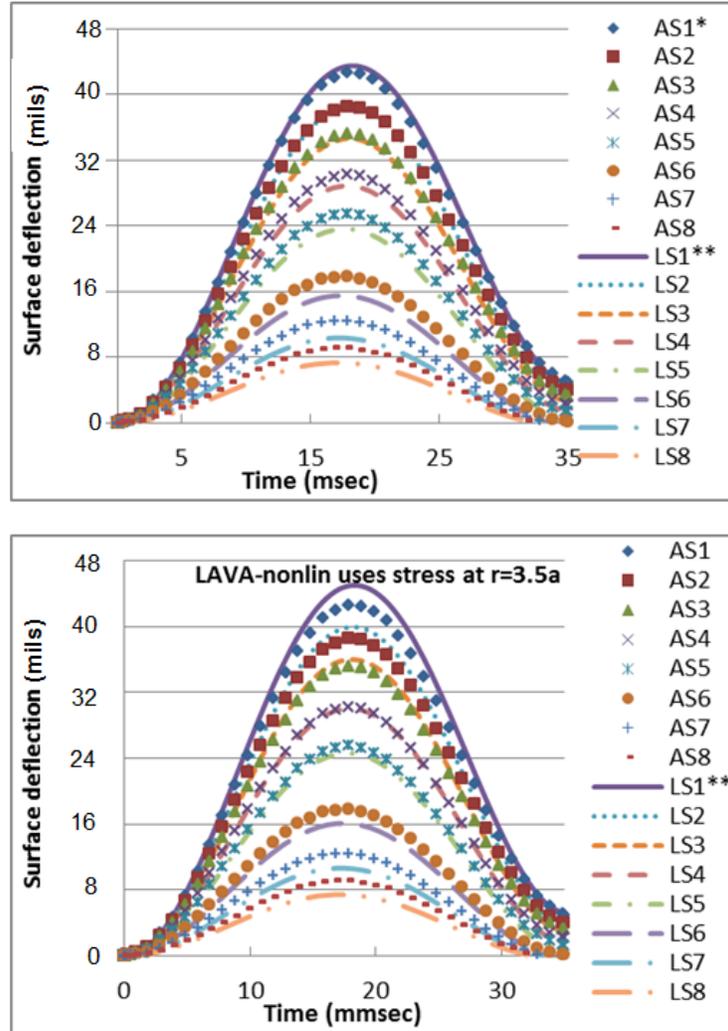
Figure 271. Graphs. Comparison of ABAQUS and LAVA for nonlinear viscoelastic structure for the CRTB mix where (top) LAVAN uses stress at *r* = 0 and (bottom) LAVAN uses stress at *r* = 3.5*a*.

As seen in figure 272, slight improvement was observed in PE_{peak} values for the control mix when stress at $r = 3.5a$ was used to obtain a resilient modulus. However, PE_{peak} values for CRTB (figure 273) showed a different trend, where first three sensors exhibited lower errors when $r = 0$ was used. The rest of the sensors did show improvement when $r = 3.5a$ was used. For both the mixes, the creep behavior of the response was well predicted by the model, which can be seen from the low PE_{avg} values in figure 274 and figure 275. However, similar to the k-θ-τ results, $r = 0$ produced relatively good results, especially in the first four to five sensors.

251
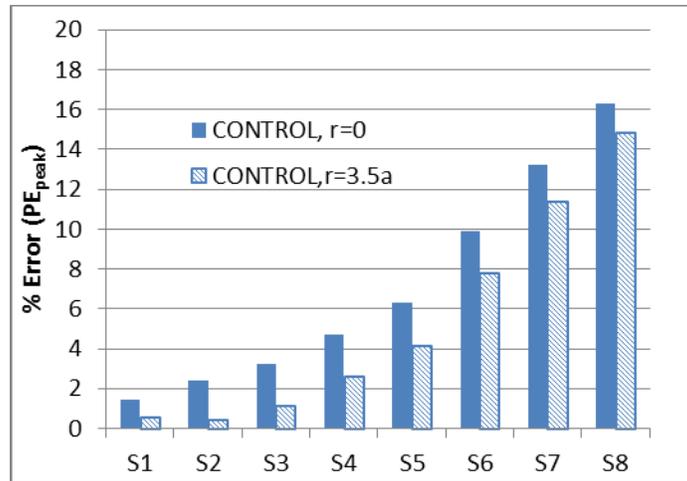
Figure 272. Graph. Percent error (PE_{peak}) calculated using the peaks of the deflections for LAVAN-ABAQUS comparison (control mix).
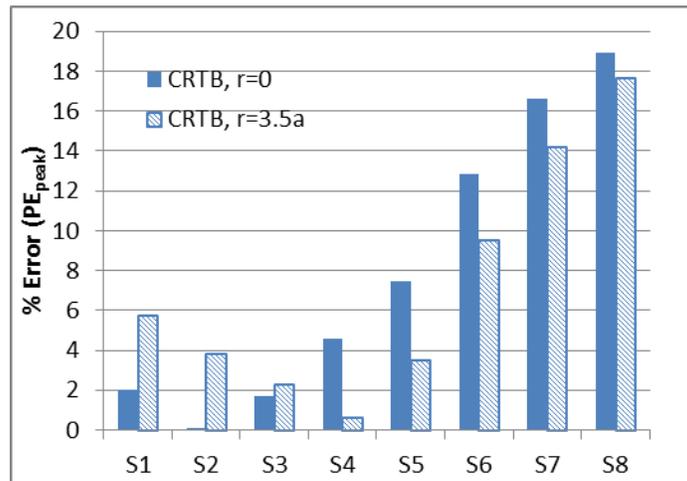
Figure 273. Graph. Percent error (PE_{peak}) calculated using the peaks of the deflections for LAVAN-ABAQUS comparison (CRTB mix).
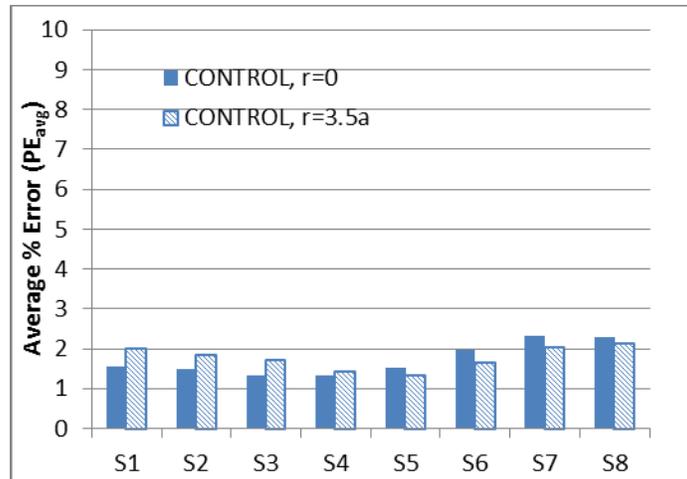
Figure 274. Graph. Average percent error (*PE*$_{avg}$) calculated using the entire time history for LAVAN-ABAQUS comparison (control mix).
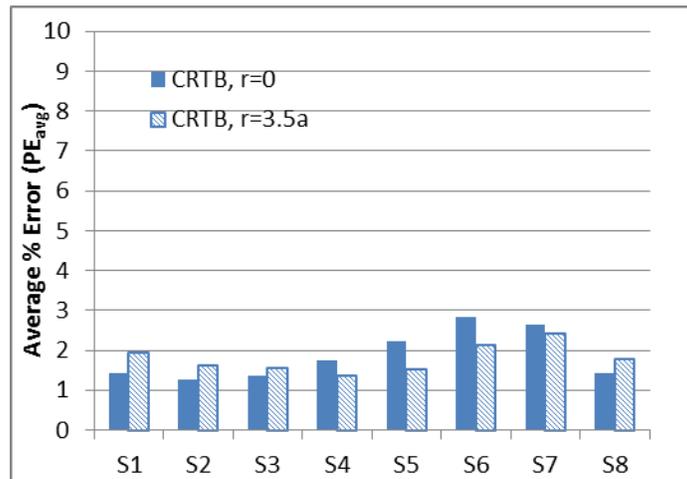
Figure 275. Graph. Average percent error (*PE*$_{avg}$) calculated using the entire time history for LAVAN-ABAQUS comparison (CRTB mix).

APPENDIX B. THEORETICAL ANALYSES ON MULTIPLE-PULSE FWD'S IN BACKCALCULATION

As discussed in chapter 4, responses of viscoelastic materials show dependence on time (or frequency), rate of loading, and temperature. The relationship of characteristic viscoelastic properties such as relaxation modulus, creep compliance, and dynamic modulus with time (or frequency) are often expressed at a specific reference temperature, in terms of a master curve. In theory, it should be possible to obtain such a curve if data containing time-changing responses at different temperature levels are known. The available analysis window for the current FWD devices is short, extending up to 25 to 35 ms of stress pulse. However, the recorded information can be used to infer part of the relaxation function. As for temperature information, it is possible to test the same location at different times within a day. Although a series of FWD tests at different temperatures could be useful in developing the entire master curve, in theory the prediction can be improved if information at different rates of loading or over a larger time interval were known. In this appendix, these possibilities are explored. Note that backcalculation in this appendix was performed using the MATLAB® optimization function fminsearch.

BACKCALCULATION USING MULTIPLE PULSES AT DIFFERENT FREQUENCIES

To illustrate the possibility of exploiting information from multiple frequencies in backcalculation of the damaged HMA master curve, two examples are presented. In the first, a typical FWD pulse was backcalculated, and in the second example, multiple FWD pulses at different frequencies were backcalculated. For these two examples, forward computations were performed using a known $E(t)$ to compute the deflection basin. Figure 276 shows the $E(t)$ master curve that was used in these examples. For simplicity, the AC layer temperature was assumed to be equal to the reference temperature of the master curve ($T_{ref} = 66.2$ °F); therefore, $t_R = t =$ actual time.
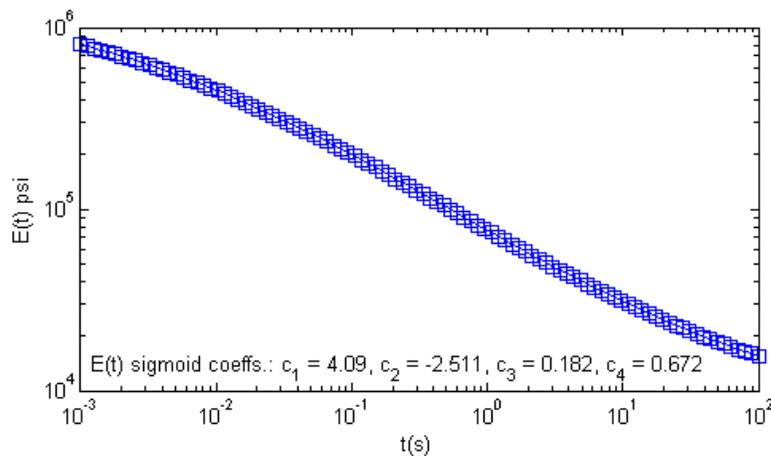
Figure 276. Graph. $E(t)$ used to compute the deflection basin in examples 1 and 2.

Example 1—Typical FWD Pulse

In this example, to simulate a typical FWD pulse, a haversine loading with a duration of 35 ms, followed by a rest period of 35 ms, was simulated (figure 277 (left)). Figure 277 (right) shows the resulting deflection basin at different radial distances from the centerline of the load.
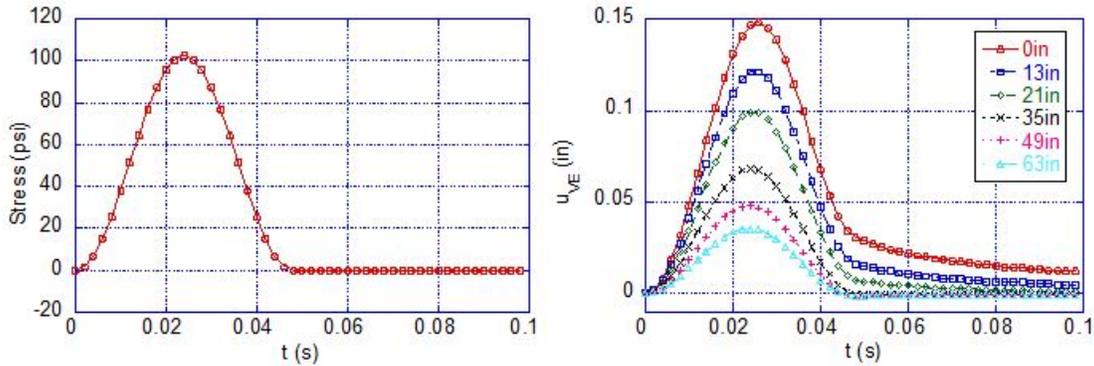
Figure 277. Graphs. FWD deflection history for example 1.

In this example, the only unknown parameter was the $E(t)$ master curve of the AC layer. Other parameters, such as unbound layer modulus, Poisson's ratio, and thicknesses of AC and unbound layers, were known. In addition, a constant Poisson's ratio of 0.35 was assumed for the AC layer. Initially, a random number generator was used to determine the initial sigmoid constants. Figure 278 (left) shows the initial sigmoid coefficients and the resulting initial $E(t)$ curve, which was quite different from the actual $E(t)$ curve. Such an initial difference was important to ensure that the backcalculation procedure worked accurately without depending on the initial values. Backcalculation results at the starting and the ending stage of optimization are shown as continuous line in the figure. Figure 278 (right) shows the final backcalculation results obtained at the end of the optimization, where a very good agreement was observed. Figure 279 shows the backcalculated $|E^*|$ and ϕ values, along with the actual values. Consistent with $E(t)$, a good match between the backcalculated and actual values was obtained at frequencies higher than 10^{-3} Hz in both $|E^*|$ and ϕ. However, curves diverged at lower frequencies. This was not unexpected because only the early portion of the $E(t)$ curve was used in calculation of deflection history shown in figure 276. Later portions of the $E(t)$ curve (and $|E^*|$ and ϕ values at low frequencies) can be obtained by increasing the pulse duration or using a different form of stress history, which is shown in the next example.
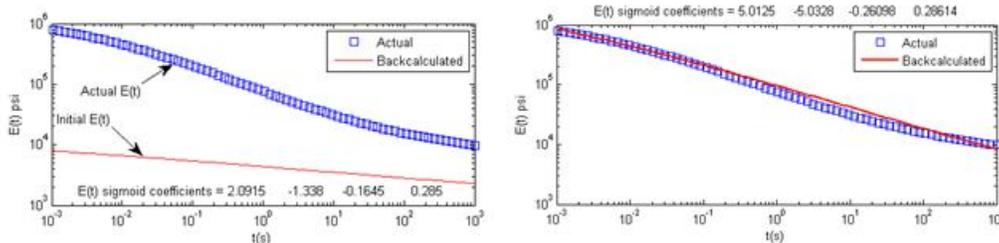
Figure 278. Graphs. *E(t)* and deflection history at the initial (left) and final (right) backcalculation stage in example 1.

256
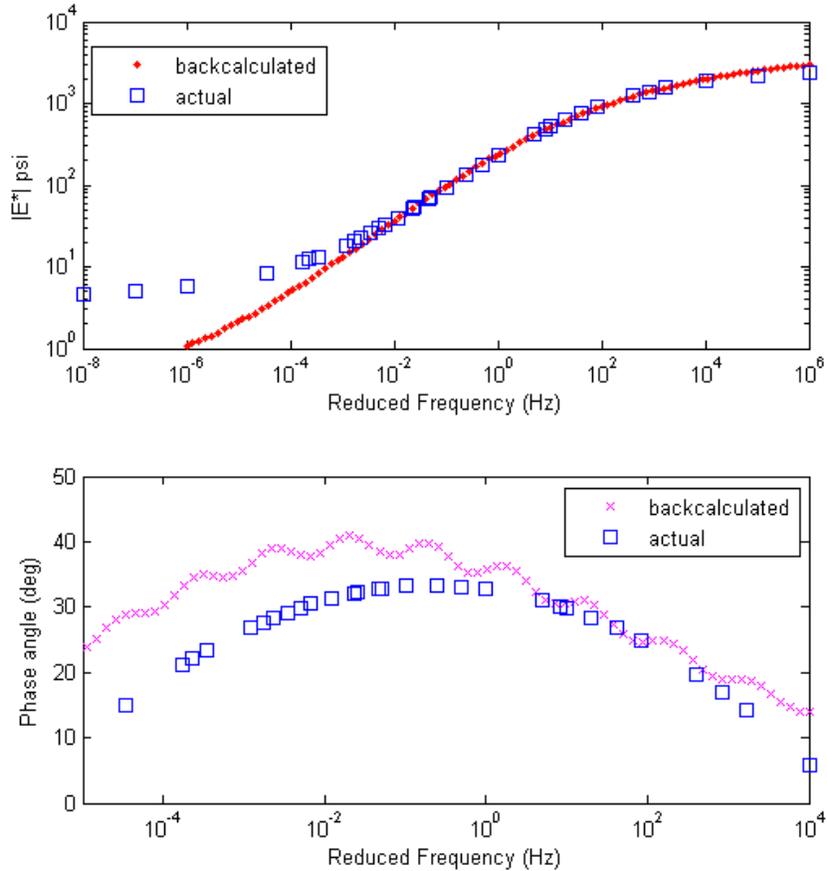
Figure 279. Graphs. Comparison of backcalculated and actual $|E^*|$ and phase angle master curves for example 1.

Example 2—Cyclic Pulses With Two Different Frequencies

In this example, four successive pulses with durations of 35 ms, followed by four pulses with 10 s durations, were simulated to generate the deflection basin (figure 280). This example was used to investigate whether a different loading history could result in better estimation of $E(t)$. Figure 281 shows the backcalculated $E(t)$, where a much better fit can be seen. Note that the accuracy of the backcalculated $E(t)$ depended on the duration of the stress pulse, where longer duration allowed calculation of $E(t)$ at longer durations. It was also important to apply high-frequency (short duration) pulse load to increase the accuracy of $E(t)$ at very short times. Backcalculation of $E(t)$ for this example took less than 5 min. Figure 282 shows the backcalculated $|E^*|$ and phase angle master curves, where a much better match can be seen compared with example 1.

257
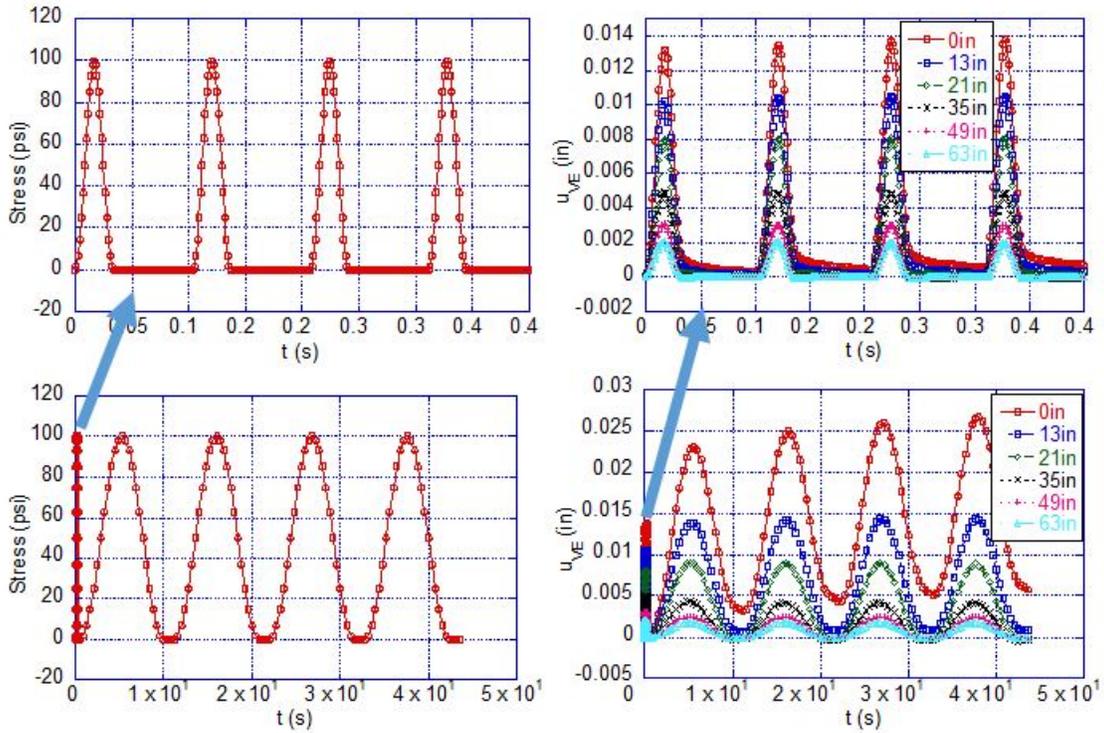
Figure 280. Graphs. Applied stress and resulting deflection basin for example 2.
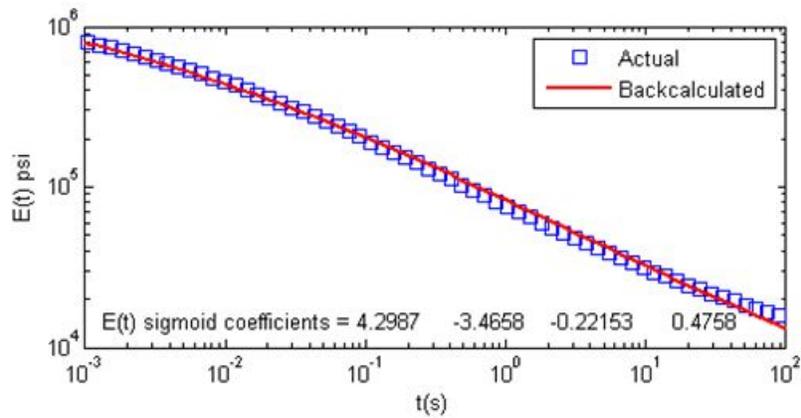
Figure 281. Graph. Backcalculated $E(t)$ using multiple stress pulses.
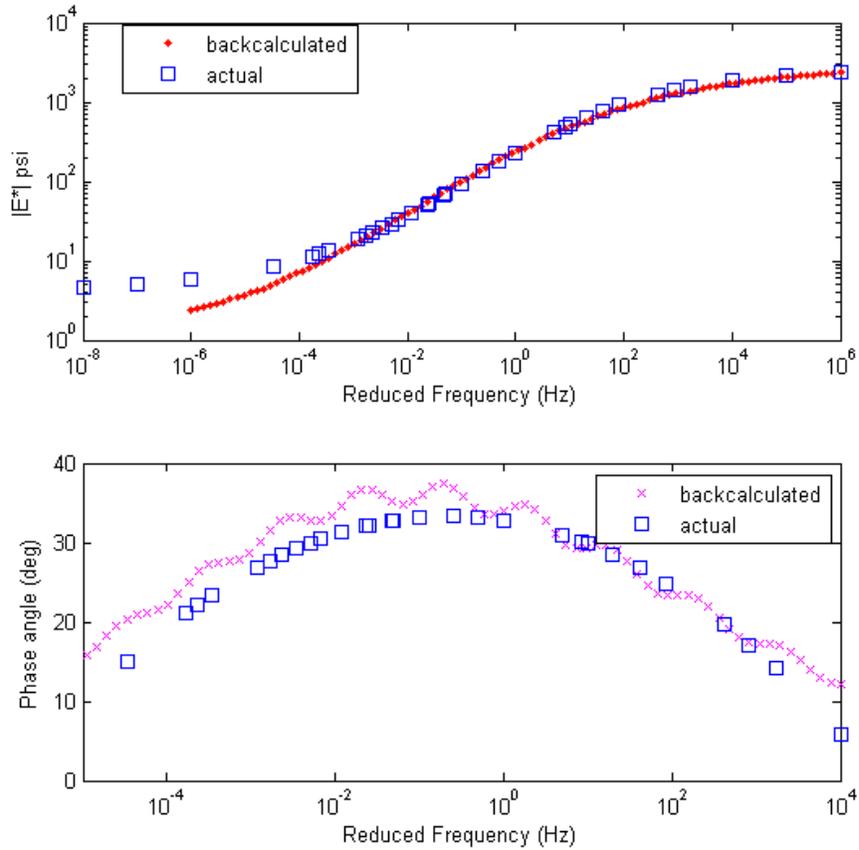
Figure 282. Graphs. Comparison of backcalculated and actual |*E**| and master curves for example 2.

BACKCALCULATION USING SERIES OF MULTIPLE-PULSE FWDS AT CONSTANT FREQUENCY AND DIFFERENT TEMPERATURE

The theoretical FWD stress history shown in figure 283 was used to investigate whether a loading history with multiple pulses at constant frequency could improve the backcalculation results. First, deflection time histories were computed at several temperatures using LAVA. Then, BACKLAVA was used to backcalculate the $E(t)$ master curve. Two examples are shown. In the first, three successive pulses with durations of 80 ms, followed by a rest period of 760 ms, were simulated to generate deflections. In the second, only the initial three successive pulses were used, and deflection over the remainder of the period was ignored.
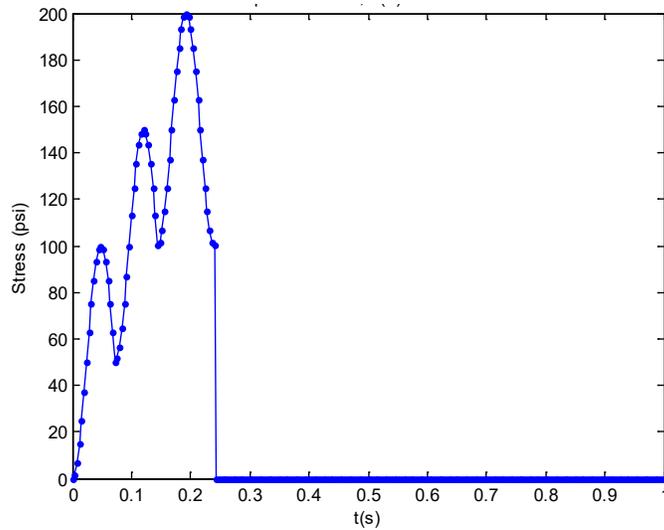
Figure 283. Graph. Stress history used in the constant frequency multiple pulse analysis.

Example 1

The LAVA algorithm was used to compute deflection histories resulting from the loading shown in figure 283 at the temperatures 50, 86, 104, 140, 176, 212, and 248 °F. Measured and backcalculated responses for temperatures 50, 86, 104, and 140 °F are shown in figure 284. The backcalculated $E(t)$ curve after 1 h 7 min is shown in figure 285. The results obtained for the backcalculation using multiple pulses were encouraging because of the increased time and relaxation due to the stress history.
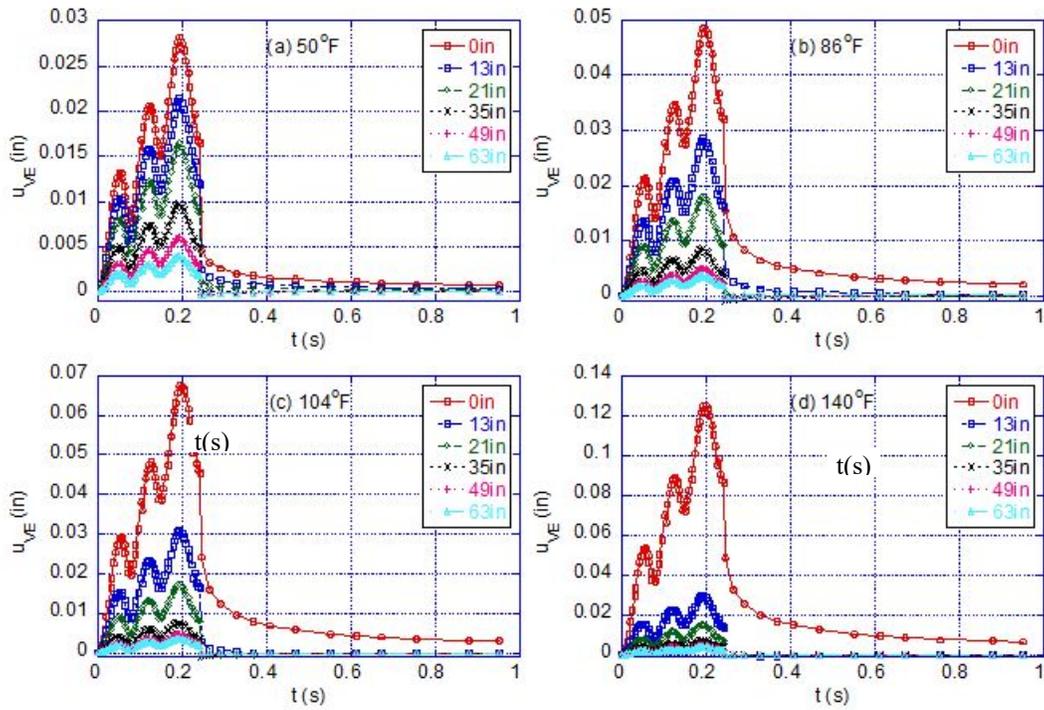
Figure 284. Graphs. Deflection at different sensors at different temperatures in example 1.
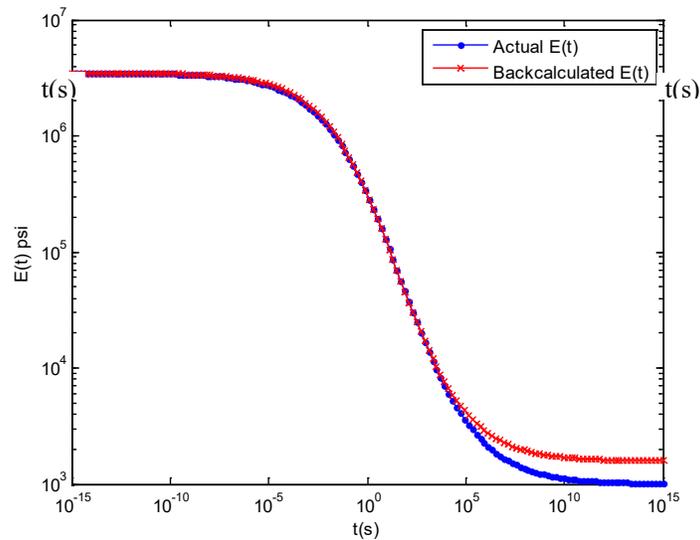
Figure 285. Graph. Result for backcalculated *E*(*t*) curve in example 1.

Example 2

In example 2, the problem was solved only for the pulse duration; the relaxation trend was omitted. The problem was solved for a temperature set of 32, 50, 68, 86, 104, 122, 140, 158, 176, 194, 212, 230, and 248 °F. The backcalculated *E*(*t*) values for example 2 at 1 h 7 min are plotted

in figure 286. Measured and backcalculated deflection histories for temperature 32, 50, 68, and 86 °F are shown in figure 287.
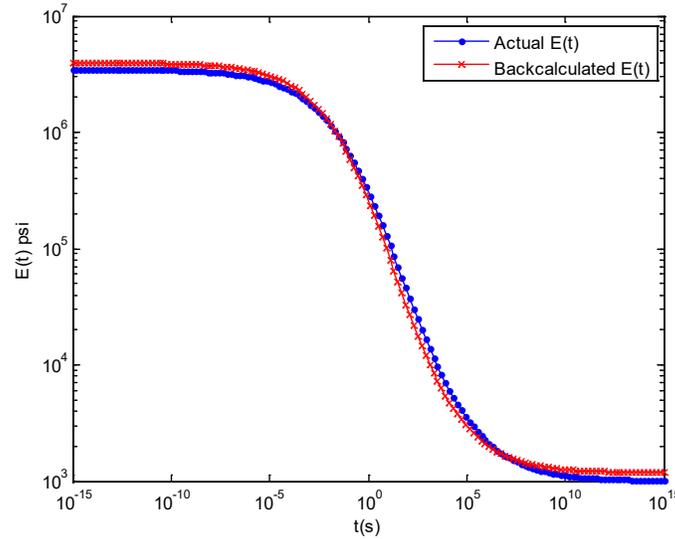
Figure 286. Graph. Result for backcalculated *E*(*t*) curve for example 2.
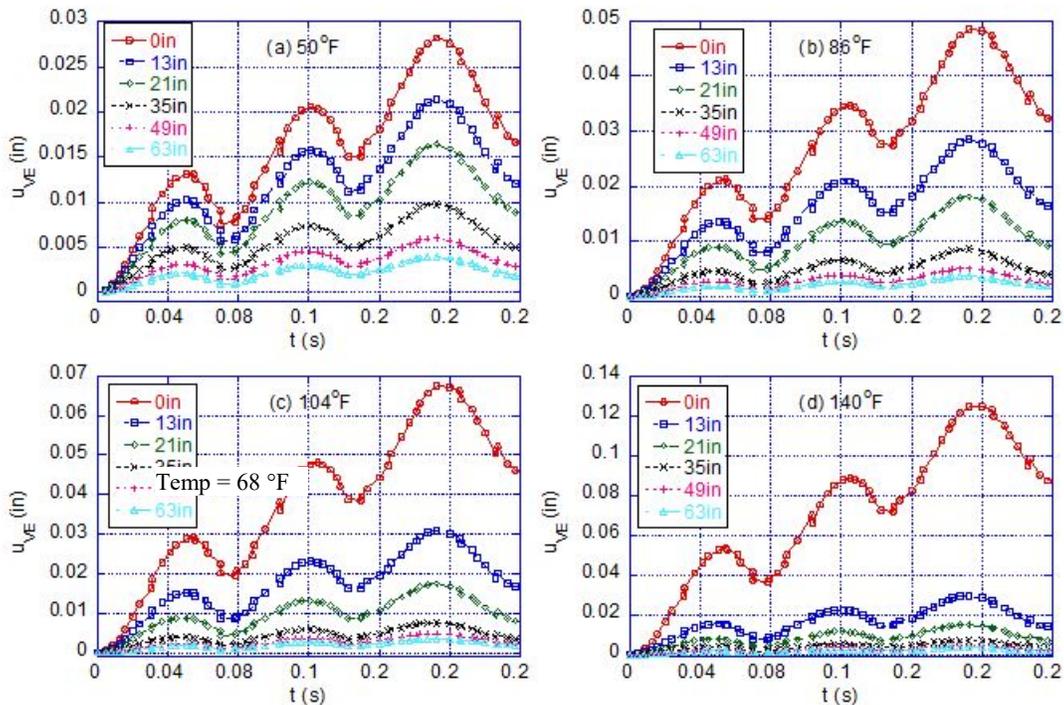
Figure 287. Graphs. Deflections at different sensors at different temperatures for example 2.

Note that the accuracy of the backcalculated *E*(*t*) curve depended on the duration and temperature of the stress pulse loading. Inclusion of high temperatures along with an elongated stress pulse in the theoretical analysis allowed calculation of *E*(*t*) at longer durations. It can be

seen from figure 285 and figure 286 that the backcalculated $E(t)$ curve obtained from using both truncated and nontruncated deflection curves showed good prediction. However, a much more accurate predicted $E(t)$ curve up to 10^5 s was obtained when nontruncated deflection curves were used in backcalculation.

CONCLUSIONS

The results from the four examples presented in this appendix suggest that including FWD pulses or multiple frequencies in backcalculation may improve the accuracy of the $E(t)$ master curve prediction. The improvement in backcalculated $E(t)$ master curve could be for two possible reasons—an increase in the deflection time history and a different rate of loading. However, more comprehensive theoretical analyses are needed to assert and determine the optimal loading history that should be applied by an FWD. Although the theoretical methods suggested in this appendix clearly have potential to improve the ability of BACKLAVA in predicting $E(t)$ master curve, the methods have the following limitations:

- Increasing the number of FWD pulses (i.e., the frequency content) increases the computational time of the backcalculation, making it computationally expensive.

- Different frequencies in the loading history alone cannot be used to obtain both the time and temperature properties of the HMA layer, which are needed for complete characterization of the HMA layer.

APPENDIX C. THEORETICAL DEVELOPMENT OF A TIME-DOMAIN FORWARD SOLUTION

GOVERNING EQUATIONS FOR VISCOELASTIC WAVE PROPAGATION

Similar to any other wave propagation problems, the proposed solution began with the classical equation of motion for a continuous medium as shown in figure 288.[101]

$$\nabla \cdot \sigma + b = \rho \ddot{u}$$

Figure 288. Equation. Equation of motion for a continuous medium.

Where:

σ = the stress tensor.
b = the vector of body forces per unit volume.
ρ = the mass density of the material.
u = the displacement vector.

According to the theory of linear elasticity, the stress-strain relationship for a linear, homogenous, and isotropic material is obtained from the generalized Hooke's law, as shown in figure 289.

$$\sigma = \lambda tr(\varepsilon)I + 2\mu\varepsilon$$

Figure 289. Equation. Stress-strain relationship for a linear, homogenous, and isotropic material.

Where:
ε = the strain tensor.
λ and μ = the lamé constants.
I = the identity tensor.

The strain tensor in figure 289 is related to the displacement vector according to the equation in figure 290.

$$\varepsilon = \frac{1}{2}\{\nabla u + (\nabla u)^T\}$$

Figure 290. Equation. Strain-displacement relationship for a linear, homogenous, and isotropic material.

For a viscoelastic material such as an AC mixture, the fundamental materials properties—in this case, the lamé constants—as well as the stresses and strains are time dependent and hence, their relationship can be written as the following in reference to the theory of linear viscoelasticity:[68,102,103]

$$\sigma = \lambda * tr(\varepsilon)I = 2\mu * \varepsilon$$

Figure 291. Equation. Stress-strain relationship for a viscoelastic material.

Where the operator * between any function $\alpha * \beta$ represents the well-known Stieltjes convolution integral defined as shown in figure 292.

$$\alpha * \beta = \int_0^t \alpha(t - \tau)\frac{\partial \beta(\tau)}{\partial \tau} d\tau$$

Figure 292. Equation. Stieltjes convolution integral.

Note that the kinematic strain-displacement relationship shown in the equation in figure 290 also applies to linear viscoelastic materials. The only difference from an elastic material is that the displacement and hence the strain are functions of not only the material (or spatial) coordinates but also time. Substituting the equations presented in figure 290 and figure 291 into the equation of motion shown in figure 288, and ignoring the body forces, results in the equation shown in figure 293 in terms of displacements:

$$(\lambda + \mu) * \nabla(\nabla \cdot u) + \mu * \nabla^2 u = \rho \ddot{u}$$

Figure 293. Equation. Equation of motion in terms of displacements.

By means of the Helmholtz decomposition, the displacement vector in figure 293 can be expressed in terms of potentials as shown in figure 294.

$$u = \nabla\Phi + \nabla \times H$$

Figure 294. Equation. Displacement vector in terms of potentials.

Where Φ represent a scalar potential, and H is a vector potential whose divergence vanishes (i.e., $\nabla \cdot H = 0$).

Similar to the spectral element solution provided by Al-Khoury et al., the cylindrical axisymmetric coordinate system shown in figure 295 is employed herein.[2]
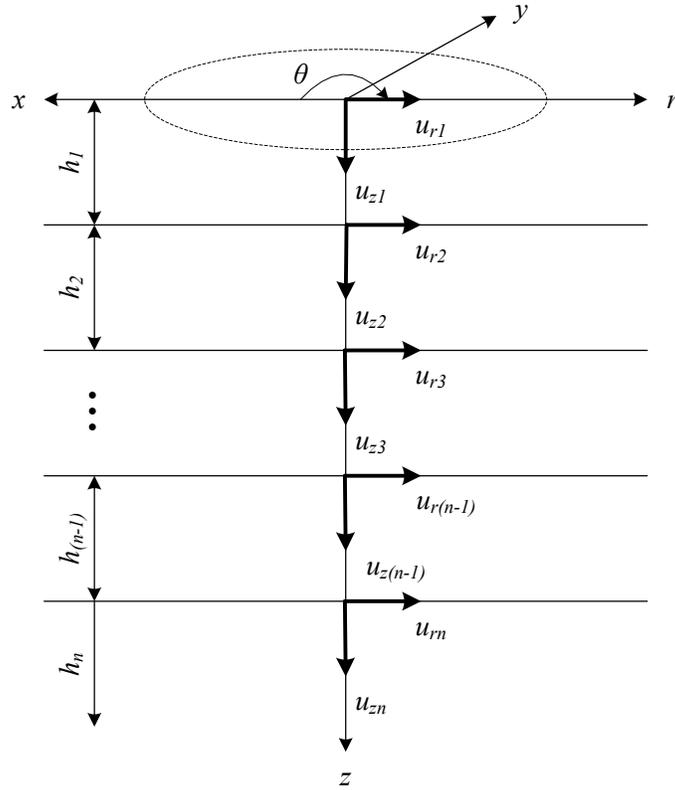
Figure 295. Diagram. Coordinate system for axisymmetric layers on a half-space.

Then, the equations shown in figure 296 and figure 297 are obtained for the potentials by substituting the equation in figure 294 into the equation in figure 293.

$$\left(\lambda + 2\mu\right) * \nabla^2 \Phi = \left(\lambda + 2\mu\right) * \left\{\frac{\partial^2 \Phi}{\partial r^2} + \frac{1}{r}\frac{\partial \Phi}{\partial r} + \frac{\partial^2 \Phi}{\partial z^2}\right\} = \rho\frac{\partial^2 \Phi}{\partial t^2}$$

Figure 296. Equation. Equation of motion in terms of the scalar potential.

$$\mu * \left(\nabla^2 H_\theta - \frac{H_\theta}{r^2}\right) = \mu * \left\{\frac{\partial^2 H_\theta}{\partial r^2} + \frac{1}{r}\frac{\partial H_\theta}{\partial r} + \frac{\partial^2 H_\theta}{\partial z^2} - \frac{H_\theta}{r^2}\right\} = \rho\frac{\partial^2 H_\theta}{\partial t^2}$$

Figure 297. Equation. Equation of motion in terms of the vector potential.

Where H_θ is the tangential and also the only component of H that does not vanish. By defining H_θ as shown in figure 298, it can be shown that the scalar potential ψ satisfies the wave equation shown in figure 299. The proof can be obtained immediately if the equation in figure 299 is differentiated with respect to r.[104]

267

$$H_\theta = -\frac{\partial \Psi}{\partial r}$$

Figure 298. Equation. Vector potential H_θ.

$$\mu * \nabla^2 \Psi = \mu * \left\{ \frac{\partial^2 \Psi}{\partial r^2} + \frac{1}{r}\frac{\partial \Psi}{\partial r} + \frac{\partial^2 \Psi}{\partial z^2} \right\} = \rho \frac{\partial^2 \Psi}{\partial t^2}$$

Figure 299. Equation. Scalar potential Ψ.

The equations in figure 296 and figure 299 are the wave equations that govern the axisymmetric wave motion in a continuous, linear viscoelastic medium. It is also worthwhile to note that if the lamé constants, λ and μ, were independent of time (i.e., the material is linear elastic), then the convolution integral in the equations reduce to an arithmetic multiplication and these two equations become the well-known axisymmetric wave equations for a linear elastic material.[104,105]

Another immediate consequence of adopting the axisymmetric coordinate system is that the displacement component in the tangential direction, u_θ, vanishes.[105] The remaining deflections can be written in terms of the scalar potentials Φ and ψ as shown in figure 300 and figure 301.

$$u_r = \frac{\partial \Phi}{\partial r} + \frac{\partial^2 \Psi}{\partial r \partial z}$$

Figure 300. Equation. Relationship between radial displacement and potentials.

$$u_z = \frac{\partial \Phi}{\partial z} - \frac{\partial^2 \Psi}{\partial r^2} - \frac{1}{r}\frac{\partial \Psi}{\partial r}$$

Figure 301. Equation. Relationship between vertical displacement and potentials.

The stresses can be written as shown in figure 302 and figure 303.

$$\sigma_{rz} = \mu * \frac{\partial}{\partial r} \left\{ 2\frac{\partial \Phi}{\partial z} - \frac{\partial^2 \Psi}{\partial r^2} - \frac{1}{r}\frac{\partial \Psi}{\partial r} + \frac{\partial^2 \Psi}{\partial z^2} \right\}$$

Figure 302. Equation. Relationship between shear stress and potentials.

$$\sigma_z = \lambda * \left\{ \frac{\partial^2 \Phi}{\partial r^2} + \frac{1}{r}\frac{\partial \Phi}{\partial r} + \frac{\partial^2 \Phi}{\partial z^2} \right\} + 2\mu * \frac{\partial}{\partial z}\left\{ \frac{\partial \Phi}{\partial z} - \frac{\partial^2 \Psi}{\partial r^2} - \frac{1}{r}\frac{\partial \Psi}{\partial r} \right\}$$

Figure 303. Equation. Relationship between vertical stress and potentials.

SOLUTIONS FOR THE WAVE EQUATIONS IN THE LAPLACE-HANKEL DOMAIN

The solution to the wave equations presented in the previous section can be worked more conveniently by using the integral transforms. Taking the Laplace transform of the equation in figure 296 results in the equation shown in figure 304.

$$s(\hat{\lambda} + 2\hat{\mu}) \cdot \left\{ \frac{\partial^2 \widehat{\Phi}}{\partial r^2} + \frac{1}{r} \frac{\partial \widehat{\Phi}}{\partial r} + \frac{\partial^2 \widehat{\Phi}}{\partial z^2} \right\} = \rho s^2 \widehat{\Phi}$$

Figure 304. Equation. Equation of motion in terms of the scalar potential Φ in the Laplace domain.

Where s is the Laplace variable, and $\widehat{f}(s) = \int_0^\infty e^{-st} f(t) dt$ is the Laplace transform of a function $f(t)$. Then, taking the Hankel transform (also known as the Fourier-Bessel transform) of order zero defined as $\bar{f}(k) = \int_0^\infty \widehat{f}(r) J_0(kr) r \, dr$ of the equation in figure 304, the equation in figure 305 is obtained.

$$s(\hat{\lambda} + 2\hat{\mu}) \cdot \left\{ \frac{\partial^2 \overline{\Phi}}{\partial z^2} - k^2 \overline{\Phi} \right\} = \rho s^2 \overline{\Phi}$$

Figure 305. Equation. Equation of motion in terms of the scalar potential Φ in the Laplace-Hankel domain.

After a simple rearrangement of the terms, figure 305 can be written as shown in figure 306.

$$\frac{\partial^2 \overline{\Phi}}{\partial z^2} - \left(k^2 + \frac{s}{\hat{c}_1^2} \right) \overline{\Phi} = 0$$

$$\hat{c}_1^2 = \frac{\hat{\lambda} + 2\hat{\mu}}{\rho}$$

Figure 306. Equation. Simplified form of the equation in figure 305.

From the equation in figure 306, the solution for the Laplace-Hankel transformed potential function, $\overline{\Phi}$, is obtained as shown in figure 307, after dropping the term that develops an unbounded result, i.e., the wave that propagates in the negative z direction.[104,105]

$$\overline{\Phi} = Ae^{-z \sqrt{k^2 + \frac{s}{\hat{c}_1^2}}} = Ae^{-zf(k,s)}$$

Figure 307. Equation. General form solution of the equation in figure 306.

Where A is an arbitrary constant.

By following the same mathematical steps shown above, the equation in figure 299 can be rewritten as shown in figure 308.

$$\frac{\partial^2 \overline{\Psi}}{\partial z^2} - \left(k^2 + \frac{s}{\hat{c}_2^2} \right) \overline{\Psi} = 0$$

$$\hat{c}_2^2 = \frac{\hat{\mu}}{\rho}$$

Figure 308. Equation. Equation of motion in terms of the scalar potential Ψ in the Laplace-Hankel domain.

Again, after dropping the term leading to unbounded results, the solution for the transformed potential, $\overline{\Psi}$, is obtained as shown in figure 209.

$$\overline{\Psi} = Ce^{-z \sqrt{k^2 + \frac{s}{\hat{c}_2^2}}} = Ce^{-zg(k,s)}$$

Figure 309. Equation. General form solution of the equation in figure 306.

Where C is also an arbitrary constant.

To use the solutions obtained above for the transformed potentials, it is also necessary to acquire the equations for the displacements and the stresses in the transformed domain. While taking the Laplace transform of the displacements and the stresses is straightforward, additional attention is needed in taking the Hankel transform because of the spatial symmetry supplied by the cylindrical coordinate system adopted for the solution. Referring back to figure 295, one finds that the displacement at any point on the z-axis (i.e., when $r = 0$) is only allowed to occur in the z-direction (i.e., $u_z \neq 0$ when $r = 0$) but is confined in the r-direction (i.e., $u_r = 0$ when $r = 0$), unless the axisymmetric assumption is to be violated. Because of these physical characteristics of the axisymmetric displacements, Hankel transforms of different orders need to be applied to u_r and u_z.

Figure 310 shows the first few cycles of the Bessel functions of the first kind and of orders zero (J_0) and one (J_1) that make up the kernels of the Hankel transform. The primary difference between the two Bessel functions shown in the figure is that while the Bessel function of order zero (J_0) has a nonzero value at $r = 0$, the Bessel function of order one (J_1) is equal to zero when $r = 0$. This implies that the Hankel transform of order zero whose kernel is composed of J_0 is appropriate for transforming the functions that exhibit nonzero values at the origin, whereas the Hankel transform of order one whose kernel is made up of J_1 is more appropriate for transforming the functions that have zero values at $r = 0$. Therefore, the appropriate Hankel transforms that should be applied to u_r and u_z are of orders one and zero, respectively.
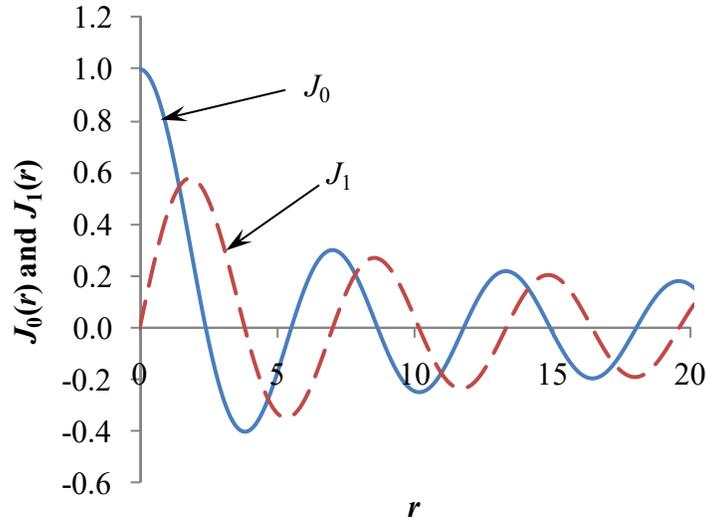
Figure 310. Graph. Bessel functions of the first kind.

Taking the Laplace and the respective Hankel transforms on the displacements u_r and u_z, shown in figure 300 and figure 301 results in the equations shown in figure 311 and figure 312, respectively.

$$\bar{u}_r = -k\bar{\Phi} - k\frac{\partial\bar{\Psi}}{\partial z}$$

Figure 311. Equation. Relationship between radial displacement and potentials in the Laplace-Hankel domain.

$$\bar{u}_z = \frac{\partial\bar{\Phi}}{\partial z} + k^2\bar{\Psi}$$

Figure 312. Equation. Relationship between vertical displacement and potentials in the Laplace-Hankel domain.

Note that although the Hankel transform of order one was used to transform u_r shown in figure 300, the Hankel transform of the potentials shown in figure 311 is still of order zero. This is a consequence of the partial derivative with respect to r that is present in both terms of the right-hand side of the equation in figure 300 and the property of the Hankel transform shown in figure 313, which associates the first order transform of a function's derivative to the zero order transform of the original function.[105,106]

$$\int_0^\infty \frac{\partial\hat{f}(r)}{\partial r} J_1(kr)r\,dr = -k\int_0^\infty \hat{f}(r)J_0(kr)r\,dr = -k\cdot\bar{f}(k)$$

Figure 313. Equation. Hankel transform of a function's derivative.

Subsequently, the Laplace-Hankel transforms need to be carried out on the relevant stresses. Based on the same mathematical arguments presented above for the displacements, the Hankel transforms of orders one and zero should be applied respectively to σ_{rz} and σ_z to allow for a

solution that is compatible with the axisymmetric coordinate system chosen for the solution. After simplifying, the equations shown in figure 314 and figure 315 are obtained.

$$\sigma_{rz} = -sk\hat{\mu}\left\{2\frac{\partial\overline{\Phi}}{\partial z} + 2\frac{\partial^2\overline{\Psi}}{\partial z^2} - \frac{s}{\hat{c}_2^2}\right\}$$

$$= -sk\hat{\mu}\left\{2\frac{\partial\overline{\Phi}}{\partial z} + 2k^2\overline{\Psi} + \frac{s}{\hat{c}_2^2}\overline{\Psi}\right\}$$

Figure 314. Equation. Relationship between shear stress and potentials in the Laplace-Hankel domain.

$$\overline{\sigma}_z = s\hat{\lambda}\cdot\left\{-k^2\overline{\Phi} + \frac{\partial^2\overline{\Phi}}{\partial z^2}\right\} + 2s\hat{\mu}\frac{\partial}{\partial z}\left\{\frac{\partial\overline{\Phi}}{\partial z} + k^2\overline{\Psi}\right\}$$

$$= \hat{\mu}\frac{s^2}{\hat{c}_2^2}\overline{\Phi} + 2sk^2\hat{\mu}\left(\overline{\Phi} + \frac{\partial\overline{\Psi}}{\partial z}\right)$$

Figure 315. Equation. Relationship between vertical stress and potentials in the Laplace-Hankel domain.

FORMULATION OF THE STIFFNESS MATRICES FOR THE LAYER ELEMENTS

The solutions presented in the previous section for the scalar potentials in the transformed domain are not readily applicable for a multilayered system such as the one shown in figure 295. To allow for the analysis of a layered system such as an AC pavement, it is necessary to develop the formulations for the layer elements whose underlying concept originates from the FEA method. In this section, two types of layer elements are developed—a two-noded element for a layer with a finite thickness (e.g., the top layer in figure 295) and a one-noded element for simulation of a semi-infinite half-space (e.g., the bottom layer in figure 295).

Two-Noded Element for a Layer With a Finite Thickness

The solutions for the scalar potentials shown in the equations in figure 307 and figure 309 only account for the incident waves that propagate from the upper boundary of a layer in the direction of the positive z-axis, i.e., downward direction in figure 295. However, a layer with a finite thickness also encompasses the waves that reflect from the lower boundary and propagate in the direction of the negative z-axis. To account for these reflected waves, an additional term must be added to each of the potentials, which results in the equations in

$$\overline{\Phi} = Ae^{-zf} + Be^{-(h-z)f}$$

figure 316 and figure 317.

$$\overline{\Phi} = Ae^{-zf} + Be^{-(h-z)f}$$

Figure 316. Equation. Scalar potential Φ in the Laplace-Hankel domain.

272

$$\overline{\Psi} = Ce^{-zg} + De^{-(h-z)g}$$

Figure 317. Equation. Scalar potential Ψ in the Laplace-Hankel domain.

Where B and D are arbitrary constants, and h is the layer thickness. Substituting these equations into the equations in figure 311 and figure 312 results in the equations for the displacements within a two-noded element shown in figure 318 and figure 319.

$$\overline{u}_r = -Ake^{-zf} - Bke^{-(h-z)f} - Ckge^{-zg} - Dkge^{-(h-z)g}$$

Figure 318. Equation. Radial displacement in the Laplace-Hankel domain.

$$\overline{u}_z = -Afe^{-zf} + Bfe^{-(h-z)f} + Ck^2e^{-zg} + Dk^2e^{-(h-z)g}$$

Figure 319. Equation. Vertical displacement in the Laplace-Hankel domain.

For the formulation of a layer element, the displacements at the upper and lower boundaries need to be extracted from these equations. The radial and the vertical displacements at the upper boundary, denoted respectively as $\overline{u}_{r1}$ and $\overline{u}_{z1}$, can be obtained by substituting $z = 0$ in the equations in figure 318 and figure 319. Similarly, the displacements at the lower boundary ($\overline{u}_{r2}$ and $\overline{u}_{z2}$) are acquired by substituting $z = h$. In matrix form, the resulting equations for the displacements can be written as shown in figure 320.

$$\begin{Bmatrix} \overline{u}_{r1} \\ \overline{u}_{z1} \\ \overline{u}_{r2} \\ \overline{u}_{z2} \end{Bmatrix} = \begin{bmatrix} -k & -ke^{-hf} & kg & -kge^{-hg} \\ -f & fe^{-hf} & k^2 & k^2e^{-hg} \\ -ke^{-hf} & -k & kge^{-hg} & -kg \\ -fe^{-hf} & f & k^2e^{-hg} & k^2 \end{bmatrix} \begin{Bmatrix} A \\ B \\ C \\ D \end{Bmatrix} = \mathbf{S_1} \cdot \begin{Bmatrix} A \\ B \\ C \\ D \end{Bmatrix}$$

Figure 320. Equation. Relationship between shape factors and boundary conditions.

It is also necessary to obtain the equations for the stresses. By substituting the equations shown in

$$\overline{\Phi} = Ae^{-zf} + Be^{-(h-z)f}$$

figure 316 and figure 317 into the equations shown in figure 314 and figure 315, one arrives at the following equations shown in figure 321.

$$\overline{\sigma}_{rz} = -s\hat{\mu}k\left\{-2Afe^{-zf} + 2Bfe^{-(h-z)f} + CKe^{-zg} + DKe^{-(h-z)g}\right\}$$
$$\overline{\sigma}_z = s\hat{\mu}\left\{AKe^{-zf} + BKe^{-(h-z)f} - 2Ck^2ge^{-zg} + 2Dk^2ge^{-(h-z)g}\right\}$$
$$K = 2k^2 + \frac{s}{\hat{c}_2^2}$$

Figure 321. Equation. Shear and vertical stress in the Laplace-Hankel domain.

Again, the stresses at the upper boundary ($\overline{\sigma}_{rz1}$ and $\overline{\sigma}_{z1}$) are obtained by substituting $z = 0$ in the equations shown in figure 321, while those at the lower boundary ($\overline{\sigma}_{rz2}$ and $\overline{\sigma}_{z2}$) are found by substituting $z = h$, all of which can be summarized in a matrix form as shown in figure 322.

$$\begin{Bmatrix} \overline{\sigma}_{rz1} \\ \overline{\sigma}_{z1} \\ \overline{\sigma}_{rz2} \\ \overline{\sigma}_{z2} \end{Bmatrix} = s\widehat{\mu} \cdot \begin{bmatrix} 2f & -2fe^{-hf} & -K & -Ke^{-hg} \\ K & Ke^{-hf} & -2k^2g & 2k^2ge^{-hg} \\ 2fe^{-hf} & -2f & -Ke^{-hg} & -K \\ Ke^{-hf} & K & -2k^2ge^{-hg} & 2k^2g \end{bmatrix} \begin{bmatrix} A \\ B \\ C \\ D \end{bmatrix} = s\widehat{\mu} \cdot \mathbf{S_2} \cdot \begin{Bmatrix} A \\ B \\ C \\ D \end{Bmatrix}$$

Figure 322. Equation. Relationship between stresses and shape factors.

Combining the equations shown in figure 320 and figure 322 by eliminating the vector of arbitrary constants, the stresses can be expressed in terms of the displacements as the equation shown in figure 323.

$$\begin{Bmatrix} \overline{\sigma}_{rz1} \\ \overline{\sigma}_{z1} \\ \overline{\sigma}_{rz2} \\ \overline{\sigma}_{z2} \end{Bmatrix} = s\widehat{\mu} \cdot \mathbf{S_2} \cdot \mathbf{S_1}^{-1} \cdot \begin{Bmatrix} \overline{u}_{r1} \\ \overline{u}_{z1} \\ \overline{u}_{r2} \\ \overline{u}_{z2} \end{Bmatrix}$$

Figure 323. Equation. Stress-displacement relationship in the Laplace-Hankel domain.

Where $\mathbf{S_1}$ and $\mathbf{S_2}$ are the four by four matrices defined in the equations shown in figure 320 and figure 322, respectively. According to the concepts of FEA, the stiffness matrix of an element defines the relationship between the displacement vector and the boundary traction vector. Owing to the Cauchy stress principle, the boundary tractions are obtained by taking the dot product between the stress tensor and a unit vector directed along the outward normal of the boundary. Calculating these tractions at the upper and lower boundaries of the element and reorganizing them in a vector form results in the relationship between the tractions, stresses, and displacements shown in figure 324.

$$\begin{Bmatrix} \overline{T}_{r1} \\ \overline{T}_{z1} \\ \overline{T}_{r2} \\ \overline{T}_{z2} \end{Bmatrix} = \begin{Bmatrix} -\overline{\sigma}_{rz1} \\ -\overline{\sigma}_{z1} \\ \overline{\sigma}_{rz2} \\ \overline{\sigma}_{z2} \end{Bmatrix} = \mathbf{S_{2-noded}} \cdot \begin{Bmatrix} \overline{u}_{r1} \\ \overline{u}_{z1} \\ \overline{u}_{r2} \\ \overline{u}_{z2} \end{Bmatrix}$$

Figure 324. Equation. Relationship between the tractions, stresses, and displacements.

From figure 324, it is seen that the four by four matrix $\mathbf{S_{2-noded}}$ is the stiffness matrix of the two-noded layer element which is calculated as shown in figure 325.

$$\mathbf{S_{2\text{-noded}}} = s\widehat{\mu} \cdot \mathbf{N} \cdot \mathbf{S_2} \cdot \mathbf{S_1^{-1}}; \mathbf{N} = \begin{bmatrix} -1 & 0 & 0 & 0 \\ 0 & -1 & 0 & 0 \\ 0 & 0 & 1 & 0 \\ 0 & 0 & 0 & 1 \end{bmatrix}$$

Figure 325. Equation. Local stiffness matrix of the two-noded layer element.

One-Noded Semi-Infinite Element

The axisymmetric one-noded element was schematically shown as the bottom layer in figure 295. As shown in that figure and as its name implies, the one-noded element has only a single boundary at the top of the layer and extends infinitely in all other directions. As a consequence, the waves in this element are only allowed to propagate away from the upper boundary (which is also the only boundary) without any waves reflecting back. Therefore, the solutions for the scalar potentials shown in the equations of figure 307 and figure 309 can be used without any modifications. Substituting these two equations into the equations shown in figure 311 and figure 312 results in the displacements shown in figure 326 and figure 327.

$$\bar{u}_r = -Ake^{-zf} - Ckge^{-zg}$$

Figure 326. Equation. Radial displacement of a one-noded layer element.

$$\bar{u}_z = -Afe^{-zf} + Ck^2 e^{-zg}$$

Figure 327. Equation. Vertical displacement of a one-noded layer element.

The displacements at the boundary are obtained by substituting $z = 0$ in these equations and can be written as the matrix form shown in figure 328.

$$\begin{Bmatrix} \bar{u}_{r1} \\ \bar{u}_{z1} \end{Bmatrix} = \begin{bmatrix} -k & kg \\ -f & k^2 \end{bmatrix} \begin{Bmatrix} A \\ C \end{Bmatrix} = \mathbf{S_3} \cdot \begin{Bmatrix} A \\ C \end{Bmatrix}$$

Figure 328. Equation. Displacements at the boundary of a one-noded layer element.

Again, the equations for the shear and normal stresses are obtained by substituting the potentials (equations shown in figure 307 and figure 309) into the equations figure 314 and figure 315, respectively, to produce the equations in figure 329 and figure 330.

$$\bar{\sigma}_{rz} = -s\hat{\mu}\{-2Akfe^{-zf} + Ck(k^2 + g^2)e^{-zg}\}$$

Figure 329. Equation. Shear stress of a one-noded layer element.

$$\bar{\sigma}_z = s\hat{\mu}\{A(k^2 + g^2)e^{-zf} - 2Ck^2 ge^{-zg}\}$$

Figure 330. Equation. Vertical stress of a one-noded layer element.

Substituting $z = 0$ in the equations shown in figure 329 and figure 330 results in the stresses at the boundary shown in figure 331.

$$\begin{Bmatrix} \bar{\sigma}_{r1} \\ \bar{\sigma}_{z1} \end{Bmatrix} = s\hat{\mu} \cdot \begin{bmatrix} 2kf & -k(k^2 + g^2) \\ (k^2 + g^2) & -2k^2 g \end{bmatrix} \begin{Bmatrix} A \\ C \end{Bmatrix} = s\hat{\mu} \cdot \mathbf{S_4} \begin{Bmatrix} A \\ C \end{Bmatrix}$$

Figure 331. Equation. Stresses at the boundary of a one-noded layer element.

From the equations shown in figure 328 and figure 331, the relationship shown in figure 332 is attained between the stresses and the displacements.

$$\left\{ \begin{array}{c} \overline{\sigma}_{rz1} \\ \overline{\sigma}_{z1} \end{array} \right\} = s\widehat{\mu} \cdot \mathbf{S_4} \cdot \mathbf{S_3}^{-1} \cdot \left\{ \begin{array}{c} \overline{u}_{r1} \\ \overline{u}_{z1} \end{array} \right\}$$

Figure 332. Equation. Stress-displacements relationship at the boundary of a one-noded layer element.

Where $\mathbf{S_3}$ and $\mathbf{S_4}$ were defined in the equations shown in figure 329 and figure 331, respectively. By applying the Cauchy stress principle, the relationship shown in figure 333 is achieved between the tractions, stresses, and displacements.

$$\left\{ \begin{array}{c} \overline{T}_{r1} \\ \overline{T}_{z1} \end{array} \right\} = \left\{ \begin{array}{c} -\overline{\sigma}_{rz1} \\ -\overline{\sigma}_{z1} \end{array} \right\} = \mathbf{S_{1-noded}} \cdot \left\{ \begin{array}{c} \overline{u}_{r1} \\ \overline{u}_{z1} \end{array} \right\}$$

Figure 333. Equation. Relationship between the tractions, stresses, and displacements at the boundary of a one-noded layer element.

Where the stiffness matrix for the one-noded element can be written in terms of the previously defined variables as the equation shown in figure 334.

$$\mathbf{S_{1-noded}} = -s\widehat{\mu} \cdot \mathbf{S_3} \cdot \mathbf{S_4}^{-1}$$

Figure 334. Equation. Local stiffness matrix of the one-noded layer element.

INCORPORATING ELASTIC AND VISCOELASTIC LAYER PROPERTIES

For a homogenous, isotropic, elastic material whose properties are independent of time, the relationship between the elastic modulus, E, and the lamé constant, μ, is given by the theory of linear elasticity as the equation in figure 335.

$$\mu = \frac{E}{2(1+v)}$$

Figure 335. Equation. Relationship between the elastic modulus (*E*) and the lamé constant (*μ*) for homogenous, isotropic, elastic material.

Because the parameters in that equation are not functions of time, the Laplace transform of the above equation is simply obtained as shown in figure 336.

$$\widehat{\mu}(s) = \frac{\mu}{s} = \frac{E}{2(1+v)} \cdot \frac{1}{s}$$

Figure 336. Equation. Laplace transform of the equation in figure 335.

However, as it was noted by the pioneer of the spectral element method for layered media Stephen Rizzi, it is advantageous to add a small amount of damping to the lamé constant, μ because no realistic material is purely elastic.[107] Following Rizzi, this artificial damping can be added to the above lamé constant as shown in figure 337.[107]

$$\hat{\mu}(s) = \hat{\mu}(s) \cdot (1 + \zeta \cdot s)$$

Figure 337. Equation. Lamé constant for elastic material.

Where ζ is the damping constant. To simulate the wave propagation through an elastic layer, the simple equation in figure 337 can be substituted into the equations for the layer elements presented earlier. To incorporate the viscoelastic material effects into the solution derived in the previous sections, it is necessary to adopt a simple function that is capable of representing the fundamental property of a viscoelastic material analytically. In addition, because all of the time-dependent variables, including stresses, displacements, and material properties (i.e., lamé constants), were transformed into the Laplace domain, it is preferable to choose a function that is easily transformable into the Laplace domain. Among the analytical functions described in chapter 3, the Prony series has been selected because it maintains a simple form while representing the viscoelastic property effectively. Again, this function is expressed as shown in figure 338.

$$E(t) = E_\infty + \sum_1^{14} \left(E_m \times e^{\left(\frac{-t_r}{TK_m}\right)} \right)$$

$$\log(t_r) = \log(t) - \log(aT)$$

$$\log(aT) = a_1 \times \left(T^2 - Tref^2\right) + a_2 \times (T - Tref)$$

Figure 338. Equation. Prony series.

Where:
E_m and TK_m = the Prony series parameters.
aT, a_1, and a_2 are the shift factor and its coefficients.
T and $Tref$ are the temperature and the reference temperature.

Taking the Laplace transform of the equation in figure 338 results in the equation shown in figure 339.

$$E(s) = E_\infty + \sum_1^{14} \left(E_m \times \frac{TK_m * aT}{TK_m \times s_r + 1} \right)$$

$$s_r = s \times aT$$

$$\log(aT) = a_1 \times \left(T^2 - Tref^2\right) + a_2 \times (T - Tref)$$

Figure 339. Equation. Prony series in the Laplace domain.

For viscoelastic material, the Poisson's ratio is also time dependent. However, the Poisson's ratio has typically been assumed to be a time-independent constant in past literature.[27] In addition, Lee and Kim showed that assuming a reasonable constant value for the Poisson's ratio still results in accurate viscoelastic responses.[108] The assumption of a constant Poisson's ratio implies that the time-dependent behavior of a viscoelastic material in shear or bulk is identical to the behavior in uniaxial mode, and simplifies the solution significantly.[109] With this assumption, the relationship between the viscoelastic lamé constant and the uniaxial relaxation modulus shown in figure 339 is found to be that shown in figure 340.

$$\hat{u}(s) = \frac{\hat{E}(s)}{2(1 + v)}$$

Figure 340. Equation. Relationship between the elastic modulus (*E*) and the lamé constant (*μ*) for viscoelastic material.

CONSTRUCTION OF THE GLOBAL STIFFNESS MATRIX

After the stiffness matrices have been obtained for all the layers that make up the structure, the global stiffness matrix can be constructed in the same way as the traditional FEA methods.[110] An in-depth explanation of the concept of the FEA as well as the relationship between the element and the global stiffness matrices is beyond the scope of this project. Hence, it is not explained herein, and interested readers are referred to a variety of textbooks available on this subject. In this appendix, only the generic conceptual schematics are outlined, and the discussion is kept to a minimum for conciseness of the report. Figure 341 shows the schematics of the global stiffness matrices for the two types of layered structures that are most widely adopted for modeling a pavement system.

Figure 341 shows how the global stiffness matrix is constructed for a layered system resting on a half-space. As previously mentioned, this pavement model is capable of dissipating the energy geometrically through the one-noded half-space and is generally used for simulating the FWD time histories that do not show free vibration at the end of the loading.

$$\mathbf{S}_{\text{Global}} = \begin{bmatrix} \mathbf{S}^1_{2-\text{noded}} & & & & \\ & \mathbf{S}^2_{2-\text{noded}} & & & \\ & & \ddots & & \\ & & & \mathbf{S}^{n-1}_{2-\text{noded}} & \\ & & & & \mathbf{S}^n_{1-\text{noded}} \end{bmatrix}$$

Figure 341. Equation. Construction of the global stiffness matrix for structures with a half-space.

Upon constructing the global stiffness matrix, the displacements at the system nodes can be found from the equation shown in figure 342.

$$\overline{\mathbf{U}} = \mathbf{S}_{\text{Global}}^{-1} \cdot \overline{\mathbf{P}}$$

$$\overline{\mathbf{U}} = \{\overline{U}_{r1} \quad \overline{U}_{z1} \quad \ldots \quad \overline{U}_{ri} \quad \overline{U}_{zi} \quad \ldots \quad \overline{U}_{rn} \quad \overline{U}_{zn}\}'$$

$$\overline{\mathbf{P}} = \{\overline{P}_{r1} \quad \overline{P}_{z1} \quad \ldots \quad \overline{P}_{ri} \quad \overline{P}_{zi} \quad \ldots \quad \overline{P}_{rn} \quad \overline{P}_{zn}\}'$$

Figure 342. Equation. The displacement at the system nodes.

$\overline{\mathbf{U}}$ is a vector of system displacements to be calculated in global coordinates with $\overline{U}_{ri}$ and $\overline{U}_{zi}$ being the radial and vertical displacements at the ith node from the top, respectively. Similarly, $\overline{\mathbf{P}}$ is a nodal force vector in global coordinates, with the radial and vertical forces at the ith node denoted as $\overline{P}_{ri}$ and $\overline{P}_{zi}$, respectively. The nodal forces in this vector should be obtained from the boundary conditions as presented in the next section.

BOUNDARY CONDITIONS FOR A CIRCULAR UNIT IMPULSE LOADING AT THE GROUND SURFACE

For the problem in hand where the loading is induced by an impact of a falling weight at the ground surface, all components of $\overline{\mathbf{P}}$ in figure 342 vanish except for $\overline{P}_{z1}$. In other words, the only external load applied to the system is in the vertical direction at the top node (node 1). In this project, this surface force is also in the form of a unit impulse load acting over a circular area, for the reasons explained in the System Response to Arbitrary Loading section. In the physical time and spatial domain, this boundary condition is mathematically expressed as shown in figure 343.

$$P_{z1}(r,t) = R(r) \cdot \delta(t)$$

$$R(r) = \begin{cases} 1 & , 0 < r \leq a \\ 0 & , r > a \end{cases}$$

Figure 343. Equation. Boundary conditions.

Where $\delta(t)$ is the Dirac delta function for the impulse loading, and a is the radius of the circular loaded area. However, note that the stiffness matrices were previously derived in the Laplace-Hankel domain rather than the physical domain. Therefore, it is also necessary to convert the above boundary condition into the one in the transformed domain. Because the Laplace transform of $\delta(t)$ is equal to 1, taking the Laplace-Hankel transforms of the equation shown in figure 343 simply results in the equation shown in figure 344.

$$\overline{P}_{z1}(k,s) = \frac{a}{k} J_1(ka)$$

Figure 344. Equation. Boundary conditions in the Laplace-Hankel domain.

INVERSION OF LAPLACE AND HANKEL TRANSFORMS

As mentioned, the displacements at all nodes of the system can be obtained through the equations shown in figure 342 from the global stiffness matrix and the force boundary condition described in the previous sections. Note again that the displacements obtained in this manner are in the Laplace-Hankel domain and need to be inverse transformed back to the physical domain. However, it has been shown that even for an elastic half-space (which simply has a single boundary) subjected to a point load, the closed form inversion of the Laplace-Hankel transformed displacement is rather complicated and is close to impossible for a generalized problem.[105] Therefore, the closed form inversion of the displacements obtained from the equations shown in figure 342 is not even attempted because of the mathematical complexity arising from the viscoelastic material behavior and the wave propagation phenomenon. Instead, the inversion is carried out numerically for both the Laplace and Hankel transforms.

NUMERICAL INVERSION OF THE HANKEL TRANSFORM

As mentioned earlier, Hankel transforms of orders zero and one were used to transform the vertical and radial displacements, respectively. Therefore, the inverse Hankel transform of respective orders must be carried out for the two displacements. In this appendix, the numerical integration scheme is outlined for the vertical displacement (i.e., the inverse Hankel transform of order zero). The inverse transform of the radial displacement can also be evaluated in a similar manner. The closed form equation for the inverse Hankel transform of the vertical displacement at node i is given as the equation in figure 345.

$$\widehat{U}_{zi}(r) = \int_0^\infty \overline{U}_{zi}(k) J_0(kr) k \, dk$$

Figure 345. Equation. Inverse Hankel transform of the vertical displacement.

This integral can also be written as the series of integrals shown in figure 346.

$$\widehat{U}_{zi}(r) = \int_{b_1}^{b_2} \overline{U}_{zi}(k) J_0(kr) k \, dk + \int_{b_2}^{b_3} \overline{U}_{zi}(k) J_0(kr) k \, dk + \cdots + \int_{b_n}^{b_{n+1}} \overline{U}_{zi}(k) J_0(kr) k \, dk + \cdots$$

Figure 346. Equation. Inverse Hankel transform as a series of integrals.

Then, each integral in the right-hand side of the equation in figure 346 must be evaluated numerically. Upon selecting the six-point Gaussian quadrature as the numerical scheme to use, the integral in the Figure 346 can be evaluated as shown in figure 347.[111]

$$\int_{b_n}^{b_{n+1}} \overline{U}_{zi}(k)J_0(kr)kdk = \frac{b_{n+1}-b_n}{2}\sum_{p=1}^{6}w_p\overline{U}_{zi}(\beta_p)J_0(\beta_p)\beta_p$$

$$\beta_p = \left(\frac{b_{n+1}-b_n}{2}\right)x_p + \left(\frac{b_{n+1}+b_n}{2}\right)$$

Figure 347. Equation. Evaluation of the inverse Hankel transform using six-point Gaussian quadrature scheme.

Where x_p and w_p are the Gaussian nodes and their corresponding weights, respectively.

The parameter b_n defines the limits for each integration, which can be chosen arbitrarily. However, Cornille indicated that the convergence of the Gaussian quadrature would be greatly improved if the limits were selected to be the successive roots of the derivative of the Bessel function that comprised the kernel of the inverse transform.[112] Based on a sensitivity analysis conducted by the research team for this project, subdividing the region between the successive roots of the Bessel function of order one (that is, the derivative of the Bessel function of order zero) into 10 smaller regions of equal intervals provided satisfactory results for the numerical integration.

Note that the upper bound of the integral shown in figure 345 is equal to infinity. This indicates that the summation of integrals shown in figure 346 should also span an infinite range. However, as was indicated by Kim, the numerical integration converges very rapidly even after the first few cycles of the Bessel function comprising the kernel of the inverse Hankel transform.[96] Therefore, in Kim's static solution for a viscoelastic layered system, the first five cycles of the Bessel function were used to invert the Hankel transform near the loaded area, and fewer cycles were used in the region far from the loading.[96] The developers of the axisymmetric spectral element method used the Fourier-Bessel series (which is the discrete version of the Hankel transform) in their solution and the summation was also carried out for approximately the first five cycles of the Bessel function.[2] Although the details are omitted for this report, the sensitivity analysis performed for the proposed algorithm also showed that the numerical integration over the first five cycles of the Bessel function is adequate for the solution.

NUMERICAL INVERSION OF THE LAPLACE TRANSFORM

For the inverse Laplace transform, a multiprecision numerical scheme known as the Fixed Talbot Algorithm is adopted in this report because of its efficiency, accuracy, and ease for implementation.[113] The Bromwich integral is the standard equation for the inverse Laplace transform is given by figure 348.

$$U_{zi}(t) = \frac{1}{\pi j}\int_B e^{ts}\widehat{U}_{zi}(s)ds$$

Figure 348. Equation. Bromwich integral.

Where $j = \sqrt{-1}$. The contour B, chosen for the above integral, is along the path shown in figure 349.

$$s(\theta) = \alpha\theta(\cot\theta + j), -\pi < \theta < +\pi$$
$$\alpha = \frac{2M}{5t}$$

Figure 349. Equation. The contour for the Bromwich integral.

In figure 349, M is the number of precision decimal digits to be used for the numerical analysis. For the sake of accuracy, this value is specified to be equal to the machine precision. Replacing the contour path in figure 348 with the one shown in figure 349 produces the result shown in figure 350:

$$U_{zi}(t) = \frac{\alpha}{\pi}\int_0^\pi Re\left[e^{ts(\theta)}\hat{U}_{zi}(s(\theta))(1 + j\gamma(\theta))\right]d\theta$$
$$\gamma(\theta) = \theta + (\cot\theta - 1)\cot\theta$$

Figure 350. Equation. Bromwich integral along the chosen contour path.

Finally, the inverse Laplace transform is obtained by approximating the integral shown in figure 350 through the trapezoidal rule shown in figure 351.

$$U_{zi}(t) = \frac{\alpha}{M}\left\{\frac{1}{2}\hat{U}_{zi}(\alpha)e^{\alpha t} + \sum_{q=1}^{M-1} Re\left[e^{ts(\theta_q)}\hat{U}_{zi}\left(s(\theta_q)\right)\left(1 + j\gamma(\theta_q)\right)\right]\right\}$$
$$\theta_q = \frac{q\pi}{M}$$

Figure 351. Equation. Evaluation of Bromwich integral through the trapezoidal rule.

SYSTEM RESPONSE TO ARBITRARY LOADING

As described in the equations shown in figure 343, the boundary condition considered in the previous sections was for a unit impulse load distributed over a circular area. As such, the vertical displacement, U_{zi}, obtained using the equation shown in figure 351 represents the unit impulse response of the layered system in time domain. The primary advantage of the time-domain unit impulse response is that the system response to any arbitrary loading can be obtained through the convolution integral.[114,3] Theoretically, this convolution integral for a continuous function is given as shown in figure 352.

$$y_{zi}(t) = U_{zi}(t) * T(t) = \int_0^t U_{zi}(t - \tau)T(\tau)d\tau$$

Figure 352. Equation. Convolution integral for a continuous function.

Where $T(t)$ could be any arbitrary time-dependent loading function, and $y_{zi}(t)$ is the corresponding vertical displacement at node i. For a discrete signal such an FWD time history, figure 352 must evaluated numerically as shown in figure 353.[114,3]

$$y_{zi}(t_n) = \sum_{t_p=1}^{t_n} U_{zi}(t_n - t_p)T(t_p)\Delta t$$

Figure 353. Equation. Numerical evaluation of the convolution integral.

Where Δt is time interval of the discrete signal, and $t_n = n\Delta t$ for an integer n.

APPENDIX D. FIELD MEASUREMENT FWD TEST DATA

FWD TEST DATA

FWD test information, sensor location, peak stress, peak load, and peak deflection for Waverly road test near Lansing, MI, at section 1 and 3 are shown in table 67 and table 68, respectively.

Table 67. FWD Test information from station 1 (afternoon test).

Contact Radius 5.9		Morning Test				Afternoon Test				Evening Test			
		Drop 1	Drop 2	Drop 3	Drop 4	Drop 1	Drop 2	Drop 3	Drop 4	Drop 1	Drop 2	Drop 3	Drop 4
Stress (psi)		57.9	86.3	111.7	147.5	54.9	83.7	108.2	142.9	55.0	83.7	108.2	142.9
Force (kip)		6.33	9.46	12.23	16.15	6.01	9.16	11.86	15.65	6.01	9.16	11.86	15.65
Sensors location (inches)		Deflection (mil)											
D1	0	12.7	19.8	26.2	34.8	15.2	24.2	32.5	44.1	15.2	24.2	32.5	44.1
D2	8	9.8	15.3	20.4	27.3	10.9	17.4	23.4	31.8	10.9	17.4	23.4	31.8
D3	12	8.2	12.9	17.3	23.1	8.4	13.6	18.3	25.0	8.4	13.6	18.3	25.0
D4	18	5.9	9.5	12.8	17.2	5.7	9.4	12.8	17.5	5.7	9.4	12.8	17.5
D5	24	4.4	7.1	9.6	13.0	4.1	6.8	9.3	12.8	4.1	6.8	9.3	12.8
D6	36	2.6	4.1	5.6	7.7	2.4	3.9	5.4	7.5	2.4	3.9	5.4	7.5
D7	48	1.7	2.6	3.6	4.9	1.6	2.5	3.5	4.8	1.5	2.5	3.4	4.8
D8	60	1.1	1.9	2.6	3.5	1.1	1.8	2.4	3.4	1.1	1.8	2.4	3.4

Table 68. FWD Test information from station 3 (afternoon test).

Contact Radius 5.9		Morning Test				Afternoon Test				Evening test			
		Drop 1	Drop 2	Drop 3	Drop 4	Drop 1	Drop 2	Drop 3	Drop 4	Drop 1	Drop 2	Drop 3	Drop 4
Stress (psi)		57.3	85.6	111.0	145.6	54.5	82.5	107.3	141.9	54.5	82.5	107.3	54.5
Force (kip)		6.28	9.37	12.16	15.95	5.98	9.04	11.75	15.54	5.98	9.04	11.75	15.54
Sensors location (inches)		Deflection (mil)											
D1	0	14.7	22.2	29.2	38.7	16.9	25.7	34.1	45.5	16.9	25.7	34.1	45.5
D2	8	11.8	17.9	23.4	30.9	12.7	19.4	25.7	34.2	12.7	19.4	25.6	34.2
D3	12	9.9	15.0	19.8	26.1	10.2	15.8	21.0	27.9	10.2	15.8	21.0	27.9
D4	18	7.3	11.2	14.7	19.6	7.0	11.0	14.7	19.7	7.0	11.0	14.7	19.7
D5	24	5.3	8.2	10.9	14.6	5.0	7.8	10.5	14.2	5.0	7.8	10.5	14.2
D6	36	3.0	4.6	6.2	8.3	2.7	4.3	5.8	7.9	2.7	4.3	5.8	7.9
D7	48	1.8	2.8	3.9	5.2	1.7	2.6	3.6	4.9	1.7	2.6	3.6	4.9
D8	60	1.2	2.0	2.7	3.7	1.1	1.8	2.5	3.5	1.1	1.8	2.5	3.5

Temperatures along the depth of the pavement were recorded each time the FWD test was performed. Variation in temperature along the depth at section 1 and section 3 at three FWD tests are shown in table 69 and table 70, respectively.

Table 69. Temperature profile at section 1.

| Time (h:min) | Temperature for Actual Depth (°F) | | | | | | Remarks |
	0 inches	2 inches	4 inches	6 inches	8 inches	10 inches	
Morning 9:40	63.1	61.0	59.7	59.2	59.2	59.4	Cloudy
Afternoon14:05	90.0	83.8	74.8	68.5	65.1	62.8	Cloudy
Evening 19:05	91.6	90.0	85.1	79.9	75.7	72.1	Cloudy

Temperature holes 5 ft behind FWD load (north).

Table 70. Temperature profile at section 3.

| Time (h:min) | Temperature for Actual Depth (°F) | | | | | | Remarks |
	0 inches	2 inches	4 inches	6 inches	8 inches	10 inches	
10:15	68.7	64.0	60.3	59.2	58.5	58.3	Cloudy
14:40	87.1	81.1	73.4	69.3	65.7	63.1	Cloudy
19:45	82.6	83.7	80.2	77.0	73.8	70.3	Cloudy

Temperature holes 10 ft behind FWD load (north).

LABORATORY-MEASURED RESULTS FOR WAVERLY ROAD

Figure 354 through figure 356 present graphs of the laboratory-measured results for Waverly Road using different sample sizes.
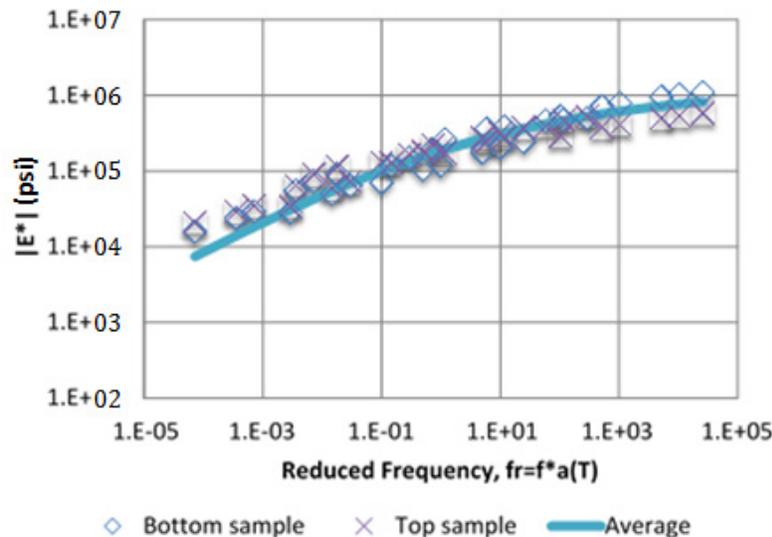
Figure 354. Graph. Laboratory-measured dynamic modulus at station 1 using 1.5- by 3.94-inch samples.
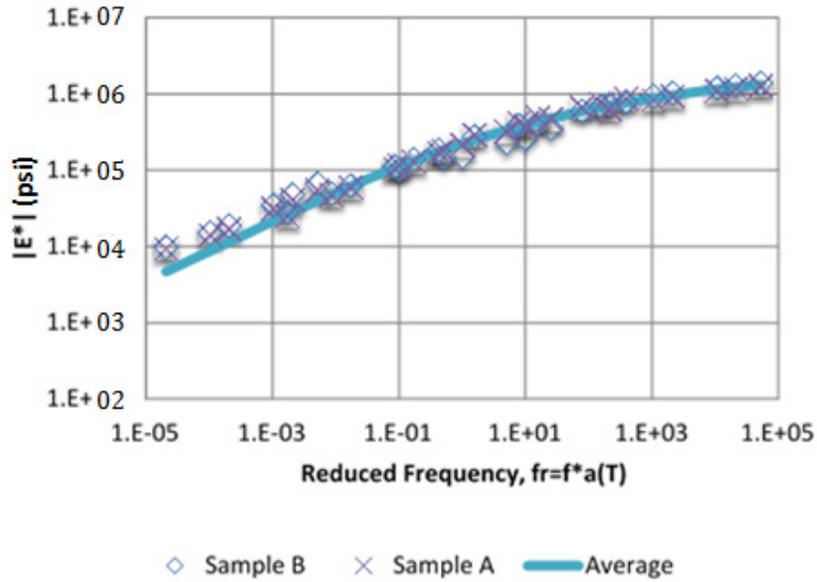
Figure 355. Graph. Laboratory-measured dynamic modulus at station 1 using 3.94- by 5.9-inch samples.
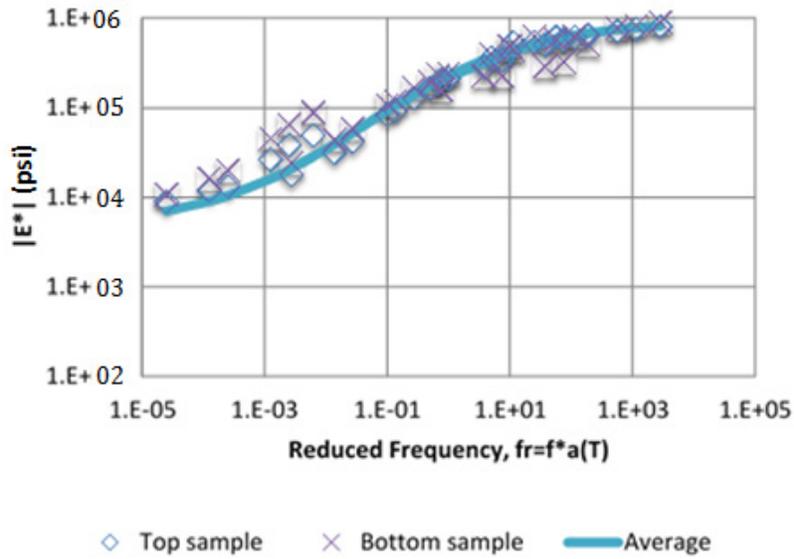
Figure 356. Graph. Laboratory-measured dynamic modulus at station 3 using 1.5- by 3.94-inch samples.

REFERENCES

1. American Association of State Highway and Transportation Officials. (2008) *Mechanistic-Empirical Pavement Design Guide—A Manual of Practice*. Publication MEPDG-(2008). American Association of State Highway and Transportation Officials, Washington, DC.

2. Al-Khoury, R., Scarpas, A., Kasbergen, C., and Blaauwendraad, J. (2001) "Spectral Element Technique for Efficient Parameter Identification of Layered Media. Part I: Forward Calculation." *International Journal of Solids and Structures*, Volume 38. Elsevier, Inc., Amsterdam, The Netherlands.

3. Bendat, J.S. and Piersol, A.G. (2010). *Random Data Analysis and Measurement Procedures.* 4th ed. John Wiley & Sons, Inc., Hoboken, NJ.

4. ASTM D-4694-96 (1996) "Standard Test Method for Deflections with a Falling-Weight-Type Impulse Load Device," *Annual Book of ASTM Standards, Volume 04.03*. ASTM International, West Conshohocken, PA.

5. FHWA-LTPP Technical Support Services Contractor. (2000) *LTPP Manual for Falling Weight Deflectometer Measurements Operational Field Guidelines*. Federal Highway Administration, Washington, DC. Available at http://www.fhwa.dot.gov/publications/ research/infrastructure/ pavements/ltpp/fwdman/fwdman1.pdf. Accessed August 3, 2009.

6. Alavi, S., Lecates, J.F., and Tavares, M.P. (2008) "NCHRP Synthesis 381: Falling Weight Deflectometer Usage." *A Synthesis of Highway Practice*, National Cooperative Highway Research Program, Transportation Research Board, Washington, DC.

7. Dynatest ®Consulting, Inc. (2009) *Dynatest Falling Weight Deflectometers*. Available at http://www.dynatest.com/structural-hwd-fwd.php. Accessed August 3, 2009.

8. JILS™. (2015) *The JILS, Foundation Mechanics, Falling Weight Deflectometers*. El Segundo, CA. Available at http://www.jilsfwd.com. Accessed October 14, 2015.

9. Applied Research Associates, Inc. (2004) *Comparison Study of the JILS Model 20T and Dynatest Model 8002 Falling Weight Deflectometers*. ARA Project No. 16214.

10. Engineering and Research International, Inc. (ERI). (2009) *KUAB Falling Weight Deflectometer*. Available at www.erikuab.com/kuab.htm. Accessed August 3, 2009.

11. National Highway Institute. (1994) *Pavement Deflection Analysis*. Report No. FHWA-HI-94-021. National Highway Institute, Arlington, VA.

12. Haas, R.C.G., Hudson, W.R., and Zaniewski, J.P. (1994) *Modern Pavement Management*. Krieger Publishing Company, Melbourne, FL.

13. Irwin, L.H. (2002) *Backcalculation: An Overview and Perspective*. FWD/Backanalysis Workshop, 6th International Conference on the Bearing Capacity of Roads, Railways, and Airfields, Lisbon, Portugal.

14. Irwin, L.H., Yang, W.S., and Stubstad, R.N. (1989) *Deflection Reading Accuracy and Layer Thickness Accuracy in Backcalculation of Pavement Layer Moduli*. First International Symposium on Nondestructive Testing of Pavements and Backcalculation of Moduli. ASTM STP 1026. ASTM International, West Conshohocken, PA.

15. Chatti, K. (2004) "Use of Dynamic Analysis for Interpreting Pavement Response in Falling Weight Deflectometer Testing." *Materials Evaluation*. *62*(7), p 764–774. American Society for Nondestructive Testing, Columbus, OH.

16. Boussinesq, J. (1885) *Application des Potentiels a l'etude de l'equilibre et du Movement des Solides Elastiques*. Gauthier-Villars, Paris, France.

17. Burmister, D.M. (1943) "The Theory of Stresses and Displacements in Layered Systems and Applications to Design of Airport Runways," *Proceedings of the Highways Research Board*. Volume 23. Highway Research Board, Washington, DC.

18. Burmister, D.M. (1945) "The General Theory of Stresses and Displacements in Layered Systems." *Journal of Applied Physics*. *16*(2, 3, and 5).

19. Ullidtz, P. (1987) *Pavement Analysis*. Elsevier Inc. Amsterdam, The Netherlands.

20. Ullidtz, P. (1998) *Modelling Flexible Pavement Response and Performance*. Polyteknisk Forlag, Narayana Press, Gylling, Denmark.

21. Warren, H. and Dieckmann, W.L. (1963) *Numerical Computation of Stresses and Strains in a Multiple-Layered Asphalt Pavement System*. California Research Corporation, Richmond, CA.

22. Thanaya, I.N.A. (1995) *Study of the Elastic Layered System Computer Program (ELSYM5) for Pavement Design*. Civil and Resource Engineering, University of Auckland, Auckland, New Zealand.

23. De Jong, D.L., Peutz, M.G.F., and Korswagen, A.R. (1979) *Computer Program BISAR, Layered Systems Under Normal and Tangential Surface Loads*. Koninklijke-Shell Laboratorium, Amsterdam, The Netherlands.

24. Irwin, L. and Speck, D. (1986) *NELAPAV User's Guide*. Cornell University Local Road Program, Report No. 86-1. Cornell University, Ithaca, NY.

25. Brown, S.F., Tam, W.S., and Brunton, J.M. (1987) "Structural Evaluation and Overlay Design: Analysis and Implementation," *Proceedings, 6th International Conference on Structural Design of Asphalt Pavements*, *1*, p. 1,013–1,028.

26. Kenis, W.J., Sherwood, J.A., and McMahon, T.F., (1982) "Verification and Application of the VESYS Structural Sub-System," *Proceedings, 5th International Conference on Structural Design of Asphalt Pavements*, *1*, p. 333–346.

27. Huang, Y.H. (2004) *Pavement Analysis and Design*, Second Edition, Prentice-Hall, Upper Saddle River, NJ.

28. Kausel, E. and Roesset, J.M. (1981) "Stiffness Matrices for Layered Soils." *Bulletin of the Seismological Society of America*, *71*(6). p. 1,743–1,761. Seismological Society of America, El Cerrito, CA.

29. Roesset, J.M. (1987) *Computer Program UTFWIBM*. University of Texas, Austin, TX.

30. Chang, D.W., Kang, Y.V., Roesset, J.M., and Stokoe, K.H. (1992) "Effect of Depth to Bedrock on Deflection Basins Obtained with Dynaflect and Falling Weight Deflectometer Tests." *Transportation Research Record 1355*. Transportation Research Board, Washington, DC.

31. Kang, Y.V. (1998) "Multifrequency Back-Calculation of Pavement-Layer Moduli." *Journal of Transportation Engineering*. *124*(1), p. 73–81, American Society of Civil Engineers, New York, NY.

32. Chen, S.S. (1987) *The Response of Multilayered Systems to Dynamic Surface Loads*. Ph.D. Dissertation. University of California, Berkeley, CA.

33. Magnuson, A.H., Lytton, R.L., and Briggs, R. (1991) "Comparison of Computer Predictions and Field Data for Dynamic Analysis of Falling-Weight Deflectometer Data." *Transportation Research Record 1293*. Transportation Research Board, Washington, DC.

34. Press, W.H., Flannery, B.P., Teukolsky, S.A., and Vetterling, W.T. (1990) *Numerical Recipes—The Art of Scientific Computing*. Cambridge University Press, New York, NY.

35. Lee, S.W., Mahoney, J.P., and Jackson, N.C. (1988) "Verification of Backcalculation of Pavement Moduli." *Transportation Research Record 1196*. Transportation Research Board, Washington, DC.

36. Uzan, J. (1994) "Dynamic Linear Backcalculation of Pavement Material Parameters." *Journal of Transportation Engineering*. *120*(1), p. 109–125. American Society of Civil Engineers, Reston, VA.

37. Uzan, J. (1994) "Advanced Backcalculation Techniques." *Nondestructive Testing of Pavements and Backcalculation of Moduli*. *2*. ASTM STP 1198. ASTM International, West Conshohocken, PA.

38. Ong, C.L, Newcomb, D.E., and Siddharthan, R. (1991) "Comparison of Dynamic and Static Backcalculation Moduli for Three-Layer Pavements." *Transportation Research Record 1293*. Transportation Research Board, Washington, DC.

39. Losa, M. (2002) "The Influence of Asphalt Pavement Layer Properties on Vibration Transmission." *International Journal of Pavements*. *1*(1), p. 67–76. Sao Paulo, Brazil.

40. Al-Khoury, R., Scarpas, A., Kasbergen, C., and Blaauwendraad, J. (2001) "Spectral Element Technique for Efficient Parameter Identification of Layered Media. Part II: Inverse Calculation." *International Journal of Solids and Structures*. Volume 38. Elsevier, Inc., Amsterdam, The Netherlands.

41. Matsui, K., Kikuta, K., Nishizawa, T., and Kasahara, A. (2000) "Comparative Studies of Backcalculated Results From FWDs With Different Loading Duration." *Nondestructive Testing of Pavement and Backcalculation of Moduli,* S. D. Tayabji and E. O. Lukanen, editors. *3*, p. 470–483. ASTM International, West Conshohocken, PA.

42. Chatti, K., Ji, Y., and Harichandran, R.S. (2004) *Development of a Dynamic Backcalculation Computer Program for Flexible Pavement Layer Parameters*. Final Report. Michigan Department of Transportation, Lansing, MI.

43. Chatti, K., Ji, Y., and Harichandran, R.S. (2006) "Dynamic Backcalculation of Pavement Layer Parameters Using Frequency and Time Domain Methods." *Proceedings, 10th International Conference on Asphalt Pavements*. Quebec City, Quebec, Canada.

44. Turkiyyah, G.M. (2004) *Feasibility of Backcalculation Procedures Based on Dynamic FWD Response Data*. WA-RD 586.1. Washington State Department of Transportation, Olympia, WA.

45. Bush, A.J. and Alexander D.R. (1985) "Pavement Evaluation Using Deflection Basin Measurements and Layered Theory." *Transportation Research Record 1022*. Transportation Research Board, Washington, DC.

46. Al-Khoury, R., Scarpas, A., Kasbergen, C., and Blaauwendraad, J. (2002) "Spectral Element Technique for Efficient Parameter Identification of Layered Media. Part III: Viscoelastic Aspects." *International Journal of Solids and Structures*. *39,* p. 2,189–2,201. Elsevier, Inc., Amsterdam, The Netherlands.

47. Meier, R.W. and Rix, G.J. (1994) "Backcalculation of Flexible Pavement Moduli Using Artificial Neural Networks." *Transportation Research Record,1448*. Transportation Research Board, Washington, DC.

48. Meier, R.W. and Rix, G.J. 1995. "Backcalculation of Flexible Pavement Moduli From Dynamic Deflection Basins Using Artificial Neural Networks." *Transportation Research Record 1473*. Transportation Research Board, Washington, DC.

49. Harichandran, R.S., Mahmood, T., Raab, A., and Baladi, G.Y. (1994) "Backcalculation of Pavement Layer Moduli, Thicknesses and Bedrock Depth Using a Modified Newton Method." *Nondestructive Testing of Pavements and Backcalculation of Moduli*, *2*. ASTM STP 1198. ASTM International, West Conshohocken, PA.

50. Ji, Y. (2005) *Frequency and Time Domain Backcalculation of Flexible Pavement Layer Parameters*. Ph.D. Dissertation, Department of Civil and Environmental Engineering. Michigan State University, East Lansing, MI.

51. Matsui, K., Maina, J.W., Hachiya, Y., and Ozawa, Y. (2011) *Wave Propagation Analysis for Flexible Pavements and Its Application to Backcalculation Analysis*. 90th Transportation Research Board Annual Meeting. Paper no. 11-2971 (CDROM). Available at http://amonline.trb.org/11-2971-1.2446683?qr=1. Accessed June 9, 2016.

52. Zhang, W., Drescher, A., and Newcomb, D.E. (1997. "Viscoelastic Analysis of Diametral Compression of Asphalt Concrete." *Journal of Engineering Mechanics*, American Society of Engineers, *123*(6), p. 596–603.

53. Zhang, W., Drescher, A., and Newcomb, D.E. (1997) "Viscoelastic Behavior of Asphalt Concrete in Diametral Compression." *Journal of Transportation Engineering*, America Society of Engineers, *123*(6), p. 495–502.

54. Ullidtz, P. (2000) "Will Non-Linear Backcalculation Help?" *Nondestructive Testing of Pavements and Backcalculation of Moduli. 3*. ASTM STP 1375. ASTM International, West Conshohocken, PA.

55. Washington State Department of Transportation. (2005) *EVERSERIES© User's Guide: Pavement Analysis Computer Software and Case Studies.* Washington State Department of Transportation, Olympia, WA.

56. Roesset, J.M., Stokoe, K.H., and Seng, C.R. (1995) "Determination of Depth to Bedrock from Falling Weight Deflectometer Test Data." *Transportation Research Record 1504*. Transportation Research Board, Washington, DC.

57. National Cooperative Highway Research Program. (2003) *Harmonized Test Methods for Laboratory Determination of Resilient Modulus for Flexible Pavement Design*. Project 1-28A. National Cooperative Highway Research Program, Transportation Research Board, Washington, DC.

58. Park, S.W. and Schapery, R.A. (1999) "Methods of Interconversion Between Linear Viscoelastic Material Functions. Part I—A Numerical Method Based on Prony Series." *International Journal of Solids and Structures*, *36*, p. 1,653–1,675.

59. Varma, S., Kutay, M.E., and Chatti, K. (2013) *Data Requirements from Falling Weight Deflectometer Tests for Accurate Backcalculation of Dynamic Modulus Master Curve of Asphalt Pavements*. 2013 Airfield & Highway Pavement Conference, Los Angeles, CA.

60. Varma, S., Kutay, M.E., and Levenberg, E. (2013) "A Viscoelastic Genetic Algorithm for Inverse Analysis of Asphalt Layer Properties from Falling Weight Deflections." *Transportation Research Record, 2369*, p. 38–46. Transportation Research Board, Washington, DC.

61. Burmister, D.M. (1943) "The Theory of Stress and Displacements in Layered Systems and Applications to the Design of Airport Runways." Highway Research Board, *Proceedings of Annual Meeting*, *23*, p. 126–144.

62. Burmister, D.M. (1945) "The General Theory of Stress and Displacements in Layered Soil Systems, I." *Journal of Applied Physics*, *16*(2), p. 89–94.

63. Burmister, D.M. (1945) "The General Theory of Stress and Displacements in Layered Soil Systems, II." *Journal of Applied Physics*, *16*(3), p. 126–127.

64. Burmister, D.M. (1945) "The General Theory of Stress and Displacements in Layered Soil Systems, III." *Journal of Applied Physics*, *16*(5), p. 296–302.

65. Kutay, M.E., Chatti, K., and Lei, L. (2011) "Backcalculation of Dynamic Modulus from FWD Deflection Data." *Transportation Research Record*, TRR 2227, *3*, pp. 87–96. Transportation Research Board, Washington, DC.

66. Levenberg, E. (2013) "Inverse Analysis of Viscoelastic Pavement Properties Using Data from Embedded Instrumentation." *International Journal for Numerical and Analytical Methods in Geomechanics*, *37*, p. 1,016–1,033.

67. Schapery, R.A. (1965) "Method of Viscoelastic Stress Analysis using Elastic Solutions." *Journal of the Franklin Institute*, *279* (4), p. 268–289.

68. Schapery, R.A. (1974) "Viscoelastic Behavior and Analysis of Composite Materials." *Mechanics of Composite Materials*, Academic Press, Inc., New York, NY, p. 85–168.

69. Levenberg, E. (2008) *Validation of NCAT Structural Test Track Experiment Using INDOT APT Facility*. Final Report, North Central Superpave Center, Joint Transportation Research Program Project No. C-36-31R SPR-2813, Purdue University, Lafayette, IN.

70. Leaderman, H. (1943) *Elastic and Creep Properties of Filamentous Materials and Other Higher Polymers*. The Textile Foundation, Washington, DC.

71. Schapery, R.A. (1969) "On the Characterization of Nonlinear Viscoelastic Materials." *Polymer Engineering and Science*, *9*(4), p. 295–310.

72. Fung, Y.C. (1996) *Biomechanics Mechanical Properties of Living Tissues*, 2d edition, Springer, New York, NY.

73. Masad, E., Huang, C., Airey, G., and Muliana, A. (2008) "Nonlinear Viscoelastic Analysis of Unaged and Aged Asphalt Binders." *Construction and Building Materials*, *22*, p. 2,170–2,179.

74. Yong, Y., Yang, X., and Chen, C. (2010) "Modified Schapery's Model for Asphalt Sand." *Journal of Engineering Mechanics*, *136*(4), p. 448–454.

75. Nekouzadeh, A. and Genin, G.M. (2013) "Adaptive Quasi-Linear Viscoelastic Modeling." *Computational Modeling in Tissue Engineering, Studies in Mechanobiology, Tissue Engineering and Biomaterials*, *10*, p. 47–83.

76. Yau, A. and Von Quintus, H.L. (2002) *Study of Laboratory Resilient Modulus Test Data and Response Characteristics*. Final Report. Report No. FHWA-RD-02-051,Federal Highway Administration, Washington, DC.

77. Taylor, A.J. and Timm, D.H. (2009) *Mechanistic Characterization of Resilient Moduli for Unbound Pavement Layer Materials*. Report 09-06. National Center for Asphalt Technology, Auburn University, Auburn, AL.

78. Hicks, R.G. and Monismith, C.L. (1971) "Factors Influencing the Resilient Properties of Granular Materials." *Highway Research Record*, *345*, pp. 15–31.

79. Uzan, J. (1985) "Characterization of Granular Material." *Transportation Research Record 1022*, Transportation Research Board, Washington, DC.

80. Witczak, M.W. and Uzan, J. (1988) *The Universal Airport Pavement Design System, Report I of IV: Granular Material Characterization*. University of Maryland, College Park, MD.

81. Hjelmstad, K.D. and Taciroglu, E. (2000) "Analysis and Implementation of Resilient Modulus Models for Granular Solids." *Journal of Engineering Mechanics*, *126*(8), p. 821–830.

82. Tutumluer, E. (1995) *Predicting Behavior of Flexible Pavements with Granular Bases*. Ph.D. Dissertation, School of Civil and Environmental Engineering, Georgia Institute of Technology, Atlanta, GA.

83. Raad, L. and Figueroa, J.L. (1980) "Load Response of Transportation Support Systems." *Transportation Engineering Journal*, *106* (1), p. 111–128.

84. Harichandran, R.S., Baladi, G.Y., and Yeh, M.S. (1989) *MICH-PAVE User's Manual*. Final Report, FHWA-MI-RD-89-023, Department of Civil and Environmental Engineering, Michigan State University, East Lansing, MI.

85. Schwartz, C.W. (2002) "Effect of Stress-Dependent Base Layer on the Superposition of Flexible Pavement Solutions." *International Journal of Geomechanics*, *2*(3), p. 331–352.

86. Kim, M., Tutumluer, E., and Know, J. (2009) "Nonlinear Pavement Foundation Modeling for Three-Dimensional Finite-Element Analysis of Flexible Pavements," *International Journal of Geomechanics*, *9*(5), p. 195–208.

87. Zhou, H. (2000) "Comparison of Backcalculated and Laboratory-Measured Moduli on AC and Granular Base Layer Materials," *Nondestructive Testing of Pavements and Backcalculation of Moduli*, *3*, ASTM STP 1375, S.D. Tayabji and E.O. Lukamen (eds.), ASTM International, West Conshohocken, PA.

88. Shames, I.H. and Cozzarelli, F.A. (1997) *Elastic and Inelastic Stress Analysis*. Revised printing. Taylor and Francis, Abington, UK.

89. Qi, X., Shenoy, A., Kutay, M.E., Gibson, N.H., Youtcheff, J., and Harman, T. (2008) *Update on FHWA ALF Tests of Modified Binder Pavements*. 3rd International Conference on Accelerated Pavement Testing, Madrid, Spain.

90. ABAQUS. (2011). *ABAQUS Analysis User's Manual*, version 6.11, Dassault Systèmes Simulia Corp., Providence, RI.

91. Fwa, T.F., Tan C.Y., and Chan, W.T. (1997) "Backcalculation Analysis of Pavement-Layer Moduli Using Genetic Algorithms," *Transportation Research Record 1570*, p. 134–142. Transportation Research Board, Washington, DC.

92. Alksawneh, W. (2007) *Backcalculation of Pavement Moduli Using Genetic Algorithms*. Ph.D. Thesis, The University of Akron, Akron, OH.

93. Park, S.W., Park, H.M., and Hwang, J.J. (2009) "Application of Genetic Algorithm and Finite Element Method for Backcalculating Layer Moduli of Flexible Pavements." *Korean Society of Civil Engineers Journal of Civil Engineering. 14*(2), p. 183–190.

94. Ullidtz, P. (1988) *Pavement Analysis*. Elsevier Science. New York, NY.

95. Appea, A.K. (2003). *Validation of FWD Testing Results At The Virginia Smart Road: Theoretically and by Instrument Responses*. Ph.D. Thesis, Virginia Polytechnic Institute and State University, Blacksburg, VA.

96. Lei, L. (2011). *Backcalculation of Asphalt Concrete Complex Modulus Curve by Layered Viscoelastic Solution*. Ph. D. Dissertation, Michigan State University, East Lansing, MI.

97. Kim, Y.R., Underwood, B., Sakhaei, F., Jackson, N., and Puccinelli, J. (2011) *LTPP Computed Parameters: Dynamic Modulus*. Report No. FHWA-HRT-10-035, Federal Highway Administration, Washington, DC.

98. Lee, H.S. (2011) *ViscoWave—A New Forward Solution for Dynamic Backcalculation*. Presentation at the 20th Annual FWD Users Group Meeting. Champaign, IL.

99. Kim, Y.R. (2009). *Modeling of Asphalt Concrete*, ASCE Press, McGraw Hill, New York, NY.

100. Ongel, A. and Harvey, J.T. (2004) *Analysis of 30 Years of Pavement Temperatures Using the Enhanced Integrated Climate Model (EICM)*. Pavement Research Center, Institute of Transportation Studies, University of California–Berkeley, and University of California–Davis, Berkeley and Davis, CA.

101. Malvern, L.E. (1969) *Introduction to the Mechanics of a Continuous Medium*. Prentice-Hall, Inc. East Saddle River, NJ.

102. Wineman, A.S. and Rajagopal, K.R. (2000) *Mechanical Response of Polymers: An Introduction*. Cambridge University Press, New York, NY.

103. Christensen, R.M. (2003) *Theory of Viscoelasticity*. 2d edition. Dover Publications, Inc., New York, NY.

104. Ewing, W.M., Jardetzky, W.S., and Press, F. (1957) *Elastic Waves in Layered Media*. McGraw-Hill Book Company. New York, NY.

105. Graff, K. (1991) *Wave Motion in Elastic Solids*. Dover Publications, Inc., New York, NY.

106. Sneddon, I.N. (1995) *Fourier Transforms*. Dover Publications, Inc., New York, NY.

107. Rizzi, S. (1989) *A Spectral Analysis Approach to Wave Propagation in Layered Solids*. Ph.D. Dissertation. Purdue University, Lafayette, IN.

108. Lee, H.S. and Kim, J. (2009) "Determination of Viscoelastic Poisson's Ratio and Creep Compliance from the Indirect Tension Test." *Journal of Materials in Civil Engineering*, *21*(8), pp. 416–425.

109. Kim, J., Lee, H.S., and Kim, N. (2010) "Determination of Shear and Bulk Moduli of Viscoelastic Solids from the Indirect Tension Creep Test." *Journal of Engineering Mechanics*. America Society of Civil Engineers. *36*, p.1,067–1,076.

110. Cook, R.D., Malkus, D.S., Plesha, M.E., and Witt, R.J. (2001) *Concepts and Applications of Finite Element Analysis*. 4th edition. John Wiley & Sons, Inc. New York, NY.

111. Abramowitz, M. and Stegun, I.A. (1972) *Handbook of Mathematical Functions with Formulas, Graphs, and Mathematical Tables*. Dover Publications, Inc., New York, NY.

112. Cornille, P. (1972) "Computation of Hankel Transforms." *SIAM Review*, *14*(2), p. 278-285."

113. Abate, J. and Valko, P.P. (2004) "Multi-Precision Laplace Transform Inversion." *International Journal for Numerical Methods in Engineering*, *60*, p. 979–993.

114. Santamarina, J.C. and Fratta, D. (1998) *Introduction to Discrete Signals and Inverse Problems in Civil Engineering*. American Society of Civil Engineers. Reston, VA.